The distribution and evolution of Antarctic surface meltwater

Peter Andrew Tuckett

PhD thesis

Submitted in accordance with the requirements
for the degree of Doctor of Philosophy

Department of Geography

July 2023

Abstract

Mass losses from the Antarctic Ice Sheet are the largest uncertainty in predicting sea level rise. The role of surface meltwater in determining Antarctic sea level contribution is poorly understood, despite its potential to impact ice sheet mass balance via a number of mechanisms and feedbacks. This thesis uses novel methodologies, implemented within Google Earth Engine, to study the distribution and evolution of Antarctic surface meltwater at unprecedented spatial and temporal scales. An automated method for mapping surface meltwater is firstly developed and applied to the Amery Ice Shelf, and then at a continent-wide scale. The method overcomes previous challenges relating to data processing capability and variability in optical satellite image visibility, enabling the production of robust, continuous time series of surface meltwater area. The first continent-wide dataset of surface meltwater, spanning 2006 to 2021, reveals a significant increasing trend in surface meltwater area across East Antarctica since 2006. For the first time, clear links between surface meltwater area and large-scale modes of atmospheric variability are demonstrated, although these cannot explain the increasing trend observed in East Antarctica. Instead, this increase is likely a consequence of ice surfaces becoming more favourable to meltwater ponding. This thesis also explores novel techniques for improving quantification of surface meltwater volumes. A multi-satellite approach is applied to improve the temporal resolution of volume data, revealing a variety of mechanisms via which supraglacial lakes evolve at the Amery Ice Shelf. Combined automated and manual analysis additionally reveals the importance of melt-albedo feedbacks in controlling the spatial distribution of meltwater in the region. The complexity of meltwater processes motivates future studies to explore drivers and impacts of meltwater at a regional scale, including assessments of ice shelf vulnerability. Furthermore, the greater abundance of surface meltwater on grounded ice than previously realised raises questions regarding the potential for meltwater to reach the subglacial environment and impact grounded ice flow. Increased understanding of these mechanisms, perhaps facilitated by the findings of this thesis, will help elucidate the role of surface meltwater in the future of the Antarctic Ice Sheet.

Acknowledgements

Table of Contents

3 Exploring styles of meltwater evolution at the grounding zone of the Amery Ice Shelf, Antarctica

4 Continent-scale mapping of Antarctic surface meltwater

5   Discussion & Conclusions

References   193

List of Figures

List of Tables

List of abbreviations

AIS	Antarctic Ice Sheet
AP	Antarctic Peninsula
ApRES	Autonomous phase-sensitive Radio-Echo Sounders
ASL	Amundsen Sea Low
DEM	Digital Elevation Model
EAIS	East Antarctic Ice Sheet
ENSO	El Nino Southern Oscillation
ETM+	Enhanced Thematic Mapper Plus
FASTER	Fully Automated Supraglacial lake Tracking at Enhanced Resolution
GEE	Google Earth Engine
GEEDiT	Google Earth Engine Digitisation Tool
GrIS	Greenland Ice Sheet
IMBIE	Ice sheet Mass Balance Inter-comparison Exercise
IVS	Image Visibility Score
LPCS	Lake Pixel Contribution Score
LVP	Lake Visibility Percentage
MODIS	Moderate Resolution Imaging Spectroradiometer
NDSI	Normalized Difference Snow Index
NDWI	Normalized Difference Water Index
OLI	Operational Land Imager
PDD	Positive Degree Day
RACMO	Regional Atmospheric Climate Model
RCP	Representative Concentration Pathway
REMA	Reference Elevation Model of Antarctica
RGB	Red, Green, Blue (satellite bands)
ROI	Region of Interest
SAM	Southern Annular Mode
SAR	Synthetic Aperture Radar

SLR   Sea Level Rise

SWIR   Short-wave infrared

TIR   Thermal infrared

TOA   Top of Atmosphere

WAIS   West Antarctic Ice Sheet

CHAPTER 1

Introduction

1.1 Significance and Rationale

The Greenland and Antarctic Ice Sheets contain the majority (99%) of freshwater on Earth, and are the largest potential contributors to global sea level rise (SLR) (Oppenheimer et al., 2019). The Antarctic Ice Sheet (AIS) holds enough freshwater to raise global sea level by approximately 58 m (Morlighem et al., 2020), greater than eight times the potential sea level contribution from the Greenland Ice Sheet (GrIS) (~7 m; Morlighem et al., 2017). The potential contribution from the AIS is therefore the largest uncertainty in predicting future SLR (Bamber et al., 2019; Edwards et al., 2021). At present, the GrIS experiences greater annual mass losses than the AIS (The IMBIE team, 2018), but continued warming could see the AIS become the dominant contributor to global SLR in the near future (Oppenheimer et al., 2019). At the Antarctic Peninsula, atmospheric warming has already been implicated in the collapse of major ice shelves (Scambos et al., 2000), resulting in accelerations and enhanced mass loss from previously buttressed outlet glaciers (Rignot et al., 2004; Scambos et al., 2004). The West Antarctic Ice Sheet is highly vulnerable to climatic warming and already potentially unstable (Rosier et al., 2021), whilst the East Antarctic Ice Sheet, once considered stable and relatively insensitive to climatic changes, could contribute substantially to global SLR if emissions targets are not met (ICCI, 2022; Stokes et al., 2022). Predicting how the AIS will respond under varying future climate scenarios is hence of great societal importance.

Despite significant scientific advances in remote sensing, numerical modelling and process understanding over recent years, uncertainty in projecting Antarctica's future contribution to SLR remains high (Bamber et al., 2019; Edwards et al., 2021). Under a 2°C (average global) warming scenario consistent with the Paris agreement, the 5th and 95th percentile estimates for Antarctic SLR contribution range from -11 cm to 56 cm respectively (Bamber et al., 2019). Whilst anthropogenic greenhouse gas emission rates will undoubtedly have a large impact, modelled projections show no clear dependence on emissions scenario for Antarctica (Edwards et al., 2021). Model uncertainty largely relates to poorly known parameters associated with processes that relate to mass gain and loss (Edwards et al., 2021). Uncertainty is especially high due to the potential influence

on mass loss of ice dynamic processes such as ice cliff failure (DeConto & Pollard, 2016) and runaway grounding line retreat at marine-based sectors of ice (Robel et al., 2019). Hence, it is clear that further ice sheet process understanding is required to reduce uncertainty in projections of Antarctic contribution to SLR.

The AIS has been losing mass over recent decades, with accelerating ice loss experienced since around 2000 (Mouginot et al., 2014). Between 1992 and 2017, the AIS lost an estimated 2720 ± 1390 Gt of ice, equivalent to an increase of 7.6 ± 3.9 mm in global mean sea level (The IMBIE team, 2018). Recent contributions to SLR from Antarctica have almost entirely been due to ice-dynamic processes (Mouginot et al., 2014; Rignot et al., 2014). This contrasts to the GrIS, where mass loss is currently roughly evenly split between ice dynamic and surface mass balance processes (Smith et al., 2020). Antarctic ice losses have been driven by increased basal melting of ice shelves and marine-terminating outlet glaciers, and iceberg calving associated with oceanic warming (Turner et al., 2017). Thinning of ice shelves from ocean warming reduces back stresses on upstream grounded ice, resulting in accelerations of grounded outlet glaciers and thus mass loss (Rignot et al., 2014). Whilst the majority of recent Antarctic mass loss has been driven by ocean warming, atmospheric forcing is becoming increasingly recognised as a crucial factor in controlling future Antarctic mass balance (Oppenheimer et al., 2019; Noble et al., 2020). In particular, increases in surface melting from anticipated atmospheric warming (Trusel et al., 2015) will have important implications on both ice dynamics and surface mass balance (Bell et al., 2018).

The AIS has traditionally been considered too cold for significant amounts of surface melting to occur, yet satellite observations over recent years have revealed that surface meltwater is more widespread than previously thought (Bell et al., 2018). Large networks of surface meltwater, comprising supraglacial lakes, surface streams and slush, are found around the margin of the AIS as a result of surface melt during the austral summer (Kingslake et al., 2017; Stokes et al., 2019; Fig. 1.1). Surface meltwater is significant for Antarctic mass balance because it can promote ice-shelf break up (Banwell et al., 2013; Scambos et al., 2000), enhance localised melting (Lüthje et al., 2006; Kingslake et al., 2017) and influence grounded ice dynamics (Iken & Bindschadler, 1986; Tuckett et al., 2019). The presence of surface water is particularly important because it reduces surface albedo, thus initiating a positive feedback which promotes further melting and ponding of water (Jakobs et al., 2021). The relationship between surface melt rates and

atmospheric temperature is therefore strongly non-linear (Trusel et al., 2015; Donat-Magnin et al., 2021), increasing the sensitivity of the ice sheet to atmospheric warming.
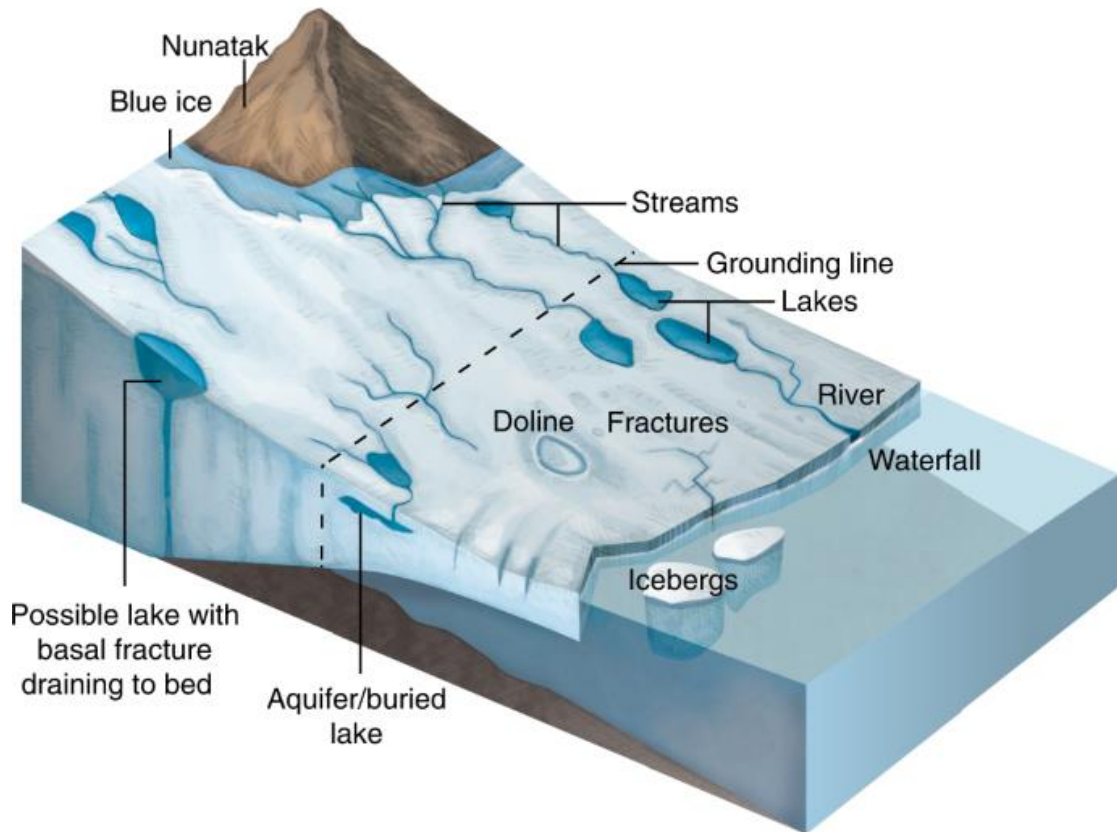
Figure 1.1. Schematic of the Antarctic surface hydrological system. Surface meltwater features, including lakes, streams and rivers, are most commonly found on ice shelves and in close proximity to the grounding line or around nunataks on grounded ice. Source: Bell et al. (2018).

The impact of surface melting on Antarctic ice dynamics has already been demonstrated, most notably via its role in triggering the collapse of ice shelves on the northeast Peninsula during the 1990s and early 2000s (Cook & Vaughan, 2010). Furthermore, there is growing evidence to suggest that surface meltwater is starting to influence grounded ice dynamics in Antarctica (Section 1.2.3.3). This interaction has been well documented in Greenland, where coupling between the supra- and subglacial environments provides a direct mechanism for ice flow dynamics to respond to atmospheric forcing (Zwally et al., 2002). Variations in surface meltwater supply on the GrIS can influence ice velocities at both land-terminating (Davison et al., 2019) and tidewater (Davison et al., 2020; Stevens

et al., 2022) glaciers on sub-daily to annual timescales (Section 1.2.3.2). Surface driven variations in grounded ice dynamics at the Antarctic Peninsula have recently been reported for the first time (Tuckett et al., 2019; Boxall et al., 2022). Despite these examples of the potential for surface meltwater to induce ice dynamic changes, the extent to which surface meltwater will impact future Antarctic mass balance is largely unknown.

Surface melt rates across the majority of Antarctica are currently insufficient to have widespread and sustained ice dynamic influences, but as surface melting increases with climate warming (Trusel et al., 2015), parts of Antarctica are predicted to experience melt rates similar to present-day ablation zones on the GrIS. Twenty-first century modelled climate simulations indicate a scenario-independent doubling of Antarctic-wide surface melt by 2050 (Trusel et al., 2015), whilst climate modelling of RCP8.5 (Representative Concentration Pathway based on an energy imbalance of 8.5 W m^{-2} by 2100) suggests that the mean volume of surface meltwater in Antarctica could be as high as 613 ± 258 Gt yr^{-1} by the end of the century (Trusel et al., 2015; Fig. 1.2). Under this high emission scenario, melt rates that are currently mainly only experienced on parts of the Antarctic Peninsula (where surface melting has already been shown to have dynamic impacts on grounded ice flow and ice shelf stability) are predicted to cover 698,820 km^2 (5%) of the AIS (Kingslake, pers. comm., 2022; Trusel et al., 2015). This area is 87% greater than the current ablation zone of the GrIS (Cooper & Smith, 2019). Such significant increases in melt rate could have profound influences on ice shelf stability and grounded ice flow at an Antarctic-wide scale (Fig. 1.2).
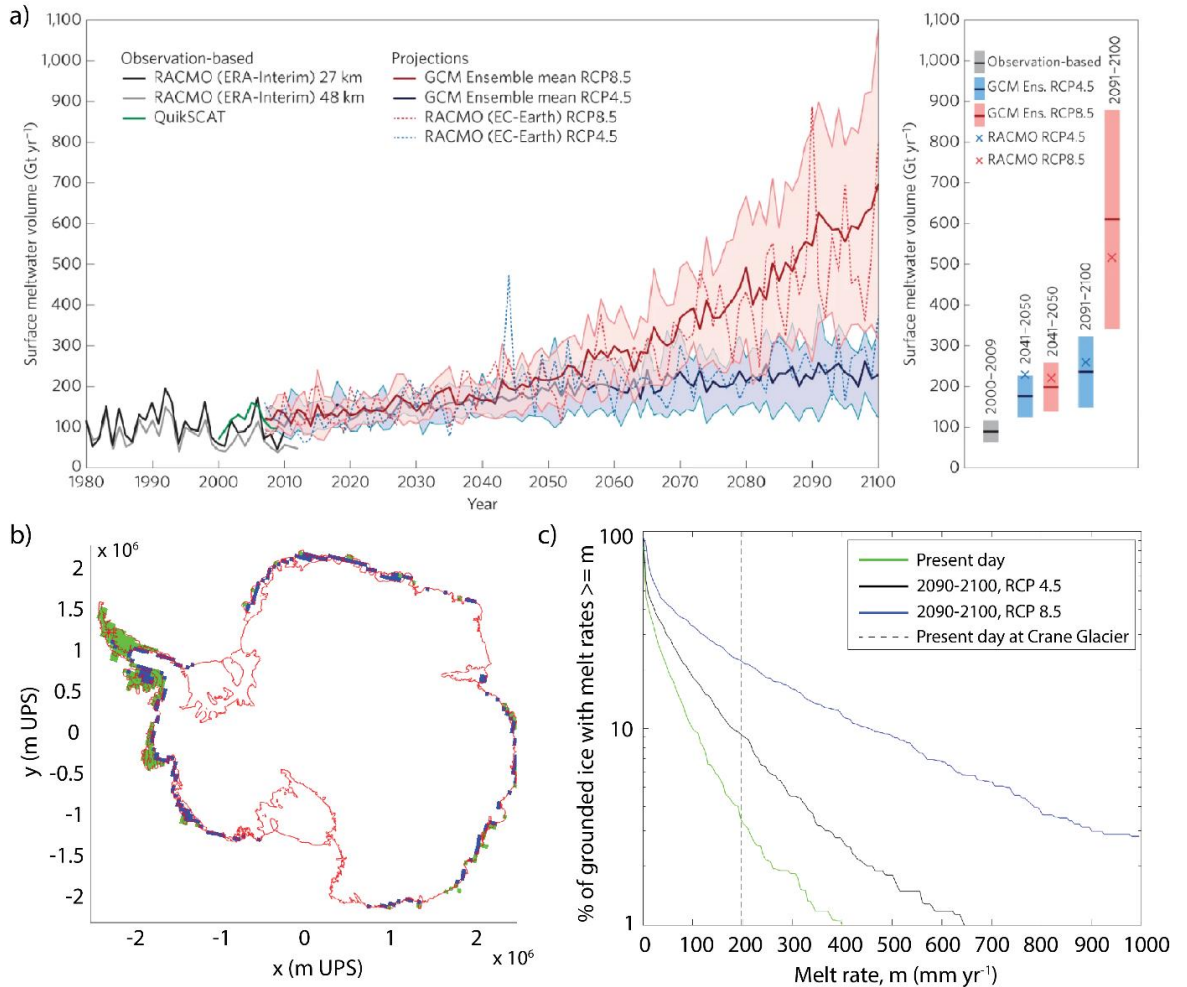
Figure 1.2. (a) Time-series of Antarctic-wide surface meltwater volume from RACMO simulations and QuikSCAT satellite observations, in addition to projected melt volumes under two future climate scenarios (RCP4.5 and RCP8.5). Note how predicted meltwater volumes are roughly the same under the two RCPs until 2050, but then their trajectories diverge. Source: Trusel et al., 2015. (b) Areas of the AIS that experience melt rates exceeding those observed on a typical Antarctic Peninsula outlet glacier (200 mm/yr, Crane Glacier) today (green), compared with the predicted area by 2100 under RCP8.5 (blue). (c) Relative areal coverage of surface melt rate for medium and high emissions scenarios across grounded ice with surface elevation below 500 m asl. Data are from Trusel et al., 2015; (b) and (c) figures produced by Kingslake (pers. comm., 2022).

To predict the impacts of anticipated increases in surface melting, we first need to improve our process understanding of present-day surface hydrology in Antarctica (Bell et al., 2018). Continent-wide estimates of surface meltwater area and volume over multi-year time periods are lacking, and there are substantial knowledge gaps in our

understanding of meltwater controls, distribution and evolution. To be able to parameterize meltwater related processes in ice-sheet models, continuous and robust observations of Antarctic meltwater and surface hydrological processes are first required (Arthur et al., 2020a). This thesis will address this requirement, using novel methods and revolutionary computational resources to study Antarctic surface meltwater at greater spatial and temporal scales than previously possible.

1.2 Research Context

1.2.1 Antarctic setting and climate

The AIS is the largest ice mass on Earth, covering an area of almost 14 million km^2. This large dome of ice, greater than 4 km thick in places (Morlighem et al., 2020), accumulates mass in the cold central interior and flows outwards towards the ocean through fast-moving ice streams and outlet glaciers. The continent is fringed by floating ice shelves which cover ~75% of the 17,968 km coastline (Depoorter et al., 2013). These ice shelves provide a crucial buttressing effect, holding back the flow of ice into the ocean and hence limiting contributions to SLR (Fürst et al., 2016).

The ice on the Antarctic continent is commonly split into three parts; the East Antarctic Ice Sheet (EAIS), the West Antarctic Ice Sheet (WAIS) and the Antarctic Peninsula (AP). The EAIS is by far the largest of the three, holding ~90% of Antarctic ice, and has the potential to raise global sea level by 52.2 m (Morlighem et al., 2020). The majority of the EAIS is grounded above sea level although some catchments, such as Wilkes Land, are marine-based (where ice rests on bedrock that lies below current global mean sea level). The WAIS is separated from the EAIS by the Transantarctic Mountains and contains a relatively mere 5.3 m sea-level equivalent (Morlighem et al., 2020). In contrast to the EAIS, the majority of the WAIS is marine-based and lies on bedrock which slopes downwards inland (Fretwell et al., 2013). This topographic setting makes the WAIS highly susceptible to dynamic instabilities (Schoof, 2007; Pollard et al., 2015), which can result in rapid retreat and mass loss. Ocean warming over recent decades has already resulted in rapid melting from the base of the ice, and the WAIS is hence widely viewed as being at immediate risk to future climate warming (Noble et al., 2020). The Antarctic Peninsula is technically part of the WAIS but is typically separately referred to due to its

differing topography and climate. The Antarctic Peninsula is characterised by a central ice plateau which overlies a high mountain range, extending ~1400 km along the length of the Peninsula. The central ice plateau feeds hundreds of large outlet glaciers (Turner et al., 2009), which flow either directly into the ocean or into ice shelves that fringe the eastern and south-west Peninsula. In total, the Antarctic Peninsula holds 0.27 m sea-level equivalent (Morlighem et al., 2020).
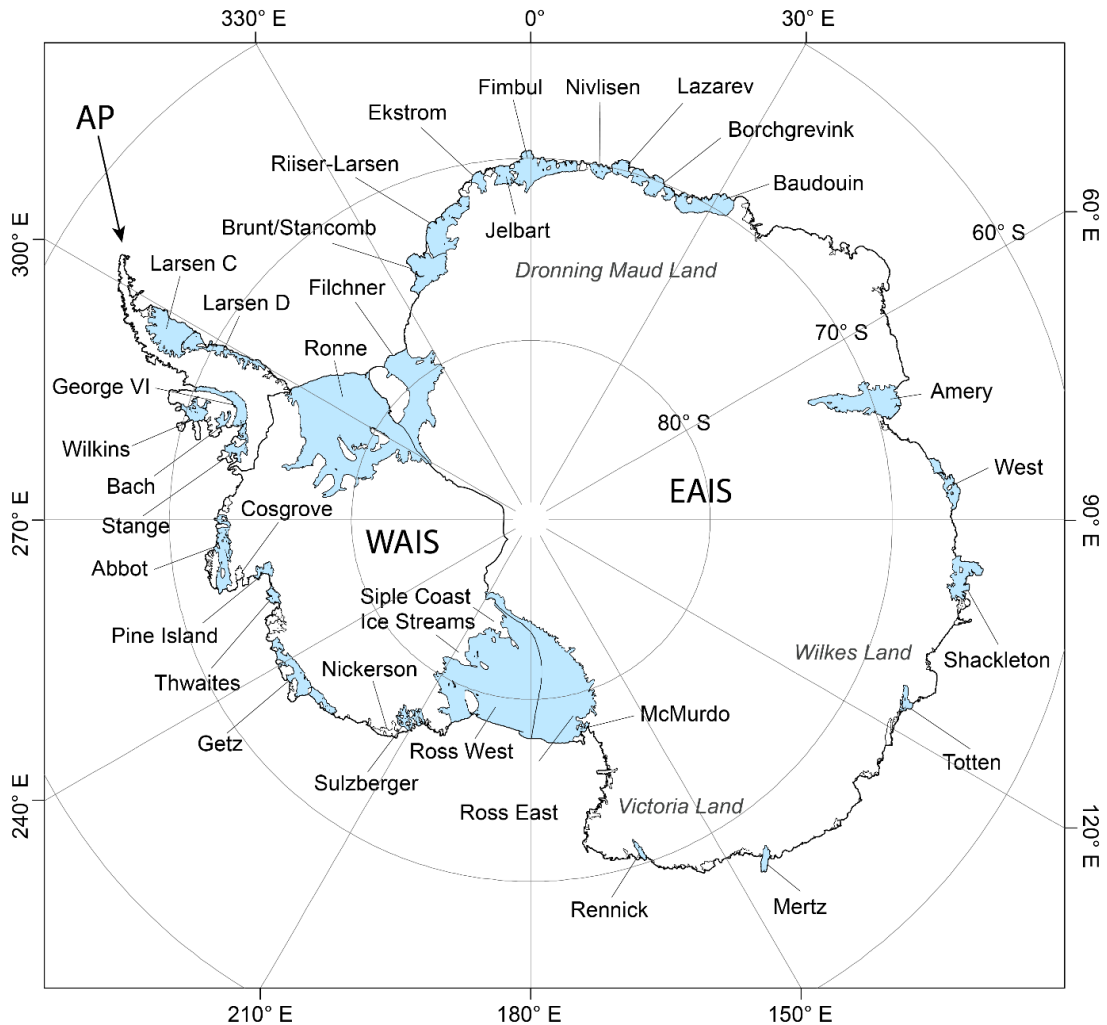
Figure 1.3. Overview map of the Antarctic Ice Sheet, showing the relative sizes of the East Antarctic Ice Sheet, the West Antarctic Ice Sheet and the Antarctic Peninsula. Ice shelves are displayed in blue, with labels indicating the location of selected major ice shelves.

The climate of Antarctica is controlled by complex interactions of topographic, atmospheric, radiative and oceanic factors. The interior of the AIS is the coldest location on earth, sometimes experiencing air temperatures lower than -90°C (Scambos et al., 2018). At locations such as the East Antarctic ice divide, extreme low temperatures are

caused by intense radiative cooling, minimal winds and a very dry atmosphere (Turner et al., 2009). By contrast, the coastal margins of the AIS are at relatively low latitudes, have low surface elevations and abundant nearby moisture sources. The warmest surface air temperatures and highest precipitation rates are thus experienced in these marginal areas. Austral summer air temperatures on the Antarctic Peninsula frequently exceed 0°C (Barrand et al., 2013), and are often enhanced via localised warming from föhn winds which descend down the eastern slopes of the Peninsula (Elvidge et al., 2016). Katabatic winds provide a similar warming effect in East Antarctica (Lenaerts et al., 2017), where relatively low latitude ice shelves can experience austral summer air temperatures above freezing. It is therefore in these coastal regions that surface melting is most prevalent.

Variations in Antarctic climate are strongly influenced by large-scale atmospheric circulation modes (Fogt & Marshall, 2020). The dominant mode of atmospheric variability in the high latitudes of the southern hemisphere is the Southern Annular Mode (SAM) (Thompson & Wallace, 2000). The SAM is a measure of the atmospheric pressure gradient between the mid and high latitudes, thus reflecting the strength and north-south movement of the westerly winds that encircle the Antarctic continent (Jones et al., 2016). Positive phases of the SAM are characterised by lower anomalous air pressure over Antarctica and higher pressure at the mid-latitudes, with the reverse during negative phases (Marshall, 2003). During a positive (negative) SAM, air temperatures are typically higher (lower) on the Antarctic Peninsula and lower (higher) over the rest of continent (Marshall & Thompson, 2016; Turner et al., 2020). Consistent with this pattern, a negative correlation between surface melt potential and the SAM index has been found for East Antarctica (Orr et al., 2022).
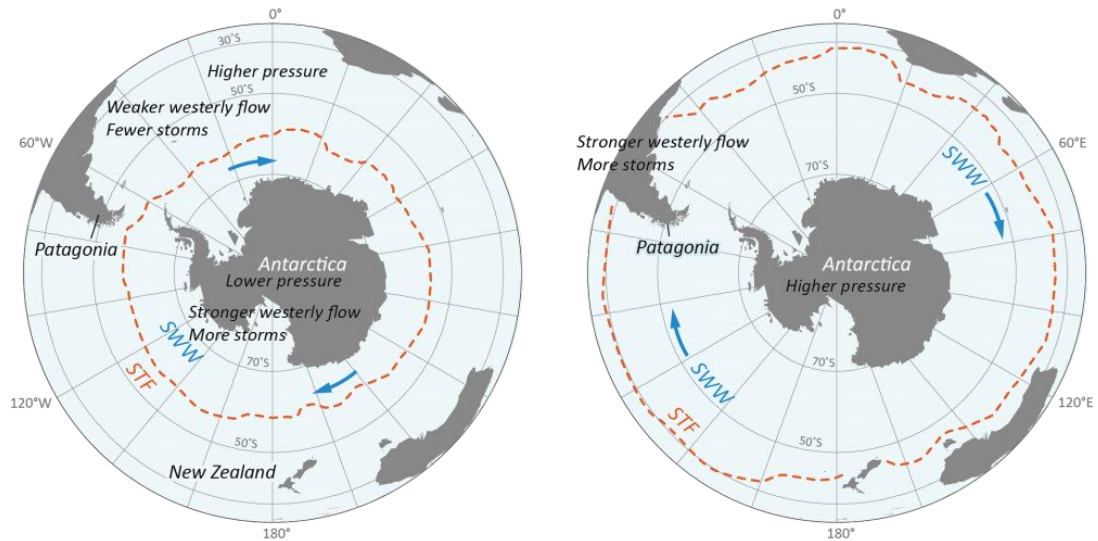
Figure 1.4. Schematic of the atmospheric conditions typically associated with positive (left) and negative (right) phases of the Southern Annular Mode. SWW = Southern Westerly Winds, STF = Subtropical Front. Adapted from (Davies et al., 2020).

Antarctic atmospheric circulations, including the SAM, are closely linked to tropical atmospheric and oceanic conditions via polar-tropical teleconnections (Li et al., 2021). Antarctic climate is particularly strongly coupled to the El Nino Southern Oscillation (ENSO). El Nino events, for example, generate stationary Rossby wave trains via convective heating of the tropical atmosphere, which induce alternating regions of low- and high- pressure anomalies around Antarctica (Fogt & Bromwich, 2006). This weakens and shifts the westerly winds further south, hence causing a strong positive correlation between ENSO and the SAM (Ding et al., 2012). Changes in the ENSO can additionally influence the strength and positioning of regional Antarctic climatic systems such as the Amundsen Sea Low (ASL). The ASL is a climatological centre of low pressure in the south Pacific sector of the Southern Ocean, and exerts a strong influence on the climate of the WAIS and the Antarctic Peninsula (Raphael et al., 2016). The absolute depth of the ASL is closely linked to both the ENSO and the SAM, with a significantly deeper low-pressure system typically associated with La Nina phases of the ENSO (Raphael et al., 2016). Variations in the longitudinal location and strength of the ASL have direct influences on air temperature, sea ice and precipitation rates over large areas of coastal Antarctica, particularly from the Ross Ice Shelf round to the western Antarctic Peninsula. The influence of large-scale atmospheric circulations and polar-tropical teleconnections

on regional climatic conditions is hence significant, and can have a large influence on the potential for surface melting to occur (Orr et al., 2022).

The AIS has experienced strongly spatially variable changes in climate over the past ~70 years, partly due to changes in the SAM (Turner et al., 2020). Increased greenhouse gas emissions and stratospheric ozone depletion have resulted in a trend towards positive phases of the SAM in recent decades (Fogt & Marshall, 2020), with regionally variable impacts on air temperatures. In West Antarctica, mean surface air temperature has increased at twice the global average since the 1950s (Steig et al., 2009; Bromwich et al., 2013). Similarly, the Antarctic Peninsula experienced rapid warming during the second half of the 20th century, especially on its west coast where mean surface air temperature increased by 2.8 °C between 1951 and 2000 (Turner et al., 2005). Rapid warming of the Antarctic Peninsula was likely amplified by a deepening of the ASL, due to a trend to a more positive SAM (Raphael et al., 2016). In East Antarctica, by contrast, there has been negligible warming or even slight cooling in recent decades (Turner et al., 2005; Li et al., 2021), largely due to a reduction in poleward heat flux associated with a more positive SAM (Turner et al., 2020). Consistent with their influence on air temperature, atmospheric circulation patterns have been shown to play a key role in driving surface melting over Antarctic ice shelves (Clem et al., 2018; Orr et al., 2022). However, the relationship between climatic modes and meltwater ponding at larger spatial scales is unclear.

1.2.2   Current understanding of Antarctic surface meltwater

Surface meltwater has been known to exist in Antarctica since the early 20th century, when explorers noted the presence of 'thaw-water streams' on the Nansen Ice Shelf (David & Priestly, 1909). Observations and aerial photography from field expeditions since the 1940s provide further historical evidence of meltwater features in locations such as the Amery (Budd et al., 1967), Shackleton and Roi Baudouin ice shelves (Kingslake et al., 2017). Ground-based studies of meltwater in Antarctica are limited, however, and it is only since the start of the satellite era (~1972) that larger-scale temporal and spatial analysis of meltwater distribution has been possible. The advent of remote sensing techniques enabled the identification of surface lakes, streams and regions of slush without the need for field observations, with the majority of research focussing on either

the Antarctic Peninsula (Scambos et al., 2000; Banwell et al., 2013; Kuipers Munneke et al., 2018) or selected glacier basins in East Antarctica (Phillips, 1998; Kingslake et al., 2015; Langley et al., 2016). Despite advances in methodological techniques and satellite data availability, Antarctic melt extent was considered spatially constrained to a few selected regions, and far more attention was given to mapping surface meltwater in Greenland (e.g. McMillan et al., 2007), where surface melting is more prevalent.

The widespread occurrence of surface meltwater in Antarctica has only recently been realised. Kingslake *et al*. (2017) conducted the first Antarctic-wide study of optical satellite imagery, finding that surface drainage networks are widespread on ice shelves and outlet glaciers around the entire continent. Since then, the scientific community has started to realise the wider importance of surface melt across Antarctica, and there has been a surge in progress towards quantifying surface meltwater extent (Arthur et al., 2020a). Studies have used a variety of remote sensing data and techniques, and have been conducted over a range of spatial and temporal scales.

The vast majority (74%) of Antarctic surface meltwater mapping studies have used optical satellite imagery as the primary data source, in comparison to synthetic aperture radar (SAR) satellite imagery (13%), aerial photography (4%) or field-based observations (9%) (Arthur et al., 2020a). Microwave scatterometer sensors, such as QuikSCAT and ASCAT, have also been used to assess Antarctic surface meltwater fluxes (Trusel et al., 2013; Bevan et al., 2018), although these sensors are primarily used to detect liquid water within the snow or firnpack melt as opposed to delineating individual surface meltwater features (de Roda Husman et al., 2022). The most common data source for meltwater mapping studies has been optical satellite imagery. This is because data are predominantly freely available, offer the longest temporal range, and have relatively simple-to-implement workflows for delineating surface water. Optical satellite data are available across a range of spatial resolutions, and there is typically a trade-off whereby higher spatial resolution imagery comes at the cost of longer time gaps between repeat imagery, and vice versa. For example, Moderate-Resolution Imaging Spectroradiometer (MODIS) imagery provides daily (or better) coverage, but at coarse spatial resolutions of 250 m or greater, whereas the Landsat and Sentinel-2 satellites offer high spatial resolutions of 15 - 30 m and 10 m respectively, but with a less frequent (5 – 8 day) return period. Whilst low spatial resolution sensors like MODIS can be beneficial for determining the presence (or lack thereof) of surface meltwater in a region, generating quantitative estimates of

meltwater area and volume typically require the use of higher spatial resolution sensors. Some studies have attempted to maximise temporal coverage by combining the Landsat and Sentinel-2 records (Stokes et al., 2019; Moussavi et al., 2020; Corr et al., 2022), although this can cause data consistency challenges and is limited to the past ~7 years that Sentinel-2 has been operational.

The primary limitation of all optical imagery is that it is detrimentally affected by spatially and temporally variable cloud cover. Time series of mapped surface meltwater from optical imagery are hence typically incomplete and inconsistent (Moussavi et al., 2020). Optical data are additionally dependent on daylight, thus limiting data availability during the polar night, and variations in solar zenith can complicate the automatic delineation of land surface types. SAR imagery overcomes some of these limitations as it is not reliant on illumination or meteorological conditions. Hence, SAR imagery can be used to generate consistent year-round data at fixed time intervals. SAR uses an active sensor which emits electromagnetic radiation to detect changes in backscatter from the Earth's surface. The potential for using SAR data to detect surface meltwater at high spatial resolutions has been demonstrated in both Greenland (Miles et al., 2017) and Antarctica (Luckman et al., 2014; Kuipers Munneke et al., 2018; M. Dirscherl et al., 2020, 2021). SAR backscatter values can, however, be highly sensitive to minor changes in topography, surface roughness and melt conditions, meaning surface meltwater can be difficult to differentiate from other land surface types (Miles et al., 2017). Whilst SAR therefore offers great potential for meltwater mapping, automated detection of surface water presents significant challenges and mapping techniques are not currently as reliable and widely implemented as optical methods.

Until recently, surface meltwater studies typically used manual delineation to assess meltwater cover for an individual ice shelf or glacier catchment (Table 1.1). For example, Langley et al. (2016) manually identified 7990 surface lakes on Langhovde Glacier (EAIS) from >150 optical images between 2000 and 2013, whilst manual techniques were used to quantify meltwater cover on the Larsen B ice shelf prior to its collapse in 2002 (Glasser & Scambos, 2008; Banwell et al., 2014). Several more recent studies have used a range of manual and semi-automated (computer-based mapping tools run by a user) techniques to detect surface meltwater changes over longer time periods for individual ice shelves, including Shackleton (Arthur et al., 2020b), Roi Baudouin (Dell et al., 2022) and Amery (Spergel et al., 2021) ice shelves (Table 1.1). Antarctic surface meltwater mapping

methodologies have been guided by remote sensing studies of the GrIS, where surface meltwater has most commonly been mapped using MODIS (McMillan et al., 2007; Sundal et al., 2009; Selmes et al., 2011) and, more recently, Landsat or Sentinel-2 (Williamson et al., 2018; Yang et al., 2019; Hochreuther et al., 2021) optical satellite data.

The recent realisation of the widespread extent of surface meltwater across Antarctica (Kingslake et al., 2017) has prompted the need to develop automated techniques for mapping at much larger spatial scales. Image classification (Halberstadt et al., 2020), machine learning (Dirscherl et al., 2020), and band reflectance threshold (Moussavi et al., 2020) techniques have been developed and trialled over various ice shelves around Antarctica, to high levels of success. Automated techniques have most regularly applied ice-adapted versions of the Normalised Difference Water Index (NDWI), which classifies image pixels as water or non-water based on their spectral information. For example, semi-automated NDWI approaches were used to map surface meltwater over the EAIS (Stokes et al., 2019) and WAIS (Corr et al., 2022) during the peak of a single melt season. Whilst these two studies provided quantitative assessments of supraglacial meltwater at ice sheet spatial scales for the first time, they analysed data from a single month (January 2017) and were hence limited in temporal scope. Progress has since been made towards combining large spatial analysis with higher temporal resolution of mapped results. Dirscherl et al. (2021) documented supraglacial lake evolution between 2015-2021 for six ice shelves across East Antarctica and the Antarctic Peninsula, whilst Arthur et al. (2022) presented a dataset of supraglacial lakes across the EAIS during January in six consecutive years. Despite these advances, a multi-annual, continent-wide study of Antarctica supraglacial meltwater has yet to be conducted.

Table 1.1. Selected studies since 2016 which provide assessments of surface meltwater features in Antarctica. Papers are listed in order of publication date. Note how studies have generally increased in spatial and temporal scope over time, but a multi-year, high temporal resolution, continent-wide dataset of surface meltwater has yet to be produced. SGL stands for 'supraglacial lake'.

Source	Paper summary	Region	Dates/temporal resolution	Method	Images analysed
Langley et al. (2016)	Seasonal evolution of SGLs on an East Antarctic outlet glacier	Langhovde glacier (EAIS)	Austral summers 2000 - 2013	Manual delineation	153 Landsat and ASTER optical images
Kingslake et al. (2017)	First Antarctic-wide survey of surface meltwater drainage systems from optical imagery	Continent-wide (mainly ice shelves)	1947 - 2015	Manual delineation	Landsat, Aster and Worldview (image numbers unspecified)
Stokes et al. (2019)	Distribution of SGLs around the margin of the EAIS	Entire EAIS margin	January 2017	NDWI (semi-automated)	312 Sentinel-2 and Landsat optical images
Moussavi et al. (2020)	A threshold-based method for Antarctic SGL detection from optical imagery	Four ice shelves (EAIS)	Austral summers 2013 - 2019	NDWI (semi-automated threshold-based method)	>1000 Landsat and Sentinel-2 images
Halberstadt et al. (2020)	A supervised classification method for mapping Antarctic surface lakes	Amery and Roi Baudouin Ice shelves (EAIS)	Austral summers 2013 – 2017	Supervised image classification	52 Landsat images
Arthur et al. (2020)	Distribution and seasonal evolution of SGLs on Shackleton ice shelf	Shackleton ice shelf (EAIS)	1999 - 2020	NDWI	Landsat and Sentinel-2 optical imagery
Leeson et al. (2020)	Evolution of SGLs on Larsen B in the decades prior to its collapse	Larsen B ice shelf (AP)	1979 - 2002	Manual delineation and NDWI	8 Landsat images, 13 SAR images
Dirscherl et al. (2021)	Seasonal evolution of SGLs on Antarctic ice shelves and links to environmental controls	Six ice shelves, 3 x AP and 3 x EAIS	2015 – 2021, biweekly repeat	Machine learning classifier	3075 Sentinel-1 images, 2167 Sentinel-2 images
Corr et al. (2022)	Inventory of SGLs across the WAIS	Entire WAIS (including AP)	January 2017	NDWI (threshold-based method)	1682 Sentinel-2 images, 604 Landsat images
Dell et al. (2022)	Supervised classification of slush and ponded water on Antarctic ice shelves	Roi Baudouin Ice shelf (EAIS)	2013 – 2020, 15-day repeat	Supervised image classification within GEE	Landsat images (image number unspecified)
Arthur et al. (2022)	Large interannual variability in SGLs around East Antarctica	EAIS margin	January, 2014 - 2020	NDWI (threshold-based method)	2175 Landsat images

Advances in remote sensing capabilities mean we now have a reasonable understanding of the spatial distribution of Antarctic surface meltwater (Stokes et al., 2019; Liang et al., 2021), and the different forms that it can take. The majority of surface melting occurs around the margin of the ice sheet, where relatively low latitudes and ice-surface elevations result in temperatures sufficient to cause melting of the ice surface during the austral summer (Trusel et al., 2012). In locations where surface meltwater is unable to drain through an impermeable surface or near-surface layer of ice, meltwater collects in surface depressions to form supraglacial lakes. These lakes are often interconnected by surface streams as part of larger meltwater networks (Kingslake et al., 2017; Dell et al., 2020), enabling the lateral transfer of water across the ice surface as runoff. In addition to surface ponding and runoff, meltwater can also exist within firn pore spaces (Montgomery et al., 2020). Extensive regions of surface slush can be formed where pore spaces in the upper firn layer become saturated with meltwater (Dell et al., 2020).

Surface meltwater is most abundant on ice shelf surfaces (Alley et al., 2018; Stokes et al., 2019), where higher temperatures at low elevations and low surface slopes provide favourable conditions for meltwater generation and ponding (Stokes et al., 2019; Arthur et al., 2020a). Supraglacial lakes on ice shelves form in surface depressions that move with ice flow (Macdonald et al., 2018), and hence their location is influenced by variations in ice velocity, thickness and flexure (Banwell et al., 2019). Meltwater features are regularly observed on ice shelves along the Antarctic Peninsula, including the Larsen (Luckman et al., 2014; Leeson et al., 2020), George VI (Banwell et al., 2021) and Wilkins (Scambos et al., 2009) ice shelves. Surface melt rates on the Antarctic Peninsula are strongly influenced by the strength and timing of föehn wind events, which can provide an intense localised warming effect (Elvidge et al., 2015). This can result in meltwater ponding, even during austral winter months (Kuipers Munneke et al., 2018). In East Antarctica, meltwater features are found on several relatively low-latitude ice shelves, including Shackleton (Arthur et al., 2020b), Amery (Spergel et al., 2021), Roi Baudouin (Dell et al., 2022) and Nivlisen (Dell et al., 2020) ice shelves. Lakes are particularly abundant around the grounding zone of ice shelves due to the influence of katabatic winds. These density-driven winds, which warm as they descend coastward from the ice sheet interior, replace cold and damp air adjacent to the ice surface (Lenaerts et al., 2017), initiating surface melting. Surface snow scouring by katabatic winds can additionally amplify albedo effects associated with blue-ice areas or exposed nunataks, which can

promote surface melting at a localised scale (Kingslake et al., 2017; Arthur et al., 2020a; Jakobs et al., 2021).

Surface meltwater on grounded ice often exists where undulations in subglacial bedrock are transferred to the surface, creating depressions in which meltwater can pond (Langley et al., 2016; Ignéczi et al., 2018; Arthur et al., 2020a). Supraglacial lakes therefore typically form in the same locations annually (Gledhill & Williamson, 2018). Surface meltwater on grounded ice is most common on the Antarctic Peninsula (Tuckett et al., 2019) and around the grounding zone of East Antarctic ice shelves, but is also often found close to nunataks and areas of blue ice (Kingslake et al., 2017). Whilst most meltwater is found at low elevations (<100 m) near the ice sheet margin, surface meltwater features can exist up to 500 km inland and at elevations of over 1500 m (Stokes et al., 2019). Stokes et al. (2019) found that at high elevations (>800 m), supraglacial lake formation appears to be strongly controlled by the presence of nunataks, with almost all lakes existing close (< 5 km) to exposed bedrock. This is likely due to a localised warming of air, whereby low-albedo rock outcrops are heated by absorption of short-wave radiation and subsequently emit long-wave radiation (Aubry-Wake et al., 2015). Overall, it is evident that several factors influence the spatial distribution of surface meltwater, including surface albedo, proximity to exposed rock, subglacial topography and elevation.
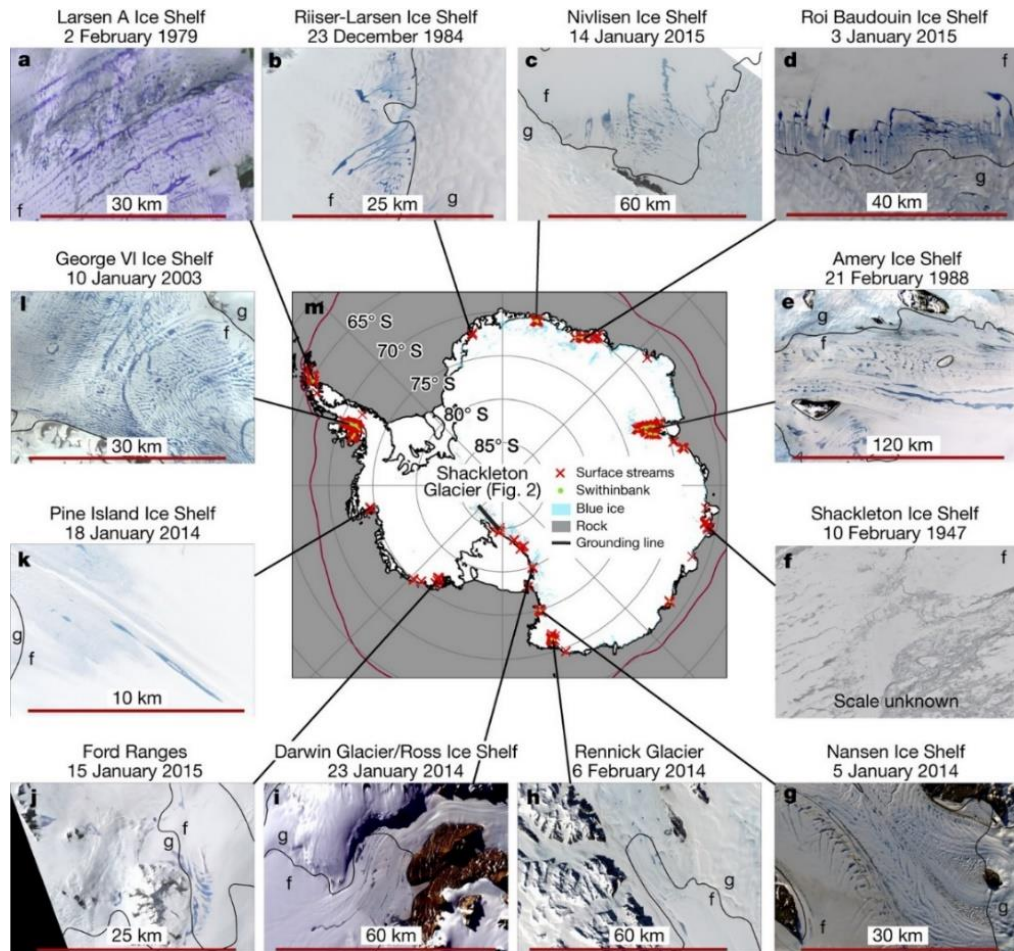
Figure 1.5. Surface drainage systems around Antarctica mapped by Kingslake et al. (2017). Note that surface melt has been observed around the entire continent, with images showing examples of melt on ice shelves on the Antarctic Peninsula, WAIS and EAIS (1947-2015). Source: Kingslake et al. (2017).

1.2.3   Influence of surface meltwater on ice sheet mass balance

As the extent and intensity of Antarctic surface melting increases (Trusel et al., 2015), surface meltwater is likely to have an increasingly strong influence on ice sheet mass balance (Bell et al., 2018). In addition to the positive feedback associated with decreased surface albedo from meltwater, surface melting can influence ice-sheet mass balance in four primary ways:

1) *Increased surface runoff and thinning*. This direct effect of surface melting is a major contributor to mass loss from the Greenland Ice Sheet (50-65%, Smith et al., 2020), but

currently contributes a negligible amount to Antarctic mass loss (Smith et al., 2020). Surface runoff that does occur in Antarctica is mainly limited to ice shelves, as the majority of surface melt on grounded ice refreezes at the end of the melt season. However, direct mass loss from thinning and runoff has the potential to become a greater factor in Antarctica as melt rates increase.

2) *Melt-induced collapse of ice shelves*. Meltwater ponding on ice shelves can trigger their catastrophic break-up via processes of hydrofracture and shelf flexure (Scambos et al., 2000). The disintegration of an ice shelf removes the associated buttressing forces on contributing outlet glaciers, causing accelerated flow and greater ice discharge (Rignot et al., 2011). This process has already been observed in Antarctica, most notably during the breakup of the Larsen B ice shelf in 2002 (Rignot, 2004; Rott et al., 2011; Leeson et al., 2020).

3) *Injection of surface meltwater to the subglacial environment*. Meltwater has the potential to create surface to ice-bed connections via hydrofracture (Krawczynski et al., 2009), injecting liquid water into the subglacial environment. This input of water can alter the basal hydrological system, affecting the flow of grounded ice (Iken, 1981; Iken & Bindschadler, 1986). This process is widespread in west Greenland (Zwally et al., 2002; Davison et al., 2019) and has been suggested to occur on outlet glaciers of the Antarctic Peninsula (Tuckett et al., 2019).

4) *Plume enhanced submarine melting of the glacier front or ice shelf.* Surface meltwater that reaches the ice bed can be discharged subglacially at the grounding line, resulting in buoyant plumes of freshwater adjacent to the glacier front or ice shelf (Slater & Straneo, 2022). These plumes can cause submarine ice melting providing a mechanism for atmospheric warming to enhance submarine melting, even in the absence of ocean warming (Jackson et al., 2020). This process has been shown to have a first-order control on submarine melting and subsequent mass loss from the GrIS (Slater & Straneo, 2022), and could become an important factor for Antarctic mass loss in the future.
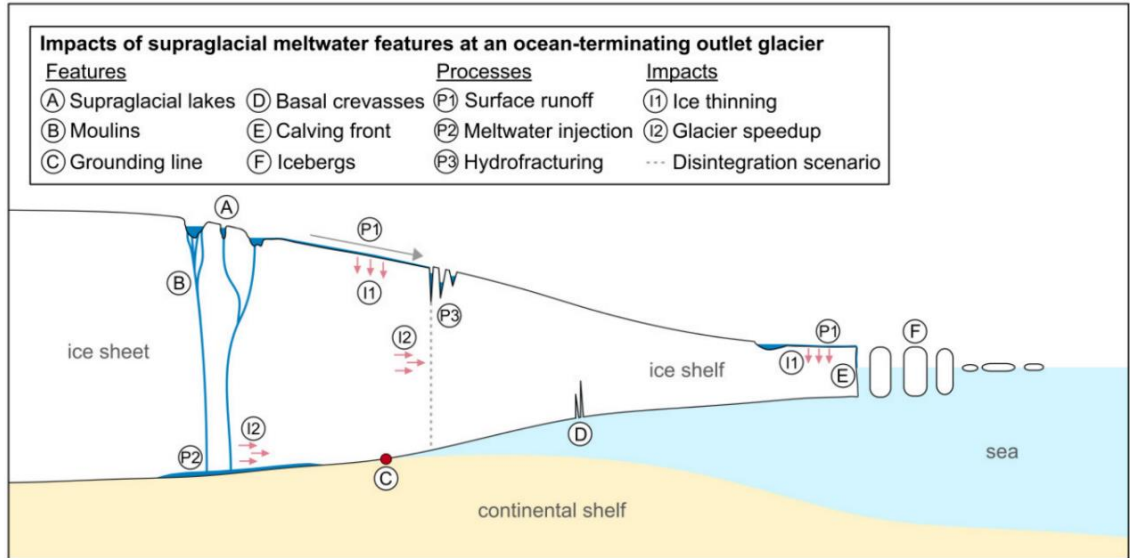
Figure 1.6. Meltwater induced processes that can occur at a marine-terminating outlet glacier with an ice shelf. Source: Dirscherl et al. (2020).

1.2.3.1 Surface meltwater influence on ice shelves

Antarctic ice shelves are crucial for determining the future mass balance of the AIS as they provide a buttressing force (lateral drag from embayment walls, and basal drag from topographic highs) against the flow of ice into the ocean (Fürst et al., 2016). The removal of this buttressing force via ice shelf collapse can result in upstream glacier accelerations, increasing net ice sheet mass loss (Rignot et al., 2004; Scambos et al., 2004). The role of surface meltwater on ice shelf stability has been widely researched, especially following extensive surface meltwater ponding on the Larsen A and B ice shelves prior to their breakup. Surface meltwater can initiate or accelerate ice shelf collapse via processes of hydrofracture and ice shelf flexure (Bell et al., 2018). Hydrofracture is the process by which water flows into existing surface crevasses, creating additional loading and promoting unstable fracture growth (Weertman, 1973). With sufficient surface meltwater supply, continued hydrofracture can result in vertical fracture propagation through the whole ice column (Scambos et al., 2009). This process can occur on both grounded and floating ice. Repeated hydrofracture on ice shelves can result in the formation of multiple through-ice fractures, connecting the ice surface with the ocean below. The spacing of through-ice fractures is key for determining the impact of hydrofracture on ice-shelf stability (Bell et al., 2018). Closely spaced through-ice fractures can trigger 'iceberg

capsizing' (MacAyeal et al., 2003), resulting in ice shelf disintegration. By contrast, widely spaced fractures do not necessarily result in ice shelf instability, and can even provide a stabilising effect by providing conduits through which surface meltwater is evacuated to the ocean (Bell et al., 2017).

Ice shelf flexure, which occurs due to repeated filling and draining of surface meltwater ponds, can additionally contribute to ice shelf collapse. The loading and unloading of water on an ice shelf surface can produce fractures around the location of lakes. If fractures from adjacent lakes intersect, a chain reaction of lake drainage events can occur (Banwell et al., 2013). It is been suggested that this chain reaction process might have triggered the collapse of the Larsen B Ice Shelf through the rapid drainage of over 2000 lakes (Banwell et al., 2013). The stability of an ice shelf is therefore largely determined by fracturing processes, rather than the existence of surface meltwater *per se*. For example, extensive meltwater ponding occurs on George VI ice shelf (on the Antarctic Peninsula, Fig. 1.3) each year, but the compressive flow regime of the ice shelf limits its ability to fracture, making collapse unlikely (Lai et al., 2020). Furthermore, it should be noted that ice shelf stability is also strongly influenced by oceanic processes, and surface meltwater is not necessarily a precursor to ice shelf collapse events (Arthur et al., 2021).

1.2.3.2 Surface meltwater influence on grounded ice

The presence of surface meltwater on grounded ice introduces the possibility for hydrofracture to create hydraulic pathways that connect the ice surface to the subglacial environment. Once such surface-to-bed connections have been established, surface meltwater can enter the subglacial hydrological system and induce ice-flow variations (Iken, 1981). Surface melt rates in Antarctica are not currently high enough for surface-to-bed connections to be common, and such pathways have only been inferred to exist on the Antarctic Peninsula (Tuckett et al., 2019; Boxall et al., 2022; Hodgson et al., 2022). Process understanding from mountain settings and the Greenland Ice Sheet, however, provide us with modern-day analogues for understanding what surface hydrological processes could become more widespread in Antarctica in the future as the climate warms (Bell et al., 2018; Tuckett et al., 2019).

In west Greenland, high surface melt rates during summer months create large networks of supraglacial lakes and rivers, tens of kilometres inland on the ice sheet surface

(McMillan et al., 2007). In these locations, crevasses undergo hydrofracture early in the melt season to form moulins which provide the connections by which meltwater drains to the ice sheet bed (Koziol et al., 2017). Supraglacial lakes commonly provide the meltwater required to sustain hydrofracture (Clason et al., 2015), and enable large volumes of water to reach the subglacial system. Whilst some lakes flow into moulins via surface streams and rivers, others can drain *in situ* through vertical propagation of fractures within the lake basin (Das et al., 2008). Supraglacial lake drainage events can occur over hourly to weekly timescales, and have been shown to have significant impacts on ice velocities (Zwally et al., 2002; Joughin et al., 2013).

The dynamic impact of surface meltwater reaching the bed of grounded ice depends on the configuration of the existing subglacial drainage system (Davison et al., 2019). Subglacial drainage systems can be broadly classed into two categories: hydraulically efficient (or channelized) and inefficient (or distributed) systems (Fig. 1.7), although an 'intermediate' system is also sometimes described. Hydraulically efficient systems have subglacial channels, which enable water to be efficiently evacuated at low basal water pressures (Nye, 1965; Röthlisberger, 1972). Conversely, inefficient systems have a lower capacity for transporting water and can therefore become more easily overwhelmed, resulting in higher subglacial water pressures (Kamb, 1987). Theory, initially developed based on measurements at Alpine glaciers (Iken, 1981), suggests that increases in basal water pressure directly reduce the effective pressure (defined as overburden of overlying ice minus basal water pressure) in the subglacial system, which controls ice-bed coupling. Increases in subglacial water pressure can hence reduce the area of ice-bed contact and cause hydraulic jacking of overlying ice, resulting in enhanced rates of basal motion (Iken & Bindschadler, 1986; Bingham et al., 2008).
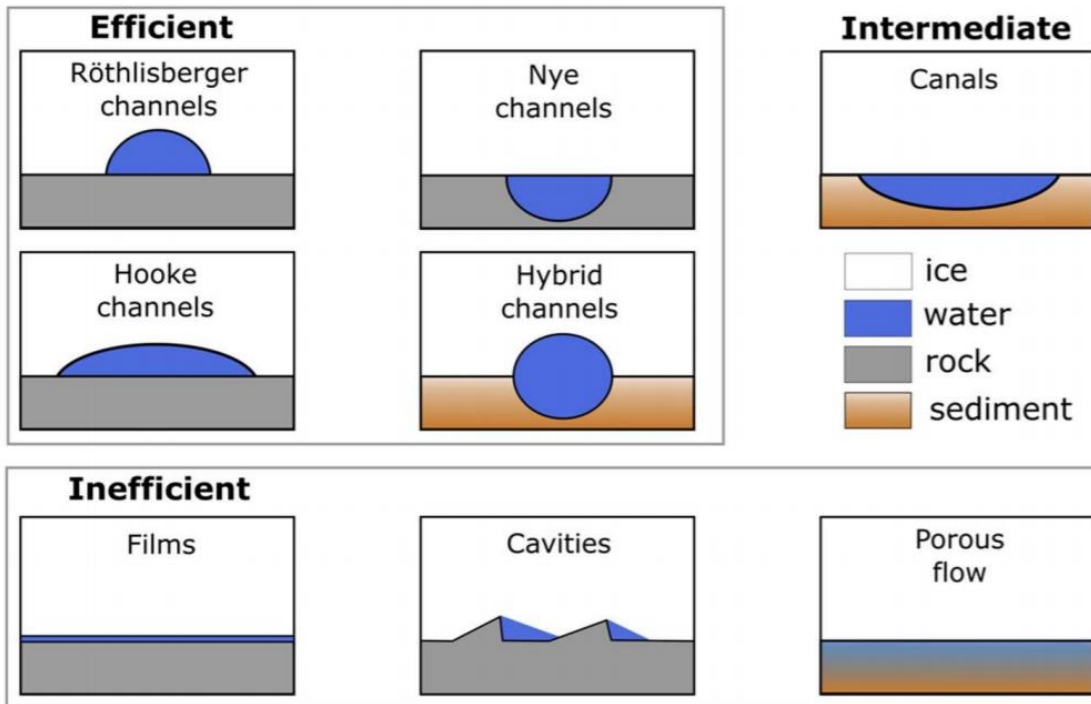
Figure 1.7. Conceptualised diagrams of efficient, intermediate and inefficient subglacial drainage systems. Note that although channels and cavities are shown as filled with water, this may not be the case if they are not in steady state. Source: Davison et al. (2019).

Whilst a subglacial system can theoretically be in 'steady state' if the outward pressure from channel wall melting equals creep closure pressure from surrounding ice, in reality, subglacial systems are constantly adjusting to varying inputs of melt to the basal environment (Schoof, 2010; Davison et al., 2019). For example, the injection of surface water to a hydrologically inefficient subglacial system has the effect of increasing subglacial water pressure and basal sliding, leading to an acceleration in ice flow (Iken, 1981; Cowton et al., 2013). Sustained meltwater input causes turbulent water flow in the subglacial environment, generating heat which initiates melting into the underside of the glacier (Röthlisberger, 1972). If a critical discharge is surpassed relating to heat generated by water flow for a given ice thickness, viscosity and bed roughness, wall melting becomes sufficient to outweigh creep closure and an efficient channel can form (Schoof, 2010). Formation of channels induces a shift to a more efficient hydrological system, resulting in a reduction in water pressure and ice deceleration (Nienow et al., 1998).

The influence of surface melt on ice dynamics varies between locations. The greatest hydrological control on ice motion is currently observed at temperate valley glaciers and

in land-terminating parts of west Greenland (Bartholomew et al., 2012). In these locations, a prolonged melt season sustains meltwater input to the subglacial environment, resulting in ice-flow variations over sub-daily to seasonal timescales which reflect evolution in the efficiency of the subglacial hydrological system. High-Arctic regions, such as Arctic Canada and Devon Ice Cap, experience shorter, less intense melt seasons than those observed in Alpine settings, resulting in a subdued seasonal velocity signal (Wyatt & Sharp, 2015). Furthermore, many glaciers in these regions experience short-lived melt-induced speed-ups which are super-imposed on the seasonal velocity signal, highlighting subglacial systems that are sensitive to surface meltwater inputs (Bingham et al., 2008; Wyatt & Sharp, 2015). Melt induced ice flow variations in Antarctica have only recently been proposed (Tuckett et al., 2019), and there is currently a poor understanding of the influence that surface melt may have on ice motion across Antarctica.

1.2.3.3 Surface melt-induced ice flow variations in Antarctica

Tuckett *et al*. (2019) provided the first evidence of surface meltwater draining to the bed of grounded glaciers anywhere in Antarctica. Strong spatial and temporal correlations were observed between spikes in surface melting and transient ice acceleration at five marine terminating outlet glaciers on the Antarctic Peninsula, with several so-called 'speed-up events' inferred to be induced by surface melt (Tuckett *et al*., 2019, Fig. 1.8). This initial discovery, and the trigger mechanism for speed-ups, has been debated (Rott et al., 2020; Tuckett et al., 2020). However, several subsequent studies have provided further evidence to support the notion that surface-to-bed connections exist on the Antarctic Peninsula. Seasonal ice-flow variability has been observed for outlet glaciers feeding George VI ice shelf on the southern Antarctic Peninsula (Boxall et al., 2022), and at more than 100 outlet glaciers on the north-western Peninsula (Wallis et al., 2022). Whilst the forcing mechanism of these seasonal signals is still uncertain, many tidewater glaciers display peaks in ice velocity coincident with spikes in surface melt, followed by an immediate slowdown to below pre-acceleration velocities; indication of a subglacial hydrological control. Hodgson et al. (2022) additionally show that a subglacial lake under Mars Glacier, situated on Alexander Island on the south-western Antarctic Peninsula, experiences peak refill rates coincident with seasonal surface meltwater activity, indicative of coupling between surface climate processes and the bed. The existence of

active subglacial hydrological systems on the Antarctic Peninsula provides a mechanism for glaciers in the region to respond directly and rapidly to atmospheric warming (Tuckett et al., 2019).

Whilst surface-to-bed connections have currently only been discovered on the Peninsula within Antarctica, it is possible that such drainage pathways are more widespread than is currently realised. Although factors such as ice temperature and thickness may limit the development of connections, theory suggests that lakes 0.25-0.8 km in diameter (which are common on grounded ice in many regions of Antarctica) provide enough water to initiate hydrofracture to the bed through over 1 km of cold ice (Krawczynski et al., 2009; Tuckett et al., 2020). Moreover, as the extent and intensity of Antarctic surface melting increases with climate warming (Trusel et al., 2015), an increasing area of the AIS will experience surface conditions akin to present-day ablation zones on the GrIS. Processes that are currently widespread in parts of Greenland, such as rapid lake drainage events, could therefore become common in some regions of Antarctica. Ice-flow dynamics are sensitive to melt supply variation rather than mean values of surface melt (Schoof, 2010). Hence, even if total Antarctic melt rates remain considerably lower than those observed in west Greenland, glacier flow rates may nevertheless be highly sensitive to variations in surface melting once drainage pathways have been established (Tuckett et al., 2019).
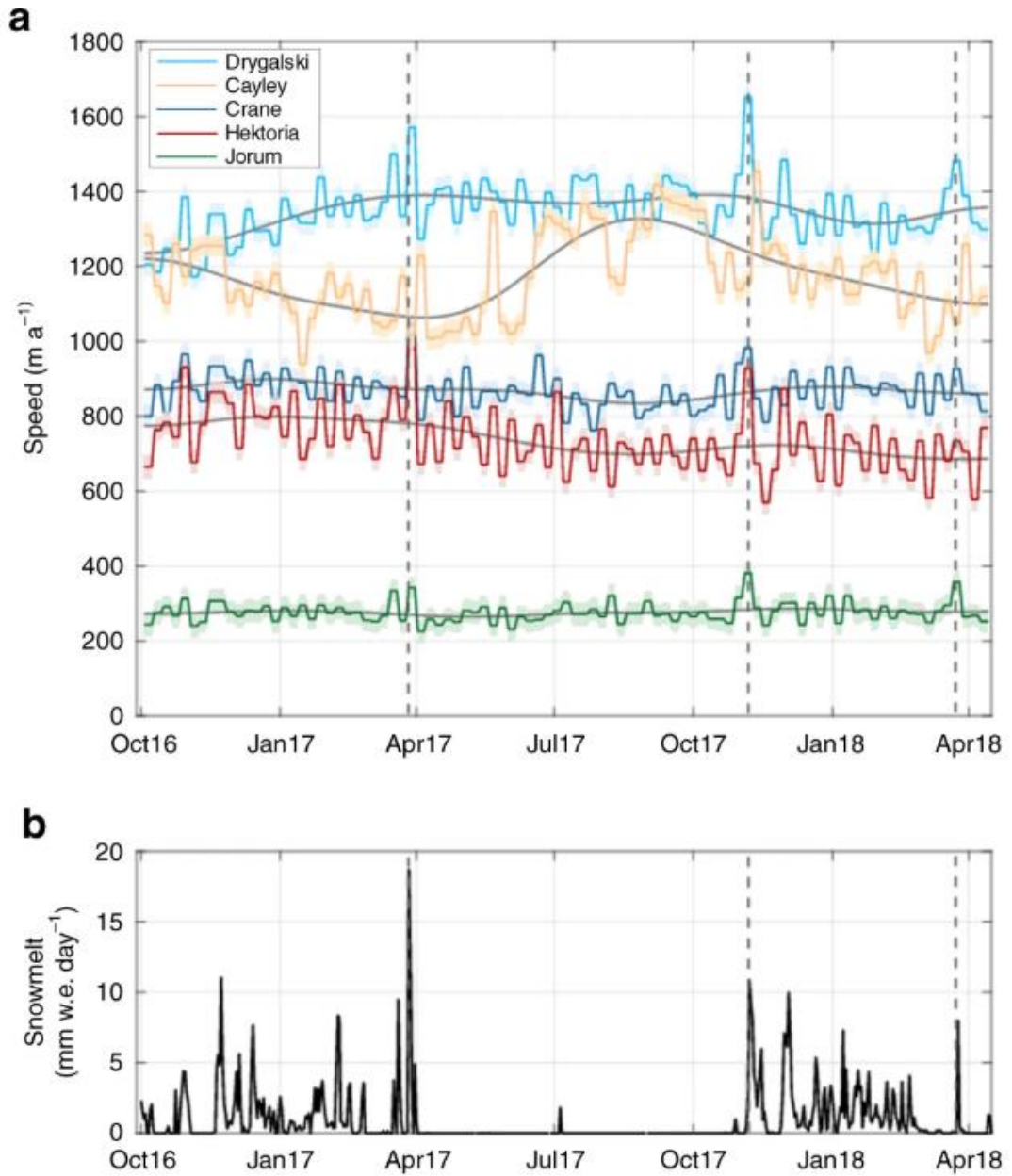
Figure 1.8. Temporal correlations between velocity (a) and modelled surface melt (b) from five outlet glaciers on the Antarctic Peninsula. Speed-up events, which correspond with spikes in modelled melt, are indicated by the dashed lines. Adapted from Tuckett et al., (2019).

A continuum of melt-dynamic regimes has been proposed (Tuckett et al., 2019; Stevens et al., 2022), whereby ice motion fluctuations depend on both the magnitude and timing of surface melt and the efficiency of the subglacial drainage system (Fig. 1.9). The Antarctic Peninsula currently experiences a relatively weak hydrological control, although the dynamic response of glaciers to meltwater supply possibly varies across the region. On the north-east Peninsula, short-lived glacier speed-ups are controlled by

sporadic, low magnitude melt events (Tuckett et al., 2019), whilst glaciers on the west coast display more seasonal velocity signals which coincide with short melt seasons (Boxall et al., 2022; Wallis et al., 2022). Meltwater production on the Antarctic Peninsula is strongly controlled by individual weather events, in particular the localised short-term warming effect of föehn winds, meaning melt supply is not sustained for prolonged periods of time. However, as the magnitude and variability of Antarctic Peninsula melting increases, it may induce a shift in melt-dynamic regime to the scenario currently observed in Arctic Canada (Bingham et al., 2008), where both seasonal and short-lived velocity variations are experienced in response to surface melting. The discovery of seasonal velocity variations (Boxall et al., 2022; Wallis et al., 2022) suggest this shift may already have happened on the western Antarctic Peninsula. Sustained meltwater supply associated with climate warming could result in Antarctic Peninsula glaciers becoming less sensitive to melt input, potentially reducing net glacier motion as the subglacial hydrological system become more efficient. This could eventually lead to a system akin to west Greenland, where reductions in ice velocity over winter months compensate for faster ice motion during the summer. This process has been observed at both land-terminating (Sole et al., 2013; Tedstone et al., 2013) and tidewater (Davison et al., 2020) glaciers in Greenland, although the net effect of future increases in surface melting on multiannual ice flow remains uncertain (Davison et al., 2019). Spatially variable future surface melt rates around Antarctica may hence result in regions lying at different stages along the melt-dynamic continuum.

Location	Characteristics	Typical melt and velocity trend

Weak hydrological influence

Antarctic Peninsula

- *Sporadic melt events*
- *Long periods of no melt*
- *Short-lived speed-up events triggered by surface melt draining to bed*
- *Inefficient subglacial hydrological system highly sensitive to surface melt input*

High Arctic Canada

- *Short melt seasons (2-3 months)*
- *Both seasonal and short-lived velocity variations driven by surface melt*
- *Largely inefficient subglacial hydrological system*
- *Some inter-decadal variations in ice motion attributed to changes in hydraulic efficiency*

Strong hydrological influence

West Greenland, Alaska, Temperate valley glaciers

- *Prolonged surface melting over a 4-5 month melt season*
- *Sustained meltwater transfer from surface to bed via moulins and lake drainage events*
- *Sub-daily to seasonal velocity variations combine to create an annual velocity signal*
- *Subglacial hydrological system adjusts to seasonal meltwater input*

Figure 1.9. Suggested continuum of melt-dynamic regimes, with different locations displaying varying influence of hydrology on ice dynamics. Adapted from Tuckett et al. (2019).

1.2.4   Knowledge and capability gaps

To assess the impact surface meltwater may have on ice shelf stability and grounded ice dynamics in the future, we first need to develop a greater understanding of its distribution and evolution at a continental scale. Despite a recent surge in scientific attention on Antarctic surface meltwater, there remain many unanswered questions regarding its evolution, controls, and impacts. Whilst the broad spatial distribution of surface meltwater across Antarctica is now relatively well known (Kingslake et al., 2017; Stokes et al., 2019), our understanding of the seasonal and multiannual evolution of surface water is poor (Arthur et al., 2020a). Previous mapping studies of Antarctic surface meltwater have largely been limited by either spatial or temporal extent, meaning long-term assessments of continent-wide meltwater areas have yet to be achieved (Moussavi et al., 2020). The generation of multi-annular, high temporal resolution quantitative estimates of surface meltwater area would significantly assist with evaluating the potential for surface melting to impact future ice sheet mass balance. Such a dataset would enable us to answer key questions such as: Is the area of surface meltwater in Antarctica increasing?

What is the variability of meltwater cover within a melt season and over multiple years? Is the proportion of surface water on grounded ice increasing?

Processes related to surface meltwater on grounded ice in Greenland have been widely researched (see Davison et al., 2019 for a review), yet our understanding of the role of surface meltwater in Antarctica has largely been limited to ice shelves, predominantly along the Antarctic Peninsula. Styles of meltwater evolution across Antarctica are hence poorly understood, and there are limited studies examining the potential for the drainage of surface meltwater into the englacial or subglacial systems. For example, do lake drainage events occur on grounded ice in Antarctica? What proportion of supraglacial lakes freeze over at the end of a melt season? How much lateral transfer of meltwater is there between lake basins on both floating and grounded ice? High temporal resolution time series of lake volume are required to answer such questions, and would allow quantification of different styles of lake behaviour over seasonal and multi-annular scales.

The relationship between climatic conditions, ice surface characteristics and meltwater ponding is highly complex and is poorly constrained (Dirscherl et al., 2021). Although several local-scale controls (such as firn density, albedo, proximity to exposed bedrock and katabatic/föehn winds) are known to influence meltwater ponding, the broader influence of synoptic scale atmospheric circulations, such as the SAM, is largely unknown. The generation of a multi-year, continent-wide meltwater dataset would enable comparison with indices of large-scale climate variability. This could help to inform how predicted changes in modes of atmospheric variability will impact the future extent of surface meltwater.

Many of the stated gaps in our understanding of Antarctic surface meltwater have remained unaddressed due to computational restrictions and time limitations associated with large-scale data analysis. Traditional methods of downloading satellite images for analysis are time-consuming and require vast quantities of data storage, thus limiting research scope. Processing at large spatial or temporal scales can additionally be highly computationally expensive, even for workflows that have been semi or fully automated. It is only since the advent of cloud-based computational platforms, such as Google Earth Engine (GEE), that much larger-scale geospatial analysis has been feasible. Such platforms have revolutionised the scale at which earth observation can be conducted

(Gorelick et al., 2017), but these platforms have yet to be fully taken advantage of by the scientific community.

1.2.4.1 Google Earth Engine

GEE is a computational platform that enables users to run geospatial analysis via Google's high-performance servers. By running jobs in parallel over multiple servers at once, large computational jobs can be completed quickly. GEE contains a large catalogue of ready-to-use, cloud-hosted geospatial data products, extending back more than thirty years into the satellite data archive. Users can access these data via Earth Engine's application programming interface, which provides a relatively simple and accessible means for performing geospatial analysis (Gorelick et al., 2017). GEE therefore provides the perfect solution to address the challenges associated with large scale analysis of surface meltwater in Antarctica.

GEE has been used across a wide range of disciplines, such as assessing global forest change, crop yield estimation and fire risk mapping (Gorelick et al., 2017). Use of the platform within cryospheric science is rapidly increasing, and tools such as the Google Earth Engine Digitisation Tool (GEEDiT) have provided a simple and user-friendly method for visualising and digitising changes in glacial environments (Lea, 2018). Examples of applications of GEE within glaciology include the automated detection of icebergs from high resolution data elevation models (DEMs) (Shiggins et al., 2023) and the assessment of long-term changes in calving front position of tidewater glaciers in Greenland (Fahrner et al., 2021). The capability for using GEE to map surface meltwater at large spatial and temporal scales has been demonstrated in Greenland (Lea & Brough, 2019), and has recently been applied to automatically map supraglacial lakes across two ice shelves in Antarctica (Halberstadt et al., 2020). GEE, however, has yet to be used to map surface meltwater at an Antarctic-wide scale.

1.3 Aims and objectives

The knowledge gaps outlined above motivate the need to study Antarctic surface meltwater at higher spatial and temporal scales than previously accomplished. GEE presents the opportunity to achieve this goal, and is key to addressing the aims and objectives of this thesis.

Aim: To improve our understanding of the occurrence and evolution of surface meltwater on the Antarctic Ice Sheet.

Objective 1: Develop a method for automatically mapping surface meltwater from optical satellite imagery that can be implemented in GEE.

Objective 2: Test the mapping method at a regional scale, and evaluate regional controls on surface hydrology.

Objective 3: Apply the method across Antarctica to generate continent-wide, long-term time series of Antarctic surface meltwater for the first time.

Objective 4: Assess the extent to which large-scale modes of climate variability influence the distribution and magnitude of surface meltwater across Antarctica.

Objective 5: Evaluate the behaviour of surface meltwater evolution and search for evidence of lake drainage events.

1.4 Thesis structure and relation to previous publications

This thesis comprises five chapters, including this introduction (Chapter 1). The five stated objectives are addressed in three main content chapters (2-4), which are subsequently followed by a discussion and conclusions chapter (5). A brief summary of the contents of each chapter is provided below. Large sections of work presented in this thesis have either already been published, or are under review, in international peer-reviewed journals. All of the papers are led by myself, have multiple co-authors, and present work conducted within my doctoral programme. The relation between thesis

chapters and publications are hence noted, and the contribution of all authors to the related papers are clearly stated.

Chapter 2

Tuckett, P. A., Ely, J. C., Sole, A. J., Lea, J. M., Livingstone, S. J., Jones, J. M., & van Wessem, J. M. (2021). Automated mapping of the seasonal evolution of surface meltwater and its links to climate on the Amery Ice Shelf, Antarctica. The Cryosphere, 15(12), 5785-5804.

In Chapter 2, I implement an existing threshold-based method for surface meltwater detection within GEE to automatically map surface meltwater over large spatial and temporal scales (Objective 1). I incorporate a novel approach for assessing ice surface visibility within the method, enabling me to quantify uncertainty induced by cloud cover and variable data coverage. I then test the method by applying it to the Amery Ice Shelf region of East Antarctica between 2005 and 2020 (Objective 2). I generate continuous, bi-weekly time series of surface meltwater area to assess trends and variability in coverage in the region for the first time. Finally, I compare my surface meltwater results with climate data to evaluate regional controls on meltwater ponding (Objective 2).

The contents of this chapter are published in *The Cryosphere*. The paper has been modified for consistency within the thesis, including removal of parts of the introduction and incorporation of supplementary figures into the main text. Aside from these minor changes, the chapter is mostly identical to the published version.

For this paper, PAT developed the methodology and GEE code (building on prior work by JML), conducted all the analysis and led the manuscript writing. All work was conducted under the supervision of JCE, AJS, SJL and JML. AJS provided assistance developing the MATLAB post-processing script. JMJ provided guidance on the climate comparison sections. JMW provided the RACMO data and gave guidance on this section. All authors contributed to research design and editing of the final manuscript. The paper was edited by Huw Horgan, and reviewed by Sammie Buzzard and one anonymous reviewer.

Chapter 3

Chapter 3 remains geographically focused on the Amery Ice Shelf region, and builds upon mapped surface meltwater outputs from Chapter 2. Here, I adapt existing methods, and develop novel approaches, to evaluate styles of meltwater evolution in the Amery region, including searching for evidence of lake drainage events on grounded or semi-grounded ice (Objective 5). I apply a method for generating lake volumes from Landsat and Sentinel optical imagery within GEE, generating 5-year volume time series for >200 lakes. I additionally use MODIS reflectance data to develop a novel method to enhance the temporal resolution of results, allowing better constraints on the timing of lake volume evolution. I analyse the results, in combination with visual interpretation of optical images, to identify styles of lake drainage events. Material presented in Chapter 3 has not yet been published, or submitted for publication.

Chapter 4

Tuckett, P. A., Ely, J. C., Sole, A. J., Livingstone, S. J., Jones, J. M., Lea, J. M., & Gilbert, E. (2022). Continent-scale mapping reveals a rise in East Antarctic surface meltwater.

Chapter 4 presents results from continent-wide application of the surface meltwater mapping method detailed in Chapter 2. I generate monthly meltwater area data between 2006 and 2021 to produce the first, long-term time series of surface meltwater across the entire Antarctic continent (Objective 3). I perform statistical analysis to assess trends in surface meltwater area for the three ice sheets of Antarctica, and produce recurrence frequency maps to identify locations where meltwater ponds on an annual basis. I compare my continent-wide surface meltwater dataset with three modes of Antarctic climate variability to assess first-order atmospheric controls on continental-scale meltwater coverage (Objective 4).

The results of Chapter 4 are written as a short-format manuscript, which is available online as a pre-print and is under peer-review for publication in *Nature Climate Change*. Due to the short-format nature of this manuscript, the results have been re-written in longer format for this chapter. Figures and sections of text from the manuscript have been re-used, and are incorporated alongside additional material.

PAT, JCE, AJS, SJL and JML developed the idea for this paper. PAT developed the surface hydrology mapping methodology, conducted all the analysis, and led the

manuscript writing. JCE, AJS, SJL and JML provided input on research design and interpretation of results. JMJ and EG provided guidance on the climate comparison sections. All authors provided input on editing of the manuscript. The paper is currently under peer-review, and is being handled by an editor, Jasper Franke.

Chapter 5

In Chapters 2-4, I present novel methods and results that help to improve our understanding of surface meltwater across Antarctica. In Chapter 5, I provide a discussion of how this work fits into the wider research context, and to what extent I have been able to accomplish the objectives posed in Section 1.3. This chapter additionally incorporates elements of work published in *Nature Communications* as a *Matters Arising* paper. This paper is based on work I conducted at the start of my doctorate, elaborating on work conducted prior to my PhD where I linked surface meltwater and ice dynamic responses on the Antarctic Peninsula (Tuckett et al., 2019). In this chapter, I only include selected material from the follow-up paper that I conducted by myself during my doctoral programme, and fits in with the wider discussion and theme of the thesis. Elements of work I conducted for a NSF-NERC grant proposal developed during my doctoral programme are also included. Chapter 5 concludes with a summary of the key findings and contributions from the thesis.

Tuckett, P. A., Ely, J. C., Sole, A. J., Livingstone, S. J., Davison, B. J., & van Wessem, J. M. (2020). Reply to:"Impact of marine processes on flow dynamics of northern Antarctic Peninsula outlet glaciers" by Rott et al. Nature Communications, 11(1), 1-4.

CHAPTER 2

Automated mapping of the seasonal evolution of surface meltwater and its links to climate on the Amery Ice Shelf, Antarctica

2.1 Introduction

Despite widespread surface meltwater around the margin of Antarctica (Kingslake et al., 2017), our understanding of surface meltwater evolution throughout melt seasons and on a multi-year timescale remains limited (Arthur et al., 2020b). Given that surface meltwater has the potential to influence ice dynamic processes and ice-albedo feedbacks in several ways (Section 1.2.3), it is important to understand how Antarctic surface hydrological systems operate and evolve through time (Arthur et al., 2020b). Several methods have been developed to map surface meltwater using remote sensing techniques, with the majority of mapping studies utilising optical satellite data (Section 1.2.2). Though successful at identifying lakes, the application of optical mapping techniques have typically been limited by two key issues. First, studies have been limited in scope due to a combination of time-expensive workflows, restricted data storage and computational resource limits. Second, spatial and temporal variability in optical image visibility, in particular resulting from inconsistent satellite coverage and cloud cover, means that resulting time series of surface meltwater area are often incomplete.

In this chapter, I utilise GEE to overcome both of these challenges. I implement an image band reflectance threshold-based method (Moussavi et al., 2020) for surface meltwater identification in GEE, creating a fully automated method for mapping meltwater across Antarctica from Landsat imagery (Objective 1). I use both Landsat 7 and Landsat 8 imagery, enabling creation of a multi-year time series of meltwater area from 2005-2020. I present mapped results at bi-monthly (two outputs per month) temporal resolution over the duration of each melt season, applying a 'time window' approach whereby individual mapped outputs are binned to record the maximum meltwater area for each time window. I also incorporate a novel approach to quantifying meltwater coverage that accounts for variability in both optical image coverage (e.g. region of interest coverage and Landsat 7 scan line corrector failure) and cloud cover. I demonstrate the method across the Amery Ice Shelf region of East Antarctica, highlighting how it will ultimately be used to map meltwater at a pan-Antarctic scale. I present the multi-year and seasonal evolution of

surface meltwater in the study region, and compare my results with climate data to investigate controls on surface melt extent (Objective 2).

2.2 Study Region

The Amery Ice Shelf lies within an embayment of East Antarctica between the Prince Charles Mountains and Princess Elizabeth Land. Covering an area of over 60,000 km^2, it is the largest ice shelf in East Antarctica and drains approximately 16% of the EAIS (Fricker et al., 2002; Spergel et al., 2021). The study area covers 188,828 km^2, of which ~32% is floating ice shelf, ~68% is grounded ice, and <1% is exposed bedrock. The area has been divided into twenty-one 100 by 100 km tiles for processing in GEE (Fig. 2.1), and has been clipped to the coastline (Depoorter et al., 2013). The Amery Ice Shelf region was selected for the following reasons:

1) The Amery Ice Shelf develops a large surface hydrological network of supraglacial lakes and surface streams on an almost annual basis (Spergel et al., 2021). Surface meltwater ponding is known to have occurred in this region for several decades (Phillips et al., 1998), hence I can be confident of generating a time series with significant amounts of surface water.

2) The Amery Ice Shelf was one of the study areas used by Moussavi et al. (2020) to develop the meltwater mapping technique that is applied within this study. Therefore, I can be confident that the optical-band thresholds used by Moussavi et al. (2020) are appropriate for identifying surface water and masking out other land-surface types such as exposed bedrock and blue ice.

3) The region is a glaciologically important area of East Antarctica, due to the size of the ice shelf and the large catchment that it drains (Budd et al., 1966). Since surface melt can have a significant impact on ice dynamic processes (Section 1.2.3), it is important to understand how surface meltwater evolves in the region, and to determine long-term trends in surface water coverage. Although the Amery Ice Shelf is currently largely resilient to hydrofracture (Lai et al., 2020), lake drainage events on grounded ice could influence ice flow dynamics in the near future (Tuckett et al., 2019).

4) The study area is large enough to be able to examine whether it is computationally feasible to apply the method at a pan-Antarctic scale. Processing requirements

within GEE are scaled to the number of polygons that are detected, meaning it takes longer to map areas with high numbers of surface meltwater features. The Amery Ice Shelf has a higher spatial density of supraglacial lakes than most regions in Antarctica (Stokes et al., 2019), so by demonstrating that the method can efficiently map surface meltwater evolution over this region, I can be confident that it can be applied at a continental scale (Objective 3).
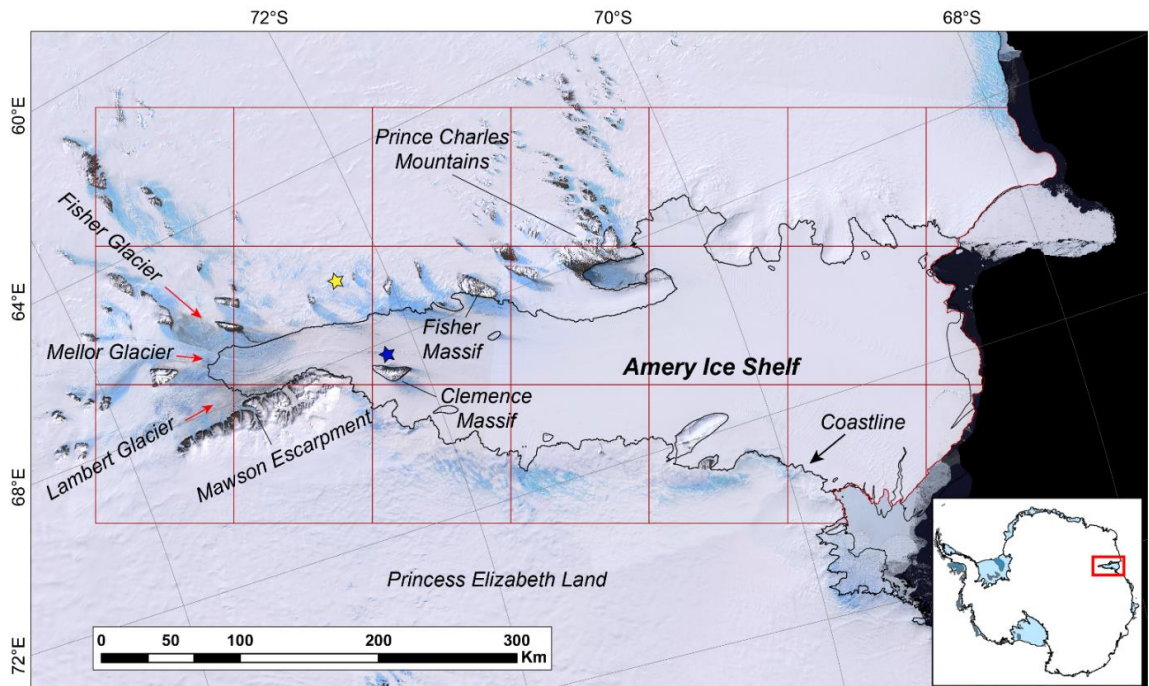
Figure 2.1. Study region over the Amery Ice Shelf, including an inset showing its location within Antarctica. The background image is the Landsat Image Mosaic of Antarctica. The red boxes indicate the area over which melt was mapped, with tiles representing twenty-one separate 100 by 100 km regions of interest (ROIs) for mapping within GEE. The black line marks the coastline from the SCAR Antarctic Digital Database (Gerrish et al., 2021). Red arrows indicate the flow direction of labelled outlet glaciers. The blue and yellow stars represent the location of Figure 2.6a and c, and 2.6b respectively.

2.3 Methods

The method comprises four stages: (i) image data collection and filtering; (ii) identification of areas of surface meltwater; (iii) image visibility assessment to quantify the area of surface meltwater missed due to cloud cover and image data coverage; and (iv) post-processing to generate polygon shapefile outputs and assign metadata. Stages 1-3

are undertaken within a single script in GEE, whilst stage four is performed in Matlab. Three inputs are required to run the automated mapping tool in GEE: 1) Start and end dates to define a date range for the image search; 2) A shapefile to specify the total area over which lakes will be mapped; 3) The temporal resolution at which results will be generated, either as a specified number of days or as a given number of time windows per month; for this study, this was set as two time windows per month. Inputs are split into several 'Region of Interest' (ROI) tiles to limit the area that is mapped at once (Fig. 2.1), thus avoiding memory limit errors in GEE. The mapping procedure loops over all the ROI tiles (twenty-one tiles for the Amery Ice Shelf region) within GEE to generate results across the study region. Below, the method is described over a single ROI tile.

2.3.1 Image Data Collection

Every Landsat 7 Enhanced Thematic Mapper Plus (ETM+) and Landsat 8 Operational Land Imager (OLI) image covering any portion of the study region between 2005 and 2020 was used during analysis, totalling 4164 image tiles. In practice this resulted in Landsat 8 images being exclusively used beyond March 2013, with Landsat 7 images used prior to this date. Images were not filtered by cloud cover to maximise the chances of detecting surface water. Level-1 Tier 2 Top of Atmosphere (TOA) Landsat image tiles were used, which are directly available for analysis through the GEE data catalogue (https://developers.google.com/earth-engine/datasets/catalog/landsat, last access: 31 March 2021). TOA reflectance values are typically used for ice sheet studies in preference to raw digital numbers to ensure that pixel values are not influenced by differences in image acquisition conditions (Pope et al., 2016; Moussavi et al., 2020). Processing was performed on a yearly basis, involving 16 runs of the GEE script (i.e. 2005-2020). For each GEE run, an image collection was generated from images that fitted the criteria of the specified time period and overlapped with the ROI. Images were additionally filtered to remove those with a sun elevation angle of less than 20°. Images with a sun elevation lower than this threshold value result in misclassification errors when using a band-threshold based approach, since in low light conditions surface water is not sufficiently spectrally different to be separated from features such as cloud and rock shadow (Halberstadt et al., 2020; Moussavi et al., 2020).

2.3.2 Delineation of surface meltwater

Surface meltwater was delineated using a method developed by Moussavi et al., (2020), who established threshold values to automatically identify surface water, cloud and rocks from Landsat 8 image bands (Table 2.1). The thresholds used in Moussavi et al. (2020) showed an accuracy of >95% when identifying lake areas from Landsat 8 imagery, and results showed high levels of agreement when compared with lake area data generated from other methods (Halberstadt et al., 2020). Whilst the thresholds developed by Moussavi et al. (2020) were designed specifically for Landsat 8 data, there are only minor differences in the band wavelengths of Landsat 7 images compared to the OLI satellite. I therefore applied the same thresholds to ETM+ imagery, enabling application of the method further back in time. A comparison of mapped meltwater outputs between Landsat 8 OLI and Landsat 7 ETM+ satellites is presented in Section 2.4.1.

As per the method of Moussavi et al. (2020), areas of exposed bedrock and seawater were removed from image tiles using a mask based on the thermal infrared (TIR) and blue bands. Cloudy pixels were removed using a combination of the Short-wave Infrared (SWIR) band, and the Normalized Difference Snow Index (NDSI; Eq. 2.1). Following application of these masks (Fig. 2.2), I then used an ice-specific version of the Normalised Difference Water Index (NDWI$_{ice}$; Eq. 2.2) to delineate areas of surface water. This is the most widely used technique for identifying water from optical imagery (Williamson et al., 2018; Arthur et al., 2020b), and has been successfully used to map supraglacial lakes on both the Greenland (Pope et al., 2016; Moussavi et al., 2016; Williamson et al., 2018) and Antarctic Ice Sheets (Stokes et al., 2019; Moussavi et al., 2020). See Table 2.1 for the threshold values used, and Moussavi et al. (2020) for further details of the method. Once surface meltwater pixels were detected in each individual image tile, images were assigned to a time window (Fig. 2.2). Lake masks from individual images within each time window were then combined to create a single maximal lake mask for each time window.

$$Normalized\ Difference\ Snow\ Index\ (NDSI) = \frac{Green - SWIR}{Green + SWIR} \qquad (2.1)$$

$$Normalized\ Difference\ Water\ Index\ (NDWI)_{ice} = \frac{Blue - Red}{Blue + Red} \qquad (2.2)$$

Table 2.1. Landsat image band reflectance thresholds (as detailed by Moussavi et al., 2020) applied during the masking and surface meltwater detection stages within GEE.

Classification	Thresholds applied
Rock/Seawater Mask	(TIRS1/Blue) > 0.35
	Blue < 0.35
Cloud Mask	(Green – SWIR1/Green + SWIR1) < 0.8
	SWIR1 > 0.1
Surface Meltwater	(Blue – Red/Blue + Red) > 0.1
	(Green – Red) > 0.07
	(Blue – Green) > 0.07
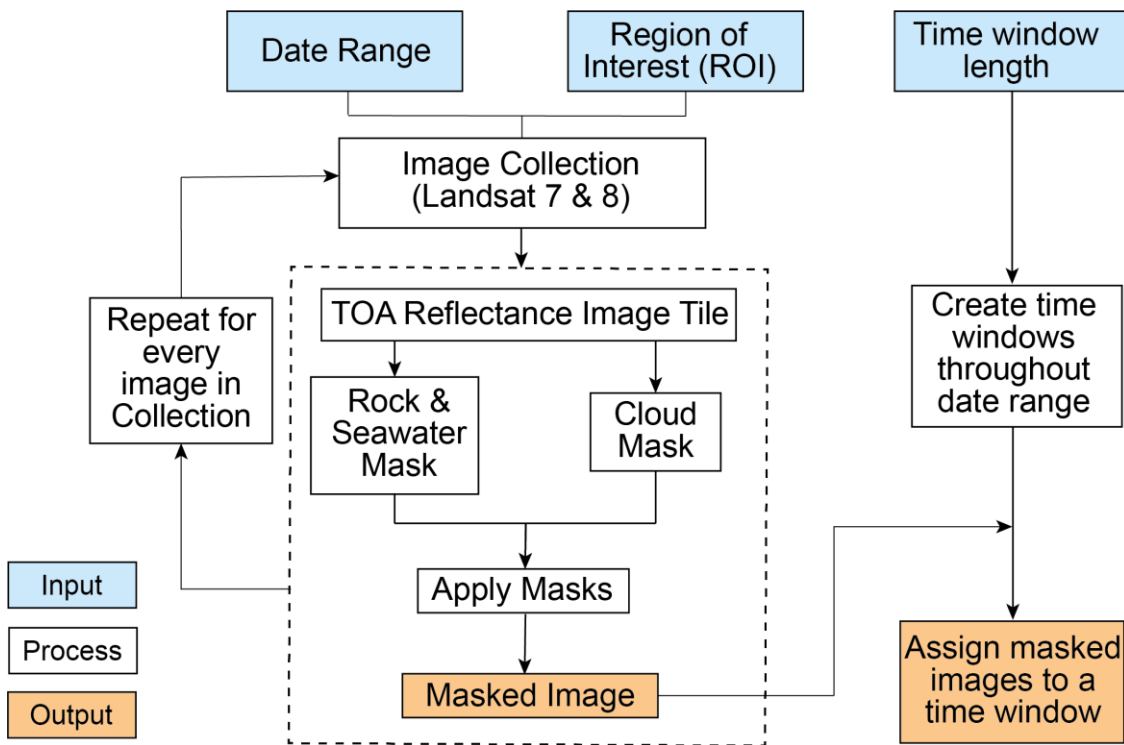
Figure 2.2. Flowchart illustrating the optical image masking steps taken within GEE, including the method by which images are assigned to time windows. See Table 2.1 for the threshold values (Moussavi et al., 2020) used during each masking stage.

2.3.3 Lake Visibility Assessments

For images affected by cloud cover, mapped lakes from optical satellite data represent minimum estimates of true lake area. Though simple metrics of cloud cover per image are informative, they do not account for variability in meltwater extent and visibility within a time window. To account for the uncertainty in lake area due to these visibility issues, I developed a novel technique which estimates the potential maximum lake area likely if clouds were not present. To evaluate meltwater visibility over the duration of each time window, two key aspects therefore needed to be assessed: i) A spatial assessment of the amount of ice visible within the intersection of each optical satellite image and each ROI, achieved by calculating an 'Image Visibility Score' (IVS) for every optical image (Fig. 2.3); and ii) A temporal assessment of the differences in meltwater extent between images within each time window. This second stage was achieved by calculating a 'Lake Pixel Contribution Score' (LPCS) for images within each time window (Fig. 2.3), enabling quantification of which images within any given time window contributed the most lake pixels to the overall output. These two metrics were then combined to estimate a 'Lake Visibility Percentage' (LVP) for each time window and ROI (Fig. 2.3).

Masked images in time window (x6)

Make NDWI band for each image

Masked image tile

Ice Mask

Identify visible ice within ROI (b)

Repeat for all images

Mosaic images based on highest NDWI values (c)

Clip to ROI (a)

Calculate Visible Ice Area

Apply thresholds to delineate lakes within ROI

Calculate Ice Mask Area

$$IVS = \frac{\text{Visible Ice Area (b)}}{\text{ROI Ice Mask Area (a)}}$$

Count number of lake pixels originating from each image (d)

Calculate lake pixel contribution per image

IVS (x6)

IVS * LPCS

LPCS (x6)

Sum results for all images

Input

Process

Output

LAKE VISIBILITY %

= Image 1 (12%)
= Image 2 (17%)
= Image 3 (1%)
= Image 4 (58%)
n/a = Image 5 (0%)
= Image 6 (10%)

a) Ice Mask — ROI outline

b) Visible over Ice

c) Image mosaic — ROI

d) Lakes

Figure 2.3. Flowchart detailing the method used to conduct lake visibility assessments within GEE for each time window. Images (a-d) provide visual examples of selected stages, and are referred to within the flowchart. The different lake colours in (d) indicate which optical image each lake pixel has originated from (e.g. Orange = Image 1, Yellow = Image 2 etc.). If the same pixel is covered by water in more than one image within a time window, the image pixel with the highest NDWI value is promoted to the mosaicked image. Six images (which are shown in Figure 2.5) were used in this example, indicated by (x6). IVS = Image Visibility Score; LPCS = Lake Pixel Contribution Score; ROI = Region of Interest.

2.3.3.1 Image Visibility Scores (IVS)

An IVS was generated for every image tile that intersected each ROI, to provide a combined measure of ROI coverage and image visibility from cloud cover (Fig. 2.4). Each IVS represents the percentage of ice cover within the ROI that was visible in the optical image. First, a 'clear-sky' ice mask covering the study region was created in GEE from cloud-free images using the rock mask thresholds stated in Moussavi et al. (2020). This enabled quantification of the area of ice covered by cloud in each image tile and facilitated removal of non-ice covered areas from IVS calculations, since I was only interested in areas where lakes could form on the ice surface. To calculate the IVS of a given Landsat image, both the cloud- and rock-masked optical image tile and the clear-sky ice mask were clipped to the extent of the ROI. These raster layers were then used to create a binary mask for each image which identified pixels within the ROI, that were both visible (not obscured by cloud) and located over ice. The areas (in km^2) of the ROI covered by both this 'visible over ice' mask and the clear-sky ice mask were then calculated within GEE. Each IVS was subsequently calculated following Eq. (2.3):

$$Image\ Visibility\ Score\ (IVS) \hspace{2cm} (2.3)$$
$$= \frac{Area\ of\ 'visible\ over\ ice'mask\ within\ ROI}{Area\ of\ 'clear-sky'\ ice\ mask\ within\ ROI}\ x\ 100$$
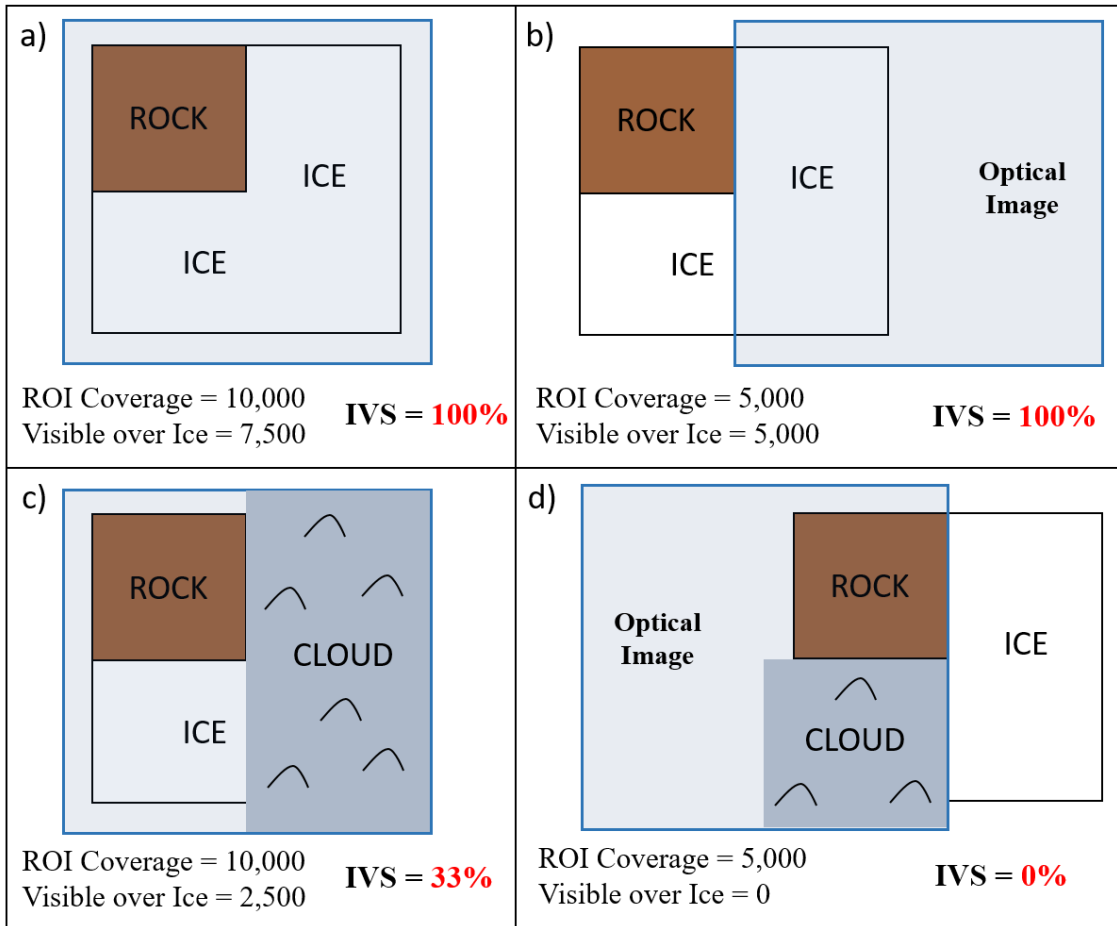
Figure 2.4. Schematic illustrations of four different image visibility scenarios, highlighting the IVS for each example. The black square boxes show a ROI tile, representing a 100 x 100 km area. The same ROI tile is used in each example, comprising 7,500 km^2 of ice (this is the 'clear-sky' ice mask value) and 2,500 km^2 of rock. Blue boxes represent Landsat optical image tiles, which cover all (a & c) or half (b & d) of the ROI. Optical images in (a) & (b) are cloud free, whilst images in (c) & (d) are partially cloud-covered. The numbers below each example signify: i) ROI Coverage = the area (km^2) of the ROI that is covered by the optical image; ii) Visible over Ice = the area (km^2) of ice within the ROI that is visible in the satellite image; iii) IVS = Image Visibility Score. The IVS score in each example as a percentage. This is calculated by dividing the 'Visible over Ice' area by the area of the 'clear-sky' ice mask within the ROI (7,500 in this example). Note how each IVS gives a combined measure of ROI coverage, cloud extent and the proportion of ice within the ROI.

2.3.3.2 Lake Pixel Contribution Scores (LPCS)

Given that several images usually covered at least part of the ROI within a time window, it was important to know which of them contributed the most to the detection of surface meltwater. To achieve a measure of this, a 'Lake Pixel Contribution Score' (LPCS) was calculated for every optical image within each time window. Following the removal of cloud and rock areas, the NDWI of images was calculated using the blue and red optical bands. A composite NDWI image for each time window was then created whereby the highest NDWI value for each pixel was promoted (using the 'qualityMosaic' function in GEE). Following this, I clipped the NDWI composite to the ROI and applied the three thresholds (Table 2.1) recommended by Moussavi et al. (2020) to identify surface meltwater pixels. Each image within a time window was assigned a unique ID prior to mosaicking to identify from which image each lake pixel had originated. This was achieved by performing a frequency count (ee.Reducer.frequencyHistogram) to determine the number of lake pixels within the ROI that were contributed by each individual image. LPCSs were then calculated based on the proportion of lake pixels from each image that were used in the composite lake mask for each time window (Fig. 2.5). For example, an image LPCS of 0.4 meant that 40% of the lake pixels identified in the time window composite were extracted from that image.
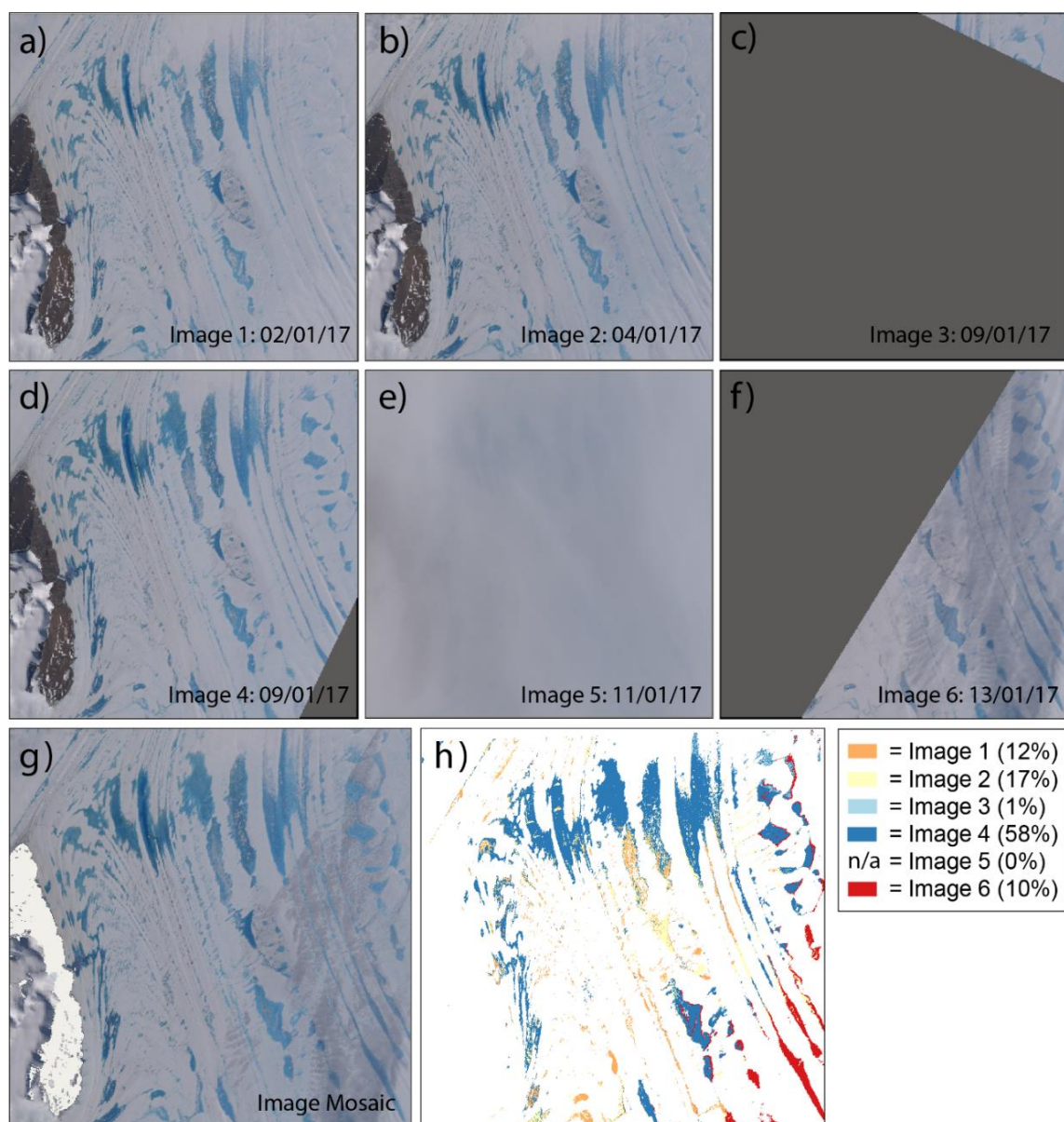
Figure 2.5. Example imagery from the time window 1ˢᵗ January – 15ᵗʰ January 2017, demonstrating how images are used to create lake pixel contribution scores (LPCS). (a-f) show six Landsat images that intersect an example ROI during the time window. Each image shows the ROI extent. Note how not every Landsat image covers the entire ROI, and some images (e) are cloud covered. The six images in (a-f) are mosaicked by promoting pixels with high NDWI values, to produce the composite image shown in (g). The different lake colours in (h) indicate which optical image each lake pixel has originated from. For example, 58% of the pixels in the composite image were contributed by Image 4 (d), whilst no pixels were contributed from Image 5 (e).

2.3.3.3 Lake Visibility Percentages (LVP)

For every image that contributed lake pixels within a given time window, the LPCS was multiplied by the IVS. These combined scores were then summed to create a 'Lake Visibility Percentage' (LVP) for that time window (Table 2.2). This final measure provided a representation of what area of meltwater coverage was likely to have been missed by the mapping approach. An LVP of 100% indicated that no lakes were missed (i.e. all of the ice surface was visible within the time window), whilst an LVP of 50% suggested that mapped results only accounted for half the likely true area of lakes. By performing this assessment of lake coverage, I was then able to scale mapped lake area results up to 100%, to attach an upper uncertainty bound to minimum mapped lake areas. This approach assumes that every image pixel is equally likely to be covered by surface meltwater, meaning scaled up results are only estimated values of surface meltwater area. In ROIs where supraglacial lakes are highly clustered, this could result in over- or under-estimates. However, by performing the method over large ROI tiles and at a bi-monthly temporal resolution (meaning several images overlap each ROI per time window), this uncertainty is minimised.

Table 2.2. Example data highlighting how pixel contribution scores and their corresponding visibility scores are combined to create an overall 'Lake Visibility Percentage' for each time window. The Landsat images used in this example are displayed in Figure 2.5.

Image Number	LPCS	IVS (%)	Combined Score
1	0.12	99.5	0.12 x 99.5 = 11.94
2	0.17	99.4	0.17 x 99.4 = 16.90
3	0.01	4.8	0.01 x 4.8 = 0.05
4	0.58	96.5	0.58 x 96.5 = 55.97
5	0.00	0	0.00 x 0 = 0
6	0.10	47.1	0.10 x 47.1 = 4.71
Lake Visibility Percentage (LVP)			89.57%

2.3.4 Post-processing steps

Mapped lake polygons and visibility statistics were exported as geoJSON files from GEE. Several post-processing stages were then undertaken in Matlab to convert the data into shapefiles, merge lake polygons between ROIs, and attach metadata. Shapefiles were firstly created (using the Antarctic Polar Stereographic projection) for every ROI tile and time window. ROI-specific shapefiles were then merged across the entire study region, to create one single dataset per time window. As part of this step, lakes split over ROI boundaries were joined together (Union), and inner polygons were 'cut' from outer lake boundaries in instances where an 'island' (typically an ice lid) was present within a lake. I then calculated the area and geometric centroid of each cleaned polygon and applied an area threshold of two pixels, giving minimum lake areas of 1800 m^2 based on a Landsat resolution of 30 m. This is lower than the area threshold applied by Moussavi et al. (2020), who removed mapped features smaller than five pixels (4500 m^2) in total and linear features narrower than two pixels. Moussavi et al. (2020) applied these filters to remove features that were likely to be slush or meltwater streams, rather than lakes. I wanted to capture all meltwater features, regardless of shape or size, within my dataset. Hence, I followed the approach of Stokes et al. (2019) by using an area threshold of two pixels. This filtered out single pixel noise, likely misclassification errors, from the raw output, whilst retaining enough data to include small lakes, especially those at high elevations that would have been missed with a higher area threshold value.

The application of a two-pixel area threshold means that the method accuracy reported by Moussavi et al. (2020) (95%) may be slightly higher than the accuracy of my dataset. This is because smaller meltwater features are more likely to be misclassification errors, compared to larger lake bodies. However, smaller meltwater features are also more difficult to manually identify, making verification harder. I therefore did not deem it beneficial to conduct a separate quantitative uncertainty estimate for my dataset. Instead, I analysed the relative contribution of different feature sizes to total meltwater area across the study region, to assess the impact that the inclusion of small (2 – 4 pixels) meltwater features had on my results (Section 2.4.1).

Unlike some other studies (e.g. Stokes et al., 2019), I decided not to aggregate lake polygons in close proximity to each other, as tests showed this sometimes resulted in the false identification of large lakes in areas of meltwater-filled crevasses. Finally, I attached

selected metadata to each identified lake based on the geometric centroid of lake polygons. The Depoorter et al., (2013) grounding line dataset was used to label lakes as either 'grounded' or 'floating', whilst the elevation and surface slope of lake centroids were extracted from the Reference Elevation Model of Antarctica (REMA) database (100 m resolution) (Howat et al., 2019). All post-processing steps were automated in Matlab, with each melt season taking approximately 2-5 hours to run.

2.3.5 Comparison with climate data

To provide an initial test of the extent to which climatic modelling can simulate surface meltwater ponding, I compared my lake area results with modelled snowmelt outputs from the Regional Atmospheric Climate Model version 2.3p2 (RACMO2.3p2) (van Wessem et al., 2018). RACMO2.3p2 has a horizontal resolution of 27 km and is coupled to an internal snow model which calculates surface melt production, refreezing, percolation, retention and runoff into the ocean. The model is forced by ERA-Interim (~80 km horizontal resolution) reanalysis data (van Wessem et al., 2018). Monthly RACMO2.3p2 melt values were summed across the study region, then divided by the total number of pixels to provide monthly mean melt values. RACMO2.3p2 snowmelt outputs serve as an upper bound for meltwater availability, as the model does not specifically account for surface meltwater ponding. Moreover, it should be noted that RACMO2.3p2 locally resolves meltwater production based on model grid boxes, and hence does not account for the process of meltwater flowing from higher elevations (Spergel et al., 2021). This analysis therefore offers a preliminary comparison between the two datasets rather than a full evaluation, which would require quantification of lateral meltwater transfer and biases highlighted in van Wessem et al. (2018). Given the catchment scale of this study, the lack of lateral meltwater transport is of less importance than for smaller scale studies (e.g. Spergel et al., 2021).

To explore the potential role of large-scale atmospheric circulation on surface meltwater ponding in the study region, I investigated the influence of the Southern Annular Mode (SAM). The SAM is the main mode of extratropical climate variability across the Southern Hemisphere, and represents changes in the strength and position of the Southern Hemisphere westerly winds and storm tracks (Marshall & Thompson, 2016; Section 1.2.1). I chose to compare my lake area results with the SAM because of its known

influence on Antarctic temperatures (Marshall & Thompson, 2016; Fogt & Marshall, 2020), and hence surface melting. Results were compared with austral summer values of the SAM index of Marshall (2003), obtained from (http://www.nerc-bas.ac.uk/public/icd/gjma/newsam.1957.2007.seas.txt. Last accessed: 31st March 2021).

2.4 Results

2.4.1 Evaluation of method

As shown by Moussavi et al. (2020), I find that the application of a band-thresholding technique within GEE is highly successful at rapidly identifying surface meltwater features over large areas and time periods. The thresholds applied were effective at masking out areas of rock and cloud over the whole study area, whilst successfully identifying surface meltwater (Fig. 2.6). Manual checking of mapped lakes against satellite imagery (from approximately ~10% of randomly selected time windows) identified very few false positives, and the technique performed well when differentiating lakes from areas of blue ice and shadow (Fig. 2.6). This is consistent with the findings of Moussavi et al. (2020), who used the same thresholds and found overall accuracies of >95% when mapping from Landsat 8 imagery. There was no particular spatial pattern to false positives, such as clustering around bedrock or shadow areas. False negative results were rare, and mainly occurred where surface water was much darker in colour, presumably either due to sediment suspended within the water column or where lakes appeared to be very deep. Instances of sediment-laden water were confined to the immediate vicinity of rock outcrops, whilst lake depths very rarely exceed 4 m in the study region (Spergel et al., 2021). These misclassification errors thus had a minimal influence on results.
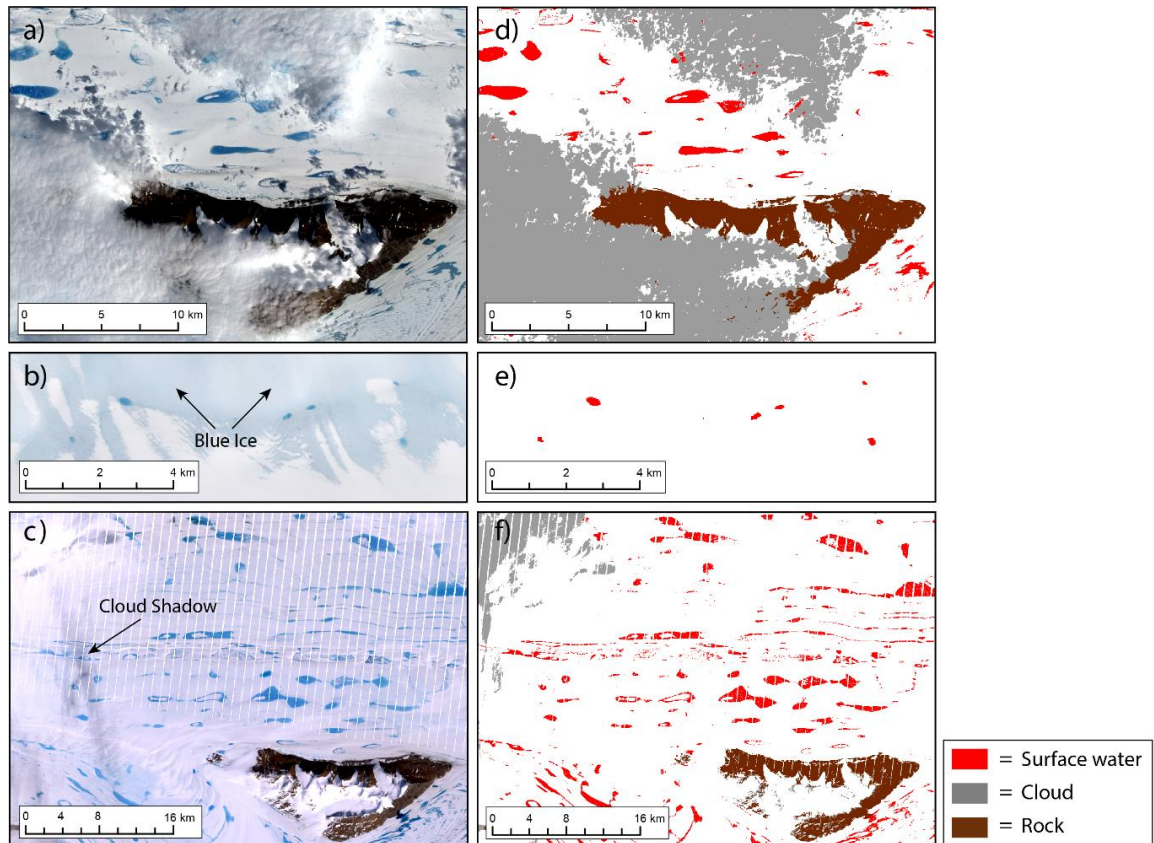
Figure 2.6. (a) Landsat 8 image from 25th January 2017 of the Clemence Massif; (b) Landsat 8 image from 1st January 2019, highlighting blue ice ~100 km south of Fisher Massif; (c) Landsat 7 image from 2nd January 2005, showing widespread surface lakes to the west of the Clemence Massif. Note the white stripes resulting from the failure of the Landsat 7 scan line corrector. (d-f) Automatic masking of cloud, rock, and surface water from Landsat imagery. The location of images (a-c) are shown in Figure 2.1.

To investigate the influence of small (< 5 pixels, or 0.0045 km²) meltwater features on meltwater area totals, I calculated the relative contribution of different sized meltwater features on total meltwater area for a sample time window. Mapped features from January 2017 (the time window studied by Stokes et al., 2019) were binned into twenty groups based on meltwater feature area (Table 2.3). Bin ranges were calculated based on a normal distribution of the data, on a logarithmic scale. Results show that small features were most frequently mapped, yet the contribution of the smallest features to total meltwater area was low (Fig. 2.7; Table 2.3). Over 14,000 features of between 2 – 5 pixels (Bins 1 & 2) were mapped, yet these features contributed just 3% to total meltwater area (Table 2.3). Hence, even if some of these smaller features are misclassification errors associated with

the NDWI thresholding approach, they will have had minimal influence on catchment wide meltwater area totals. The greatest area contributions came from medium sized lakes (Fig. 2.7b). Lakes ranging between 0.64 – 2.7 km^2 (bin numbers 13-15) contributed almost 30% of the meltwater area total (Table 2.3).

Table 2.3. Descriptive statistics for twenty bins of meltwater feature size, based on mapped meltwater features from January 2017.

Bin Number	Bin area (km^2)	Number of meltwater features	Contribution to total area (km^2)	% of total area
1	< 0.0029	10431	21.60	1.7
2	0.0029 – 0.0048	3783	15.01	1.3
3	0.0048 – 0.0078	2774	17.01	1.5
4	0.0078 – 0.0127	2387	23.78	2.1
5	0.0127 – 0.0208	1577	26.27	2.3
6	0.0208 – 0.0339	1092	29.08	2.5
7	0.0339 – 0.0553	877	37.99	3.3
8	0.0553 – 0.0901	592	41.77	3.6
9	0.0901 – 0.1470	472	54.58	4.7
10	0.1470 – 0.2398	316	59.21	5.1
11	0.2398 – 0.3912	238	72.97	6.3
12	0.3912 – 0.6381	163	80.04	6.9
13	0.6381 – 1.0409	140	113.13	9.8
14	1.0409 – 1.6980	80	106.26	9.2
15	1.6980 – 2.7698	55	115.94	10.0
16	2.7698 – 4.5181	25	88.19	7.6
17	4.5181 – 7.3700	17	97.90	8.5
18	7.3700 – 12.0221	9	88.54	7.7
19	12.0221 – 19.6105	1	13.13	1.1
20	>19.6105	2	53.24	4.6
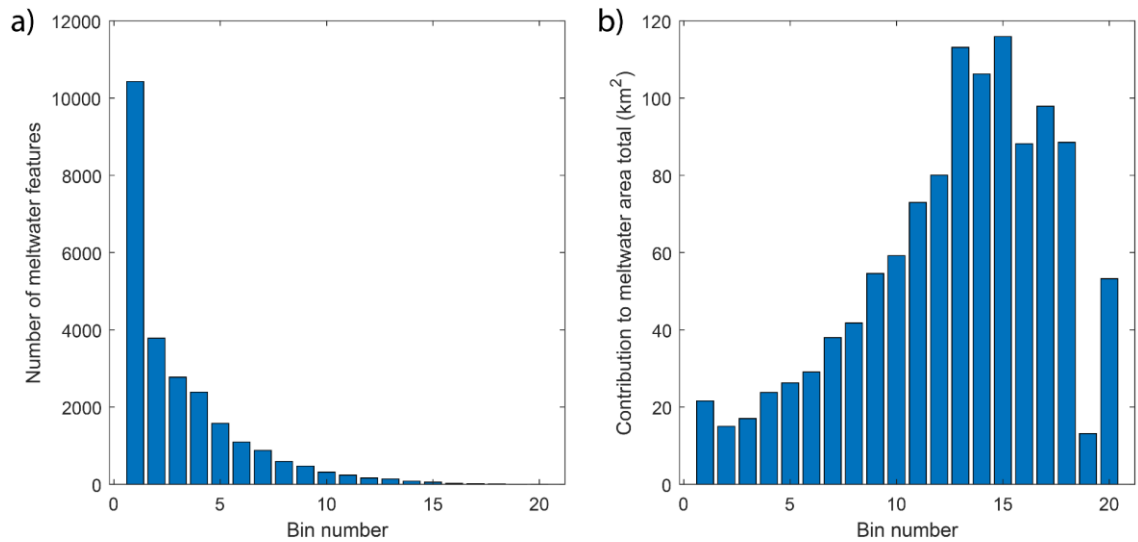
Figure 2.7. (a) The number of meltwater features mapped in January 2017 for each of the feature area bins displayed in Table 2.3. (b) The contribution (km^2) from each bin to the catchment-wide meltwater area total in January 2017.

LVPs ranged from 0-99.9%, with a mean LVP of 50.4% and a median LVP of 52.7% across the whole dataset. However, there were large differences between LVPs from Landsat ETM+ and OLI images, largely due to data gaps present within Landsat 7 ETM+ images as a result of the failure of the Scan Line Corrector. The median LVP from time windows using Landsat 7 imagery was 43.5%, compared to 61.6% when Landsat 8 images were used. By using LVPs to generate maximum lake area estimates, I was able to account for lake area underestimations resulting from data gaps in Landsat 7 imagery. On average, incorporating LVPs into lake area estimates resulted in a 58% increase in lake area per ROI and time window when using Landsat 7, and a 42% increase when using Landsat 8 images. When results were aggregated to generate cumulative lake area estimates per melt season, maximum potential lake area estimates were 42% greater than mapped values on average across the entire study period.

2.4.1.1 Comparison of Landsat 7 ETM+ and Landsat 8 OLI mapped outputs

To evaluate the success of applying the thresholds developed by Moussavi et al. (2020) to ETM+ imagery, I analysed differences in mapped meltwater outputs between the two satellites. Mapped lake outputs were compared between two images (from the two different satellites), taken over the same region at approximately the same time (24 hours apart). As no ETM+ and OLI images taken within the same week were available in Antarctica, analysis was conducted over a 2000 km^2 region in north-west Greenland (Fig.2.8). The closest temporal match over a lake-covered region was 24 hours, with images compared between the 21st (ETM+) and 22nd (OLI) July 2013. Manual inspection of imagery suggested meltwater area change between the two dates was sufficiently minor for the test to be appropriate. Whilst this analysis has several limitations (including potential lake area changes in the 24 hour period between the two images), it enabled a broad assessment of the differences in surface meltwater identification between the two different satellites.
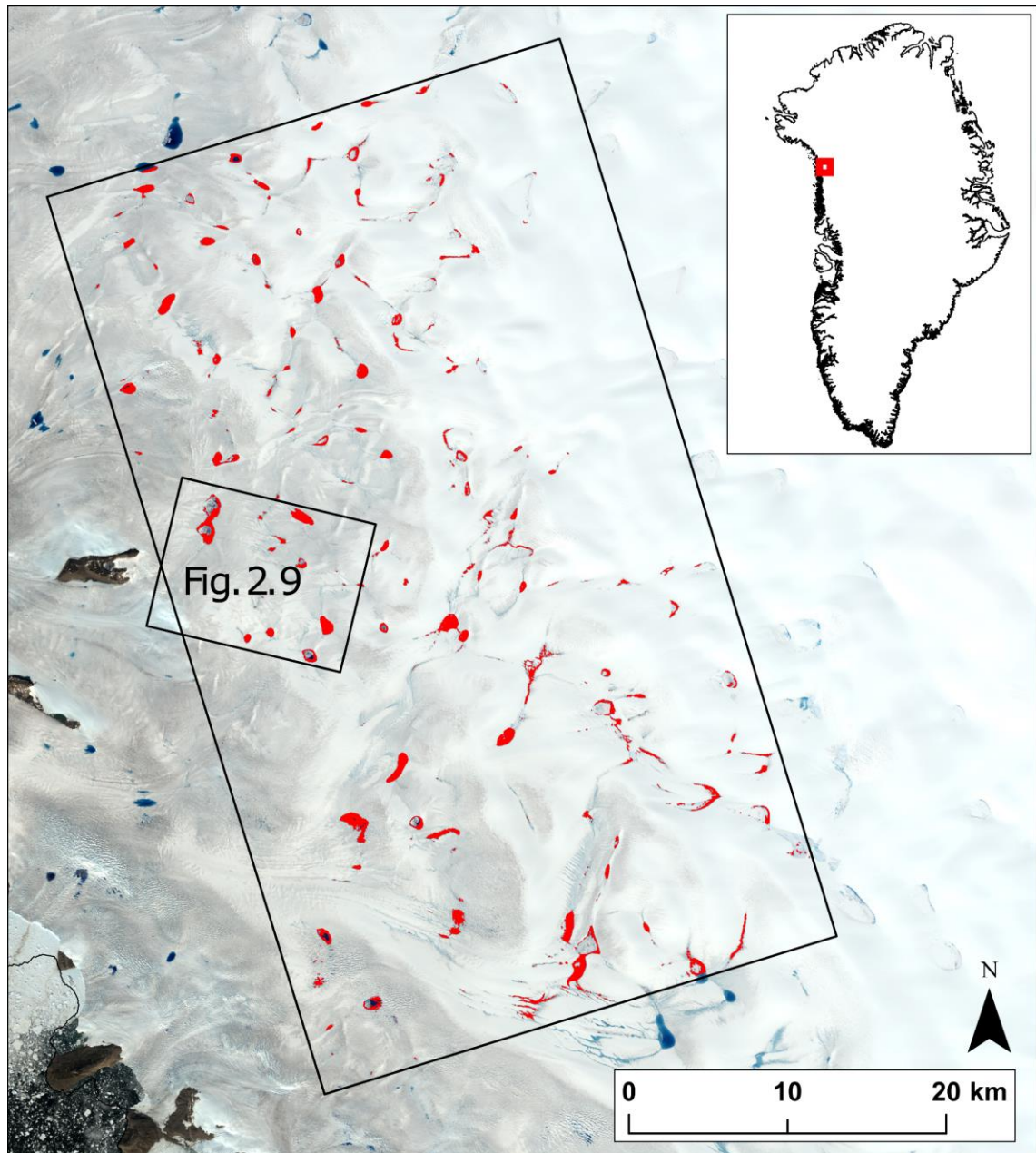
Figure 2.8. Region in north-west Greenland where Landsat 7 and Landsat 8 mapped lake results were compared. The larger box shows a 2000 km^2 region over which lake area results were compared between a Landsat 7 image (21st July 2013) and a Landsat 8 image (22nd July 2013, displayed), taken 24 hours apart. Automatically mapped lakes from the Landsat 8 image are shown in red. The smaller box labelled 'Fig. 2.9' indicates the region shown in Figure 2.9.

Overall, results demonstrate that it is appropriate to apply the same thresholds (Moussavi et al., 2020) to ETM+ imagery. Visual inspection of mapped meltwater outputs against raw imagery shows that the thresholds are highly successful at delineating surface meltwater in ETM+ imagery (Fig. 2.9). Delineated meltwater areas of larger bodies of

water were almost identical between both satellites (Fig. 2.9). The largest difference in method performance was in the detection of the smallest meltwater features (typically two or three pixels in size) in regions of high crevassing. These features were detected more frequently in OLI imagery, possibly contributing to the slightly higher total mapped meltwater area across the test region (Table 2.4). Differences were minor, however, and the small size of these features mean this difference in performance will have had minimal influence on meltwater area totals across the whole Amery catchment.
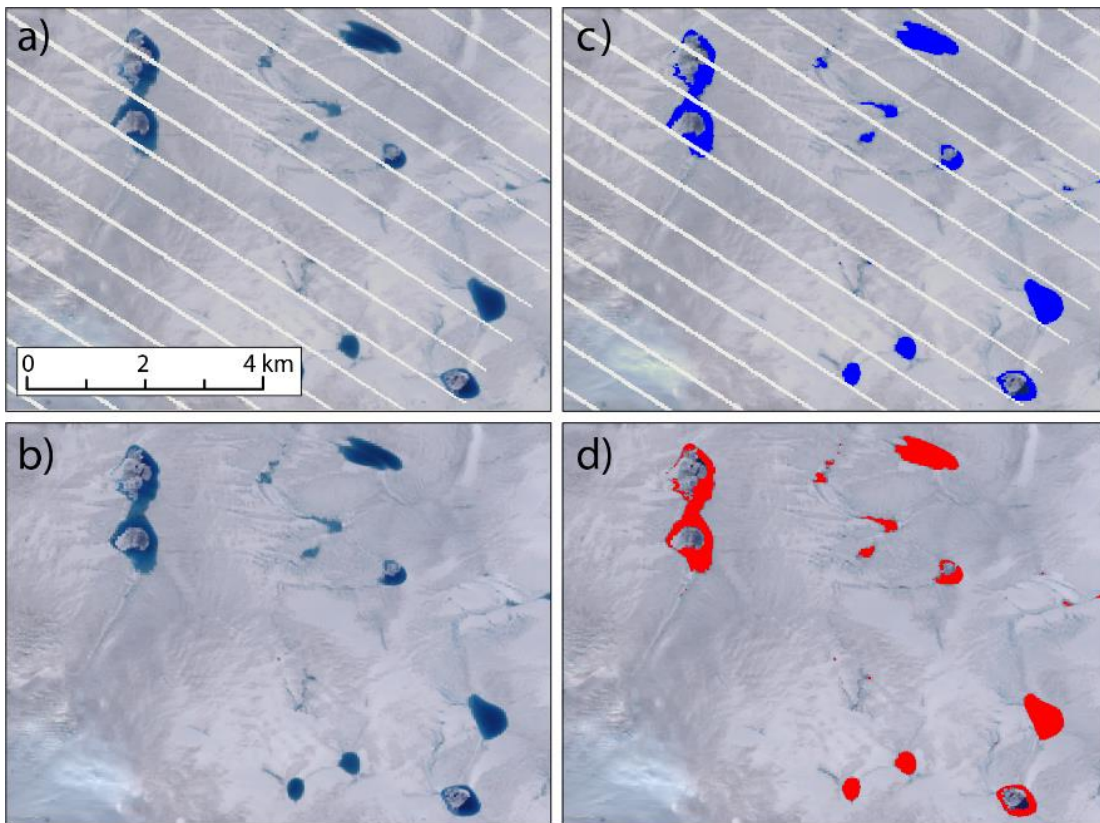
Figure 2.9. Automated masking of surface meltwater from Landsat 7 and 8 images. (a) Landsat 7 image from 21st July 2013, with automatically masked lakes shown in blue in (c). (b) Landsat 8 image from 22nd July 2013, with automatically masked lakes shown in red in (d). The area shown is displayed in Fig. 2.3. Note how the identification of surface water appears almost identical between the two satellites.

Comparison of mapped meltwater area totals between ETM+ and OLI imagery additionally reveals minimal difference in method performance. Comparison of meltwater area outputs from the GrIS study region (Fig. 2.8) shows an average agreement

of ~90% between the two satellites (Table 2.4). However, some of this ~10% difference can likely be attributed to real changes in meltwater area during the 24 hour period; minor increases in meltwater area were observed for some lakes between the ETM+ and OLI image. To account for missing data in the ETM+ image from Scan Line Corrector striping, I artificially added the same stripes to the OLI image. This enabled a more accurate comparison of thresholding performance between the two satellites, and allowed me to quantify the effect of visibility assessments in accounting for the missing data. Results show that application of the LVP method to the artificially altered OLI image increased the total mapped meltwater area from 33.1 km^2 to 35.02 km^2 (Table 2.4). This was only 0.06 km^2 greater than the true meltwater area as mapped from the original Landsat 8 image. Whilst not all results will be as accurate as this, especially when extrapolating area results from lower visibility scores, this demonstrates the success of the method at accounting for data gaps in ETM+ imagery.

Table 2.4. Lake area comparison results between a Landsat 7 image and a Landsat 8 image from north-west Greenland (Fig. 2.8). Results are displayed from the region shown in Figure 2.8. The third column displays results following the artificial addition of Landsat 7 striping to the Landsat 8 image.

Measure	Landsat 7	Landsat 8	Landsat 8 (with SLC stripes added)
Number of lakes	361	400	437
Minimum individual lake area	0.0027 km^2	0.0027 km^2	0.0027 km^2
Maximum lake area	1.39 km^2	1.54 km^2	1.54 km^2
Mean area	0.082 km^2	0.087 km^2	0.076 km^2
St dev. area	0.159	0.195	0.171
Lake visibility %	94.2 %	100	94.2 %
Minimum mapped total lake area	29.46 km^2	34.96 km^2	33.10 km^2
Estimated maximum total lake area	31.17 km^2	34.96 km^2	35.02 km^2

2.4.2 Spatial distribution of surface meltwater

Supraglacial lakes form on inland areas of the Amery Ice Shelf where the ice shelf is narrowest, and on portions of grounded ice within close proximity to the grounding zone (Fig. 2.10). On average, ~70% of total lake area within the study region exists on the ice shelf and ~30% on grounded ice. In high melt years (e.g. Fig. 2.11), lakes are widespread across the width of the ice shelf between ~72-73 °S, and along the Prince Charles Mountains side of the ice shelf to around 71 °S. Very few lakes form on the ice shelf interior further north than this latitude, although a cluster of lakes sometimes forms in a sub-inlet of the ice shelf near the Prince Charles Mountains (Fig. 2.10). Lakes on the ice shelf most frequently form on the south-east side of the Clemence Massif, and on the eastern side of the Fisher Massif (Fig. 2.10). Supraglacial lakes in these locations are typically elongate in shape, and are connected by surface streams and channels to form a distributed surface drainage network. During high melt years, the largest lakes are found along the central flowline of the ice shelf below 71°S; the largest mapped lake had an area of 107 km^2 in January 2005. However, these central lakes vary greatly in size and occurrence between melt seasons, whilst lakes nearer the grounding zone and next to areas of exposed bedrock form more frequently (Fig. 2.10).

Supraglacial lakes on grounded ice predominantly form within approximately 20 km of the grounding zone, and are particularly abundant along a 200 km stretch of the Princess Elizabeth Land ice shelf boundary between 70 – 72 °S (Fig. 2.10b). Lakes in this region, which can be up to 6 km^2 in area, typically form in the same location on an annual basis. Whilst the spatial extent of lakes varies between years, several lakes were noted in this region that formed in the same location during all 14 of the complete melt seasons studied (Fig. 2.10b). No large lakes form on the three main glaciers which feed the southern-most portion of the ice shelf, but extensive areas of meltwater-filled crevasses are often observed on Lambert glacier.
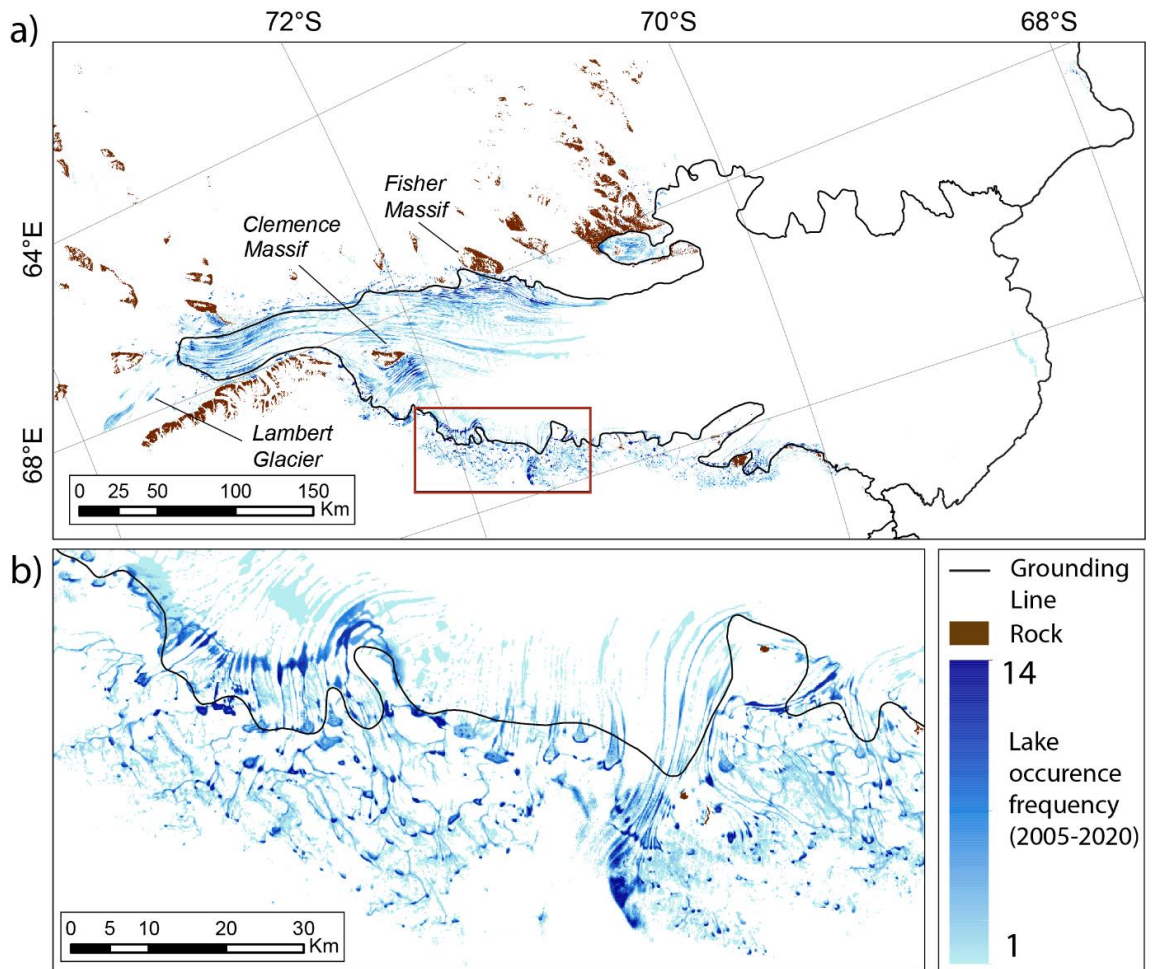
Figure 2.10. Spatial distribution of surface meltwater over the study region, showing the recurrence frequency of meltwater between 2005 and 2020. The maximum recurrence frequency is 14, due to the exclusion of the 2004/05 and 2018/19 melt seasons. Pixels were assigned values of 1 (melt) or 0 (no melt) per year, based on the occurrence of surface water at any stage during each melt season. Pixels were then summed to derive recurrence frequency. The linear light blue feature near the ice shelf calving front is a misclassification error associated with a large calving event that occurred in September 2019 (Walker et al., 2021).
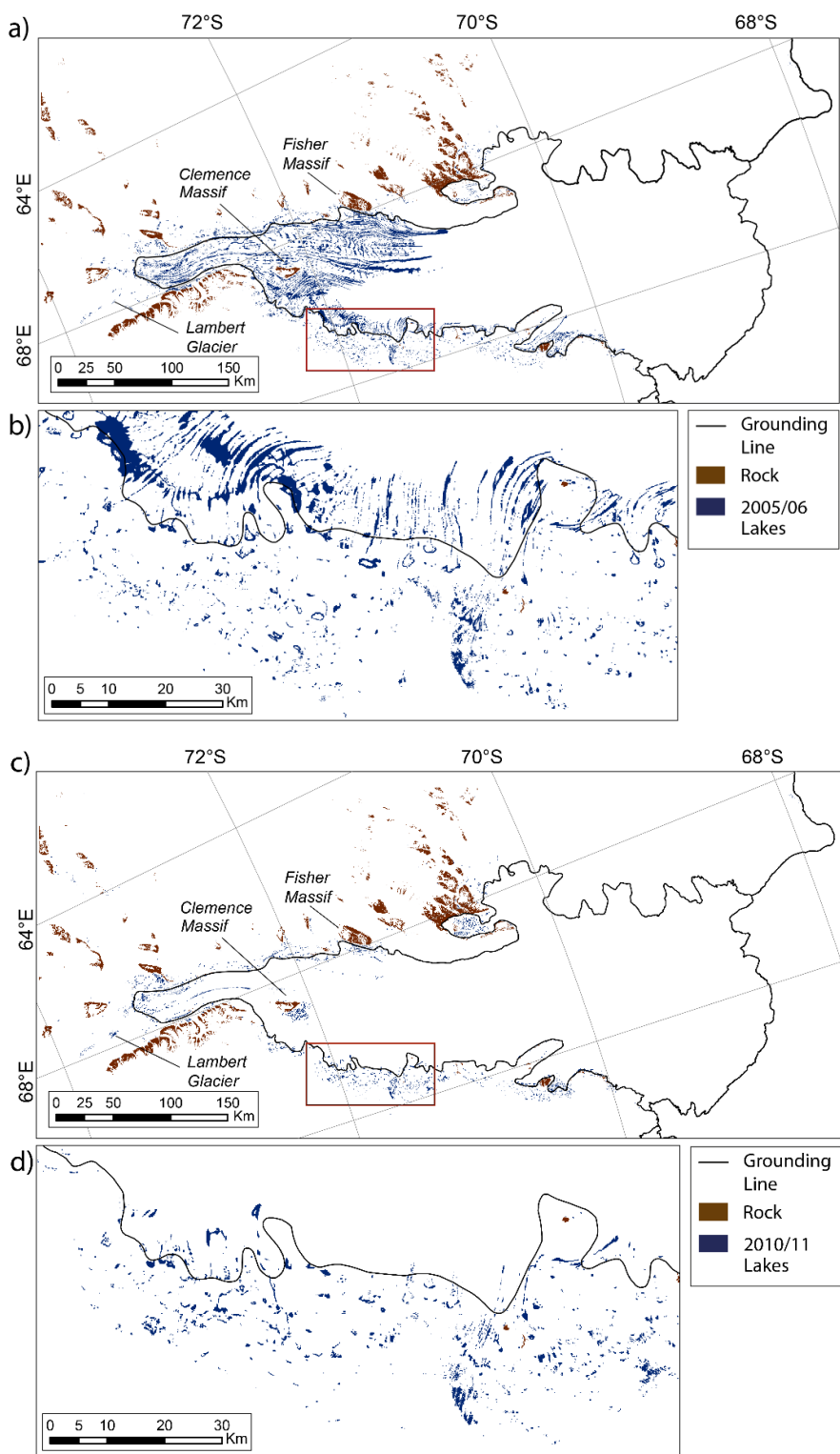
Figure 2.11. Spatial distribution of surface meltwater during a high (a/b) and low (c/d) melt season. (a/b) The 2005/06 melt season, which had the highest cumulative meltwater area of the study period. (c/d) The 2010/11 melt season, which had the lowest cumulative meltwater area of the study period. Note the large difference in meltwater extent, particularly on the ice shelf. The red box in (a) and (c) indicates the area shown in (b) and (d).

Surface meltwater is found up to elevations of ~1500 m, with the highest confirmed lake (with a minimum area threshold of 1800 m^2) existing at 1591 metres above sea level (m a.s.l.). Lakes are most common at low elevations, with the greatest lake area totals identified between 100-200 m a.s.l. This is the elevation band that covers the majority of the southern part of the ice shelf. The majority of the northern half of the ice shelf lies below 100 m a.s.l. but there is low runoff and ponding in this region (Fig. 2.10). Average lake area decreases with an increase in elevation, with the majority of surface meltwater above ~600 m a.s.l. existing in the form of small, isolated ponds within crevasse fields (mostly on Lambert Glacier). However, larger supraglacial lakes (up to ~5 km^2 in area) are common at elevations up to 500 m a.s.l. on sections of grounded ice in Princess Elizabeth Land. Lake areas are greatest between 100 and 200 m a.s.l. during all five months of the melt season (Fig. 2.12), regardless of annual variations in absolute melt supply. There are, however, slight differences in the distribution of lake area across elevation bands between high and low melt years. During low melt years, total lake area is more evenly distributed across elevations ranging between 100 and 400 m a.s.l. (Fig. 2.12b), whereas in high melt years, lake surface areas are more concentrated between 100 and 200 m a.s.l. (Fig. 2.12a).
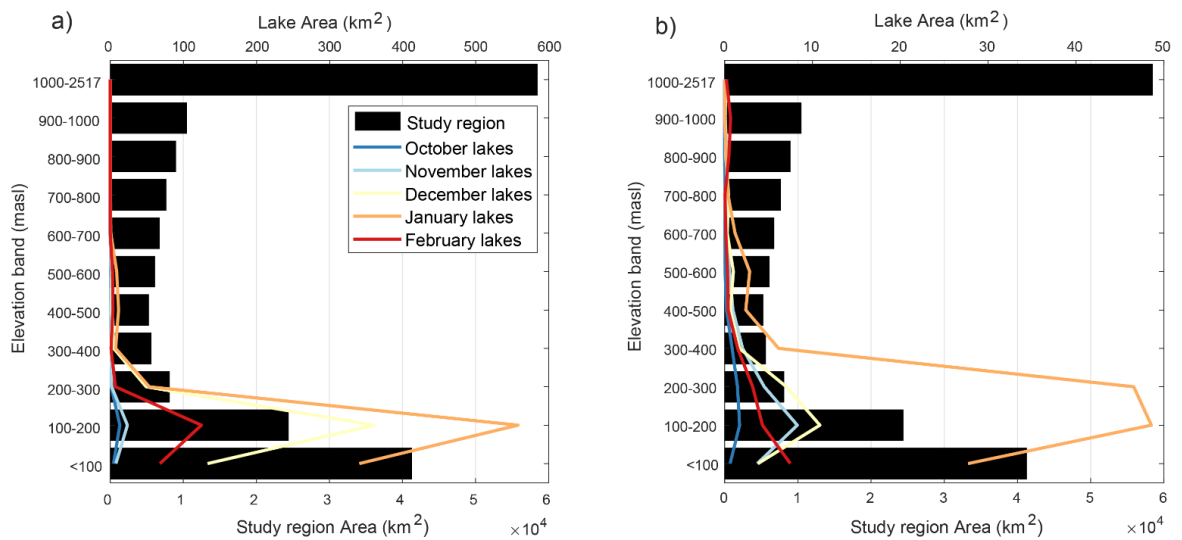
Figure 2.12. Averaged total lake areas per month by elevation bands, for a high melt season (a, 2005/06) and a low melt season (b, 2015/16). Black horizontal bars show the hypsometry of the study region. Note the total lake area is an order of magnitude greater during the high melt year (see lake area scales).

2.4.3 Temporal evolution of surface meltwater

The seasonal and multi-year evolution of lakes for the Amery region is shown in Figure 2.13. I used 'cumulative number of lakes' as a metric to provide an indication of the longevity of surface lakes throughout a melt season, in addition to the maximum number during any given time window. The highest cumulative number of lakes was observed during the 2016/17 melt season, during which the cumulative total number of lakes exceeded 100,000 (Fig. 2.13a). By contrast, less than 30,000 lakes were cumulatively observed during both the 2010/11 and 2011/12 melt seasons. There were relatively few lakes between 2006 and 2013; cumulative seasonal lake numbers remained below 50,000 for every melt season during this period, whereas five out of the six subsequent melt seasons had seasonal cumulative totals of more than 75,000 lakes. It should be noted that this cumulative metric could be skewed by lots of small lakes (or an area of meltwater filled crevasses), and will also be influenced by the switch from Landsat 7 to Landsat 8 in 2013.

The highest lake area totals during an individual time window were identified during the 2004/05 and 2005/06 melt seasons (Fig. 2.13b). During the first half of January 2005, surface meltwater covered an estimated maximum total area of 2814 km^2. This was almost three times greater than the average total lake area for the first half of January (963 km^2 for maximum estimates) throughout the study period. As observed with lake numbers, the seven year period between late 2006 and early 2013 was characterised by low lake area coverage (Fig. 2.13b). The average estimated cumulative lake area per season during this time period was 1062 km^2. This was around three times lower than the equivalent average of 2997 km^2 between 2014 and 2020 (excluding 2018/19 due to incomplete data availability), despite the 2015/16 melt season having very low areas of lake coverage.

Although there is high variability in both the number and total areas of lakes observed between melt seasons, there is not an overall increasing or decreasing trend. A strong correlation ($r = 0.81$, $p = 2.1$ x 10^{-32}) is observed between lake numbers and total lake area for individual time windows. In addition to having the highest number of lakes, the 2016/17 season also had the highest cumulative lake area, with an estimated (based on lake visibility corrected scores) maximum lake area total of 5179 km^2. High lake area totals were recorded during the 2005/06 season, despite only having the sixth highest number of lakes.

Clear seasonal patterns of lake numbers and areas can be observed within each melt season (Figs. 2.13 & 2.14). Between October and early December, total lake areas were typically very low, with any meltwater forming in crevasses or pooling in small depressions close to exposed bedrock. For all studied years, there was a sharp increase in total lake area during the second half of December, including in melt seasons when absolute lake area was relatively low. On average, total lake area increased by an order of magnitude during this time window compared to the first half of December. Lake area coverage typically continued to increase into the first half of January, when maximum lake areas for the melt season were most commonly observed. Peak lake area totals were experienced during the first half of January on eight out of the fourteen occasions for which data were generated throughout the entire melt season (Table 2.5). In low melt years, it was more common for lake areas to peak later in the melt season, usually during the second half of January and on one occasion (2009/10) during the first half of February. In most years, total lake area decreased through late January and early February, and by the second half of February, most lakes had frozen over. The average estimated total lake area for late February was 97 km^2, compared with 348 km^2 during the first half of the month. Despite these seasonal trends in total lake area, no shift was observed in meltwater cover to higher elevations throughout each melt season (Fig. 2.12).
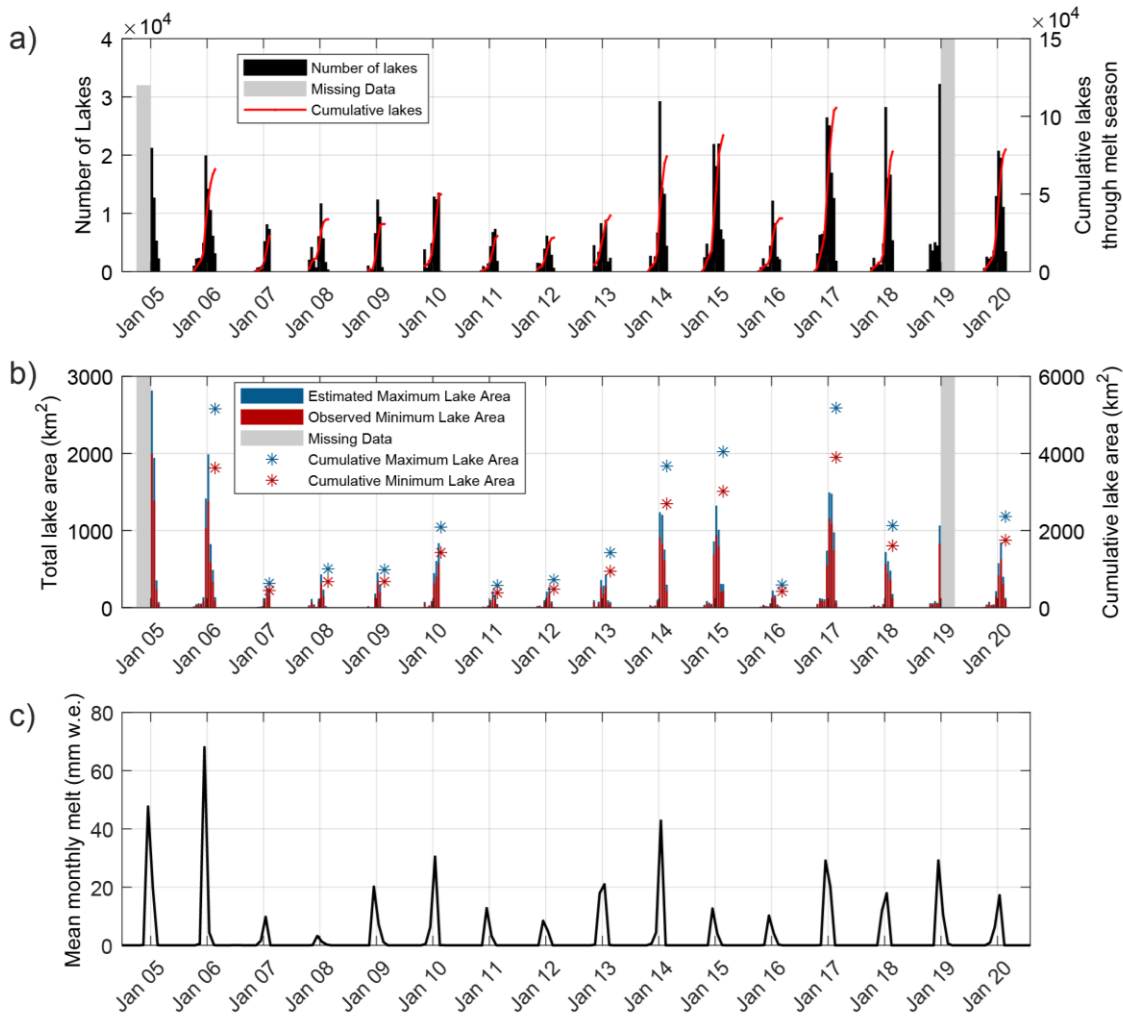
Figure 2.13. Time series showing the temporal evolution of lakes over the Amery Ice Shelf region between 2005 and 2020. (a) Number of lakes per time window and cumulatively over each melt season; (b) Observed minimum and estimated maximum lake area per time window, in addition to seasonal cumulative totals; (c) Mean monthly modelled melt over the study region, from RACMO2.3p2. Cumulative totals are not included for 2004/05 and 2018/19 due to incomplete data availability over these melt seasons. Note that lake number totals prior to 2013 may be slightly higher than reality, due to large lakes sometimes being 'dissected' by Scan Line Corrector striping associated with Landsat 7 imagery. However, the spacing of the Scan Line Corrector stripes, the average size of lakes, and the scale of lake numbers involved, means that such overestimates will have been negligible. It was therefore deemed unnecessary to try to account for this in lake number totals. Separate plots of lake areas and RACMO2.3p2 melt estimates for each melt season are shown in Fig. 2.14, enabling seasonal variations to be more clearly observed.
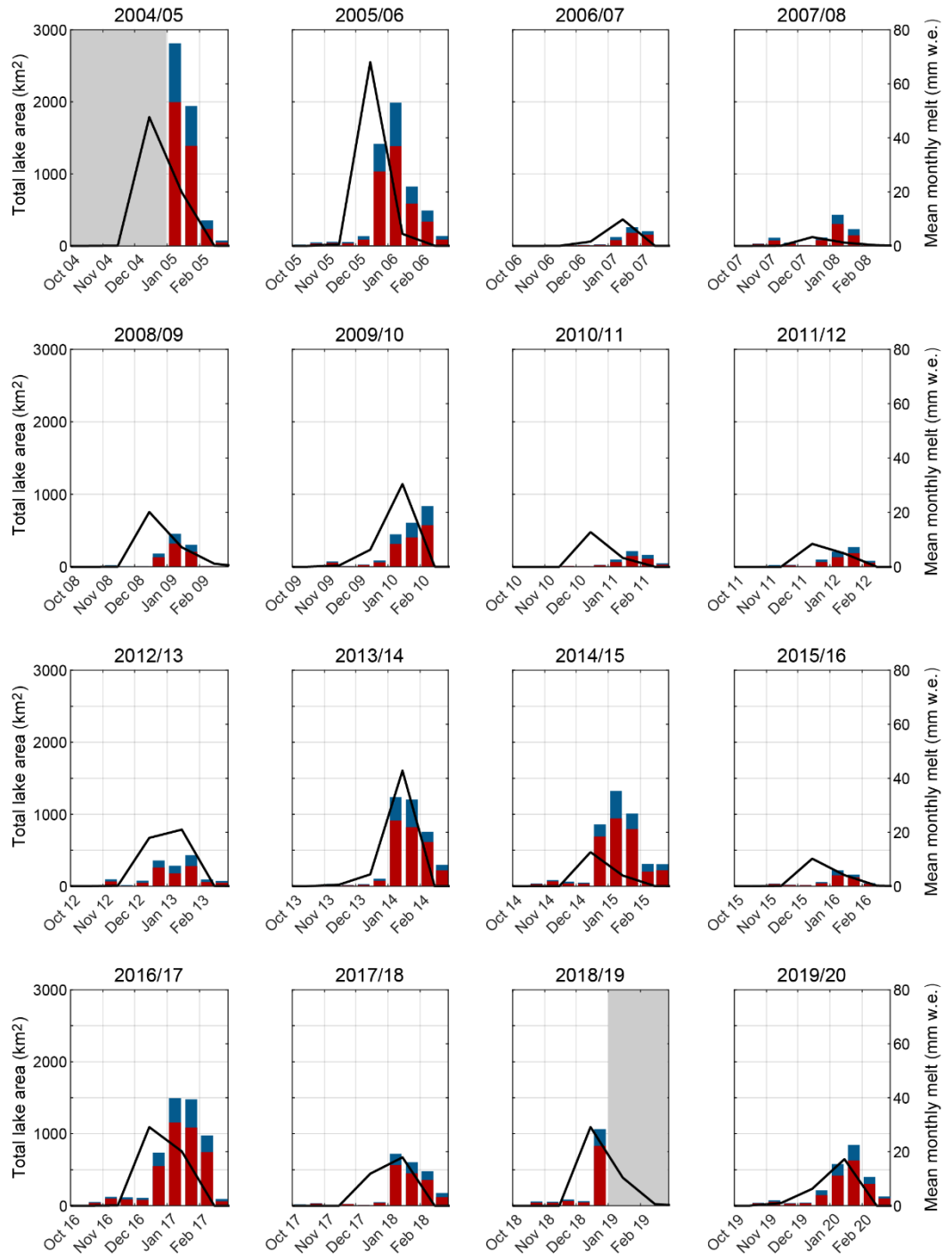
Figure 2.14. Individual time series plots for each melt season in the study period, showing total lake area and RACMO2.3p2 monthly melt estimates. As in Figure 2.13, red bars display observed minimum lake areas whilst blue bars display estimated maximum lake areas. Grey areas indicate missing lake area data. Black lines show mean monthly melt over the study region from RACMO2.3p2.

Table 2.5. Descriptive statistics for the time window with the greatest total lake area, for each melt season included in the study.

Melt season	Time window of highest total lake area	Largest lake area (km^2)	Standard deviation of lake area	Elevation of 95th percentile lake (min 4 pixels) (m a.s.l.)	% Lake Area Grounded
04/05	1-15 January 2005	107.1	1.08	430	18
05/06	1-15 January 2006	57.5	1.03	389	13
06/07	16-31 January 2007	4.8	0.11	469	53
07/08	1-15 January 2008	5.1	0.11	434	43
08/09	1-15 January 2009	7.1	0.13	422	52
09/10	1-14 February 2010	17.9	0.28	459	32
10/11	16-31 January 2011	2.9	0.09	368	53
11/12	16-31 January 2012	4.9	0.16	348	36
12/13	16-31 January 2013	3.0	0.10	332	28
13/14	1-15 January 2014	21.6	0.27	406	47
14/15	1-15 January 2015	52.2	0.59	382	22
15/16	1-15 January 2016	1.8	0.05	405	64
16/17	1-15 January 2017	32.0	0.40	436	28
17/18	1-15 January 2018	7.4	0.12	418	56
18/19	16-31 December 2018	15.4	0.20	451	39
19/20	16-31 January 2020	23.2	0.29	452	33

2.4.4 Comparison with climate data

Lake area results were compared with monthly surface snowmelt rates from RACMO2.3p2 to investigate the relationship between observed and modelled results. There is strong positive correlation between the seasonal totals of the two datasets (r = 0.76, p = 0.002), showing that the RACMO model captures the temporal variations in melting indicated by lake observations reasonably well (Fig. 2.15). The two melt seasons with the highest cumulative total lake area (2016/17 and 2005/06) also had the highest mean seasonal snowmelt estimates. However, the mean seasonal melt total for 2005/06 was 23.7 mm w.e. greater than the 2016/17 estimate, despite displaying very similar cumulative lake areas. The biggest discrepancy between the two datasets was in 2014/15 when modelled melt rates were low, whereas the cumulative lake area was the third highest throughout the study period.

Figure 2.13c reveals minor inter-annual variations in both the spread and the maximum estimates of modelled melt rates. Mean monthly RACMO melt was highest during

December in most of the study years, but peak melt was modelled to have occurred during January in six melt seasons. In years when maximum melt was modelled to have occurred during December, total lake area typically (75 % of the time) peaked during the first half of January, indicating a lag between peak melt and peak lake storage of ~15-30 days. Similar lag times were observed in years when modelled melt values were highest in January, with total lake area in these years most commonly peaking in either the second half of January or early February (Table 2.5). The duration of high (>30 mm w.e.) melt rates also varied between years. In 2005/06, high melt rates were experienced over a single month (December), whilst remaining very low during other months of the melt season. This matches well with the lake area data for that year, where a sharp increase in total lake area was observed between mid-December and mid-January, before rapidly dropping again by the end of January. In some years, maximum melt rates were sustained over both December and January, although absolute values of melt rate were usually lower in these years. In 2012/13, for example, the maximum monthly melt estimate was 21.0 mm w.e., but because this level of relatively low melt was sustained over a period of two months, mean seasonal melt was the fourth highest during the study period (Fig. 2.15).
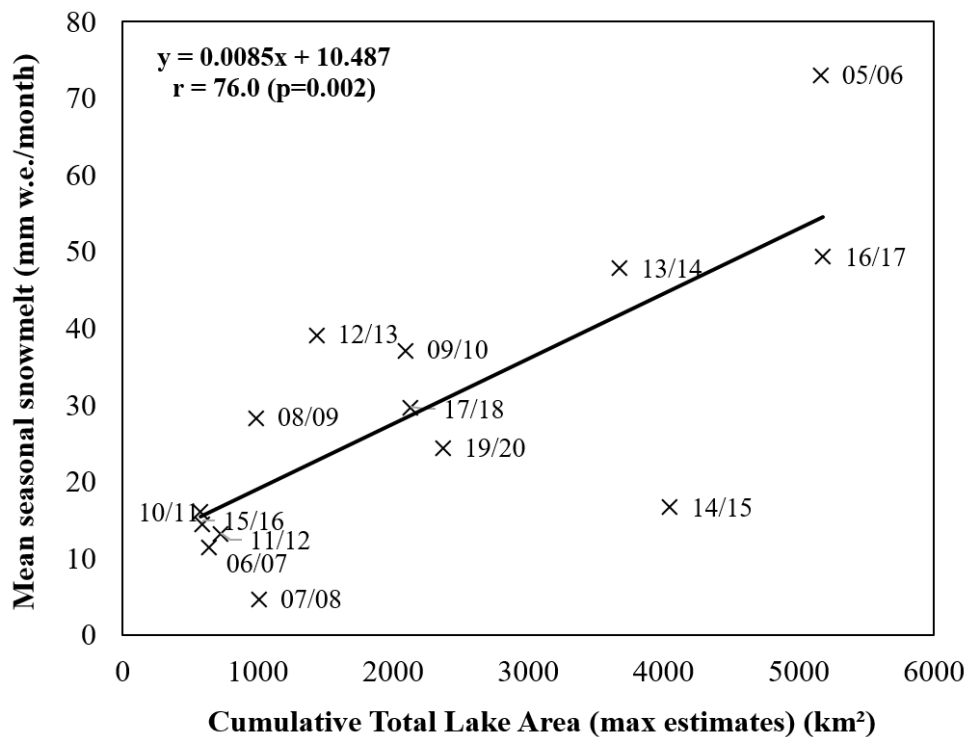
Figure 2.15. Scatter plot and correlation statistics of the relationship between mean seasonal RACMO melt and cumulative lake area over the study region per melt season.

To investigate the extent to which large scale variability in Antarctic climate influences surface meltwater area, lake area results were correlated against the SAM Index (Fig. 2.16). There is a significant negative correlation ($r = -0.54$, $p = 0.029$) between total lake area and the SAM index for austral summer months. Melt seasons with a negative summer SAM index correlated with years when total lake areas were greatest, whilst years with a positive summer SAM index were associated with low total lake areas. The SAM index was below minus one on two occasions throughout the study period (2005/06 and 2016/17), the same two years that the greatest cumulative lake areas were observed (excluding the 2004/05 melt season where data were only available during the second half of the melt season). Years with a positive SAM index of two or more were characterised by low surface meltwater cover, with the notable exception of the 2014/15 season. This melt season was associated with the highest SAM index of the whole study period, yet had the fourth highest cumulative lake area total.
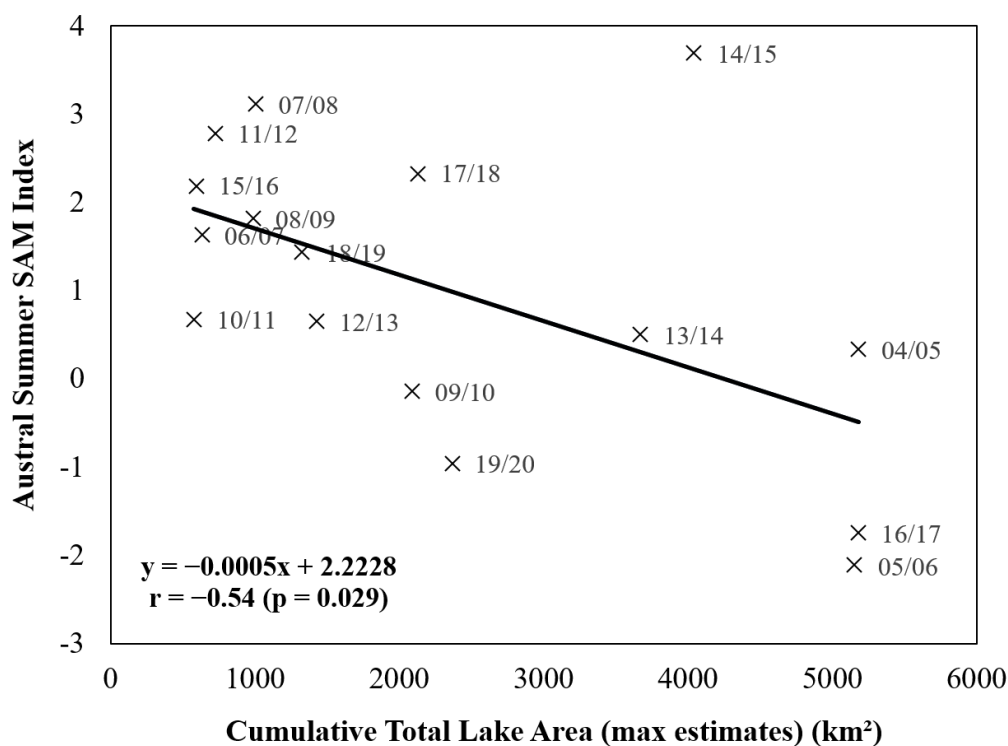
Figure 2.16. Scatter plot and correlation statistics of the relationship between the austral summer SAM index and cumulative total lake area per melt season.

2.5 Discussion

2.5.1 Improvement in the assessment of surface meltwater extent

In this chapter, I have overcome two key factors which previously restricted the generation of robust high-resolution time series of surface meltwater extent from optical satellite imagery. First, by incorporating a threshold-based method for lake detection within GEE, with results generated by time windows, I have created a fully automated method for generating lake area time series that is quick and simple to run. The majority of surface meltwater mapping studies in Antarctica have been limited in spatial and/or temporal resolution, partly due to methodological constraints relating to the computational expense of processing large imagery datasets. Despite having a relatively high spatial density of supraglacial lakes compared to most other areas of Antarctica (hence reducing the speed of processing within GEE), I was able to map an area of >185,000 km^2 over a 15-year time period in less than a week of wall-clock time. This rapid processing opens up the possibility of investigating surface meltwater evolution over vastly increased spatial and temporal scales, compared to what would be possible using manual or semi-automated methods. The method requires minimal inputs and user intervention (file transfers are required between the GEE and Matlab automated stages), meaning it can be quickly adapted to generate lake area time series for other regions of Antarctica, and ultimately at pan-ice sheet scales (Chapter 4). By using a time window approach whereby the length of time-windows can be varied (e.g. daily, monthly or yearly mapping), the method could be used to investigate surface meltwater processes at a range of temporal resolutions (depending on image availability).

Second, the surface meltwater mapping procedure incorporates a robust new method for assessing image visibility, enabling me to account for variability in cloud cover and image data coverage when generating time series. Whilst multiple studies have provided Antarctic supraglacial lake area and volume estimates from optical mapping (Arthur et al., 2020; Dell et al., 2020; Moussavi et al., 2020), accounting for low image visibility from cloud cover has remained the primary limiting factor in creating a continuous and consistent time series (Moussavi et al., 2020). Furthermore, reported lake areas and volumes based on optical mapping likely underestimate ground-truth meltwater extent, since very few optical images are entirely cloud-free. Here, I performed image visibility assessments on every image analysed, enabling me to quantify levels of uncertainty for

lake area results. Maximum lake area estimates, which incorporated visibility assessments, increased mapped lake areas for time windows on average by approximately 50%. This highlights the importance of accounting for image visibility when reporting lake area results, especially when working with Landsat 7 imagery (due to the Scan Line Corrector failure) or mapping frequently cloud-covered regions, such as the Antarctic Peninsula (van Wessem et al., 2016).

Accounting for image visibility in meltwater area assessments represents an important advance, but there are some limitations to the method that should be considered. My method assumes that lakes have an equal chance of occurring across ice covered areas of a ROI. In reality, lakes are often spatially clustered and occur in similar locations between years. This uneven spatial distribution is a potential source of error for the maximum lake area estimates. The sign and size of this error will be dependent upon the degree of lake clustering and the position of clustered lakes relative to cloud cover within each ROI for each time window. The scaling up of minimum mapped areas is based on the probability that meltwater has been missed, introducing uncertainty to 'scaled-up' area totals. In particular, the method has the potential to overestimate the quantity of meltwater that has been missed due to image visibility under certain scenarios (e.g. where all meltwater pixels have been captured, but cloud in a separate part of the image results in the meltwater area total being increased based on scaling). Estimated maximum lake area totals should therefore be considered an upper bound for 'true' meltwater area totals. Future applications of the method could consider sampling a range of values between 'minimum mapped' and 'estimated maximum' area totals, to investigate the robustness of trends in the data. Particular consideration should be given to any changes within a time series between Landsat 7 and Landsat 8, given that Landsat 7 results typically incur greater scaling due to missing image pixels from SLC striping.

2.5.2 Spatial distribution of surface meltwater on Amery Ice Shelf

Supraglacial lakes are often widespread on inland sections of the ice shelf during austral summer months, whilst almost no surface meltwater forms on the northern half of the ice shelf nearer the ocean. The spatial distribution of surface lakes on the Amery Ice Shelf is strongly influenced by variations in firn air content across the study area, as similarly

observed across other ice shelves in Antarctica (Lenaerts et al., 2017; Arthur et al., 2020a; Dell et al., 2020). The lack of surface meltwater ponding in the northern half of the study region (Fig. 2.10) is likely a consequence of high rates of snow accumulation near the calving front (Budd, 1966). A thick snowpack near the ice front has large pore spaces within the firn layer, meaning surface meltwater can percolate downwards and be accommodated within the pore spaces (Bell et al., 2017). By contrast, low accumulation rates further inland on the ice shelf likely result in a lower firn air content, meaning the firn layer becomes saturated with meltwater more quickly causing ponding of surface water (Bell et al., 2017; Arthur et al., 2020a). Cycles of melting and re-freezing increase the grain-size of particles within the firn layer, reducing the albedo of the surface compared to fine-grained fresh snow (Zwally & Fiegles, 1994; Phillips, 1998). This can induce a positive feedback whereby previously melted areas are more likely to experience further melting, due to the increased absorption of short-wave radiation associated with low albedo surfaces (Kingslake et al., 2017). It is possible that this feedback is further enhanced by the presence of ice slabs and lenses which can form beneath areas of intermittent pond formation (Hubbard et al., 2016). These dense layers of ice inhibit meltwater percolation, and can be several degrees warmer than ice that has not undergone lateral heat fluctuations that result from the melting and refreezing of ice (Hubbard et al., 2016). Such ice slabs have been shown to have important implications for lake development over multiple melt seasons, based on modelling of the Larsen C ice shelf (Buzzard et al., 2018).

The clustering of surface lakes around the grounding line at southern latitudes of the Amery Ice Shelf can further be explained by the influence of katabatic winds. Near-surface air temperatures in coastal regions of East Antarctica are strongly influenced by katabatic winds which originate from the ice sheet's interior (Lenaerts et al., 2017). These winds, which are commonly strong and directionally persistent (Lenaerts et al., 2017), generate localised surface and atmospheric conditions that are conducive to surface melting. Katabatic winds warm adiabatically as they flow down surface slopes, disrupting the natural temperature inversion and resulting in warmer, more humid air adjacent to the ice surface at the break in slope of the grounding zone (Doran et al., 1996). These atmospheric conditions, combined with the occurrence of low surface slopes on the ice shelf, optimise the local environment for meltwater ponding, resulting in supraglacial lake formation around the grounding zone of Antarctic ice shelves (Arthur et al., 2020b;

Elvidge et al., 2020). Particularly high numbers of lakes are observed on the narrowest part of the Amery Ice Shelf, as this is likely the focal point for katabatic winds that are channelised, and hence strengthened, down Lambert, Fisher and Mellor glaciers (Zwally & Fiefles, 1994). Furthermore, increased numbers of flow stripes in this narrow section of the ice shelf provide greater surface roughness within which lakes can form (Glasser & Gudmundsson, 2012; Ely & Clark, 2016). My results show that lakes form to lower latitudes along the Prince Charles Mountains side of the ice shelf compared with the Princess Elizabeth Land margin (Fig. 2.10). I suggest this is because katabatic winds continue to be channelised by the Mawson Escarpment once on the ice shelf, causing them to flow out naturally along the western margin of the ice shelf. Once the ice shelf widens and is no longer as confined by topography, the winds likely weaken in strength, thus negating the localised warming effect and limiting lake growth.

Strong katabatic winds can also erode the surface snow layer within which melt could be stored, exposing highly compacted, less permeable surfaces. Continued wind scouring around the grounding zone can expose areas of blue ice, which have a lower albedo (~0.57) than refrozen snow (~0.7) (Lanaerts et al., 2016). The presence of blue ice, in addition to the high number of low-albedo nunataks that surround the inland portion of the Amery Ice Shelf, increases net surface absorption of solar energy, providing a localised warming effect and enhancing surface melt rates (Kingslake et al., 2017). Surface melt rates on other ice shelves in Antarctica, such as Roi Baudouin and Shackleton, have been shown to be strongly controlled by melt-albedo feedbacks (Lenaerts et al., 2017; Jacobs et al., 2019; Arthur et al., 2020a; Dell et al., 2020). My results support these findings, as I observe a clear spatial association between low albedo surfaces and areas of high lake occurrence, such as the large number of lakes that form annually next to the Prince Charles Mountains (Fig. 2.10). The spatial distribution of surface meltwater in the study region is hence closely controlled by melt-albedo coupling between exposed bedrock, blue ice and surface melting (Kingslake et al., 2017).

On both grounded and floating sections of the study region, lakes typically form in the same location on an annual basis (Fig. 2.10). Surface topography controls the hydrological routing of surface water, resulting in the ponding of water in small hollows and basins (Bell et al., 2017). Longitudinal surface structures on the ice shelf surface, caused by lateral compression and longitudinal extension of ice (Glasser et al., 2015; Ely et al., 2017), channelise surface meltwater downstream, likely explaining the elongate

shape of lakes observed on the ice shelf. Variations in the downstream extent of lakes between years are therefore likely to partly be a consequence of variable melt supply (Spergel et al., 2021). The distribution of surface basins on grounded ice is controlled by subglacial topography, meaning lakes can form annually in fixed surface depressions (Echelmeyer et al., 1991; Igneczi et al., 2018).

2.5.3 Temporal variation in ponded surface meltwater on the Amery Ice Shelf

There is a clear intra-seasonal pattern of total lake area; it remains low through the early part of the melt season, before rapidly increasing during late December and reaching a maximum in January (Fig. 2.13; Table 2.5), and then decreasing sharply during February. This matches with results from scatterometer studies which show large decreases in backscatter values over the Amery Ice Shelf in January, indicating a rapid increase in the intensity of surface melting (Oza et al., 2011). The sudden increase in lake area (up to an order of magnitude increase within half a month) is likely a consequence of the hypsometry of the study region. Over 35 % (~65,000 km^2) of the study region lies at an elevation lower than 200 m a.s.l., meaning that a minor increase in temperature increases melt potential over a vast area of ice. This contrasts with the typical hypsometry of the Greenland Ice Sheet, where relatively steep slopes at the ice sheet margin mean that an equivalent rise in temperature would initiate melting over a much smaller area (McMillan et al., 2007; Sundal et al., 2009). The large lake area contribution from low elevations possibly explains why a major elevation shift in peak area contribution throughout the melt season is not observed (Fig. 2.12), as the signal from the ice shelf masks any changes in total lake area contribution at higher elevations. Following the initial appearance of meltwater ponds, overall lake area is likely further enhanced by positive feedbacks, whereby lowered surface albedo from melting promotes further melting. Furthermore, the development of surface streams enables lateral transfer of surface water, rapidly increasing the spread of water across the ice shelf surface (Kingslake et al., 2017). Sharp decreases in lake area during February are presumably indicative of the widespread freezing of supraglacial lakes, although evidence of lake drainage events has also been observed in the region (Fricker et al., 2009; Spergel et al., 2021; Trusel et al., 2022).

There is a strong association between annual cumulative lake area and the summer SAM index (Fig. 2.16), suggesting that ice-shelf wide annual variations in lake area cover are influenced by large-scale climate variability. Phases of the SAM naturally oscillate on a multi-decadal timescale (Picard et al., 2007), possibly explaining the observed multi-year phases between periods of low and high lake area coverage (Fig. 2.13). When SAM is in a positive phase, air temperatures are typically higher over the Antarctic Peninsula and lower over the rest of the continent, whilst the reverse is the case during a negative SAM phase (Marshall & Thompson, 2016; Turner et al., 2020). My results broadly support this relationship, as observed by the statistically significant negative correlation between lake area and summer SAM index (Fig. 2.16). For example, the seven-year period between 2006 and 2013, which was largely characterised by positive summer SAM indexes, coincided with low annual cumulative surface meltwater coverage. The only year during this period with a negative summer SAM index (where slightly warmer temperatures would be expected) was in 2009/10. This melt season had the highest cumulative lake area of this seven-year period, suggesting that the summer SAM index is linked to melt rates on an annual basis. This wider climatic control on surface meltwater formation suggests that the Amery Ice Shelf has an abundance of basins within which meltwater can be accommodated, resulting in a linear relationship between melt rates and meltwater ponding (Fig. 2.15). This may not necessarily be the case in other regions of Antarctica, where steeper topography may limit the number and size of depressions able to host meltwater, thus resulting in enhanced surface runoff and a non-linear relationship between melt and surface meltwater area.

There was high variability in the austral summer SAM index from 2013-2020, ranging from -1.75 in 2016/17 to 3.69 in 2014/15. In general, lake areas followed the broad pattern that would be expected based on their association with the SAM throughout this time period, with the main exception of the 2014/15 melt season. Large lakes formed during this melt season, despite there being a negative SAM and low melt rates predicted by RACMO. Greater than expected meltwater ponding during this melt season can be explained by enhanced scouring of the ice shelf surface by strong katabatic winds. Following a snowfall event in late November 2014, large areas of low-albedo blue ice were exposed on the ice shelf by mid-December (Fig. 2.17a, b), suggesting strong wind-scouring throughout the first half of December. Between the 21st and 28th of December, the ice shelf was transformed from being almost entirely lake-free to widely covered by

supraglacial lakes (Fig. 2.17c). The following melt season, by contrast, snow cover persisted across most of the ice shelf throughout December (Fig. 2.17e), meaning any meltwater could be accommodated within the firn pack rather than ponding as surface water.
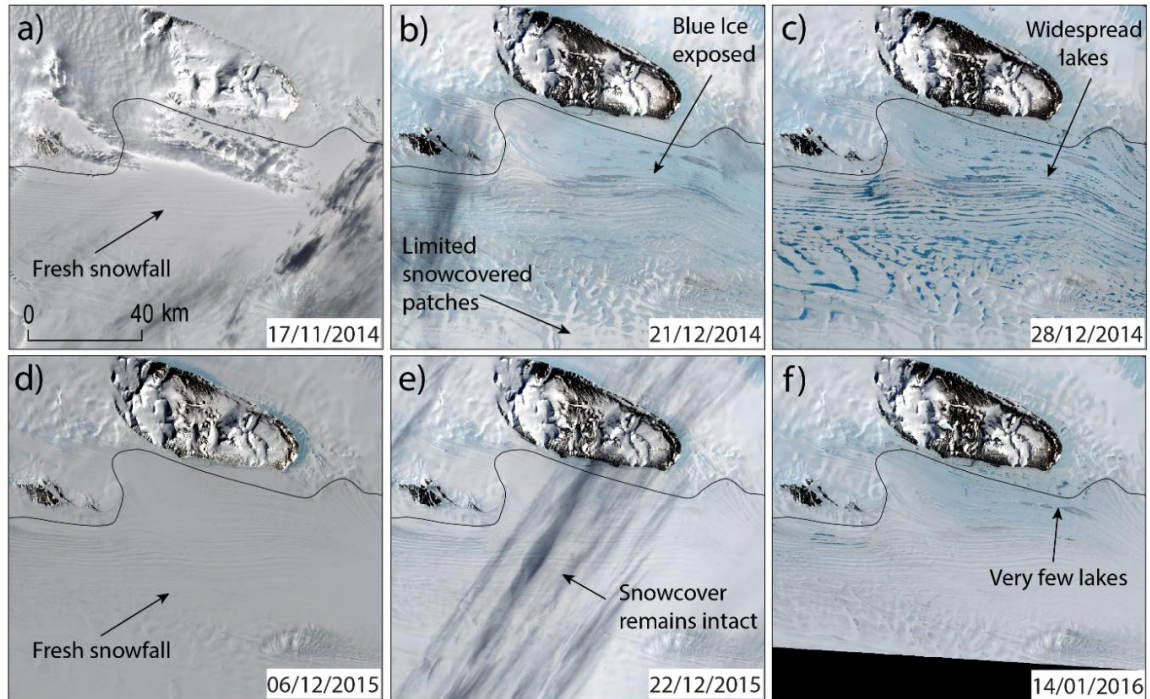
Figure 2.17. Landsat 8 images showing the evolution of the ice shelf surface to the east of the Fisher Massif in the 2014/15 (a-c) and 2015/16 (d-f) melt seasons. Note the contrast in the extent of ponded meltwater between seasons, potentially due to differences in snow cover and the extent of exposed blue ice.

The formation and extent of surface meltwater is highly sensitive to minor fluctuations in surface air temperature (Langley et al., 2016). During December 2014, the ice shelf was pre-conditioned as a low-albedo, impermeable surface, optimising the conditions required for surface meltwater ponding. Given this, it is likely that a transient increase in air temperature, possibly induced by a strong katabatic event, could have resulted in a large change in surface meltwater characteristics. Surface melt rates depend on all terms of the surface energy balance (Oza et al., 2011), meaning air temperature is not the sole factor in determining surface melt rates. Whilst RACMO modelled melt estimates include a surface albedo parameterization, melt-albedo feedbacks are difficult to resolve due to the

lack of representation of blue ice within the model, and the relatively coarse resolution of the data (27 km). Previous studies have shown that RACMO often under predicts meltwater production in areas of Antarctica where blue ice is warmed by katabatic winds (Trusel et al., 2013; Leanaerts et al., 2017). This possibly explains why there were such major differences in lake area coverage between 2014/15 and 2015/16, despite RACMO mean seasonal snowmelt estimates differing by only ~2 mm w.e. (Figs. 2.13 & 2.15). Jakobs et al. (2019) found that surface albedo was the main difference in ice surface characteristics between high and low melt years on the Ekstrom ice shelf, supporting the hypothesis that large variations in melt extent can be caused by variations in surface reflectance characteristics. Over the entire study period, however, RACMO shows a good agreement with lake area.

2.6 Conclusions

In this chapter, I have applied an optical image band reflectance threshold-based method for identifying surface meltwater from Landsat imagery (Moussavi et al., 2020) within GEE, enabling the automatic identification of meltwater over large spatial and temporal scales (Objective 1). Furthermore, my approach incorporates a robust method for assessing image visibility, allowing me to attach quantitative uncertainty estimates to mapped lake areas. By applying a time window approach and accounting for image visibility in the interpretation of results, I have generated the first continuous and consistent time series of lake area for the Amery Ice Shelf region between 2005 and 2020 (Objective 2).

I show that there is high annual variability in lake area cover in the Amery Ice Shelf region, and that seasonal surface meltwater coverage is significantly influenced by variations in the SAM. Positive phases of the SAM are associated with low meltwater coverage, whilst melt seasons with a negative austral summer SAM index are typically associated with high melt years and widespread surface meltwater extent. For a typical year, lake area remains low during the early melt season (November – mid December) before rapidly increasing during the second half of December. Maximum total lake area is most commonly observed during January, before sharply declining during February as lakes presumably freeze over. The spatial distribution of lakes on the ice shelf is strongly influenced by melt-albedo feedbacks, especially the exposure of blue ice from the

persistent scouring of the surface by strong katabatic winds. I find a strong correlation between RACMO modelled snowmelt and cumulative lake area, providing confidence in the ability to predict future surface meltwater ponding based on regional climate model projections in this region. Potential implications of my findings for the future of the region are discussed in Chapter 5.

This chapter demonstrates a reliable and easy to implement workflow for robustly quantifying Antarctic surface meltwater extent through time. Chapter 4 will present results from application of this method at a continent-wide scale. Whilst this chapter presents important findings from quantification of surface meltwater area, it does not address the mechanisms via which surface meltwater evolves. For example, meltwater area time series cannot explain whether increases or decreases in surface meltwater area are the result of factors such as surface melt rate variability, the freezing or unfreezing of liquid surface water, or variations in snowpack saturation. Furthermore, meltwater area decreases could also be the result of drainage over the ice surface or, potentially more significantly, vertical drainage into the englacial or subglacial system. In Chapter 3, I build upon the meltwater area outputs produced in this chapter to evaluate styles of supraglacial lake evolution at the grounding zone of the Amery Ice Shelf.

CHAPTER 3

*Exploring styles of meltwater evolution at the grounding zone
of the Amery Ice Shelf, Antarctica*

3.1 Introduction

In Chapter 2, I demonstrate the success of using an automated technique for mapping changes in surface meltwater area. However, quantification of meltwater volumes are additionally required to understand the processes via which surface meltwater evolves. In this chapter, I explore remote sensing techniques designed to identify meltwater evolution processes, produce supraglacial lake volume estimates, and refine the timescales over which lake volume changes can occur.

Supraglacial lakes evolve over the course of a melt season, and can gain or lose water volume via a variety of mechanisms (Fig. 3.1). The evolution of supraglacial lakes has been well studied on the GrIS, with field-based (Doyle et al., 2013; Chudley et al., 2019) and remote sensing (McMillan et al., 2007; Sundal et al., 2009; Selmes et al., 2011) techniques used to investigate the timescales over which lake volume changes occur. One commonly used remote sensing approach for studying supraglacial lake evolution is to calculate lake volumes from optical satellite imagery (Sneed & Hamilton, 2007; Pope et al., 2016). Research from the GrIS has used MODIS (McMillan et al., 2007; Sundal et al., 2009), Landsat (Pope et al., 2016) and Sentinel-2 (Yang et al., 2019; Hochreuther et al., 2021) data to generate lake volume time series, enabling quantification of magnitudes and rates of lake volume change (Section 1.2.2). All of these methods use the optical properties of the surface to estimate lake volume. This means that interpretation of lake volume time series can be complicated by the freezing and unfreezing of lake surfaces, which can result in large 'apparent' volume changes in satellite-derived time series. This occurs even if liquid water remains underneath a frozen or partially frozen lid, because freezing of the lake surface hides water in the lake from the satellite sensor. Manual analysis of optical satellite imagery can therefore be required in addition, to identify the processes responsible for the volume change of any individual lake.

The mechanisms by which 'apparent' increases or decreases in lake volume might occur are illustrated in Figure 3.1. Volume increases from catchment infill (Fig. 3.1a) and *in*

situ lake melting (Fig. 3.1d) might typically be expected to occur relatively slowly (over several weeks), and would likely be highly dependent on near-surface temperature and surface melt rates. These processes typically result in exponential increases in volume throughout a melt season due to melt-albedo feedbacks (Kingslake et al., 2017; Jakobs et al., 2021). The over-ice transfer of meltwater via a channel from another lake (Fig. 3.1b) provides a mechanism for a lake to accumulate volume more rapidly (within a few days). Over-ice drainage events can occur following the incision of a channel into a lake watershed, with the speed of lake drainage dependent on the rate of channel incision relative to lake level drawdown (Kingslake et al., 2015). Volume increases can also result from the unfreezing of a frozen lake surface (Fig. 3.1c), with the 'apparent' lake volume dependent on the area of liquid water visible at the surface.
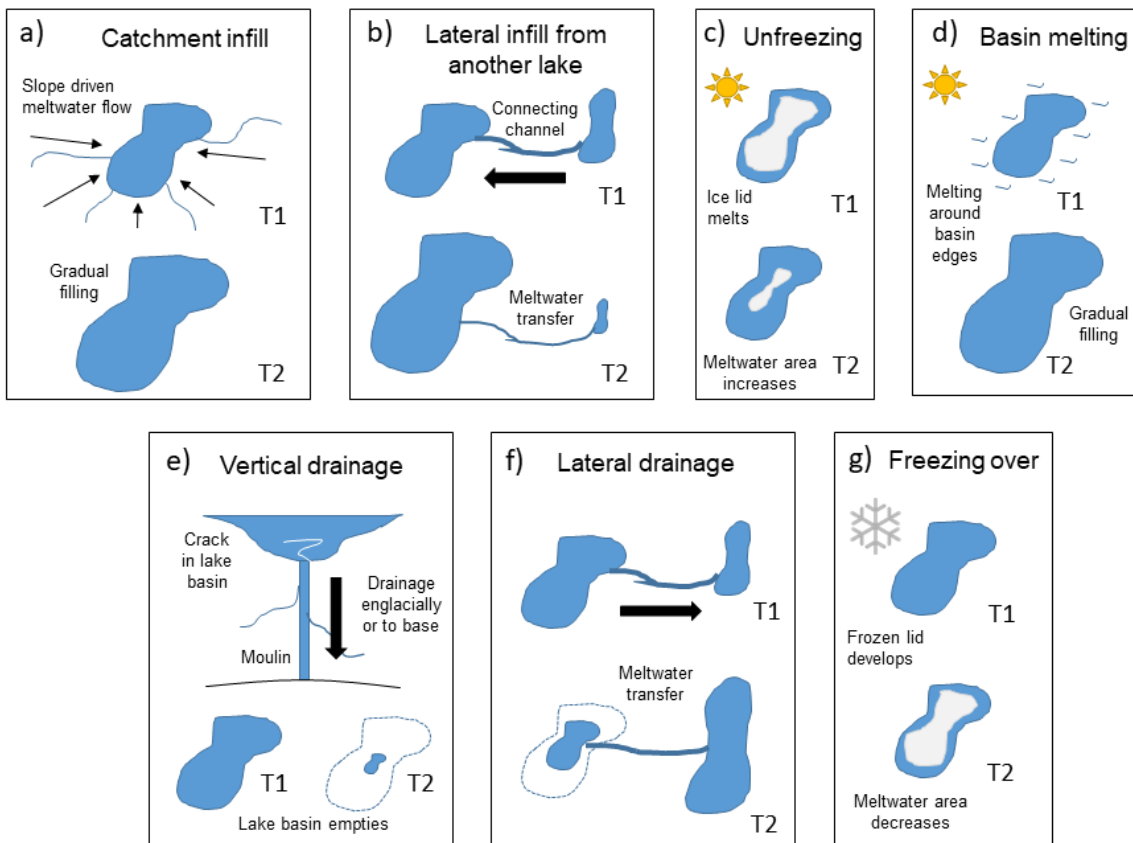
Figure 3.1. Schematic illustrating the processes by which increases (upper row) or decreases (lower row) in water volume can be explained from automatically generated lake volume calculations. Note how the freezing or unfreezing of a lake surface can result in 'apparent' lake volume changes, even if liquid water remains beneath a frozen lid. In each example, changes in lake characteristics are displayed between time periods 1 (T1) and 2 (T2).

Decreases in apparent lake volume can result from a lake surface freezing over (Fig. 3.1g) or the lateral drainage of water out of a lake watershed (Fig. 3.1f). The complete freezing over of a lake results in a volume measurement of zero due to the lack of water pixels from which to base depth measurements on. Volume losses can also occur due to vertical lake drainage events, resultant of hydrofracture at the base of the lake (Das et al., 2008; Fig. 3.1e). Studies from the GrIS show how supraglacial lakes can drain vertically through kilometre-thick ice to the bed of the ice sheet (Krawczynski et al., 2009), resulting in ice flow variability (Zwally et al., 2002; Das et al., 2008; Tedesco et al., 2013). Vertical lake drainage events in Greenland can happen over hourly to weekly timescales (Williamson et al., 2018; Davison et al., 2019), and have the potential to trigger substantial ice dynamic impacts (Section 1.2.3.2).

Compared to work conducted in Greenland, there has been a relative lack of research on the evolution of supraglacial lakes in Antarctica (Section 1.2.4). Several studies have investigated the evolution of surface meltwater on ice shelves (Phillips, 1998; Kingslake et al., 2017; Dell et al., 2020; Spergel et al., 2021), yet studies of supraglacial lakes on grounded ice are rarer. Furthermore, quantitative studies of lake volume changes in Antarctica are lacking, and there remains limited understanding of how Antarctic supraglacial lakes evolve on daily to yearly timescales (Arthur et al., 2020a). Whilst Trusel et al. (2022) and Spergel et al. (2021) present detailed analysis of the evolution of individual lakes from the Amery region, assessments of lake volume changes for multiple lakes over a wider study area have not been conducted. Therefore, uncertainty remains over the occurrence and abundance of different lake evolution processes across Antarctica. For example, vertical lake drainage events have been documented on floating ice (Scambos et al., 2009; Langley et al., 2016; Leeson et al., 2020; Warner et al., 2021) and in the grounding zone of ice shelves (Dunmire et al., 2020; Trusel et al., 2022), but are largely unobserved on areas of grounded ice. Remote sensing evidence suggests that surface meltwater could be draining to the ice sheet bed in regions of grounded ice on the Antarctic Peninsula (Tuckett et al., 2019; Boxall et al., 2022; Hodgson et al., 2022), but this process is debated (Rott et al., 2020) and there is currently no evidence of surface-to-bed connections from other regions of Antarctica.

In this chapter, I use a combination of manual and automated methods to explore the evolution of supraglacial lakes across a grounding zone of the Amery Ice Shelf (Objective 5). Recent work has identified several instances of apparent relatively fast (< 6 days)

volume losses from supraglacial lakes on grounded ice along the eastern margin of the Amery Ice Shelf (Doocey, 2020). In the same region, Trusel et al. (2022) observed the repeated filling and draining of a supraglacial lake at the grounding zone, which they infer drains vertically as a result of tidally induced hydrofracture. I build upon these findings, in addition to previous work in the region (Phillips, 1998; Spergel et al., 2021; Trusel et al., 2022; Doocey, 2020), to investigate the mechanisms, frequency and spatial extent of supraglacial lake evolution in the Amery region. I utilize results from Chapter 2 to explore different lake evolution processes, both across a wide catchment area and at individual lake scales. I generate lake volume time series for 215 lakes spanning 2016 to 2021, enabling me to explore different patterns of lake volume change within a melt season and over multiannual timescales. I additionally develop a novel method to explore how the temporal resolution of lake volume estimates can be enhanced, aiming to provide better constraints on the timing and rate of lake filling and emptying events.

3.2 Study Region

A ~300 km stretch along the eastern margin of the Amery Ice Shelf was selected as a study region (Fig. 3.2). Lake drainage events have already been observed along this margin (Trusel et al., 2022; Doocey, 2020), whilst results from Chapter 2 show that surface lakes are abundant in the grounding zone between approximately 70-72 °S, forming on grounded and floating ice on an annual basis (Fig. 2.10). The study region therefore offers an ideal location to explore styles of meltwater evolution and lake drainage events. Lake volume analysis builds on mapped lake polygons from Chapter 2. Three ROI tiles (from the lake mapping procedure, Fig. 2.1) were used to define the limits of the study region (Fig. 3.2). Whilst my primary aim was to assess meltwater evolution on grounded ice, the study region covers both grounded and floating ice to enable assessment of lateral meltwater transfer across the grounding zone.

Two case study areas, smaller than the ROIs, from within the wider study region were selected for detailed analysis (Fig. 3.2). These are referred to as case study areas 1 and 2:

Case study area 1): A ~2.5 x 2 km grounded area (central co-ordinates: -71.75°, 71.21°) approximately 10 km inland from the grounding line. The area covers a lake

(Lake A) that is known to fill and drain on an annual basis (Doocey, 2020; Fig. 3.2), in addition to a secondary smaller lake (Lake B).

Case study area 2): A ~30 x 25 km area (central co-ordinates: -71.75°, 70.75°) across the grounding zone (Fig. 3.2), which is covered by complex interconnected meltwater networks each year. This area was selected to explore the potential lateral movement of surface meltwater from grounded to floating ice within a melt season.
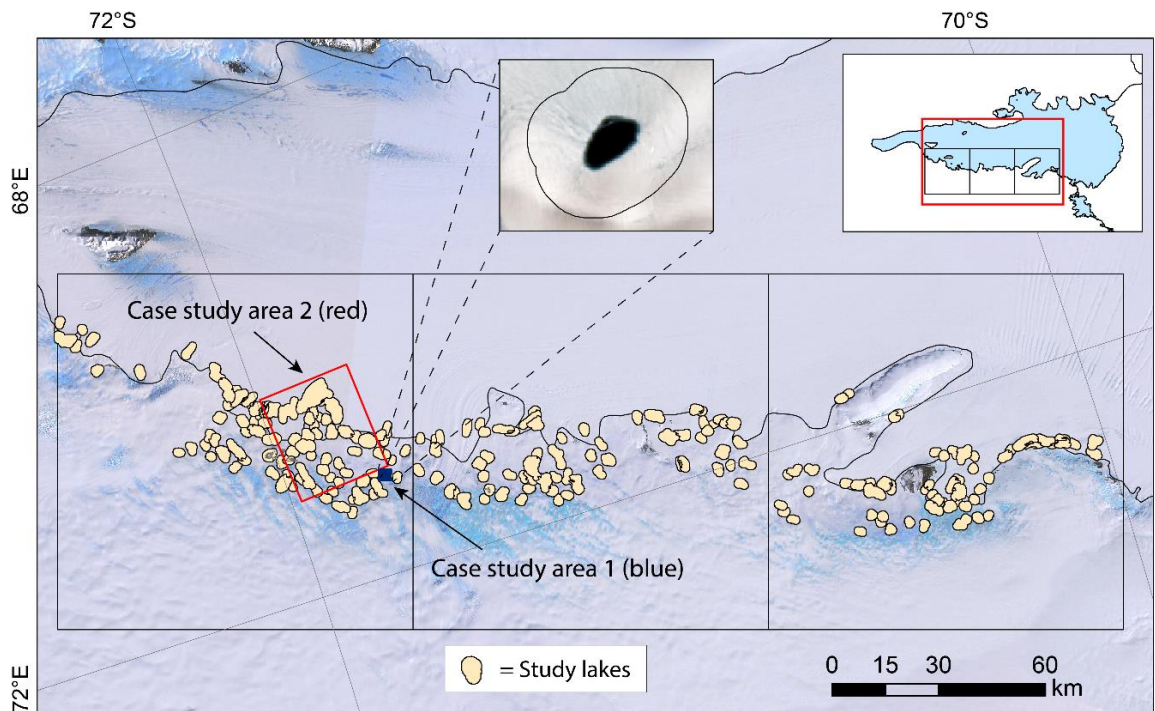
Figure 3.2. Study region along the eastern margin of the Amery Ice Shelf. Black square boxes show three ROIs (Chapter 2), from which study lakes were selected for lake volume processing. The black line marks the grounding line from Depoorter et al. (2013). Note how the majority of studied lake basins are on grounded ice, but some lie directly above the grounding line or just onto the ice shelf. The case study areas are shown by the blue (1) and red (2) boxes. The inset for case study area 1 displays a Landsat 8 image of Lake A from 7th January 2018; the circle around the lake indicates the total basin area used during automated volume processing (Section 3.3.3). The background image is the Landsat Image Mosaic of Antarctica.

3.3 Methods
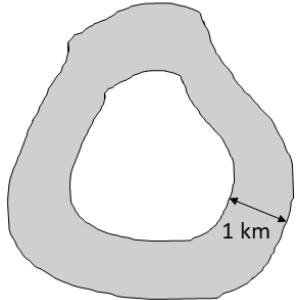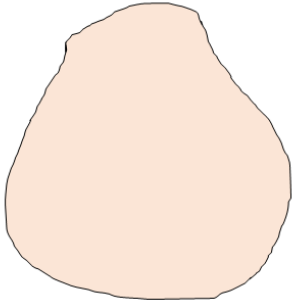
3.3.1 Overview

In this chapter, I use a combination of semi-automated and manual techniques to gain insight into meltwater evolution processes. Chapter 2 demonstrates how automated remote sensing methods can enable rapid and large-scale geospatial analysis of surface meltwater area from satellite imagery. Interpretation of surface processes from automatically generated results can be challenging, however, and manual inspection of optical satellite images can often highlight processes that would have otherwise gone undetected. Here, I briefly describe the process and rationale behind the different methods that I applied in this chapter.

I manually inspected optical satellite imagery (Landsat 8 and Sentinel-2) to assess the different ways that lake basins accumulate and lose meltwater, and the extent to which lake basins are connected by surface channels (Section 3.3.2). Optical images were collected for case study areas 1 and 2 to observe the evolution of surface meltwater over a melt season, and to manually search for lake drainage events. To quantify the timing and magnitude of changes in meltwater, I then used an automated approach to generate lake volume time series for individual lake basins across the study region (Section 3.3.3), with temporal resolution typically ranging from a few days to a few weeks. However, the potential for lake drainage events to occur on hourly to daily timescales (Das et al., 2008), means that this temporal resolution is insufficient to accurately constrain the timeframe of drainage events. I therefore explored methods to enhance the temporal resolution of lake volume time series, developing a novel method to generate daily volume estimates based on MODIS reflectivity data (Section 3.3.4).

Throughout this chapter, I use specific terminology to refer to different input geometries regarding the calculation of volume data for any given lake. Key terms referring to three frequently used geometries are hence described in Table 3.1, alongside an illustrative schematic for each, to aid with understanding. The generation and application of each geometry is explained in subsequent method sections.

Table 3.1. Description and illustrations for three polygon geometries used during lake volume calculations. These can be referred back to throughout the chapter.

Example Illustration			
Term Used	**Lake Outline (Polygon)**	**Lake Buffer**	**Lake Neighbourhood (Polygon)**
Description	Maximum extent lake outline from annual meltwater polygons between 2016-2021 (generated in Chapter 2)	1 km buffer area around the lake outline. This term only refers to the buffer area, and does not include the lake outline area.	Area covering *both* the lake outline and the lake buffer.

(1 km scale indicated in the Lake Buffer illustration)

3.3.2 Manual analysis of optical image time series

Optical image time series were generated to visually observe how surface meltwater evolves over short (daily – weekly) timescales within a melt season. I used GEE to rapidly search and export Sentinel-2 (10 m resolution) and Landsat 8 (30 m resolution for most bands) optical images for case study areas 1 and 2. This method enabled significantly faster generation of image time series than possible when downloading entire satellite image tiles. Shapefiles for the two case study areas were created in ArcMap, and imported into GEE. Image collections were created within GEE for each satellite, based on the input geometry (case study area) and a defined date range. Images were sorted by acquisition date within each collection. The 'Red', 'Blue' and 'Green' (RGB) bands were selected for all images, whilst the 'Panchromatic' band was additionally retained for Landsat-8 images. This enabled Landsat RGB bands to be pan-sharpened to 15 m resolution for ease of visual interpretation. Within each collection, images with identical time stamps were mosaicked to ensure consistent image outputs for areas that were split by a satellite tile boundary. All images within each collection were then exported as geoTIFF files using a batch export function. GeoTIFFs were loaded into ArcMap as RGB composite images for manual visual analysis and interpretation.

3.3.3 Lake volume time series

Lake volume estimates were automatically calculated in GEE using an adapted version of the 'Fully Automated Supraglacial lake Tracking at Enhanced Resolution' (FASTER) algorithm (Williamson et al., 2018). T. Chudley (pers. comm., 2021) previously implemented a simplified version of the FASTER algorithm within GEE, allowing a user to manually draw a box around a single lake to generate lake volume measurements. The original FASTER method was designed for application in Greenland (Williamson et al., 2018). Here, I build on the work of Chudley (pers. comm., 2021) by creating an automated method to loop through multiple pre-defined lake basin polygons at once, enabling rapid generation of lake volume data across a whole catchment. I additionally adapted the method for suitability to Antarctica by incorporating the lake detection thresholds of Moussavi et al. (2020) (Chapter 2). Applying the updated method, volume time series were generated for 215 lake basins between 2016 and 2021. This study period enabled me to assess both multiannual and seasonal changes in lake volumes. My method used two GEE scripts: 1) A master script to set input variables, loop through each lake basin for volume calculation, and export the data; 2) A function script (which is called via the master script) to calculate lake areas and volumes for a single lake basin, building on the work of Chudley (pers. comm., 2021).

3.3.3.1 Lake neighbourhood polygons

To generate volume time series for multiple lakes across the study region, I created a set of 'lake neighbourhood polygons' (Table 3.1), which were used as input geometries for lake volume calculations. The FASTER method requires non-water pixels (i.e. surrounding ice) to be included within input geometries to control for variations in local ice albedo. The inclusion of surrounding non-water pixels thus enables 'lake bottom albedo' to be estimated as part of water depth calculations (Williamson et al., 2018). It was therefore necessary to delineate a set of study lakes (termed 'lake outlines'; Table 3.1), and then create larger 'lake neighbourhood polygons' with a sufficient area of surrounding ice around each lake outline.

Annual mapped meltwater outputs (generated in Chapter 2) between 2016 and 2021 were merged to generate a 5-year maximum meltwater extent dataset (Fig. 3.4a). This dataset

was clipped to the study region (Fig. 3.2) and then filtered to isolate lake outlines (Fig. 3.3). First, meltwater polygons with an area of less than 0.5 km^2 were removed, since I was interested in generating volume time series for only the largest lakes. This threshold was chosen because larger lakes are likely to show greater magnitude volume changes, and are covered by more than one MODIS pixel. Second, polygons with 'holes' (typically resulting from a topographic high within a basin forming an island, or a partial ice lid) were filled to ensure the entirety of lake outlines were captured. Third, I removed thin sections of meltwater polygons, representing meltwater streams. To achieve this, I used a square structuring element within MATLAB (strel) to identify sections of polygons with a width of less than 6 pixels (180 m). Morphological opening (imopen) was then applied to remove these thin interconnecting meltwater pathways, isolating the individual lakes. Lake outline polygons were filtered by area for a second time using a 0.5 km^2 threshold, and lakes further than 10 km onto the ice shelf from the grounding line were removed, since the focus of this chapter is on meltwater evolution on grounded ice and in the grounding zone. Finally, manual filtering using optical imagery was performed to remove polygons in regions of high crevassing, where lakes had mistakenly been identified as a result of the advection of meltwater filled crevasses over successive years.

Filtered lake outline polygons were given a unique 'Lake ID' number, and imported into GEE for creation of lake neighbourhood polygons. Within GEE, a 1 km buffer was added to lake outlines to add a region of surrounding ice to each lake (Fig. 3.4b). In instances where a lake buffer overlapped with the outline of a different lake, the buffer was clipped to remove the neighboring lake outline from that lake neighbourhood polygon (see example in Fig. 3.3). This step ensured volume time series for any given lake would not include volume contributions from nearby lakes. Lake neighbourhood polygons were exported from GEE as shapefiles, and multipart features were removed in MATLAB in rare instances where the clipping process had created smaller, unwanted polygon features. Finalised lake neighbourhood polygons were re-imported to GEE for volume calculation. Subsequent methods describe processes conducted for a single lake neighbourhood polygon.

Meltwater outputs (Chapter 2):
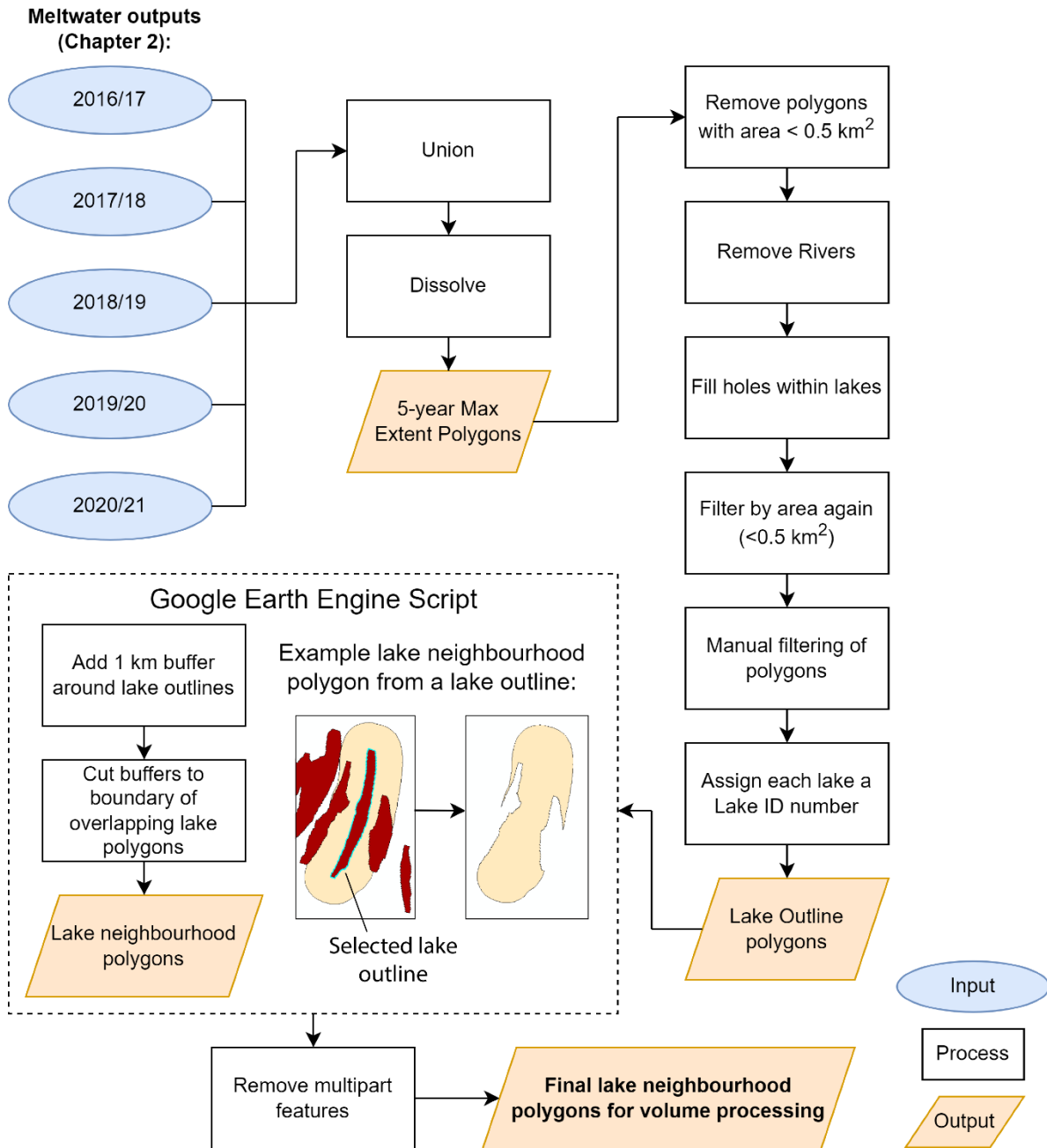
Figure 3.3. Steps taken to create lake neighbourhood polygons from annual meltwater outputs generated in Chapter 2. An example showing the progression from mapped meltwater outputs to lake neighbourhood polygons is shown in Figure 3.4.
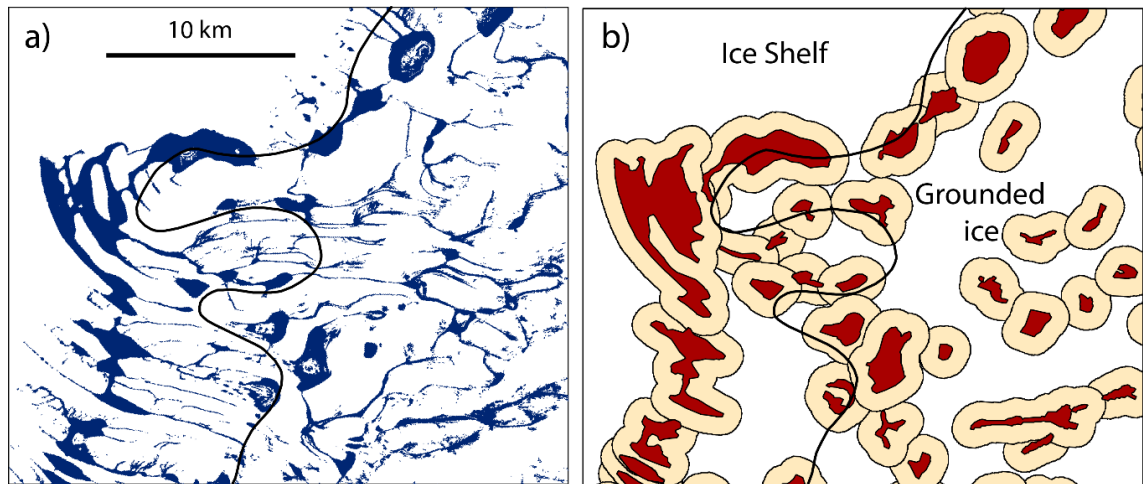
Figure 3.4. (a) 5-year maximum extent meltwater cover for case study area 2 between 2016 and 2021. Note how lake polygons are connected by streams and rivers. (b) Lake outlines (red) and lake neighbourhood polygons (beige) for the same region, following the filtering and processing stages shown in Figure 3.3. The black line in both images shows the grounding line position (Depoorter et al., 2013).

3.3.3.2 Image collection and filtering

Following the approach of Williamson et al. (2018), I used both Landsat 8 (Level-1 Tier-2 TOA) and Sentinel-2 (Level-1C) optical satellite imagery to increase the temporal resolution of the lake volume time series. Every Landsat or Sentinel image covering the lake neighbourhood between November 2016 and April 2021 was collated into two image collections (one per satellite) and clipped to the lake neighbourhood polygon. These preliminary image collections were then filtered (Fig. 3.5) to ensure water depth measurements were only calculated for images where the whole lake was visible, preventing volume estimates from being skewed. Images were only retained if they: (1) had a sun elevation angle greater than 20°, following Moussavi et al. (2020) and Halberstadt et al. (2020); (2) covered at least 95% of the lake neighbourhood; and (3) had less than 5% cloud cover over the lake neighbourhood. Cloud cover was assessed by counting the number of 'cloudy pixels' from the 'Quality Assessment' (QA) bands of both Landsat (BQA band) and Sentinel (QA60) images. For Landsat images, pixels were classed as cloud if 'Bits' 5-6 or 11-12 (representing cloud and cirrus cloud confidence respectively) had binary values of greater than two, implying higher than medium confidence of being cloud. Pixels were counted as cloud in Sentinel-2 images if 'Bits' 10

(cloud) or 11 (cirrus clouds) had binary values of one, implying cloud presence. Since cloud assessment was purely for the purpose of image filtering, QA bands offered a simple, time-efficient method for quantifying cloud cover, rather than the threshold-based masking conducted in Chapter 2. Filtered Landsat and Sentinel image collections were then taken forward for volume calculations.
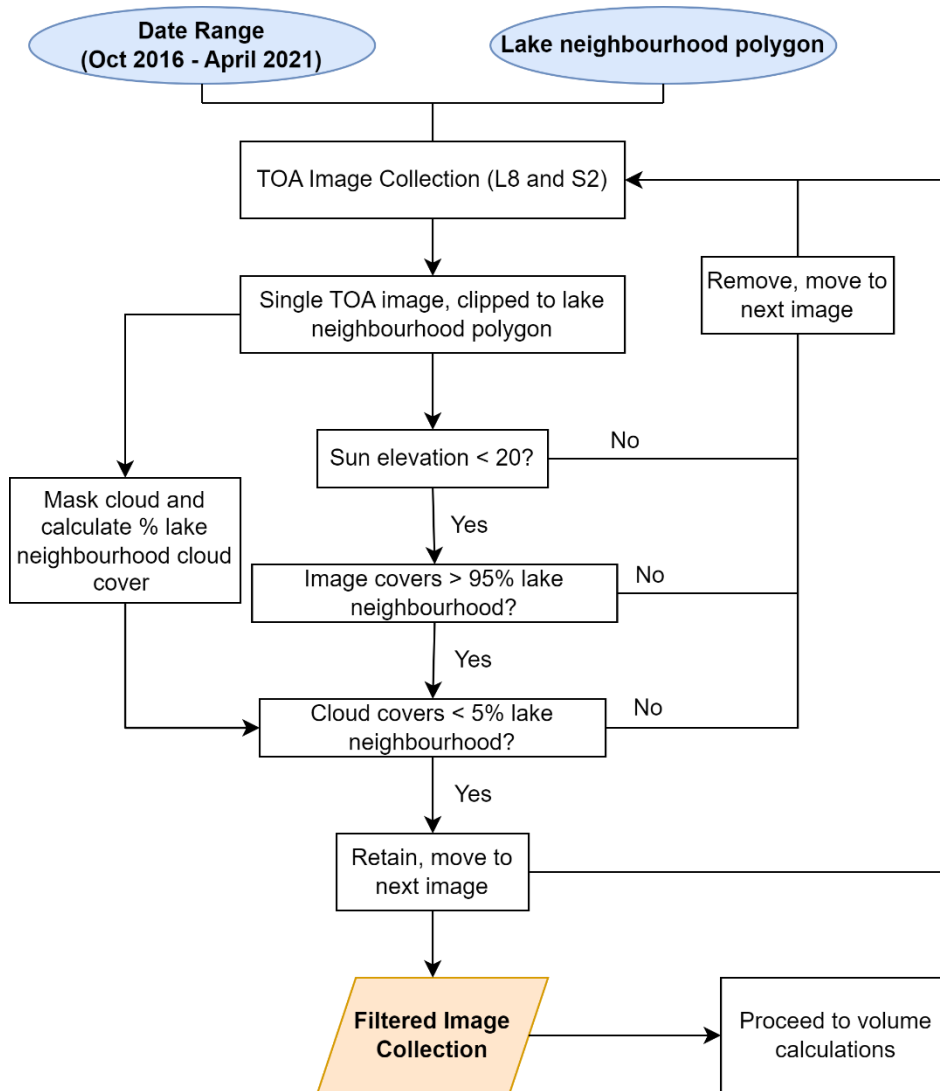
Figure 3.5. Image collection and filtering steps taken prior to lake volume calculations. TOA stands for 'Top of Atmosphere'. Note that separate image collections are generated for the two different satellites, but the same filtering steps are applied to both collections.

3.3.3.3 Lake depth and volume measurements

Following Williamson et al. (2018), and based on previously established work (Sneed & Hamilton, 2007; Pope et al., 2016), lake depths and volumes were calculated using a physically-based model. The model is based on the premise that lake pixel reflectivity values vary according to water depth, whereby the attenuation of light through a water column increases with depth. For each clipped lake neighbourhood image, pixels were classed as ice or water using the NDWI$_{ice}$ (Section 2.3.2). Water pixels were delineated using the same thresholds applied during meltwater mapping (Moussavi et al., 2020; Table 2.1). Lake depth (z) was calculated for any given pixel using the following expression (Eq. 3.1):

$$z = \frac{ln(A_d - R\infty) - ln(R_{pix} - R\infty)}{g} \quad\quad (3.1)$$

where A_d is lake bottom albedo, $R\infty$ is the reflectance of optically deep (> 40 m) water, R_{pix} is the observed water reflectance (TOA reflectance) and g is an attenuation coefficient that accounts for losses in upward and downward travel through the water column. Lake depth estimates for Landsat 8 images were calculated by averaging depth values derived using the red and panchromatic bands (Pope et al., 2016; Williamson et al., 2018), whilst depth measurements from Sentinel images were solely based on the red band. A_d was calculated on an image-by-image basis using the median reflectance value of ice pixels within the lake neighbourhood polygon. This approach assumes that reflectance values immediately surrounding a lake are equivalent to those at the lake bed if it were not covered in water (Pope et al., 2016), and is more accurate than using a static albedo value across a region (e.g. Sneed & Hamilton, 2007). In the absence of optically deep water (e.g. ocean water), previous studies have found that R∞ is close to zero (Banwell et al., 2019; Arthur et al., 2020b). I therefore used an R∞ value of zero for all depth measurements, following Banwell et al. (2019) and Arthur et al. (2020b). Values for *g* of 0.7507 and 0.3817 were used for the red and panchromatic Landsat 8 bands respectively (Pope et al., 2016), whilst a value of 0.8304 was used for Sentinel-2 images (Williamson et al., 2018). Lake volumes were calculated by summing the depth values of water pixels within the lake neighbourhood, multiplied by the pixel area (10 x 10 m^2 for Sentinel-2

images, and 30 x 30 m^2 for Landsat 8). Lake volume measurements showed broadly consistent magnitudes between the two satellites on dates where data were acquired from both sensors, providing confidence in the methods applied.

Lake volume data for any given lake basin were calculated using the 'function script' within GEE. Once volume data had been generated for all lake neighbourhood polygons (by looping through the function script using the master script), volume data for all lakes were exported from GEE as a single GEOJSON output file. Output data comprised lake ID numbers, lake volumes, lake areas, and the date and satellite (Landsat 8 or Sentinel-2) from which each measurement was derived. Processing and plotting of volume data was conducted in MATLAB. In instances where volume measurements were generated on the same day from both satellites, the lower of the two measurements was removed.

3.3.4 Enhancing the temporal resolution of lake volume time series

Here, I explored whether daily MODIS reflectivity data could be used as a water volume proxy to increase the temporal resolution of lake volume time series. MODIS data have been widely used in Greenland to calculate supraglacial lake area (e.g. Sundal et al., 2009; Williamson et al., 2017; Selmes et al., 2013), but the low spatial resolution of the data (~250 – 500 m) limits its suitability for estimating volume of individual lakes, without additionally using higher spatial resolution data (Section 1.2.2). I therefore developed a method to combine the benefits of the high temporal resolution MODIS data, with the high spatial resolution Landsat 8 and Sentinel-2 data. The method involved calculating a proxy for lake volume based on the relative MODIS reflectivity values of pixels within the lake outline compared to surrounding ice, for any given lake. I then compared these proxy values against the volume measurements derived from higher spatial resolution sensors (Section 3.3.3) to assess the level of agreement between the two methods on a lake-by-lake basis. For lakes that showed high agreement, I used the lake-specific relationship derived from coincident reflectivity proxy and volume data to estimate daily lake volumes from the MODIS data. MODIS-enhanced time series were generated for a single melt season (2017/18) to test the method.

Assessment of relative reflectivity between lake outlines and their surrounding ice required two separate sets of input geometry: 1) 'lake outlines' (already created in Section 3.3.3.1) and 2) 'lake buffers', that did not include the lake outline (Table 3.1). To create

the buffer polygons, lake outlines were 'cut' from lake neighbourhood polygons (Section 3.3.3.1) using the 'Erase' tool in ArcMap. The two sets of shapefile polygons were then loaded into GEE for processing. As in Section 3.3.3, processing within GEE involved using a function script to acquire MODIS reflectivity values for a single lake outline and corresponding buffer, whilst a master script was used to loop through the set of 215 study lakes.

3.3.4.1 MODIS reflectivity data processing

Reflectivity data were acquired from Level-2 processed MOD09GA (version 6) daily MODIS images within GEE. Images have a spatial resolution of 500 m, and provide estimates of surface spectral reflectance at ground level, without the effects of atmospheric scattering or absorption. Reflectivity data were acquired for lake outlines and lake buffers (Table 3.1) using a function script in GEE. An image collection was created containing every MODIS image covering any given lake outline between November 2017 and March 2018. Images were then clipped to the lake outline. Cloud pixels were identified based on a value of one for 'Bit 10' of the 'state_1km Bitmask' quality assessment band, signifying cloud cover. Cloud pixels were subsequently masked out of images. Lake outline reflectivity was then calculated based on the median pixel value of band one ('sur_refl_b01') from each masked image. Band one provides surface reflectance at wavelengths of 620-670 nm, with reflectivity values ranging from -100 to 16,000. Once median reflectivity values and their derived image dates were acquired for the lake outline, the same procedure was run for the corresponding lake buffer. The master GEE script was used to run the above process on all 215 lake outlines and buffers, with data (Lake ID, outline reflectivity values, outline reflectivity dates, buffer reflectivity values and buffer reflectivity dates) exported from GEE as a single GEOJSON file.

MODIS reflectivity data were processed in MATLAB. Acquisition dates were mostly consistent between lake outlines and lake buffers, but there were some instances where reflectivity data had only been generated for one of the two input geometries (e.g. on days where cloud had covered the entirety of the lake outline but not all of the lake buffer). Such instances were removed from the dataset, ensuring data were only retained for dates which had reflectivity values for both outlines and buffers. A 'MODIS proxy' value was

subsequently created by dividing buffer reflectance values by lake outline reflectance for each date. This provided a measure of reflectivity change within the lake outline relative to the surrounding ice (Fig. 3.6). For example, similar reflectivity values would be expected between the lake outline and its buffer when there is no surface water, resulting in a proxy value of one. The accumulation of water within a lake outline would result in lower reflectivity values relative to the surrounding ice, resulting in a proxy score greater than one (Fig. 3.6). For ease of visual comparison and interpretation, proxy values were reduced by one (i.e. so a lake with zero water volume has a proxy score of zero, rather than one).

Lake outline Reflectance	10,000	9,000	5,000	3,000	10,000
Buffer Reflectance	10,000	9,000	9,000	10,000	10,000
Buffer/Outline	1	1	1.8	3.3	1
MODIS proxy	0	0	0.8	2.3	0
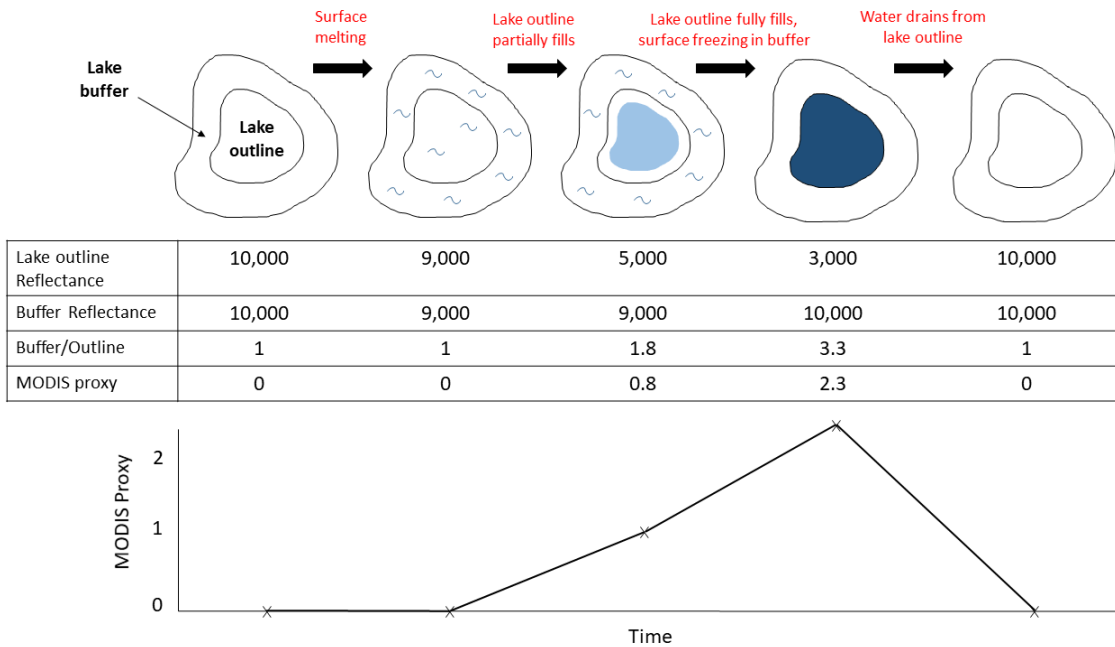
Figure 3.6. Schematic showing the evolution of an example lake. MODIS proxy values were generated based on the relative difference in reflectivity between lake outlines and their buffers. The blue curved lines represent surface melting, whilst the light and dark solid blue colours indicate shallow and deep lake water respectively. Red text describes processes occurring between time steps of lake cartoons. Note how proxy values are reduced by one (MODIS proxy = (Buffer/Outline) – 1), so that empty lakes have a value of zero.

3.3.4.2 Daily lake volume calculation

MODIS proxy values were compared with Landsat/Sentinel lake volume data on a lake-by-lake basis to assess the association between the two datasets. For each lake ID, dates were identified where both MODIS and Landsat/Sentinel data had been generated. This resulted in approximately 15-25 dates from which a linear relationship could be derived for each lake (Fig. 3.7). An orthogonal least squares (OLS) regression model (Linortfit2) was used in MATLAB to determine a linear equation and significance level between the datasets per lake. Lakes that displayed a statistically significant relationship ($p < 0.01$) between MODIS proxy and Landsat/Sentinel lake volume were deemed appropriate for temporal enhancing of volume time series. This higher significance level (compared to the commonly used threshold of $p < 0.05$) was used to increase confidence in MODIS-derived volume estimates. If the significance value was greater than 0.01, MODIS data were deemed insufficiently accurate at estimating water volume for that particular lake. This approach assumed that Landsat/Sentinel measurements were accurate representations of lake volume, and were used as the benchmark for comparison.
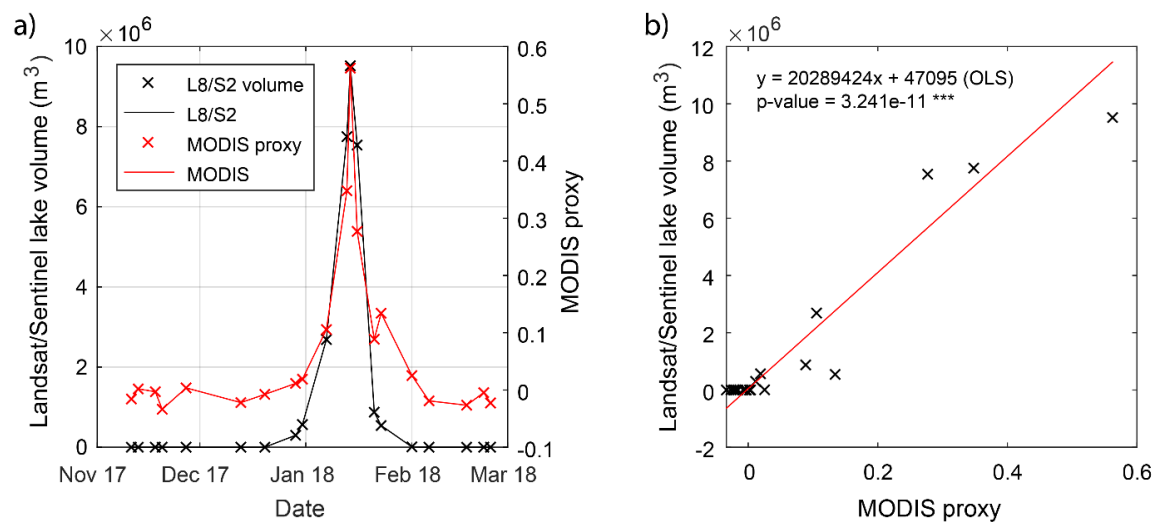
Figure 3.7. (a) Example time series displaying Landsat/Sentinel lake volumes plotted against MODIS proxy values. In this example (displaying data for lake 182; Fig. 3.15), there were 21 dates when data were generated from both datasets. Note how MODIS proxy values display strong agreement with the timing of lake volume increases and decreases shown in the Landsat/Sentinel data. (b) Scatter plot showing the linear relationship between the two datasets. This lake displays a statistically significant ($p < 0.01$) relationship.

For lakes where MODIS data provided a sufficiently close representation of Landsat/Sentinel volume data, MODIS proxy values were inserted into the relevant linear equations to determine lake volume estimates for all dates that MODIS data were acquired. This enabled daily estimates of lake volume to be produced, with gaps in the time series only present on days where MODIS reflectivity estimates had not been generated due to cloud cover. Negative volume estimates (in rare instances where negative MODIS proxy values had been generated due to higher reflectivity from the lake outline than the buffer) were set to zero. Daily volume data were smoothed using a moving median time window (four days), and filtered using a low pass Butterworth filter. Raw and smoothed MODIS derived volume data were plotted alongside Landsat/Sentinel volume data for ease of comparison between the datasets.

3.4 Results & Discussion

Due to the exploratory nature of this chapter, results and their interpretation are combined for ease of discussing the findings. This section is split into three parts. First, I discuss the evolution of meltwater across the study region, in particular focusing on large scale lateral transfer of water between grounded and floating ice. Second, I explore ways in which an individual lake can increase or decrease in water volume, presenting results from lake-specific volume time series, which highlight rates at which lake volume changes can occur. Third, I discuss ways that the temporal resolution of automatically generated lake volume time series could be enhanced, and evaluate the success of using MODIS reflectivity data to produce daily lake volume estimates.

3.4.1 Seasonal and interannual evolution of lakes across the study region

To investigate interannual changes in lake volume across the study region, I compared the maximum annual volume of each lake between the five studied melt seasons. This analysis was based on Landsat/Sentinel derived volume time series (Section 3.3.3). Maximum lake volumes ranged from 3.7×10^3 m^3 to 1.6×10^7 m^3, and there was a relatively normal distribution of lake volumes across the study region (Fig. 3.8a). Of the 215 study lakes, 179 experienced their greatest annual maximum volume during either

the 2016/17 or 2018/19 melt season (Fig. 3.8b). This is consistent with higher modelled surface snowmelt across the Amery region during these two melt seasons, compared to the other three melt seasons studied in this chapter (Section 2.4.4; Fig. 2.13). Approximately half of the sampled lakes experienced their maximum lake volume in each of the two high melt seasons (Fig. 3.8b), and there was no clear spatial pattern of the year in which lakes experienced their greatest lake volume (Fig. 3.8c). The large lake investigated by Trusel et al. (2022) (here referred to as lake 182) had its greatest lake volume during the 2017/18 melt season (Fig. 3.8d), despite low meltwater area across the Amery region in general (Fig. 2.13) and only 10% of study lakes having their maximum lake volume during this year. These results suggest that in any given melt season, meltwater is not evenly distributed across lake basins, and that meltwater may preferentially pond in different basins during different years.
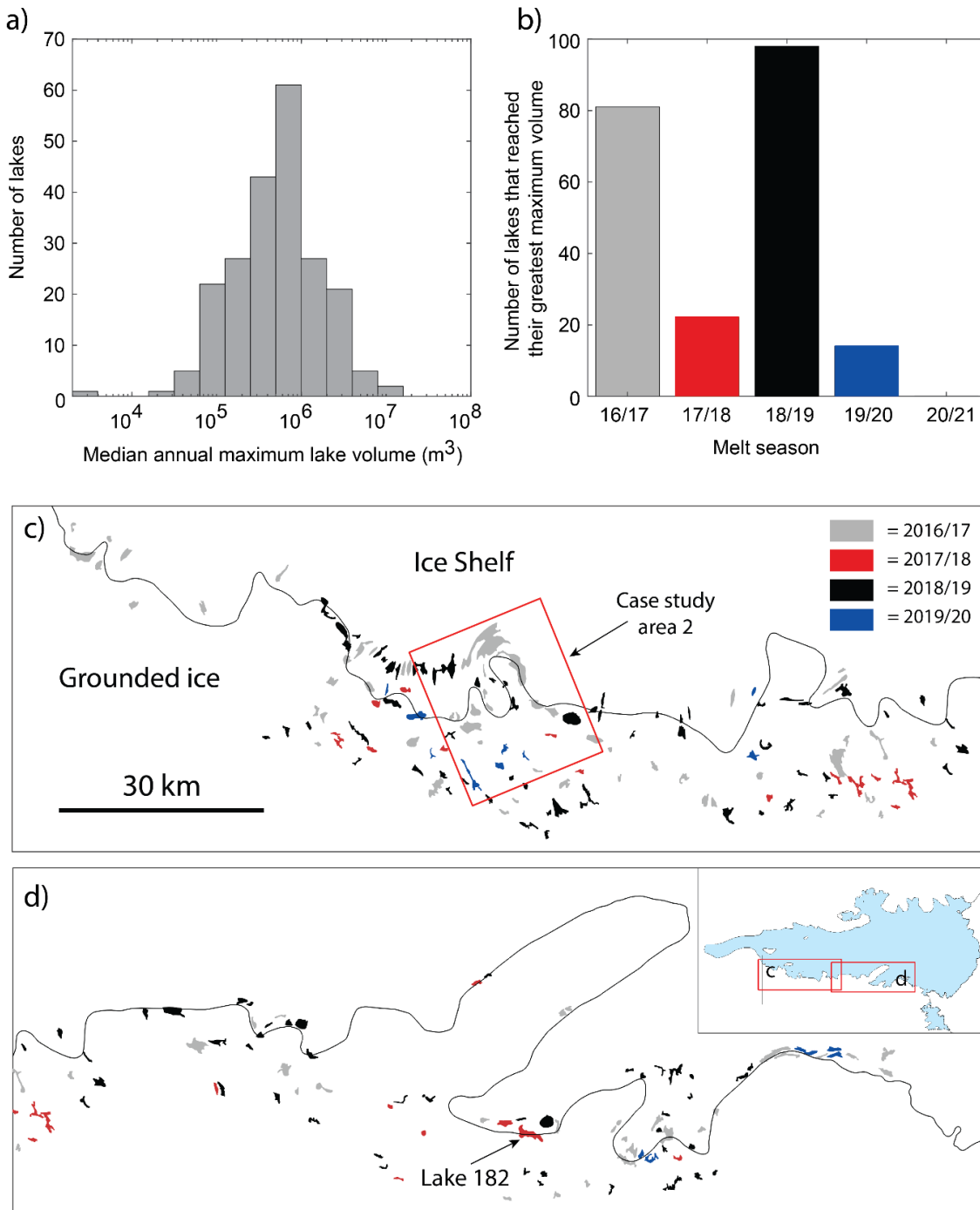
Figure 3.8. (a) Histogram displaying the 5-year median of maximum annual lake volumes. (b) Bar chart displaying the melt season during which lakes experienced their greatest lake volume. Note how no lakes experienced their greatest annual maximum lake volume in 2020/21. (c-d) Maps showing the spatial distribution of data displayed in (b). Lakes are coloured by the melt season of their greatest annual maximum volume, with colours matching the bar colours in (b). Lake 182 is labelled, highlighting the lake analysed in Trusel et al. (2022). The black line shows the grounding line position (Depoorter et al., 2013), whilst the inset map displays the areas covered in panels (c) and (d).

Manual analysis of Landsat 8 and Sentinel-2 images covering case study area 2 between 22nd December 2016 and 27th January 2017 reveal a migration of surface meltwater from grounded onto floating ice (Fig. 3.9). In late December, large (up to 2 km diameter) supraglacial lakes are observed above the grounding line, with limited surface meltwater on the ice shelf (Fig. 3.9a-b). The downslope flow of water subsequently formed meltwater channels, facilitating water transport across the grounding line onto the ice shelf throughout the first half of January to form large, interconnected networks of meltwater by the middle of the month (Fig. 3.9f). By the end of January, the large majority of surface meltwater lies on, or within ~ 2 km of the ice shelf, with lake basins higher up on grounded ice (away from the grounding line) containing less meltwater than at the start of the month (Fig. 3.9c,i). Analysis of automatically generated lake volume estimates confirms this pattern, suggesting that the surface movement of meltwater from grounded to floating ice occurs on an annual basis (Fig. 3.10). On average, lakes situated adjacent (< 2 km) to the grounding line or on the ice shelf experience peak lake volume at a later date during the melt season than lakes higher up on grounded ice (Fig. 3.10). Several lakes located > 10 km inland of the grounding line experience peak seasonal volumes in late December or early January, whereas almost all lakes on the ice shelf display peak volumes in late January (Fig. 3.10). Whilst this is evident for case study area 2, not all parts of the study region show such a clear pattern (Fig. 3.10).

Results also broadly suggest that peak lake volume occurs at a later date for larger lakes (Fig. 3.10). This is likely because small lakes are able to fill, and subsequently drain laterally due to channel incision (Kingslake et al., 2015), over relatively short time periods, compared with larger lakes which take longer to fill with meltwater. It is also likely that lateral expansion of lakes happens more readily on flatter ice shelf surfaces (Spergel et al., 2021), whereas on steeper grounded ice slopes, channel incision results in more typical fill-drain cycles.
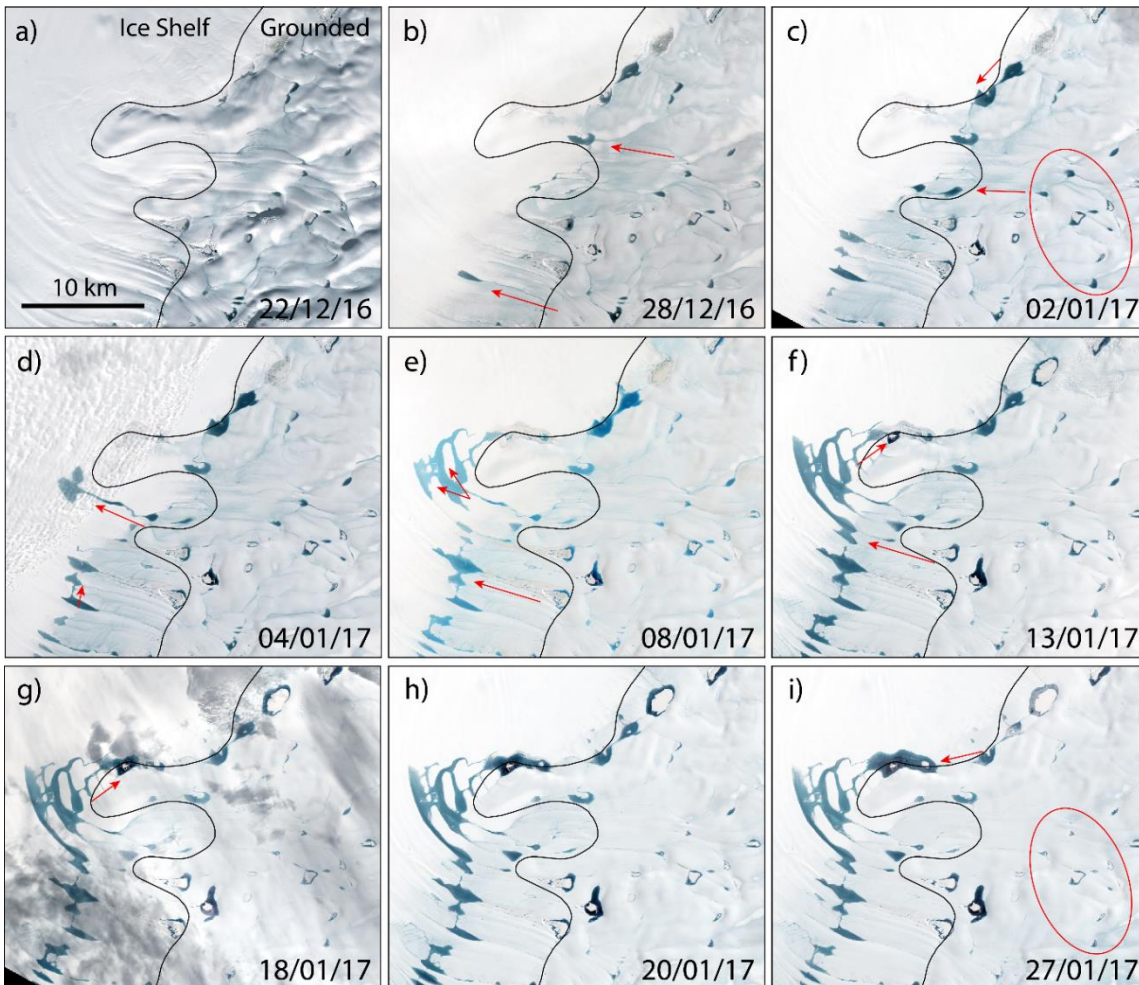
Figure 3.9. The evolution of surface meltwater over case study area 2 between 22nd December 2016 and 27th January 2017. Satellite image dates are displayed in the bottom right of each panel. All tiles display Landsat 8 pan-sharpened (15 m resolution) images except for (e), which shows a Sentinel-2 image (10 m resolution). The black line indicates the grounding line position (Depoorter et al., 2013). Red arrows highlight the direction of lateral meltwater flow direction, whilst the red circles highlight lower amounts of water in grounded lake basins at the end of January compared to the start of the month.
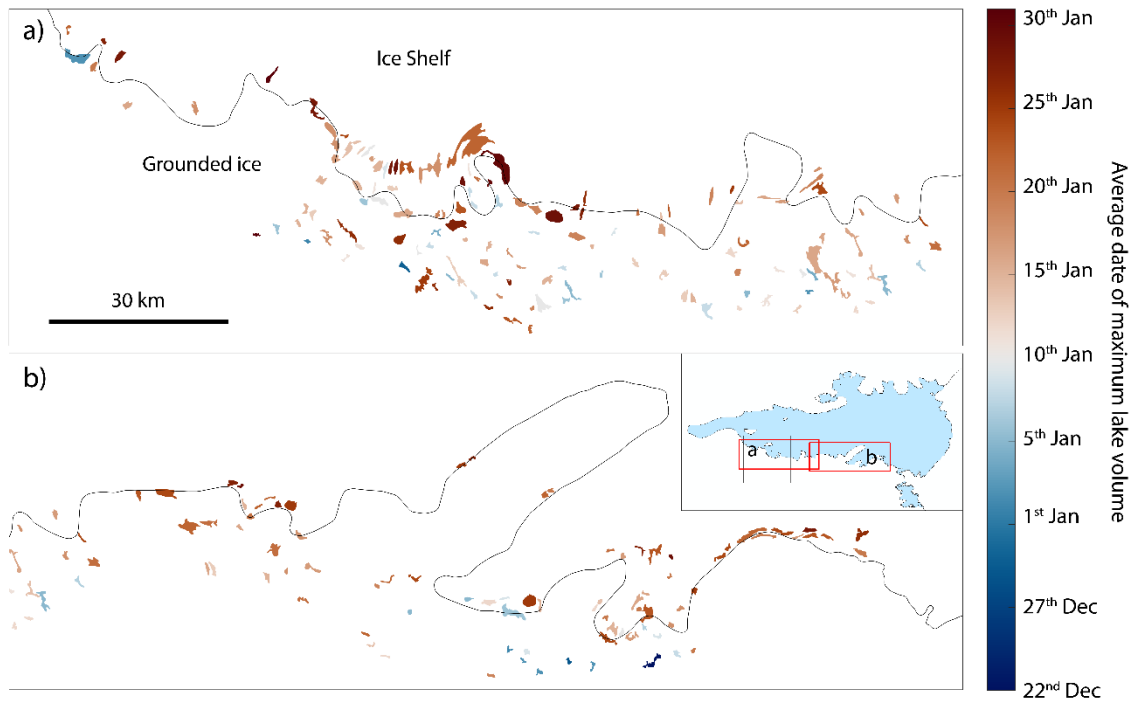
Figure 3.10. The mean date each year that lakes experienced their maximum volume. Colours represent the date of the calendar year. Blue colours indicate lakes which reached peak volume earlier in the melt season (late December to early January), whist red colours indicate lakes which typically reached peak volume later in January. The black line shows the grounding line position (Depoorter et al., 2013).

Whilst large-scale surface meltwater drainage onto and across ice shelves has been previously reported in Antarctica (Bell et al., 2017; Kingslake et al., 2017; Dell et al., 2020), my analysis provides specific examples of the timescales over which such processes can occur in the Amery region. The transition from a relatively meltwater-free ice shelf surface to one that hosts extensive meltwater networks, can occur in under a week (Fig. 3.9). However, one uncertain factor is the distinction between ice shelf meltwater that has originated on grounded ice and flowed downslope across the grounding line, compared with meltwater produced from *in situ* ice shelf melting. Results from Chapter 2 demonstrate the importance of firn air content for controlling the distribution and timing of meltwater ponding (Section 2.5.2). Further evidence of this control is shown here. Figure 3.9c (02/01/2017) shows a clear separation between exposed, low-albedo ice on grounded sections of case study area 2, and a predominantly snow and firn covered ice shelf. The limit of surface meltwater ponding almost exactly matches this separation line, suggesting that on 2nd January 2017, the snowpack has

sufficient firn air content to avoid full saturation of meltwater. Over the following week (Fig. 3.9d-e), meltwater crosses this dividing line, initially due to lateral meltwater transfer via a surface stream. The rapid subsequent expansion in meltwater area on the ice shelf is likely partly due to melt-albedo feedbacks (Kingslake et al., 2017; Jakobs et al., 2021), and the large volume of meltwater on the ice shelf by the end of the month is significantly greater than the volume initially ponded on grounded ice.

These results suggest that early in the melt season, surface meltwater initially develops on the ice shelf due to the overland transfer of meltwater from grounded ice. Once meltwater is established on the ice shelf surface, meltwater area expansion occurs via progressive saturation of the surface firn pack. This process likely occurs due to a combination of melt-albedo feedbacks and continued input from surface meltwater transfer over the grounding line. Future work could therefore compare spatial variability in modelled surface melt data with runoff integrated across a grounded catchment, to get an approximate estimate of the different relative sources of ice shelf meltwater.

3.4.2 Patterns in meltwater volume change for individual lakes

Here, I present results highlighting the various ways that an individual lake can gain or lose volume, firstly showing results from analysis of case study area 1. I interpret combined evidence from optical satellite imagery, lake volume time series, and surface temperature data to evaluate varying styles of lake evolution and their controls in different melt seasons. I then provide a summary of the mechanisms via which lakes in the study region evolve, and explore the extent to which the specific mechanism of any given change in lake volume can be automatically attributed.

3.4.2.1 Analysis of case study area 1

To explore the different ways that an individual lake can accumulate or lose water, I analysed lake volume time series for Lake A (from case study area 1) in combination with evidence from optical satellite images. Lake A is the larger of the two lakes in case study area 1, and was identified as an ideal lake to explore varying evolution processes based on the repeated occurrence of lake drainage events (Doocey, 2020). Lake volume

estimates covering five melt seasons from 2016 to 2021 are shown in Figure 3.11a, with time series insets displayed for three melt seasons (2016/17, 2017/18 and 2019/20) highlighting contrasting patterns of volume change (Fig. 3.11b-d). Optical image time series are shown for selected dates from the 2018/19 (Fig. 3.12), 2019/20 (Fig 3.13) and 2020/21 (Fig. 3.14) melt seasons to provide visual evidence of lake evolution styles. These years were selected due to the high number and frequency of cloud-free images, and to provide comparison of melt seasons where different lake evolution processes were observed. Comparison with ERA reanalysis data additionally aids with the identification of trends in surface temperature, but absolute 2 m temperature values have some uncertainty due to the resolution of the model.
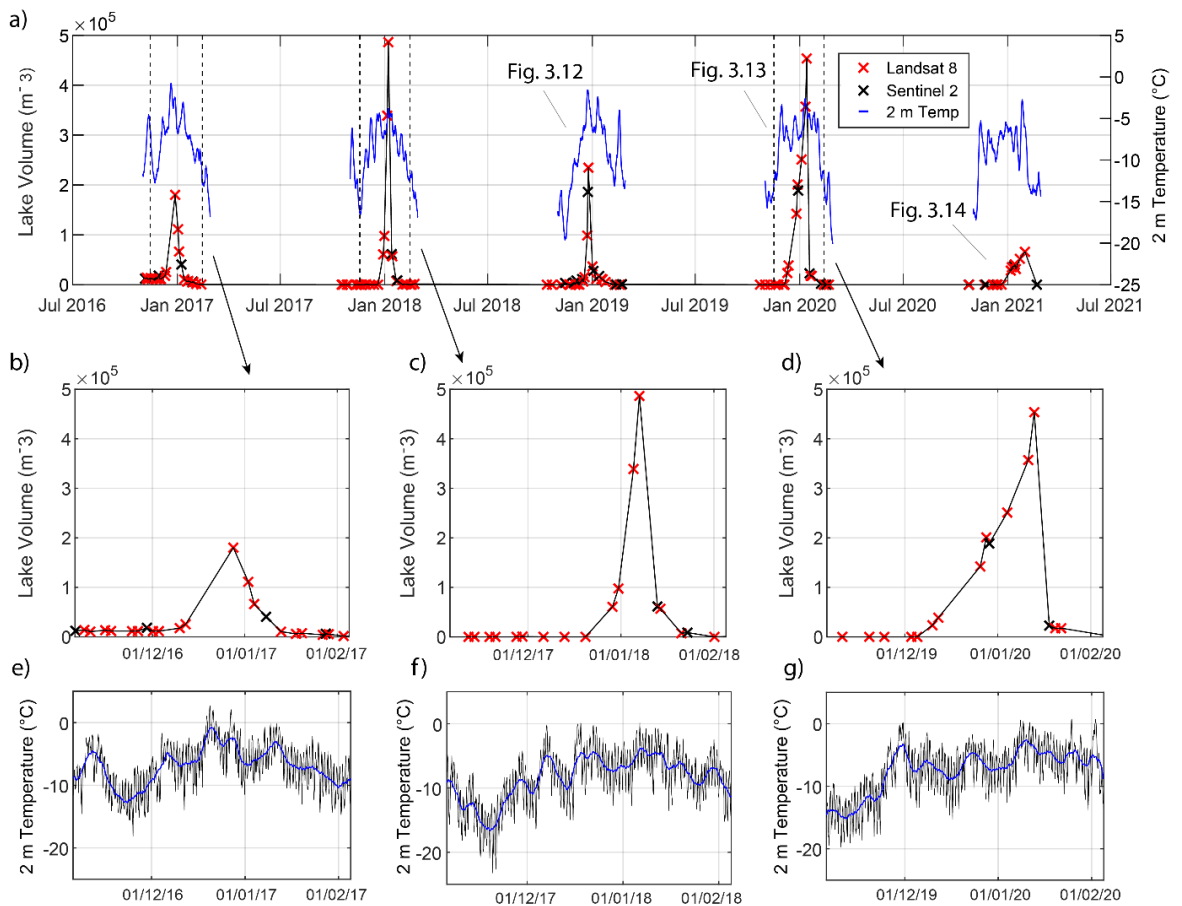
Figure 3.11. (a) 5-year automatically generated lake volume time series for Lake A in case study area 1 (Fig. 3.1). ERA 2 m smoothed (4-day moving average based on hourly data) temperature data are additionally displayed (blue) from November to February each year. (b-d) Zoomed in plots for three of the melt seasons: 2016/17 (b), 2017/18 (c) and 2019/20 (d). Note how peak volumes and the rate of volume increases and decreases vary between years. (e-g) Corresponding hourly (black) ERA 2 m temperature data for the melt seasons shown in (b-d). The blue lines show 4-day moving averages of the hourly data.

Lake A appears to predominantly fill via the delivery of surface meltwater through streams (approximately 10-30 m wide) that flow downslope into the lake from its catchment (Figs. 3.12b & 3.13d). Volume time series suggest that lake filling can occur gradually (Fig. 3.11d) or more rapidly (Fig. 3.11c). During the 2019/20 melt season, for example, Lake A steadily filled from early December 2019 to a peak volume on 13th January 2020, whereas in 2017/18, an equivalent volume increase occurred over just two weeks (Fig. 3.11c). Figure 3.11g shows how surface temperature reached ~0 °C in late November 2019, likely explaining the earlier onset of lake water accumulation in this year compared to the 2017/18 season. The rapid filling of the lake in 2017/18 (Figs. 3.11c) did not coincide with a particularly rapid increase in 2 m temperature (Fig. 3.11f), suggesting surface temperature is not the only control on filling rate. Contributions to volume increases from melting of ice beneath the lake are harder to observe. The initial presence of lake water likely enhances melting of the ice beneath via thermal energy transfer, whilst the lower albedo of water will promote further melting around the lake margin (Jakobs et al., 2021). These processes can induce a positive feedback of ice melt, and possibly contribute to the exponential rate of volume increase that is observed during the 2019/20 melt season (Fig. 3.11d). A slight increase in surface temperature in early January 2020 (Fig. 3.11g) likely also contributed to the observed increased filling rate prior to drainage.
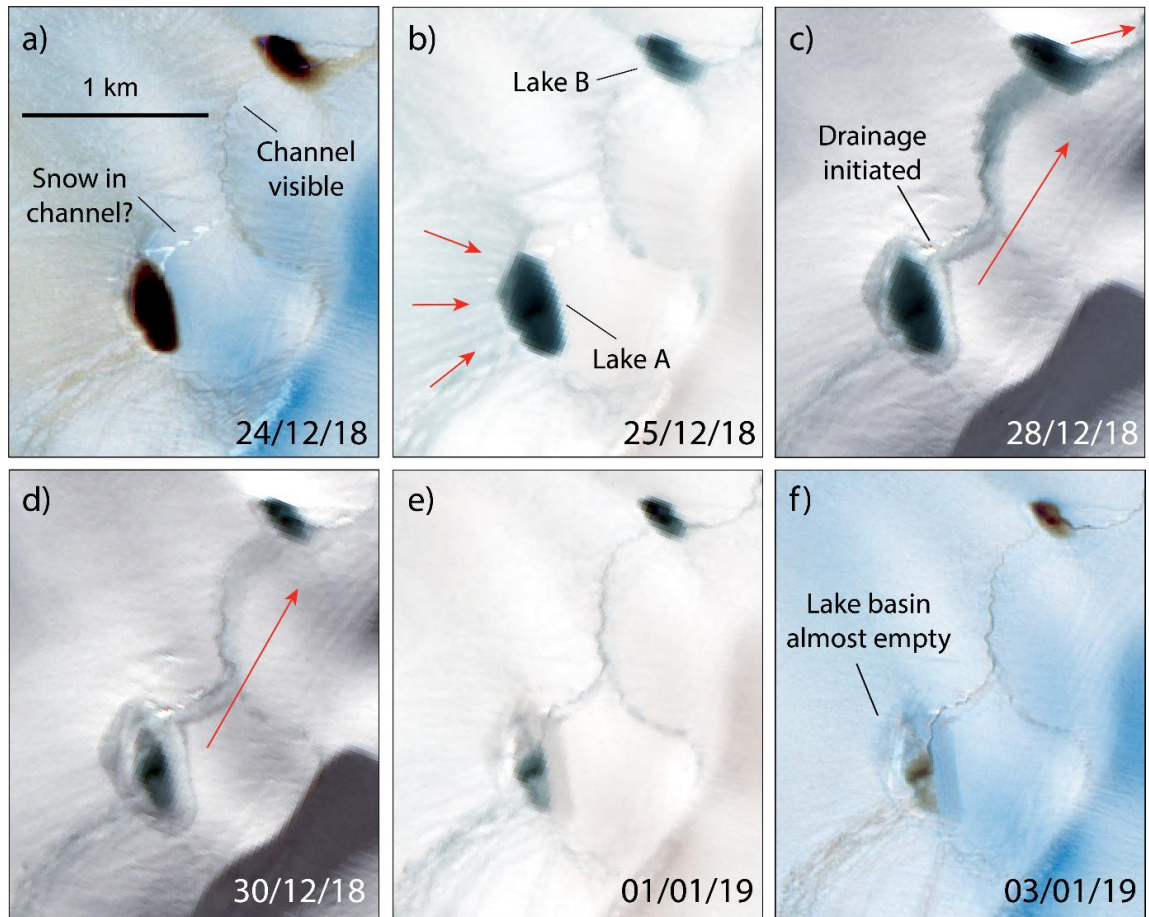
Figure 3.12. Evolution of surface meltwater within case study area 1 over an 11-day period spanning 24th December 2018 to 3rd January 2019. Images (a) and (f) show Sentinel-2 images, whilst images (b-e) show Landsat 8 images, with acquisition dates displayed for each tile. The lake basin in the bottom left of images fills to a maximum apparent volume on 25th December, before partially (c-d) and then almost fully (e-f) draining via a meltwater channel, incised at an undefined date between 25th and 28th December. Red arrows indicate the direction of surface meltwater movement.
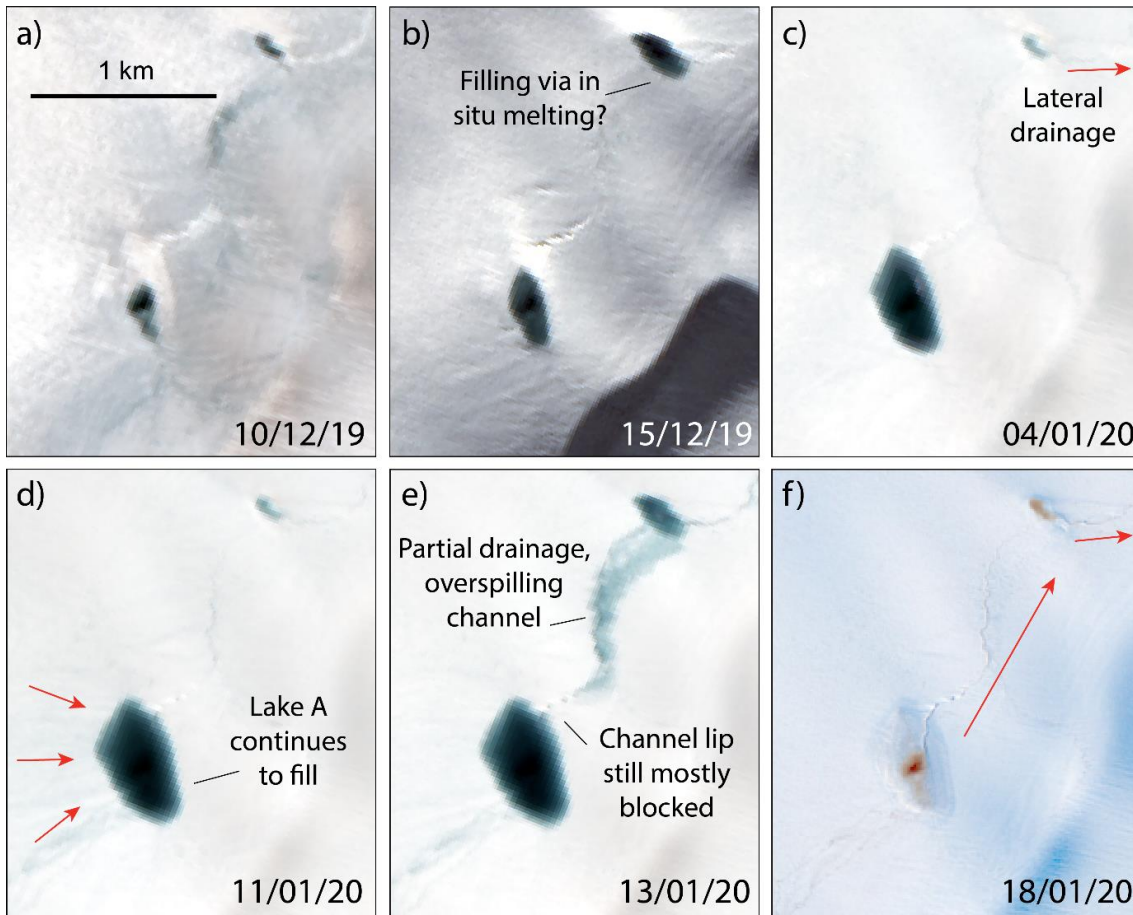
Figure 3.13. Evolution of meltwater within case study area 1 during the 2019/20 melt season, between 10th December 2019 and 18th January 2020. All tiles show Landsat 8 images apart from (f) which shows a Sentinel-2 image. Note how Lake A gradually fills over approximately one month (a-e), before emptying within a five day period (e-f).

Peak volume for Lake A typically occurs in late December or early January. In all melt seasons studied, peak volumes were short-lived and were followed by an immediate, often rapid, reduction in volume (Fig. 3.11). In January 2020, Lake A lost ~95% of its peak volume (4.54×10^5 m^3) within five days (Figs. 3.11d & 3.13e-f), although this is a minimum rate due to a lack of satellite image availability. Similarly rapid volume losses occurred in January 2018 and late December 2018, although a more gradual reduction in lake volume occurred during the 2016/17 melt season (Fig. 3.11b). Analysis of optical imagery shows that in all studied melt seasons except for 2020/21, volume losses primarily occurred by lateral drainage via a channel incised into the lake watershed (Figs. 3.12 & 3.13). During the 2018/19 melt season, for example, water drained over-ice from Lake A into Lake B through a large (50-100 m wide) meltwater channel, and subsequently

from Lake B further down-ice via another channel (Fig. 3.12). Channelized drainage from Lake A was initiated between 25th – 28th December 2018, although satellite images show that the channel already existed prior to drainage (Fig. 3.12a). It is therefore likely that the channel had remained from a previous year and been filled with snow over winter, which acted as a dam to water flow. The onset of water flow through the channel could have been triggered following a critical amount of snowmelt within the channel, or by the lake waterline becoming sufficiently high to overflow the basin lip.

The lake volume at which lateral drainage occurred varied between the four melt seasons that the process was observed (Fig. 3.11). However, it should be noted that temporal gaps in the optical satellite record mean that maximum lake volumes prior to drainage may not have been captured, especially given the potential for rapid fill rates. During the 2017/18 and 2019/20 seasons, drainage occurred once the lake reached a volume of approximately $4.5 \times 10^5 \, \text{m}^3$. By contrast, drainage occurred when the lake reached approximately half this volume during 2016/17 and 2018/19. This implies no single 'threshold volume' at which the lake level is high enough for water to overflow into the channel.

Instead of there being a single threshold volume at which surface drainage occurs, I interpret that the timing of drainage is dependent on how quickly it takes for the channel to undam. This rate is likely dependent on a number of factors, perhaps most significantly the thickness of the snow within the dam. During the 2018/19 melt season, for example, the bare ice surface is clearly visible in the days prior to drainage (Fig. 3.12a-b), suggesting a lack of recent snowfall or wind-blown snow accumulation. Furthermore, rapid and continuous temperature increases during December 2018 (Fig. 3.11a) likely enhanced the rate of deterioration of the snow dam. Between the 25th and 28th December, the channel likely became free of a critical amount of remaining snow, enabling water to flow out from within the basin. Fresh snowfall visible in Figure 3.12c possibly occurred after the drainage had begun, which may have subsequently slowed the rate of water outflow. By contrast, during 2019/20, the ice surface was covered in snow during later December and early January (Fig. 3.13), which likely acted to block the channel until later in the melt season. Drainage in this year occurred no earlier than the 13th of January (Fig. 3.13e), with a higher peak volume likely the result of an additional 2-3 weeks during which the basin was able to accumulate meltwater.

The alternating, repeated pattern of high and low peak volumes between 2016/17 and 2019/20 (Fig. 3.11a) is possibly indicative of pre-conditioning of the drainage channel from one year to the next. The channel is visible in the same location each year, but the depth and width of the channel may have varied relative to the magnitude of volume discharge in any given year. In years where drainage occurs at a relatively low peak volume (e.g. 2016/17 and 2018/19), water flux through the channel would be relatively low, thus limiting channel incision and widening. Snowfall and wind-blown snow accumulation over winter months might fill the channel more readily. In the subsequent melt season, a shallow, snow-filled channel would enable the lake to accumulate meltwater for longer and reach a higher peak volume. Drainage in this year would consequently have a greater water flux, thus causing greater incision and widening of the channel, possibly pre-conditioning the channel for an earlier drainage event during the following year. Whilst this mechanism is one hypothesis to explain the data presented here, longer volume time series and higher resolution optical and/or elevation data would be required to test this.

The 2020/21 melt season was the only melt season that overland drainage was not observed at Lake A, and was consequently the only studied year where the lake was observed to freeze over towards the end of the melt season. Peak volume in this year was substantially lower ($< 1 \times 10^5 \, \text{m}^3$; Fig. 3.11a), consistent with low meltwater area across the Amery region as a whole (Chapter 4, Fig. 4.11). The lack of drainage in this year suggests that the lake never acquired enough meltwater to overflow into the channel, regardless of whether the channel was clear of a dam. In any individual melt season, peak volume for Lake A appears to depend on both meltwater supply and the time taken for the channel to undam, which triggers over-ice drainage. Figure 3.14 shows how through early February 2021, the surface of Lake A partially froze over, unfroze again, before completely refreezing and becoming snow-covered by 21st February. The freezing of the lake surface was the consequence of a sharp drop in surface temperature between 5th and 10th February (Fig. 3.11a). Figure 3.11a highlights how a lake freezing event is displayed as a rapid volume decrease in automatically generated lake volume time series. This hence makes freezing events difficult to distinguish from lake drainage events, without corresponding optical image evidence.
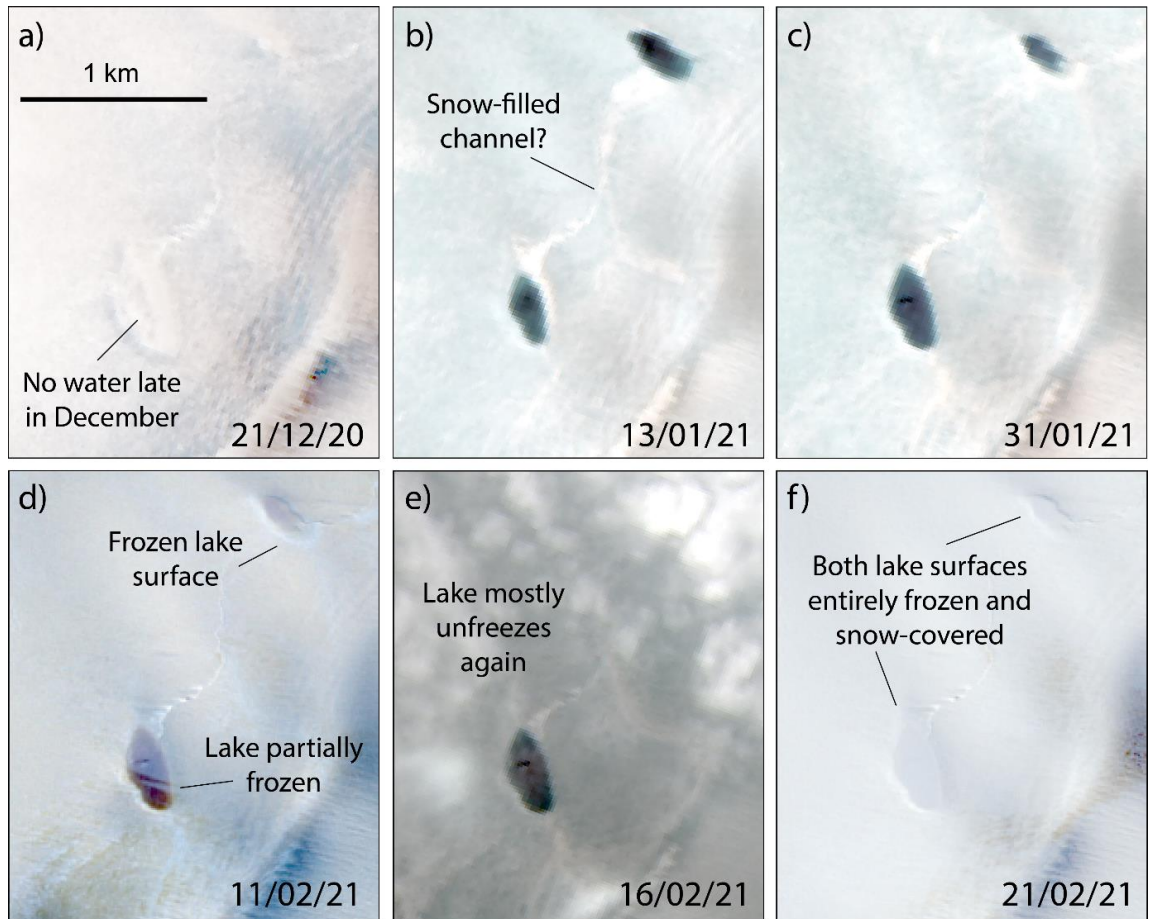
Figure 3.14. Meltwater evolution within case study area 1 between 21st December 2020 and 21st February 2021. (d) and (f) display Sentinel-2 images, whilst the other four tiles show Landsat 8 images. Note how there is substantially less water in Lake A compared to other melt seasons, and how the lake surface freezes over between the 16th and 21st February 2021 (e-f).

3.4.2.2 Vertical lake drainage events

Analyses of case study area 1 (Section 3.4.2.1) reveals various lake evolution processes, but Lake A was not observed to drain vertically during any of the studied melt seasons. Therefore, I conducted a wider search of the study region (Fig. 3.1) for evidence of vertical lake drainage events. Vertical lake drainage events are harder to visually identify from medium resolution optical satellite imagery than cases of over-ice drainage. Vertical drainage pathways (moulins) are often undetectable from 10-15 m resolution optical images, and, unlike lateral drainage events, it is not possible to trace the routing of water. Manual identification of vertical drainage events, in the absence of field measurements or enhanced resolution remote sensing images (e.g. 2 m Worldview data or Reference

Elevation Model of Antarctica (REMA) elevation data), is largely based on the disappearance of water from a lake basin without coincident evidence for alternative mechanisms of volume loss.

No definitive examples of vertical lake drainage were identified from visual analysis of lakes in the study region, with the exception of the lake analysed by Trusel et al. (2022) (Lake 182; Fig. 3.15). Lake 182, which lies directly above the grounding line, lost 8.6 x 10^6 m^3 of water within seven days between 14th and 21st January 2018 (Fig. 3.15f), equivalent to the volume of 346 Olympic sized swimming pools. Similar magnitudes of volume loss were observed from the lake in other years. As shown in Figure 3.15, connected neighbouring lakes did not have coincident increases in volume during this period. Additionally, satellite images clearly show that the decrease in lake volume was real, and not due to the lake freezing over. A large crack in the centre of the basin is observed following the removal of the lake water, indicating that the water drained vertically downwards (Fig. 3.15c). The magnitude of volume loss and size of the basin makes it easy to identify this as a vertical drainage event, but diagnosing drainage style for smaller lake basins is more challenging.
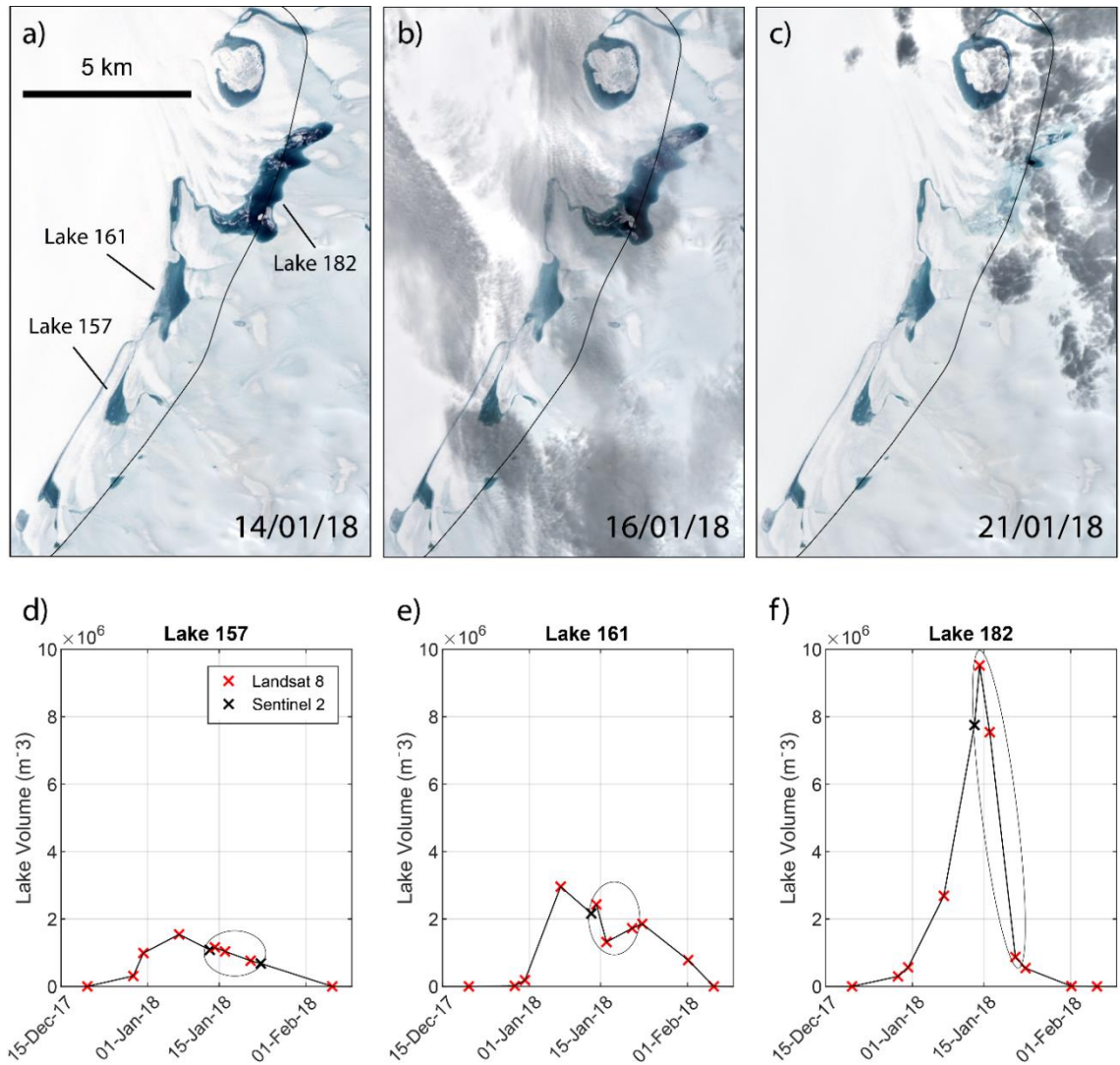
Figure 3.15. (a-c) Landsat 8 images showing the evolution of three lakes (numbered 157, 161 and 182) between 14th and 21st January 2018. Note how lake 182 drains, seemingly vertically rather than laterally, between images (b) and (c), whilst lakes 157 and 161 display minimal volume change over the same time period. The black line shows the grounding line position (Depoorter et al., 2013). (d-f) Lake volume time series for the same three lakes, spanning 15th December 2017 - 5th February 2018. The circled areas indicate the three data points (red crosses) representing the dates of the three images in (a-c). The location of the lakes are shown in Figure 3.8.

3.4.2.3 Identifying mechanisms of volume change

My method for automatically generating lake volume time series (Section 3.3.3) enables quantification of water volume change within any given lake. As highlighted by manual

and automated analysis, there can be several explanations for apparent increases or decreases in lake volume, and analysis of a single automatically generated lake volume time series cannot necessarily indicate the processes responsible. The partial, or complete, freezing and unfreezing of a lake surface (Fig. 3.14c,g) is particularly challenging to account for when interpreting lake volume time series. Whilst manual inspection of optical imagery can provide insight into causes of volumetric changes, it is also useful to consider how automated techniques could be used to characterise different evolution processes (Fig. 3.1) in lake volume time series.

Analyses from case study areas 1 and 2 highlight how the most rapid lake volume losses are associated with lateral, and very occasionally vertical, drainage events (excluding apparent volume losses due to lakes freezing over). To explore whether I could automatically identify such drainage events, I compared volume changes between lakes across the study area. Drainage events are controlled by a physical mechanism (i.e. water evacuation via a vertical or lateral channel) dependent on the specific geometry of an individual lake basin, and would therefore not be expected to occur at the same time for multiple lakes. The freezing of lake surfaces, however, is more likely to occur simultaneously across multiple lake basins due to a region-wide reduction in surface temperature. To try and separate these processes, I calculated the date at which lake volume dropped below 20% of its maximum seasonal volume, after reaching peak volume, for all 215 study lakes of the 2017/18 melt season. I then plotted the time taken for each lake to transition from peak volume to this 'critical lower volume', to observe temporal patterns of volume loss (Fig. 3.16a). However, a key limitation of this approach is the limited temporal resolution of data, and it should be noted that the dates of peak and 'post-drainage' volume are limited to dates where cloud-free satellite data were available.
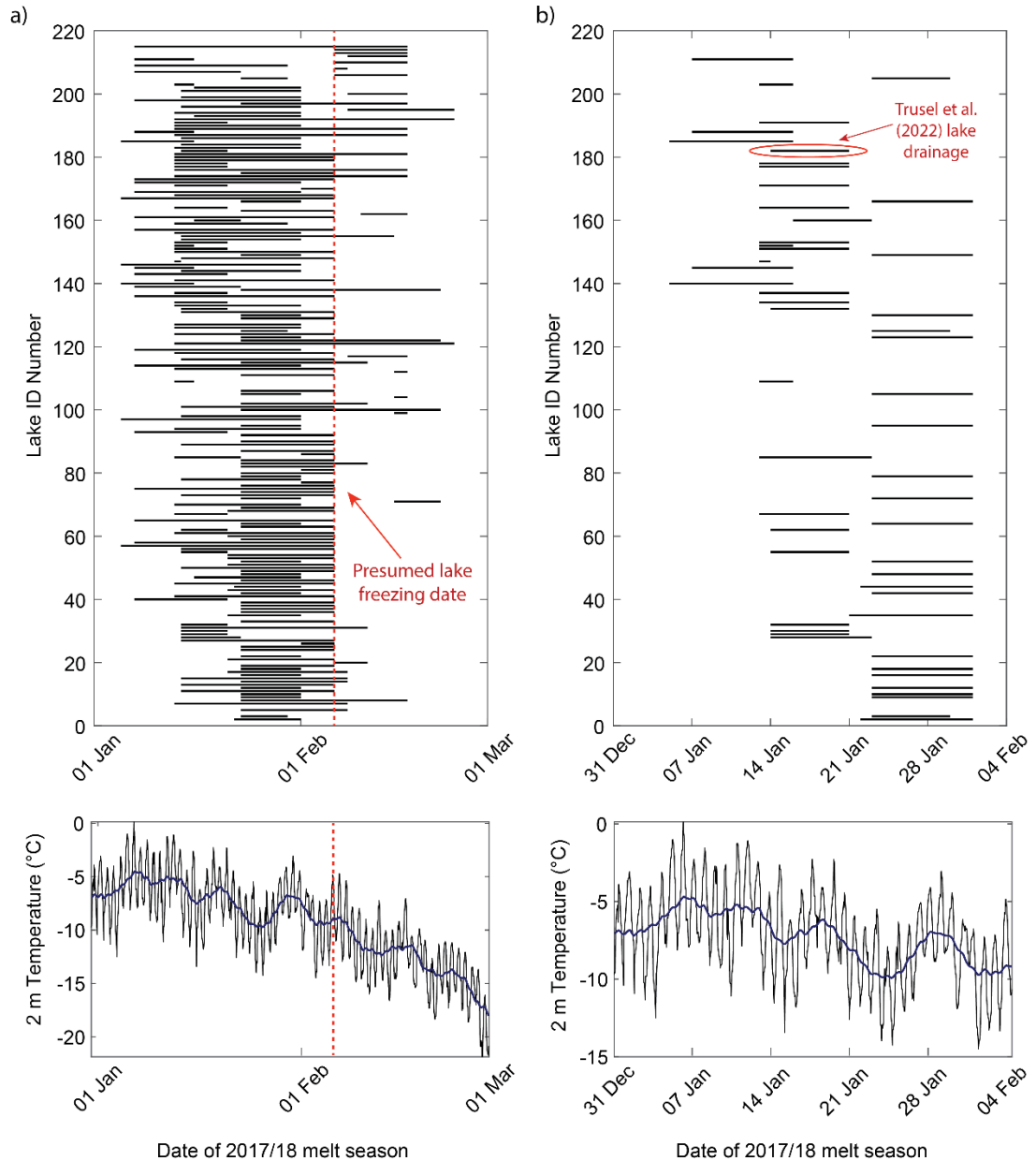
Figure 3.16. (a) The timing and rate of volume losses for all 215 study lakes during the 2017/18 melt season. For each lake, the start of the black bar indicates the date of peak volume, whilst the bar ends at the subsequent date at which lake volume drops below 20% of peak volume. The length of each bar hence signifies the rate of volume loss. It should be noted that this represents a maximum drainage period due to the resolution of the data. The vertical dashed red line signifies the presumed date (6th February) of widespread lake freezing. (b) A filtered version of the dataset shown in (a), only displaying lakes that dropped below 20% of peak volume before 6th February, and which lost 80% of volume in less than 14 days. Hourly ERA 2 m temperature data, averaged across the study region, are displayed below (a) and (b) for comparison. The blue lines show a 4-day moving mean of the hourly temperature data.

To remove instances of suspected lake surface freezing events, I assumed that the most common date that lakes reached 'low volume' was when lakes started to freeze over. This occurred on the 6th February during the 2017/18 melt season, when 69 lakes dropped below 20% of peak volume (Fig. 3.16). Comparison with ERA 2 m temperature data shows that the mean daily temperature across the study region on this date was around -10 °C, with a maximum daytime high of -5 °C. This is a lower temperature than might be expected for the widespread freezing of lakes surface to occur, and is possibly a reflection that ERA model resolution is not able to resolve surface temperature to a high level of accuracy. It is also possible that liquid water in the Amery region is able to exist at lower surface temperature thresholds due to other climatological and glaciological conditions (van Wessem et al., 2023). The continuous decline in surface temperature beyond the 6th February means it is unlikely that lake surfaces unfroze again after this date.

I assumed that volume losses from lakes which reached low volume on or after 6th February were primarily due to lake surface freezing, and that these lakes did not experience substantial drainage. I additionally removed lakes that took more than 14 days to lose 80% of seasonal peak volume, since I was most interested in identifying lakes that drained relatively quickly. Studies from the GrIS have typically used much lower temporal thresholds, typically two to six days (Selmes et al., 2013; Fitzpatrick et al., 2014; Williamson et al., 2017), for classifying 'rapid lake drainage events'. However, these studies have specifically focussed on hydrofracture induced vertical drainage events in an environment known to facilitate rapid drainage over very short timescales (Das et al., 2008; Tedesco et al., 2013). Since such processes are not thought to be common in Antarctica, my aim was not to automatically detect rapid vertical drainage events, but rather to highlight a subset of lakes that drain relatively quickly and could warrant further investigation. The potential for lakes to drain vertically on hourly time scales (Das et al., 2008; Doyle et al., 2013) means it is not possible to separate these events from slower drainage mechanisms using Landsat/Sentinel data. I hence chose a relatively low temporal threshold of 14 days to account for variability in satellite coverage and visibility, and to allow for variable rates of drainage. Application of these filtering stages reduced the dataset from 215 to 53 lakes (Fig 3.16b). Of these 53 lakes, an average (mean) of eight days was taken to lose >80% of seasonal maximum volume.

As shown in Figure 3.16b, large numbers of lakes lost 80% of their peak volume in the same number of days, and there were only a few dates associated with peak or low

volumes. This is a reflection of specific dates where cloud-free optical images were available, making it impossible to constrain the true timings and duration of drainage events. Therefore, it was at this stage of my methodological approach that I explored how I could increase the temporal resolution of volume data.

3.4.3 Exploring methods to increase the temporal resolution of lake volume time series

Remote sensing of the evolution of supraglacial lakes typically involves a trade-off between high spatial or temporal image resolution, with any individual satellite typically unable to offer both benefits (Section 1.2.1.1). Results from Sections 3.4.1 and 3.4.2 demonstrate the success of automatically generating lake volume time series from Landsat and Sentinel optical data, but constraining the timeframes over which lake volume changes occur is limited by relatively long time (typically 3-7 days) gaps between repeat imagery. The dual use of Landsat 8 and Sentinel-2 imagery aids in this regard, but Sentinel-2 image repeat times in the region are low, with Landsat providing the majority (>90% on average) of volume data for any given melt season (e.g. Fig. 3.12). Increasing the temporal resolution of time series therefore requires incorporation of data from additional satellites.

One potential future option is to use radar data, in addition to optical data, to fill in some of the gaps in lake volume time series. SAR imagery has successfully been used to detect Antarctic surface meltwater (Luckman et al., 2014; Kuipers Munneke et al., 2018; Dirscherl et al., 2021), and the potential for combining SAR and optical data has been demonstrated for mapping meltwater area change (Miles et al., 2017; Dirscherl et al., 2021). However, lake depth estimates have not yet been made from SAR data. Manual analysis of radar images can occasionally aid with constraining the timing of lake changes, but surface meltwater is significantly harder to visually detect in radar images compared to optical products (Fig. 3.17). Figure 3.17b shows how there can be high variability in backscatter from surface meltwater (which is clearly distinguishable in a Landsat 8 image from the same day; Fig. 3.17a). Some lakes have backscatter values of approximately -15 dB, whilst others have backscatter values close to 0 dB. Variations in backscatter can occur due to differences in surface roughness (e.g. from waves on lake surfaces), orientation relative to the satellite viewing angle, and inherent radar speckle

(Arthur et al., 2020a). Whilst radar data could aid with the generation of lake volume time series in the future, further work is first required to develop a method for retrieving lake depths from SAR imagery.
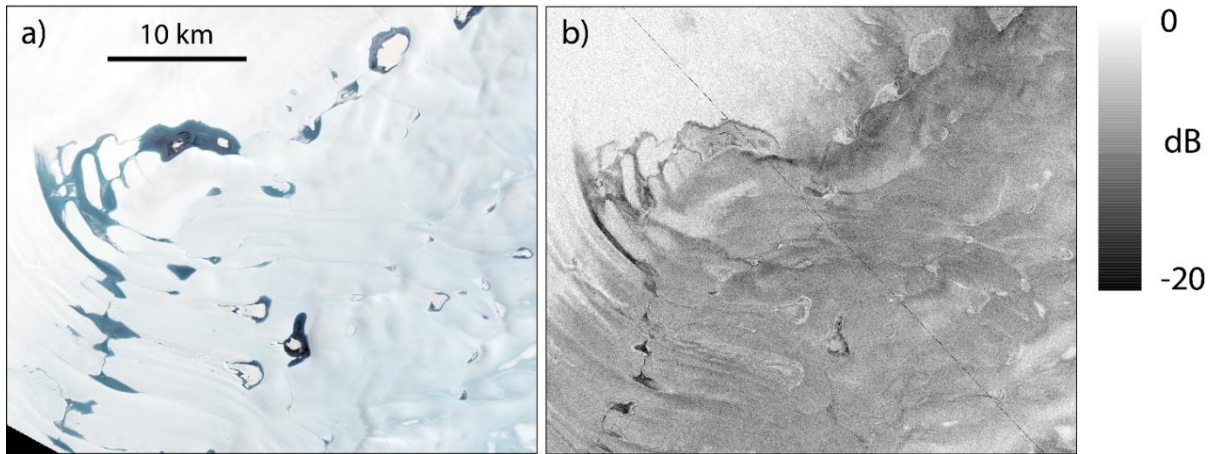
Figure 3.17. Comparison of a Landsat 8 optical image and a Sentinel-1 Ground Range Detected (GRD) radar image over case study area 2. Both images were taken on 3rd February 2017. Note how meltwater is much easier to manually distinguish in (a), and how there is large variability in decibel values for meltwater covered areas in (b). This has the effect of some lakes appearing bright (near 0 dB), whilst others are dark (closer to -20 dB) on the image.

Incorporation of additional optical satellite data therefore offers the simplest and most reliable way to increase temporal coverage of lake volume estimates. Other high spatial resolution optical satellites, such as Planet or Worldview, could be used to further increase the chances of lake data being available on any given day. However, data from these satellites are not currently fully open access, limiting their use by the scientific community. Studies of supraglacial lakes from Greenland have hence typically used MODIS satellite data for assessing lake evolution, which compromises on spatial resolution but provides the benefit of daily satellite coverage (Section 1.2.1.1). Here, I present results and discuss the success of using MODIS data, in combination with previously generated volume data from Landsat and Sentinel data (Section 3.4.1 and 3.4.2), to create near-daily lake volume time series.

3.4.3.1 MODIS lake volume time series

Comparison of Landsat/Sentinel and MODIS proxy data show statistically significant relationships ($p < 0.01$) for 85 of the 215 study lakes (Fig. 3.18). MODIS derived volume time series were generated for these 85 lakes, whilst the remaining 130 lakes were discarded due to the lack of close agreement between the two datasets (Section 3.3.4.2). In general, statistically significant relationships were more common for larger lakes. The median outline area for lakes with a significant relationship was 1.36 km^2, compared to 0.93 km^2 for lakes which did not reach the 0.01 p-value threshold. Lakes smaller than 0.6 km^2 in area consistently showed poor association between the datasets, with only five of 32 lakes of this size displaying significant relationships. Of lakes greater than 2 km^2 (50 lakes), 26 had a significant relationship between MODIS and Landsat/Sentinel data. The coarse pixel size of MODIS data (500 m) likely explains this broad pattern. The smallest lake outlines (minimum size 0.5 km^2) are typically only covered by two MODIS pixels, whereas a lake outline greater than 2 km^2 is covered by at least eight pixels. Larger lakes therefore have more pixel values from which to calculate median reflectance, thus reducing chances of error. However, the lack of significant relationships for several of the largest lakes demonstrates the limitation of using low spatial resolution data, and highlights the importance of only generating MODIS volume time series for lakes that closely match the Landsat/Sentinel derived data.

Lakes which demonstrated significant relationships between the two datasets showed no clear spatial pattern (Fig. 3.18). Lakes on the ice shelf had significant relationships more frequently than lakes on grounded ice, but this is likely because ice shelf lakes are large compared to the more confined lake basins that typically exist on grounded ice. Since MODIS proxy values are based on the relative reflectivity difference between a lake outline and its buffer, it might have been expected that isolated lakes (where the lake buffer is not partially cut into by a closely neighbouring lake outline) would be more likely to be significant than tightly clustered lakes. However, I observed no such pattern. Several tightly clustered lakes on the ice shelf display a significant relationship, and the majority of widely spaced lakes have p-values greater than 0.01 (Fig. 3.18). This suggests that a buffer size of 1 km is sufficient for acquiring water-free reflectance values, even in instances where the buffer is partially removed due to an overlapping lake outline, and that lake size is the more crucial factor for determining statistical significance.
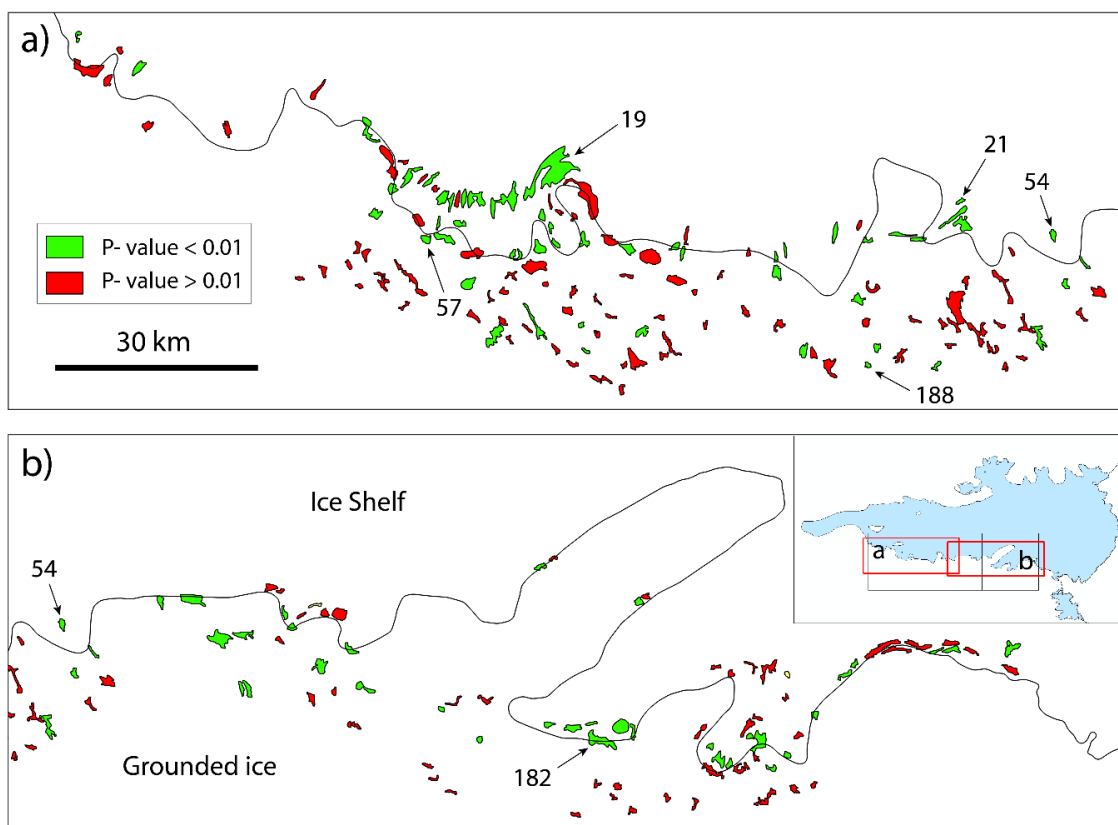
Figure 3.18. Study lakes that displayed a statistically significant (p < 0.01) relationship between MODIS and Landsat/Sentinel data (green), and those that did not (red). The areas covered in (a) and (b) are displayed in the inset. Lake ID numbers are displayed for the relevant lake volume time series shown in Figure 3.19.

For the 85 lakes for which lake volume time series were generated (Section 3.3.4.2), MODIS data show strong potential for improving temporal constraints on volume changes. For the majority of lakes, MODIS derived lake volume estimates closely matched the magnitude and temporal patterns of Landsat/Sentinel data, despite a relatively high amount of noise in the data (e.g. Fig. 3.19e-f). In several instances, MODIS data reveal rapid volume decreases occurring over 2-4 days, which had previously been poorly constrained by the low temporal resolution of Landsat/Sentinel data. For example, Landsat/Sentinel time series for lake 21 shows a large reduction (9.8×10^5 m^3) in lake volume between 21st January and 6th February 2018 (Fig. 3.19a), but a lack of data between these dates make the rate of volume loss highly uncertain. MODIS data reveal that this volume loss occurred over just two days, with a peak volume of 12.4×10^5 m^3 on 22nd January dropping to 9.4×10^5 m^3 and 0.6×10^5 m^3 respectively on the following

two days. MODIS data subsequently show only minor variations in volume following the sharp volume decrease, providing confidence in the validity of the result. A similar example is shown for Lake 54, where MODIS data reveal that 81% of peak volume was lost over three days between $21^{st} - 24^{th}$ January 2018 (Fig. 3.19b). However, the coarse resolution of MODIS data make the mechanism of volume loss difficult to identify from manual image analysis. The close proximity of both lakes to the grounding line (Fig. 3.18) makes tidally induced hydrofracture a plausible explanation (Trusel et al., 2022), whilst it is also possible that the volume loss was the result of over-ice drainage. MODIS data successfully capture the vertical drainage event of Lake 182 (Fig. 3.15) and shows very close association with the Landsat/Sentinel data (Fig. 3.19c), providing further confidence in the method.
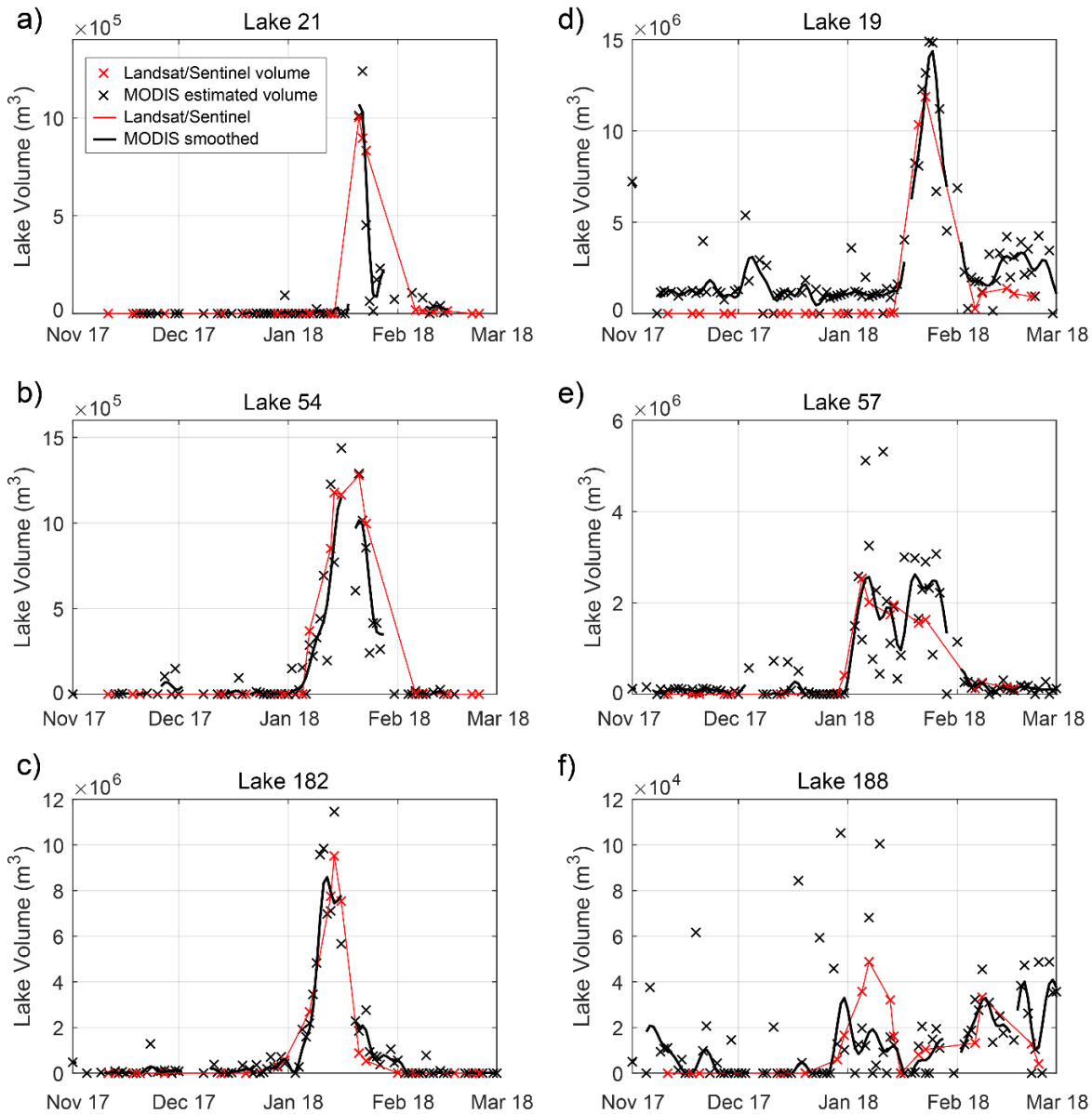
Figure 3.19. (a-d) Examples of lake time series where MODIS data show close agreement with Landsat/Sentinel volume data, and successfully help to constrain rates of volume change. MODIS volume data in (d) are consistently higher than the Landsat/Sentinel results, but still help to constrain the rate of drainage. (e-f) Examples of lakes where the MODIS method performed less well. These time series display lots of noise in the MODIS data and show no consistent pattern of volume change.

Whilst these examples show instances of successful method performance, MODIS data were not always accurate in matching lake volume estimates derived from Landsat/Sentinel imagery. Time series for Lake 19, for example, shows MODIS proxy

volumes that are consistently around 1 x 10^6 m^3 greater than those measured by Landsat/Sentinel (Fig. 3.19d). This is likely due to a shortage of non-zero Landsat/Sentinel data points upon which the linear relationship was based, including a set of four consecutive volume values of around 1 x 10^6 m^3 which likely skewed calibration of the relationship (Fig. 3.19d). A threshold number for 'high' volume estimates could hence be incorporated into the method to remove such examples. In other instances, there was too much noise in the MODIS data to be able to discern meaningful patterns of volume change. In Figure 3.19e, for example, there is close agreement between the two datasets regarding the timing of Lake 57 containing liquid water, but MODIS volumes are too variable to have any confidence in the data. Similarly, Lake 188 shows a high range of MODIS volume estimates early in the melt season, when Landsat/Sentinel data consistently show that the lake basin was empty (Fig. 3.19f). This demonstrates how high confidence can only be attributed to MODIS lake volume data that consistently match the magnitudes and rates of change of the Landsat/Sentinel data. Lakes that show relatively poor agreement, or where there are repeated large volume changes over a short space of time, are less trustworthy. My method hence shows strong potential for increasing process understanding of lake evolution, but further testing and verification are required before scaling up of the method could be achieved.

3.5 Conclusions

In this chapter, I have built upon previous work to develop novel methods to explore the evolution of supraglacial lakes across the grounding zone of the Amery Ice Shelf. Analysis of automatically generated lake volume time series, combined with manual analysis of optical satellite images, reveal the timescales over which lakes can gain or lose volume via various mechanisms. Gradual increases in volume occur via steady catchment infill and melt-albedo enhanced basin melting, whilst the freezing and unfreezing of a lake surface can result in sudden apparent changes in lake volume, complicating the interpretation of volume time series. More rapid volume losses can occur from lateral drainage events, whereby large volumes of meltwater are transferred between lakes via connecting meltwater channels. Lakes on grounded ice typically fill earlier in the melt season, with water subsequently flowing downslope onto the ice shelf, forming large interconnected meltwater networks. Rapid drainage events, either due to

lateral or hydrofracture-induced vertical drainage, are shown to occur over less than two days for some lakes. The majority of lake drainage events occur laterally across the ice surface, with only one instance of vertical drainage confirmed. However, vertical drainage events are harder to detect, and further instances (possibly including some of the large volume changes detected by MODIS) cannot be ruled out based on the available data.

The methods presented in this chapter represent a step forward in our ability to automatically assess lake volume changes over seasonal and multiannual timescales. By implementing the methods in GEE, there is potential to scale up lake volume analysis to larger spatial and finer temporal scales, although further method refinement would be required to achieve this. Results highlight the importance of using high temporal resolution data to investigate the evolution of supraglacial lakes, since lake drainage events can occur over daily or potentially even sub-daily timescales. The use of MODIS reflectance data, combined with volume estimates derived from higher spatial resolution optical satellites, show strong potential for constraining the timing of lake volume changes. Careful interpretation of data is required, however, and manual inspection of satellite images will likely always be required for informing process understanding and for validating automatically generated results.

This chapter has addressed Objective 5, and concludes the method development sections of the thesis. It additionally brings to a close my regionally focused analysis of the Amery Ice Shelf. A wider discussion of my findings, including assessment of the contribution of methods presented in Chapters 2 and 3 to the scientific community, are presented in Chapter 5. In the next chapter (4), I scale up my analysis of Antarctic surface meltwater to a continent-wide scale. The methods developed in this chapter are not yet suitable for Antarctic-wide application, but the meltwater area mapping method presented in Chapter 2 shows strong potential for large scale application. In Chapter 4, I hence apply this method across Antarctica to generate the first continent-wide meltwater area dataset.

CHAPTER 4

Continent-scale mapping of Antarctic surface meltwater

4.1 Introduction

Surface meltwater has the potential to influence a range of ice dynamic and surface mass balance processes (Section 1.2.3). Assessment of the distribution and evolution of surface meltwater at an Antarctic-wide scale is therefore important to predict what impacts it may have in the future (Arthur et al., 2020). Despite a recent surge in Antarctic surface meltwater research (Section 1.2.2), quantifying surface meltwater area at a high temporal resolution and at a pan-Antarctic scale has yet to be achieved (Arthur et al., 2020; Moussavi et al., 2020). Previous studies have been limited in temporal or spatial scope, primarily due to computational limitations, whilst time series of meltwater area based on optical satellite data have been hindered by uncertainty introduced by cloud cover and image extent (Section 1.2.2). In Chapter 2, I present a method for mapping surface meltwater which overcomes these challenges. Results from the Amery Ice Shelf region demonstrate the success of applying the method at a regional scale (Section 2.4), and highlight the potential for application at larger spatial scales. Furthermore, I demonstrate how the production of robust, continuous meltwater area time series enables comparison with modes of climate variability to assess their influence on meltwater ponding (Section 2.4.4). The work in Chapter 2 focussed solely on the Amery region. At an Antarctic-wide scale, understanding links between meltwater and large-scale atmospheric circulations is important for predicting how future changes in meltwater area may vary regionally under different climate scenarios.

In this chapter, I apply my meltwater mapping method (Section 2.3) across Antarctica to produce the first long-term, continent-wide, surface meltwater area dataset (Objective 3). By conducting mapping within GEE, I am able to conduct rapid processing over spatial and temporal scales that would have otherwise been unachievable. I generate monthly meltwater area data from 2006 - 2021, enabling me to assess seasonal and interannual variability and long-term trends in meltwater coverage. I present results showing the spatial distribution of meltwater on ice shelves and grounded ice around the continent, and identify locations where meltwater accumulates most frequently throughout my study

period. I compare my surface meltwater results with three modes of Antarctic climate variability to evaluate the extent to which changes in large-scale atmospheric conditions influence surface meltwater ponding on an annual basis (Objective 4).

4.2 Methods

4.2.1 Surface meltwater mapping

Full details of the surface meltwater mapping method are described in Chapter 2. Here, I provide a brief recap of the method, and describe its application at a continent-wide scale.

Surface meltwater, ice, rock and cloud were automatically detected from Landsat 7 and 8 optical satellite imagery using a band-thresholding technique (Moussavi et al., 2020) . Cloud and rock areas were masked from image tiles, and an ice-specific version of the normalised difference water index (NDWI$_{ice}$; Eq. 2.2) was subsequently used to delineate areas of surface meltwater. Mapping was undertaken in GEE, using Landsat Level-1 Tier-2 top-of-atmosphere images stored in the GEE data catalogue. Surface meltwater was mapped monthly between 2006 and 2021. Prior to 2006, image coverage was insufficient to generate comprehensive continent-wide data. The mapping procedure incorporated a robust method for assessing image visibility (Section 2.3.3), enabling me to quantify variability in image coverage and cloud cover. Using this approach, I estimated the maximum area of surface meltwater that would be expected under cloud-free conditions, in addition to the observed mapped values (Fig. 2.3). I mapped both monthly and annual (June – June to cover the melt season) maximum extent of surface meltwater, for ease of comparison with climate datasets.

A total area of ~12.32 million km^2 (~87% of the whole continent; Section 1.2.1) was covered during surface meltwater mapping, including both the grounded ice sheet and surrounding ice shelves. Every Landsat image covering this study area between 2006 and 2021 was utilised during analysis, totalling 133,497 image tiles. My mapping procedure involved automatically looping through an Antarctic-wide grid of 1151 region of interest (ROI) shapefile tiles, ordinarily 108 x 108 km in area (Fig. 4.1). This tile size maximized spatial coverage for mapping, whilst remaining within the memory capacity of an individual task within GEE. Landsat image coverage does not extend to latitudes greater

than approximately 85° south, hence this area (~ 1.28 million km^2) was not mapped (Fig. 4.1). However, given the high elevation and very low temperature of the region around the South Pole, little meltwater ever exists at this location. The grid was clipped to the Antarctic coastline (Depoorter et al., 2013), meaning coastal ROI tiles varied in shape and area. Tiles were given a unique ID based on longitude and latitude for identification purposes. In instances where the coastline clipping process split a tile into multiple portions, tile segments were merged to adjacent tiles to ensure no two tiles had the same ID.
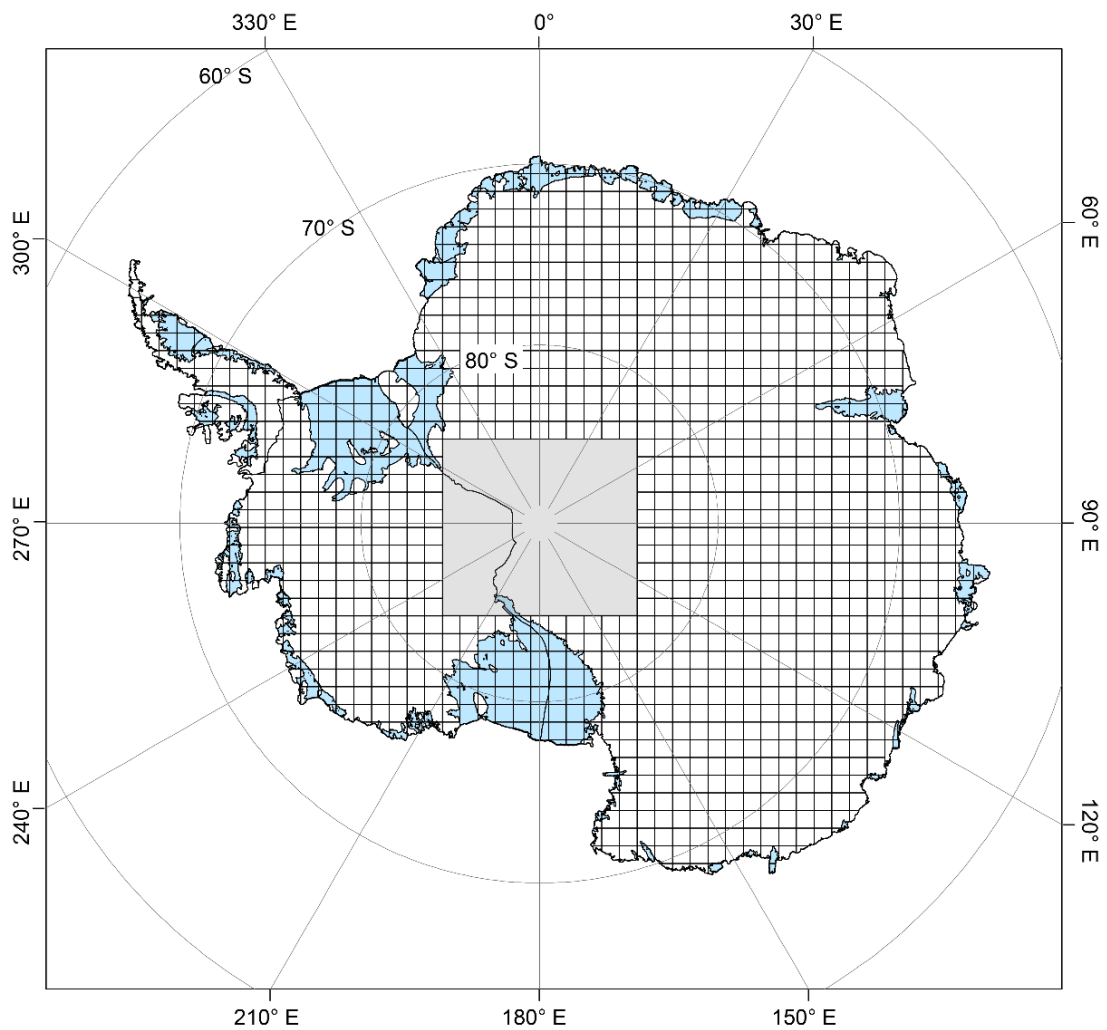
Figure 4.1. The 1151 ROI tiles over which surface meltwater was mapped, totalling 12.32 million km^2 in area. Note how surface meltwater was mapped over both grounded ice and ice shelves (blue). Coastal ROIs have been clipped to the coastline (Depoorter et al., 2013). The grey box indicates the region around the South Pole that was not mapped due to a lack of Landsat images.

Processing was performed on a yearly basis for up to ~350 ROI tiles at a time. Memory capacity and timeout limits within GEE were exceeded when attempting to process larger regions than this. Vector outputs were exported from GEE as geoJSON files, and post-processing steps were undertaken in MATLAB to clean the raw data, add selected metadata, and to produce final shapefile outputs (Section 2.3.4).

4.2.2 Surface meltwater quality control

Surface meltwater quality control was conducted to identify any artifacts within the continent-wide dataset. Shapefiles representing the annual maximum extent of surface meltwater were merged to produce a single continent-wide map. Quality control was then performed via manual inspection of this 15-year maximum extent layer, as this offered the quickest method for flagging invalid meltwater polygons. Manual inspection involved searching for polygons that: (1) existed in highly improbable locations (e.g. at high elevations in the cold interior of the ice sheet); (2) had straight or cornered edges; or (3) formed an ordered or repeated pattern. Polygons that satisfied some or all of the above criteria were highlighted for verification, and checked against the optical images from which they originated. In all cases highlighted by the above process, flagged meltwater areas were the result of artifacts in Landsat 7 imagery (Fig. 4.2), and were removed from the final dataset. In total, 699 polygons were removed during this process, totaling 9.87 km^2 of incorrectly identified meltwater area.
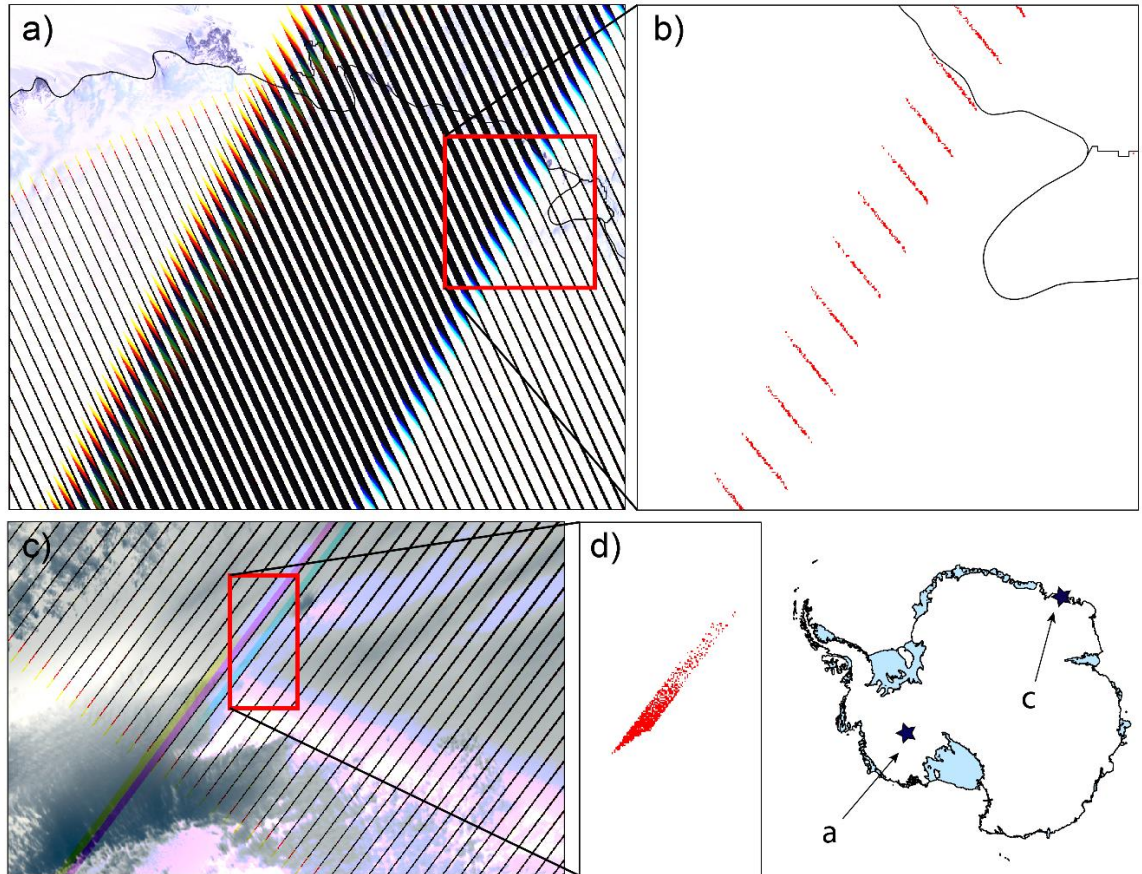
Figure 4.2. Examples of invalid surface meltwater polygons resulting from artifacts in Landsat 7 imagery. (b & d) Meltwater polygons (red) that were flagged during manual inspection. (a & c) The Landsat 7 images from which the artifacts originate; from 24th November 2006 (a) and 16th January 2010 (c) respectively. Red boxes indicate the areas shown in (b) and (d). In both examples, the meltwater polygons are clear misclassification errors associated with artificial blue colouring in the Landsat 7 images. These polygons were hence removed from the dataset.

Due to the vast spatial and temporal scale of mapping, it was not realistic to conduct systematic manual verification of each individually mapped instance of surface meltwater against its corresponding optical imagery. This lack of validation of my results means that I have not been able to attach quantitative uncertainty estimates to reported statistics. To assess the success of the thresholding approach, a sample of mapped results were visually compared against optical imagery when trialing the method in different regions of Antarctica. Overall, the thresholds were extremely effective at identifying surface meltwater across all regions of Antarctica (results of method performance are provided in Section 4.3.1). Furthermore, the thresholds applied to delineate surface meltwater,

developed by Moussavi et al. (2020), were established based on a range of spectral conditions around Antarctica. Their verification against optical imagery showed an accuracy of >95% (Moussavi et al., 2020), and their mapped outputs showed high similarity with meltwater area data produced by alternative methods (Halberstadt et al., 2020). Although my dataset may have slightly lower accuracy than Moussavi et al. (2020) due to the use of a lower feature area threshold (Section 2.3.4), visual inspection did not indicate this had caused a noticeable increase in misclassification errors. I therefore deemed the method to be sufficiently accurate for continent-wide application, without needing to adjust thresholds for different regions.

4.2.3 Time series analysis

Surface meltwater area data from November – February throughout the 15-year study period were used for trend analysis, totalling 59 timesteps (data for February 2019 were missing due to a Landsat georeferencing error). Meltwater area trends were assessed for the East and West Antarctic ice sheets, the Antarctic Peninsula (AP), and for individual ice shelves and their associated grounding zones. IMBIE (The IMBIE team, 2018) Antarctic masks were used to define ice sheet scale (EAIS, WAIS and the AP) and ice shelf regions. Grounded catchments and ice shelves were merged in ArcMap based on their ice sheet classification by IMBIE, to produce polygons for the EAIS, WAIS and the AP. 'Ice shelf regions' included the ice shelf as defined by IMBIE, plus a 20 km buffer onto grounded ice inland from the grounding line. This additional step was taken to ensure that surface meltwater in the grounding zone of an ice shelf, where it is typically most abundant (Arthur et al., 2020), was included in regional analysis. Surface meltwater area data for any given region were de-seasonalised by subtracting the 15-year average for each month from the corresponding month in the raw data. A Mann-Kendall test was then used to determine the statistical significance of any trend. Standardised Z-scores of annual surface meltwater area totals were additionally calculated in MATLAB, enabling quantification of surface meltwater area for individual years relative to the study period mean. Z-scores were calculated for the same regions as used in the trend analysis.

4.2.4 Comparison with climate data

Datasets for three modes of Antarctic climate variability were compared against my surface meltwater area data: 1) The Southern Annular Mode (SAM) Index, from the observation-based index following Marshall, 2003; 2) The Oceanic Nino Index, one measure for the El Nino-Southern Oscillation (ENSO), from the National Oceanic and Atmospheric Administration; (3) Amundsen Sea Low Indices (ASL) of 'Relative Central Pressure' and 'ASL Longitude', following Hosking et al., 2016. For all the datasets, monthly index values for December, January and February were averaged to generate single, austral summer values. Times series for each index are shown in Figure 4.3. These 'annual' values were then compared against the annual maximum extent of surface meltwater. Climatic and surface meltwater data were detrended prior to conducting regression analysis. Robust linear regression was used in MATLAB, which is less sensitive to outliers than standard linear regression. This enabled me to better assess the statistical relationship for each individual mode of climatic variability, without results being skewed by anomalously high or low melt years, which could have been strongly influenced via teleconnections with other climatic modes (Li et al., 2021).

I performed composite analysis (Marshall et al., 2011; Fogt & Marshall, 2020) to explore how extreme conditions (i.e. extreme high or low index values) for each atmospheric mode influence surface meltwater area. For each climatic mode, thresholds were determined to categorise subsets of 'low' and 'high' yearly values. Composite surface meltwater fields for each category were then produced by averaging the surface meltwater totals for each subset of years. Mean surface meltwater area totals were calculated on a tile-by-tile basis, using the Antarctic-wide grid used during mapping (Fig. 4.1).
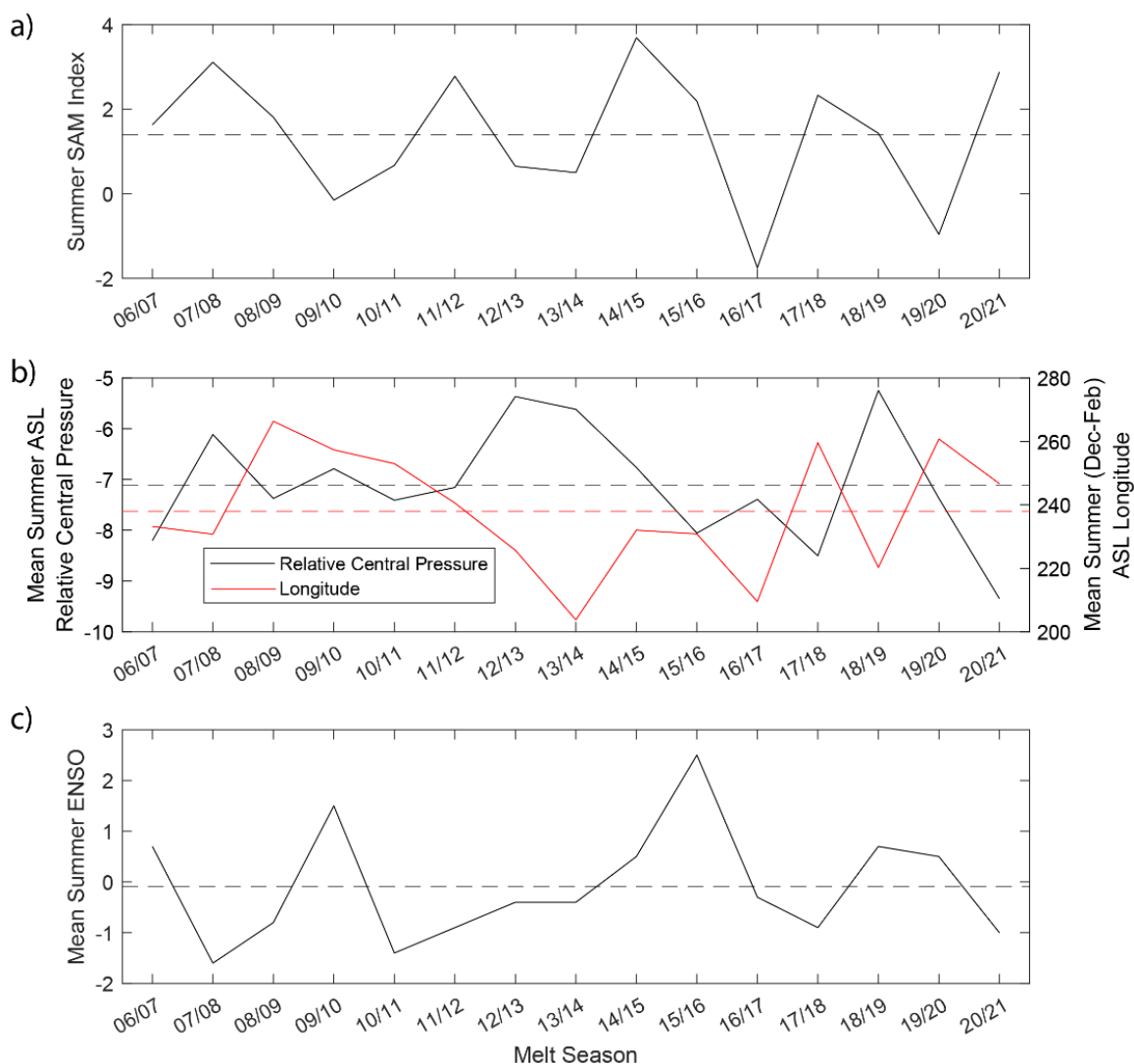
Figure 4.3. Mean austral summer (Dec-Feb) values for three climate indices, between 2006 and 2021. (a) Southern Annular Mode (SAM) Index, (b) Amundsen Sea Low (ASL) relative central pressure and longitude, (c) Oceanic Nino Index, one measure of the ENSO. The 15-year average for each index is shown by the dashed lines.

4.2.5 Positive Degree Days

To provide a first order assessment of the influence of surface air temperature on meltwater ponding, I compared my meltwater area dataset against positive degree days (PDDs). This approach assumes that air temperature is a broad proxy for surface melting, and it should be noted that multiple other climatic and surface factors that influence surface melt rates are not considered here. Monthly PDD totals were calculated using

hourly 2 m air temperature ERA5 reanalysis data to provide a measure of above-freezing air temperatures. ERA5 data has a horizontal resolution of 0.25° (approximately 31 km). Hourly values that exceeded 0 °C within any given month were summed to generate monthly total PDDs per grid cell. Region specific PDD totals were calculated on a monthly basis by summing grid cell values which fell within the regional polygons of interest. Cell values were only included if the grid cell centre intersected the regional polygon in question. To help compare regional PDD and surface meltwater area, I created a ratio measure by dividing the PDD values by the surface meltwater values. This enabled me to assess the controlling influence of PDDs on surface meltwater through time. Future work could use modelled snowmelt or runoff from a regional climate model to conduct a more comprehensive analysis of drivers of surface meltwater ponding.

4.3 Results

4.3.1 Method performance

Application of the meltwater mapping method at a continent-wide scale was highly successful, with very few manually identified misclassification errors. Unsurprisingly, no meltwater was detected for the majority of ROIs in the interior of Antarctica, providing reassurances that the thresholds do not misclassify rock, cloud or large areas of topographic shadow as surface meltwater (e.g. Fig. 4.4c-d). Visual comparison of mapped meltwater outputs against optical imagery show strong agreement across ice shelf surfaces and associated grounding zones, where meltwater is most abundant. In regions with highly variable surface characteristics (e.g. the Antarctic Peninsula, where nunataks, mountain shadow, cloud shadow and blue ice are all common), the thresholds were successful at avoiding misclassification errors, whilst still identifying surface meltwater (Fig. 4.4a-b).

Misclassification errors were most common in regions of dirty ice, variable slush presence, and in regions with highly crevassed surfaces. For example, Figure 4.4e-f demonstrates how shadows associated with deep crevasses and regions of ice shelf breakup are sometimes misclassified as surface meltwater. Although such errors were recorded in several locations around Antarctica, including on Thwaites, Recovery and Lambert glaciers, errors were spatially limited constituting individual or small clusters of pixels (typically $0.0018 - 0.0081$ km^2), rather than covering more extensive areas. As similarly demonstrated at a catchment scale (Section 2.4.1), analysis of continent-wide meltwater area results shows that the smallest (<0.0045 km^2) meltwater features only contribute ~3% to total meltwater area (Fig. 4.5 & Table 4.1; based on analysis of mapped meltwater features in January 2017). These misclassifications will hence have had a relatively small impact on regional or ice sheet scale meltwater area totals. Furthermore, some pixels classified as meltwater in crevassed areas (such as on Lambert Glacier, which flows into the Amery Ice Shelf) may be valid, as meltwater filled crevasses can be difficult to distinguish from dry crevasses and crevasse shadows in satellite imagery.
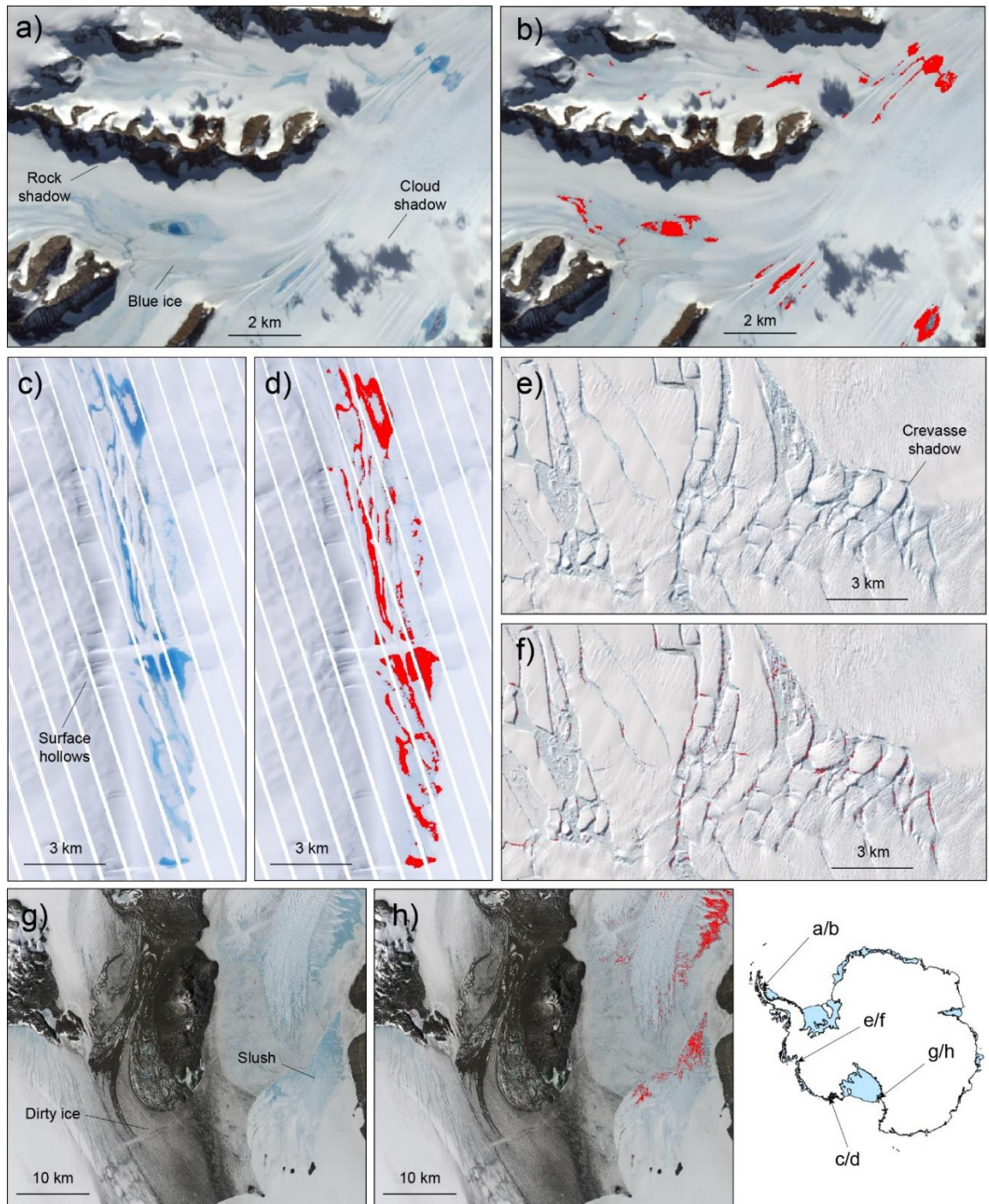
Figure 4.4. Examples of automated mapping performance for selected images with varied spectral characteristics. (a-b) Landsat 8 image of Flask Glacier on the Antarctic Peninsula, 07/02/2016. Note how surface water is successfully differentiated from areas of rock, rock shadow, ice or cloud shadow. (c-d) Landsat 7 image of meltwater ponds on Nickerson Ice Shelf, West Antarctica on 04/01/2013. Note how water is identified equally well in Landsat 7, and there are no misclassification errors with shaded surface hollows. (e-f) Landsat 8 image of the fracture zone of Thwaites Ice Shelf, 10/01/2019. There are some minor misclassification errors in areas of crevasse shadow, but these are spatially limited and will not have had a significant influence on

West Antarctic Ice Sheet area totals. (g-h) Landsat 8 image of McMurdo Ice Shelf, 02/01/2017. Note how some surface water features have been missed, but dirty ice has not been mistaken for surface water.

Table 4.1. Descriptive statistics for twenty bins of meltwater feature size, based on mapped meltwater features across the entire Antarctic continent in January 2017.

Bin Number	Bin area (km^2)	Number of meltwater features	Contribution to total area (km^2)	% of total area
1	< 0.0026	37046	46.45	1.4
2	0.0026 - 0.0044	17461	53.39	1.6
3	0.0044 - 0.0118	8101	126.98	3.9
4	0.0118 - 0.0224	5408	88.17	2.7
5	0.0224 - 0.0423	3707	113.16	3.5
6	0.0423 - 0.0799	2279	132.08	4.1
7	0.0799 - 0.1510	1501	164.02	5.1
8	0.1510 - 0.2852	914	187.17	5.8
9	0.2852 - 0.5389	524	203.02	6.3
10	0.5389 - 1.0181	269	197.71	6.1
11	1.0181 - 1.9234	182	251.58	7.8
12	1.9234 - 3.6339	94	245.94	7.6
13	3.6339 - 6.8656	52	255.06	7.9
14	6.8656 - 12.9712	16	157.94	4.9
15	12.9712 - 24.5064	8	123.81	3.8
16	24.5064 - 46.3000	5	159.34	4.9
17	46.3000 - 87.4745	2	149.90	4.6
18	165.2654 - 165.2654	0	0	0.0
19	165.2654 - 312.2356	0	0	0.0
20	> 312.2356	1	589.91	18.2
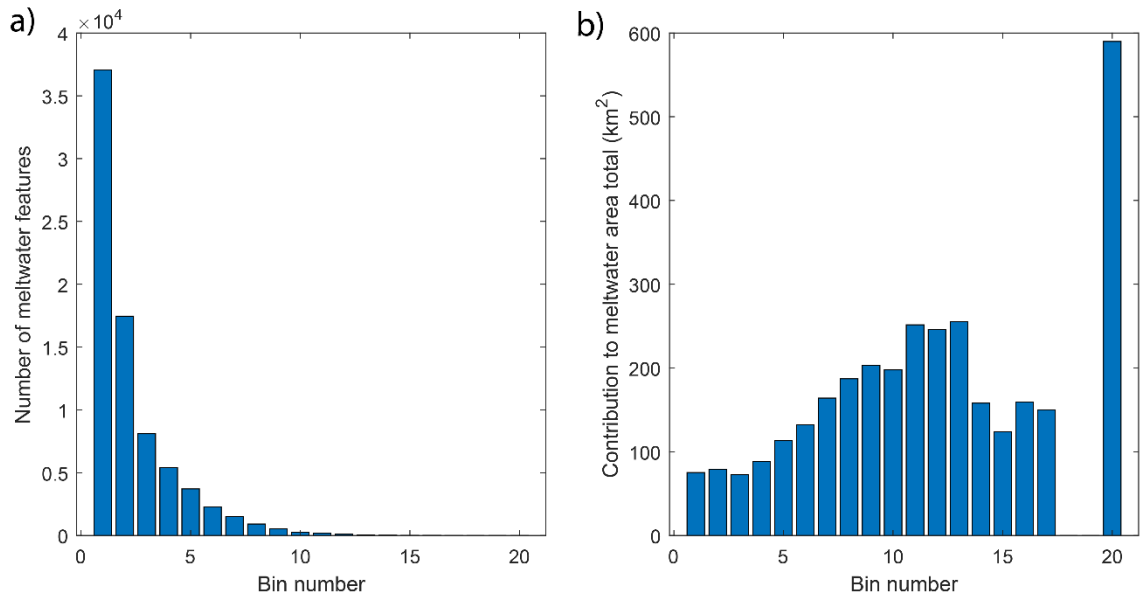
Figure 4.5. (a) The number of meltwater features mapped in January 2017 for each of the feature area bins displayed in Table 4.1. (b) The contribution (km^2) from each bin to the continent-wide meltwater area total in January 2017. Note that the large contribution from bin 20 is resultant of a single large, interconnected area of surface lakes and rivers across Roi Baudouin Ice Shelf.

The inclusion of slush (or lack thereof) within the dataset varied spatially across Antarctica. Regions of slush on ice shelves in East Antarctica, for example, were generally not identified as surface meltwater by the thresholds. However, the separation between ponded water and slush is arbitrary and the two entities lie on a spectrum of meltwater existence. Regions of variable slush presence therefore sometimes resulted in visually inconsistent results. For example, Figure 4.4g-h shows variability in the identification of slush on McMurdo Ice Shelf in East Antarctica. Slush was captured more frequently on the Antarctic Peninsula. Figure 4.6 shows large areas of slush adjacent to nunataks on an Antarctic Peninsula outlet glacier, which were identified as surface meltwater by the thresholds.
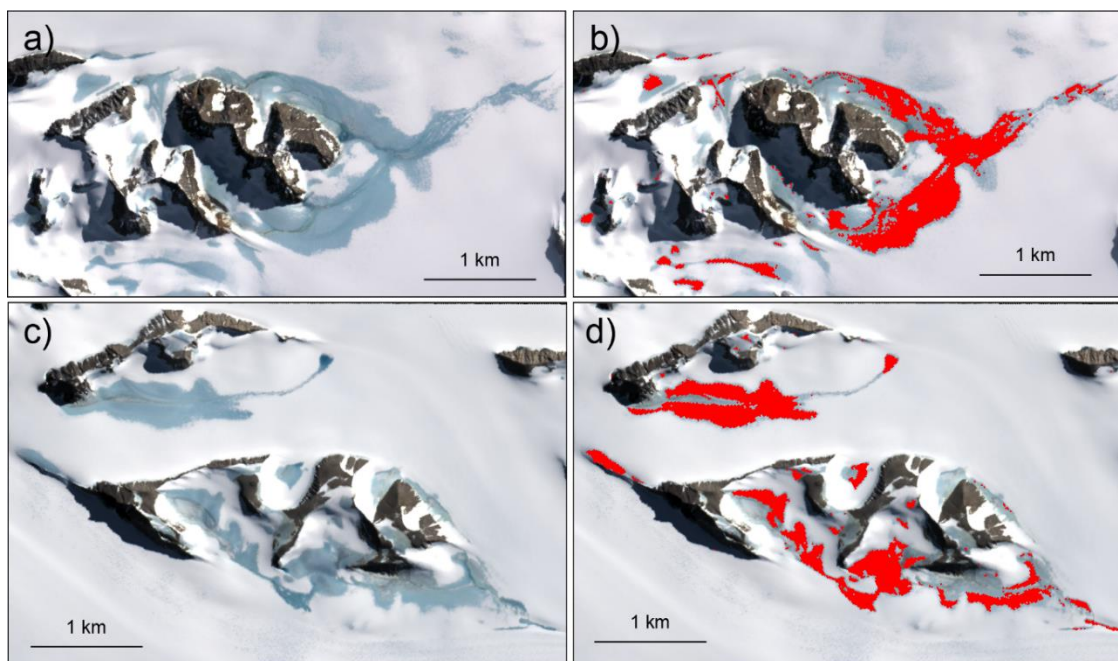
Figure 4.6. Examples of slush immediately south of Flask Glacier, Antarctic Peninsula. (a) and (c) show a Landsat 8 image from 03/03/2016. (b) and (d) highlight areas automatically identified as surface meltwater by the threshold-based method. Note how some ponded water and surface streams are visible within the wider regions of slush, and how most but not all of the slush has been captured by the method.

A key part of my surface meltwater method is the scaling up of mapped meltwater area based on image visibility assessments. Optical image visibility varies significantly across Antarctica, as shown by the IVSs generated during the mapping procedure (Section 2.3.3). IVSs are lowest at latitudes greater than ~80°S and for interior sections of the EAIS, since Landsat satellites rarely cover these regions (Fig. 4.7). The dark blue rings (displaying IVSs of <5%) around the South Pole in Figure 4.7 indicate the limit of Landsat satellite coverage. The highest IVSs occur around the margin of the EAIS, the Amundsen Bay sector of the WAIS, and the south-west AP (Fig. 4.7). ROI tiles in these regions have mean monthly IVSs of >80% (Fig. 4.7a). Northern and eastern sections of the AP typically have lower IVSs, since these regions are frequently covered by cloud. On the AP as a whole, 'high visibility' (defined as an IVS of >66%) was recorded for 36 (ROI average) from a possible 60 austral summer months (November - February) during the 15-year study period. By contrast, many regions around the coast of East Antarctica experienced 'high visibility' in more than 50 austral summer months (Fig. 4.7b). The

mean IVS across the whole study area was 59.9%, but this increases to 77.4% when only including ROI tiles where meltwater was mapped (359 tiles), and excluding low IVSs in interior regions. When splitting this second figure by ice sheet region, mean IVS was 80.3% for the EAIS, 75.1% for the WAIS and 67.5% for the AP. On average, the incorporation of image visibility scores into annual maximum area estimates resulted in an increase in estimated meltwater area of 42% for the EAIS, 49% for the WAIS and 55% for the Antarctic Peninsula.
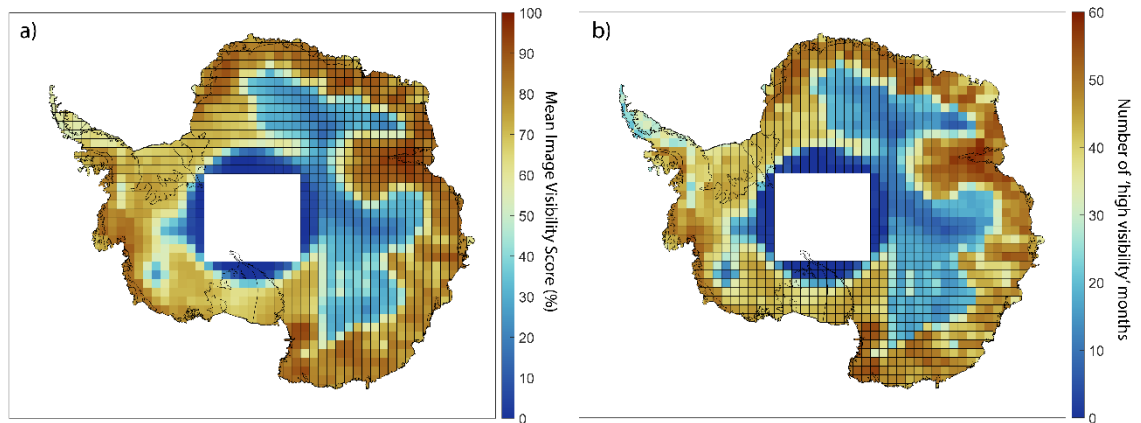
Figure 4.7. (a) Mean monthly Image Visibility Score (IVS) per ROI tile during austral summer months (Nov-Feb). (b) Number of austral summer months (Nov-Feb) between 2006 and 2021 where the visibility score is greater than 66%. A score of 60 means that an ROI tile had an IVS of greater than 66% during every austral summer month of the 15-year study period.

To check the influence of image visibility on surface meltwater mapping results, meltwater area data were compared against IVSs using a regression model. Regression analyses were performed on a monthly, tile by tile basis. Results show that across the whole of Antarctica, image visibility had minimal influence on mapped surface meltwater area. On average, only 13% of the variation in surface meltwater area was explained by IVS in the model ($R^2 = 0.13$). High R^2 values (> 0.4) were limited to single, isolated ROI tiles, and only occurred in locations with very low meltwater area totals (Fig. 4.8).
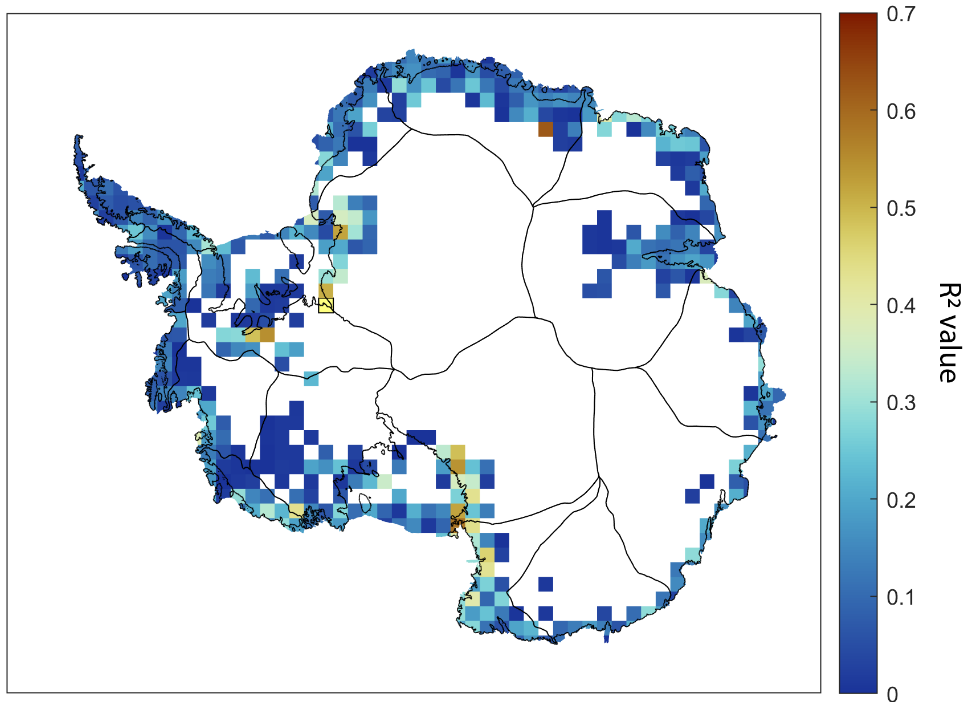
Figure 4.8. R squared values showing the influence of image visibility on maximum estimated surface meltwater area, on a tile-by-tile basis. Note how R squared values are very low across Antarctica, indicating that image visibility has not had a significant influence on surface meltwater results.

4.3.2 Distribution of Antarctic meltwater

Ice-surface meltwater systems, comprising interconnected lakes, streams and regions of slush, are observed around the majority of the Antarctic margin (Fig. 4.9). Surface water covered $3732 \pm 1547 \text{ km}^2$ (1σ) on average (mean) during each melt season, with 70% of water located on ice shelves. On the flatter topography of ice shelves, lakes are often elongate and connected by streams (e.g. Fig. 4.10b), with subtle along-flow topographic corrugations encouraging lakes to extend parallel with ice flow (Fig. 4.10d, f, h). Fewer, more isolated lakes occur in topographically confined basins on grounded ice and often reform in the same location in multiple years (Fig. 4.10). The greatest surface meltwater area was observed during the 2016/17 melt season, covering 4574 km^2 and 2218 km^2 of floating and grounded ice respectively. By contrast, during the 2011/12 melt season, surface meltwater only covered 1004 km^2 of floating ice and 516 km^2 of grounded ice.
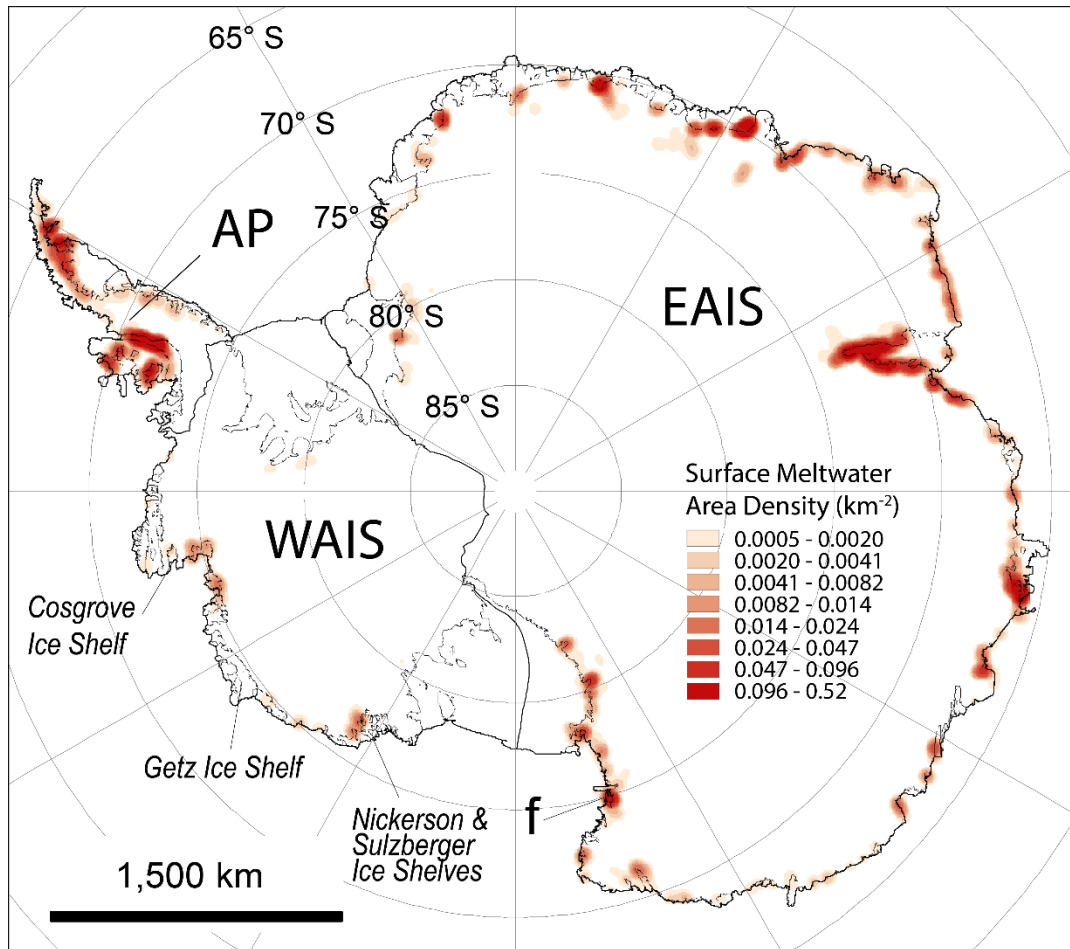
Figure 4.9. The spatial density of surface meltwater features around the Antarctic continent Antarctica. Note how the highest densities of meltwater (darker red) are found on and around ice shelves on the Antarctic Peninsula and in East Antarctica, but lower densities of meltwater are found around the majority of the periphery of the continent.
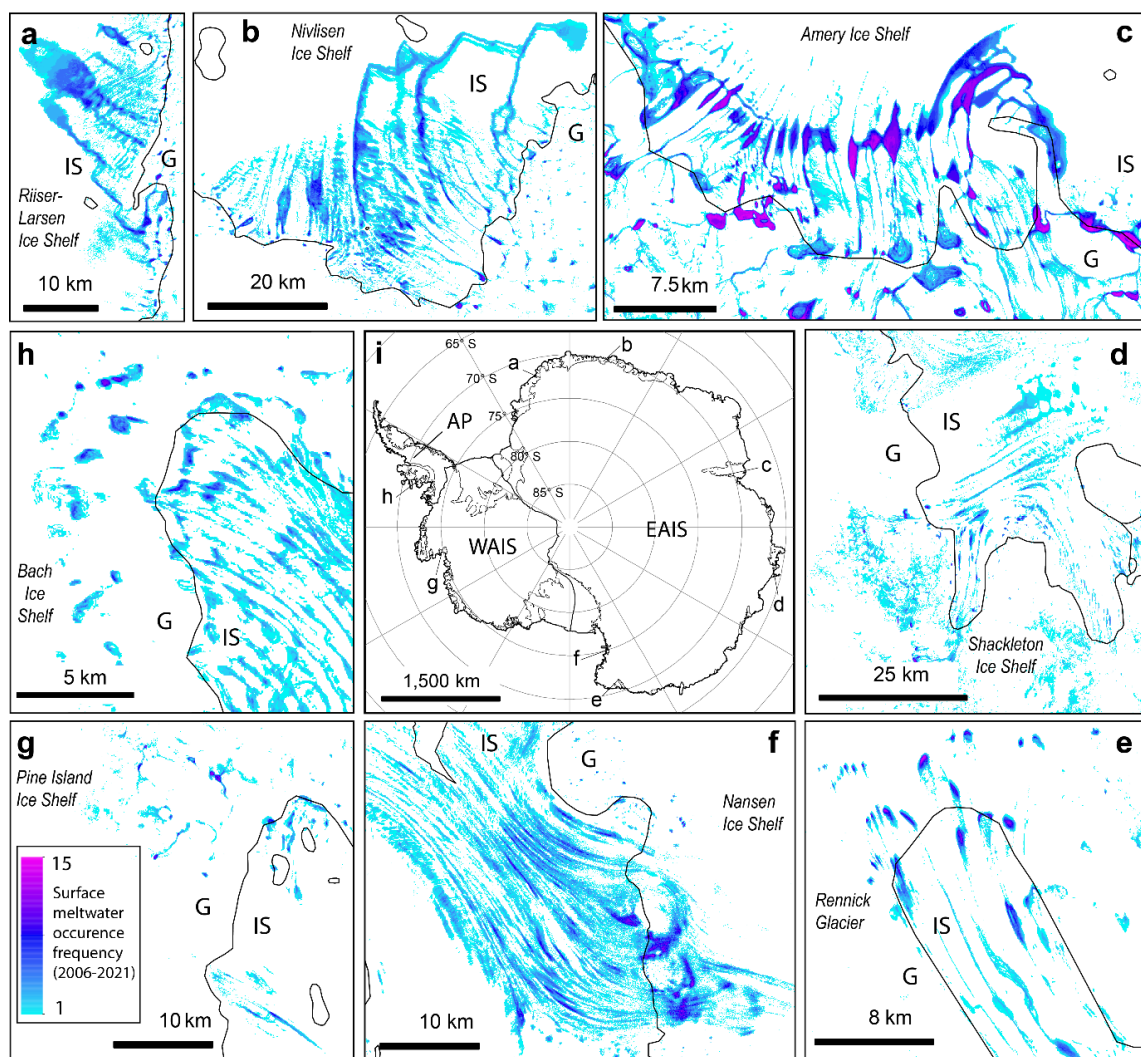
Figure 4.10. (a-h) Occurrence frequency of surface meltwater for key ice shelves and outlet glaciers. Lighter blue colours indicate meltwater presence in one or two melt seasons, whilst purple colours indicate areas covered in meltwater on a mostly annual basis. The location of each subpanel is shown in the central map (i).

The EAIS has the largest area of surface meltwater (2812 ± 1478 km^2 mean total area per melt season). EAIS-wide totals are dominated by large lakes (up to ~90 km^2) on ice shelves and their associated grounding zones, with 64% of total meltwater area situated on floating ice and 91% of water on grounded ice located within 20 km of the grounding line. Surface meltwater forms around the majority of the margin of the EAIS, but is particularly abundant on and around ice shelves in Dronning Maud Land, Wilkes Land and Victoria Land. Surface meltwater is less common on the coastline between Totten and Rennick Glaciers (Fig. 4.9). Mean annual meltwater area totals are greatest for the

Amery (1110 ± 791 km^2), Roi Baudouin (516 ± 402 km^2), Shackleton (260 ± 192 km^2) and Nivlisen (138 ± 118 km^2) ice shelf regions, although there is high variability between melt seasons (Fig 4.10). The proportion of each ice shelf covered in meltwater is nevertheless low; the highest for a single year being ~5% for Nivlisen Ice Shelf in 2007/08.

Surface meltwater in East Antarctica is predominantly clustered around the grounding line, and there is a close spatial association between meltwater and exposed bedrock. The median distance of meltwater features to the grounding line is 5.3 km, whilst the median distance to bedrock is 11.9 km. 81% of EAIS surface meltwater area lies below an elevation of 200 m, but meltwater is also found at high elevations. In the highest melt year (2016/17), 0.4% of total meltwater area existed above 1000 m elevation. The highest discovered elevation of surface meltwater (of at least 6 pixels in area to avoid potential misclassifications of small numbers of pixels) was 2320 m, located within a region of nunataks approximately 100 km south-west of Roi Baudouin Ice Shelf.

The AP hosts the second highest meltwater area (855 ± 665 km^2 per melt season), despite it being over six times smaller than the WAIS (Fig. 4.9). In northerly sections of the Peninsula (at latitudes of less than ~70°), surface meltwater is strongly confined to the eastern side of the Peninsula's mountain range, with very little surface meltwater present on the west coast. By contrast, the opposite pattern exists on the southern half of the Peninsula. Here, relatively little surface meltwater forms on the east coast, whilst large areas of surface meltwater are frequently found on the ice shelves on the south-western Peninsula. Complex meltwater networks often cover central sections of the George VI, Wilkins and Bach ice shelves in contrast to the Larsen C ice shelf where meltwater is largely confined to the grounding zone. The proportion of George VI ice shelf covered in meltwater each melt season (>2% median, maximum of ~6% during 2019/20) is larger than any other ice shelf in Antarctica (Fig. 4.11). Surface meltwater on grounded ice often includes extensive regions of slush (Fig. 4.6), and is especially abundant on the north-east outlet glaciers of the AP, and on glaciers feeding the southerly ice shelves. Variability in the proportion of AP meltwater on grounded versus floating ice is far greater than either the WAIS or EAIS, ranging from 1% on grounded ice in 2009/10 to 68% during the 2013/14 melt season (Table 4.2).

Meltwater on the Antarctic Peninsula is found at elevations ranging from sea level up to 2400 m. Whilst the majority of surface meltwater exists at low elevations, 2.6% of

meltwater area is found at elevations above 800 m on average each year. For example, on the steep outlet glaciers of the north-eastern Peninsula, surface meltwater regularly forms 10-20 km upglacier from the grounding line at elevations exceeding 400 m. Across the Peninsula as a whole, meltwater features typically form in very close proximity to the grounding line, with a median distance of 2.78 km.

Surface meltwater is less abundant on the WAIS, although almost half (48% mean) occurs on grounded ice. Previously reported meltwater features around Pine Island, Cosgrove and Getz ice shelves (Corr et al., 2022) recur throughout my time series (Fig. 4.10g). Surface lakes of up to ~2 km^2 also commonly occur on grounded ice in close proximity to nunataks surrounding Nickerson and Sultzberger ice shelves (Fig. 4.4c-d). No surface meltwater is detected around the western section of the Ross Ice Shelf or on any of the Siple Coast ice streams. Very small meltwater features (<0.0018 km^2) are detected on Thwaites Glacier, but these are likely misclassification errors associated with highly crevassed areas, and had a negligible influence on overall surface meltwater totals (Fig. 4.4e-f). The peak in surface meltwater extent across the WAIS is typically of the order of 40-90 km^2 each melt season (64 ± 22 km^2 mean). Meltwater features in West Antarctica predominantly form at very low elevations, with a median elevation of 13.5 m. Meltwater at higher elevations is strongly spatially associated with nunatak presence, although instances of meltwater at high elevations (>500 m) are rare.
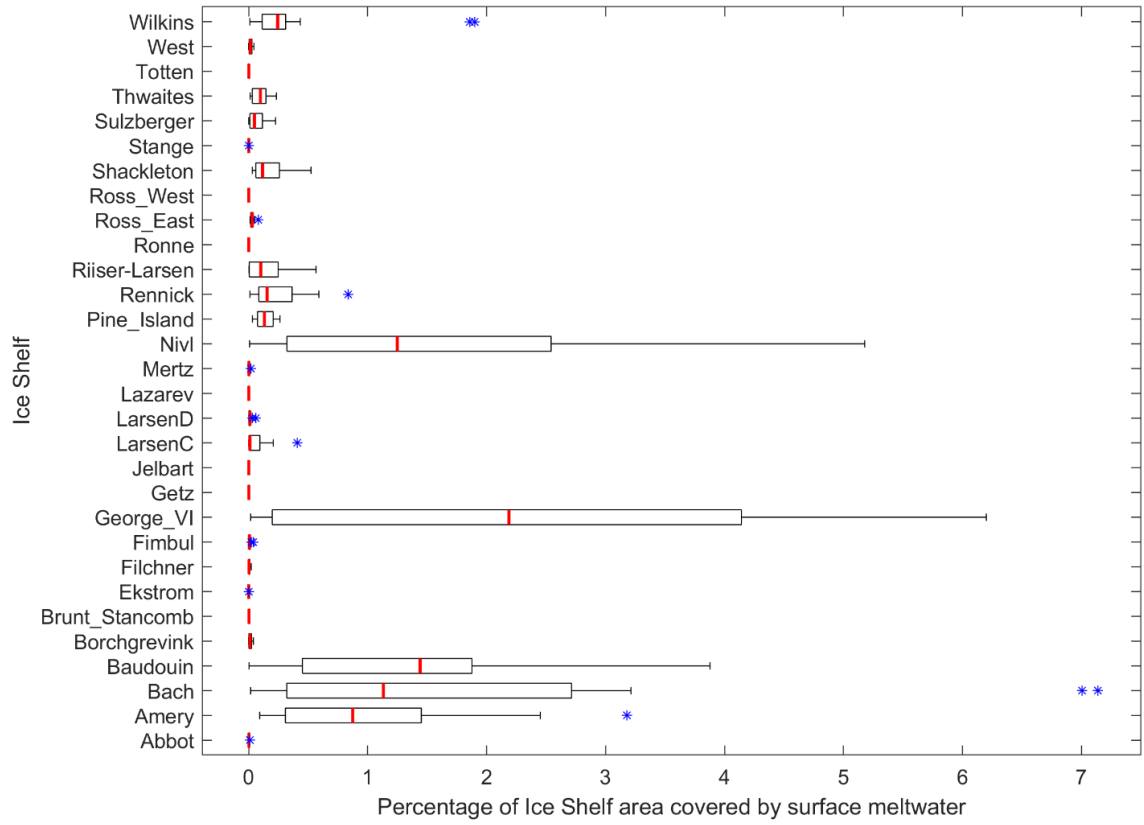
Figure 4.11. Variation in percentage meltwater cover for selected Antarctic ice shelves, between 2006 and 2021. Boxes indicate the median (red), and the 25th and 75th percentiles of the data. Outliers are plotted in blue, whilst whiskers show the minimum and maximum data points that are not considered outliers. See Figure 1.1 for ice shelf locations.

Table 4.2. Surface meltwater area totals on grounded and floating ice per melt season for the EAIS, AP and WAIS. All area totals are yearly maximum meltwater area estimates.

Melt Season	EAIS			AP			WAIS		
	Grounded Area Total (km²)	Ice Shelf Area Total (km²)	% Grounded	Grounded Area Total (km²)	Ice Shelf Area Total (km²)	% Grounded	Grounded Area Total (km²)	Ice Shelf Area Total (km²)	% Grounded
2006/07	546	809	40	29	1135	2	37	29	56
2007/08	832	1165	42	24	251	9	10	8	54
2008/09	697	761	48	17	491	3	17	17	51
2009/10	867	1529	36	15	1465	1	27	30	48
2010/11	629	1400	31	22	799	3	44	39	53
2011/12	463	562	45	10	414	2	43	28	60
2012/13	678	1713	28	36	1469	2	38	67	36
2013/14	1328	2768	32	39	18	68	27	33	45
2014/15	1217	3496	26	31	89	26	47	40	54
2015/16	715	1097	39	250	337	43	38	45	45
2016/17	1796	4149	30	388	383	50	33	42	44
2017/18	1063	2235	32	44	1159	4	24	33	42
2018/19	1547	2698	36	13	45	23	23	39	37
2019/20	1283	2740	32	177	2154	8	31	37	46
2020/21	658	750	47	133	1396	9	23	19	55

4.3.3 Variability and trends in meltwater area

For the EAIS, WAIS and AP, meltwater area displays high seasonal variability. Around the EAIS, surface meltwater is apparent throughout the austral summer months (Fig. 4.12a), with a gradual increase in meltwater area during November and December, a peak in meltwater in January, followed by a rapid decline during February (Fig. 4.12a). On average (mean), total meltwater area across the EAIS in January (1992 km²) is over double that in December (770 km²). On the Antarctic Peninsula, there is typically minimal surface meltwater during the first half of the melt season, with mean meltwater area totals of 25 km² and 39 km² in November and December respectively. High melt years are associated with a sharp increase in meltwater area, sometimes greater than an order of magnitude, during January, which often decreases only slightly into February (Fig. 4.12b). For example, during the 2009/10 melt season, total meltwater area across the AP increased from 9 km² in December to 1382 km² in January. The largest monthly meltwater area on the AP was in January 2020, when total meltwater area was 1614 km². In low melt years, negligible increases in meltwater area occur during January, such as in January 2014 when only 10 km² of the Peninsula was covered in surface meltwater. In West

Antarctica, seasonal meltwater variability is lower than for the EAIS and AP (Fig. 4.12c). WAIS surface meltwater area typically gradually increases through the early melt season to a maximum in January, but peaked in December on four occasions (Fig. 4.12c). Mean meltwater cover across the WAIS during January is 39 km^2, dropping to 6 km^2 in February.
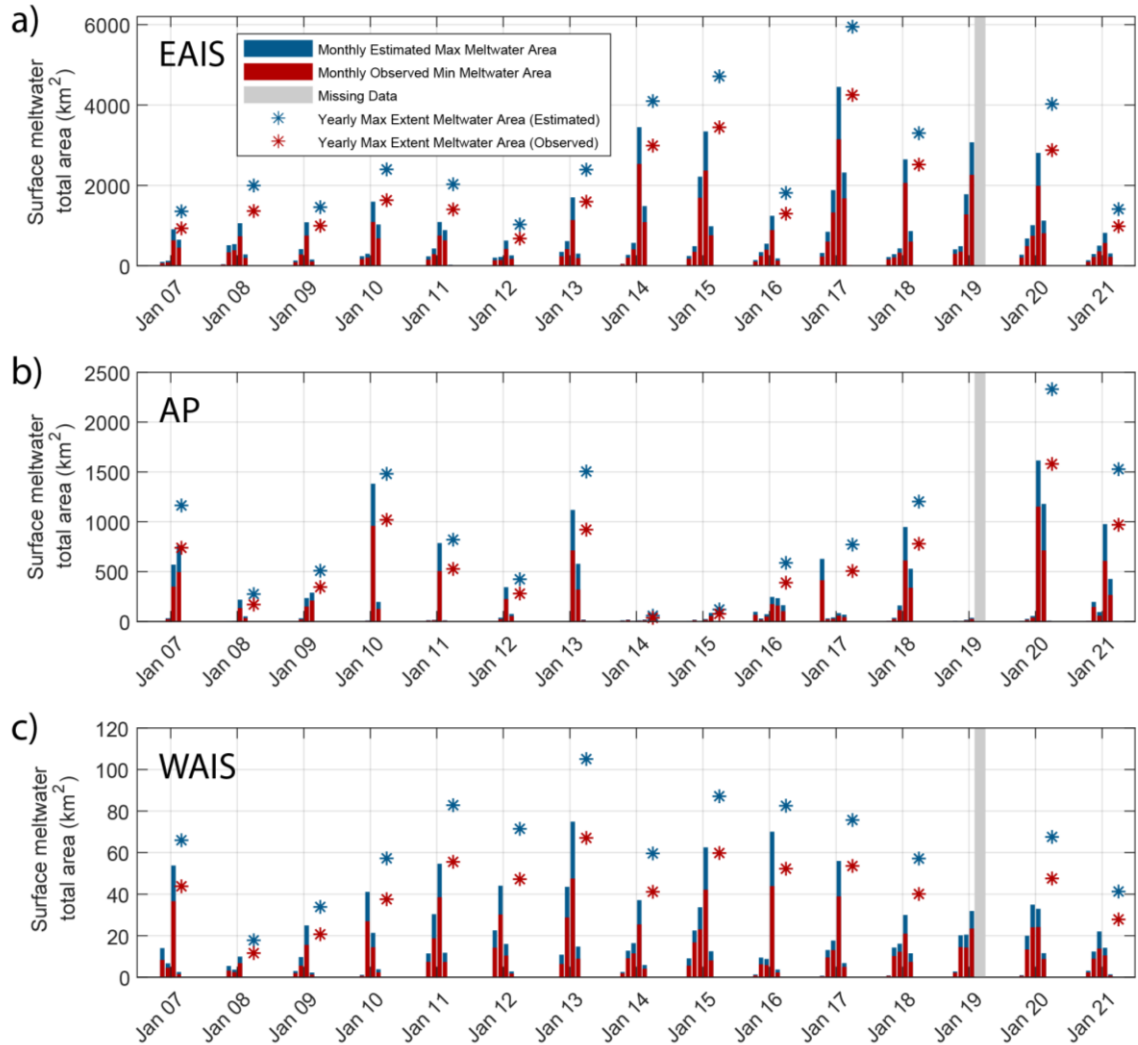
Figure 4.12. The seasonal and interannual evolution of surface meltwater across the EAIS (a), AP (b) and WAIS (c). Observed minimum data are shown in red, whilst estimated maximum area data incorporating visibility assessments are shown in blue (Section 4.2.1). Note the scale change between the three plots. A shift from lower to higher annual surface meltwater area is observed for the EAIS (starting in the 13/14 austral summer), while the AP shows extreme interannual variability.

In addition to experiencing high seasonal variability, all regions of Antarctica also display high interannual variability in meltwater area. East Antarctic annual meltwater area totals ranged from 1026 km^2 during the 2011/12 melt season to 5946 km^2 in 2016/17, with mean coverage of 2813 km^2 (Table 4.2). At a regional scale, annual variability in meltwater area is typically consistent between EAIS ice shelf regions, with notable exceptions. For example, Nivlisen ice shelf's greatest surface meltwater area occurred during the 07/08 melt season, when the majority of the EAIS experienced lower than average coverage (Fig. 4.13). The AP experiences the largest interannual variability in surface meltwater area of the three ice sheet regions. The relative standard deviation of annual meltwater area is 77.8% for the AP, compared with 52.6% and 34.2% for the EAIS and WAIS respectively. During the 2013/14 melt season, a maximum of 57 km^2 of the AP was covered in meltwater, whereas the 2019/20 season experienced 2330 km^2 of meltwater area cover, the highest of the study period (Table 4.2). In this exceptional year, significantly higher than average meltwater area was experienced across the Wilkins, Bach and George VI ice shelf regions (Fig. 4.13), with 92% of total meltwater situated on floating ice shelves across the AP (Table 4.2). The WAIS experiences significantly lower annual variation in meltwater area, although this is primarily due to the lower absolute meltwater totals. The highest surface meltwater area (105 km^2) across the WAIS occurred during the 2012/13 melt season, whilst the lowest meltwater area (18 km^2) was in 2007/08.

Interannual variability in meltwater area is not always consistent across the three ice sheets. For example, the 2014/15 and 2016/17 melt seasons had the highest annual meltwater area totals across the EAIS, yet on the AP, both of these years had lower than average meltwater cover (Fig. 4.13). The WAIS experienced slightly higher than average meltwater cover during these years. Conversely, in 2012/13, the AP and the WAIS experienced higher than average meltwater cover, whilst across the EAIS there was relatively little surface meltwater. This melt season also demonstrates how there can be large differences in meltwater area between geographically close regions. Both Bach and George VI ice shelves experienced above average meltwater cover (Z-score > 1) during 2012/13, yet Wilkins Ice Shelf, which is located less than 150 km from both other ice shelves, had lower than average surface meltwater area (Fig. 4.13). Similar patterns of spatially variable meltwater area anomalies are observed for ice shelf regions in the EAIS in several years (Fig. 4.13). Some years show consistent meltwater area results across the

whole continent. Higher than average surface meltwater was experienced across all of Antarctica during the 2019/20 melt season, whilst there was consistently low surface meltwater area across the continent in 2008/09 (Fig. 4.13).
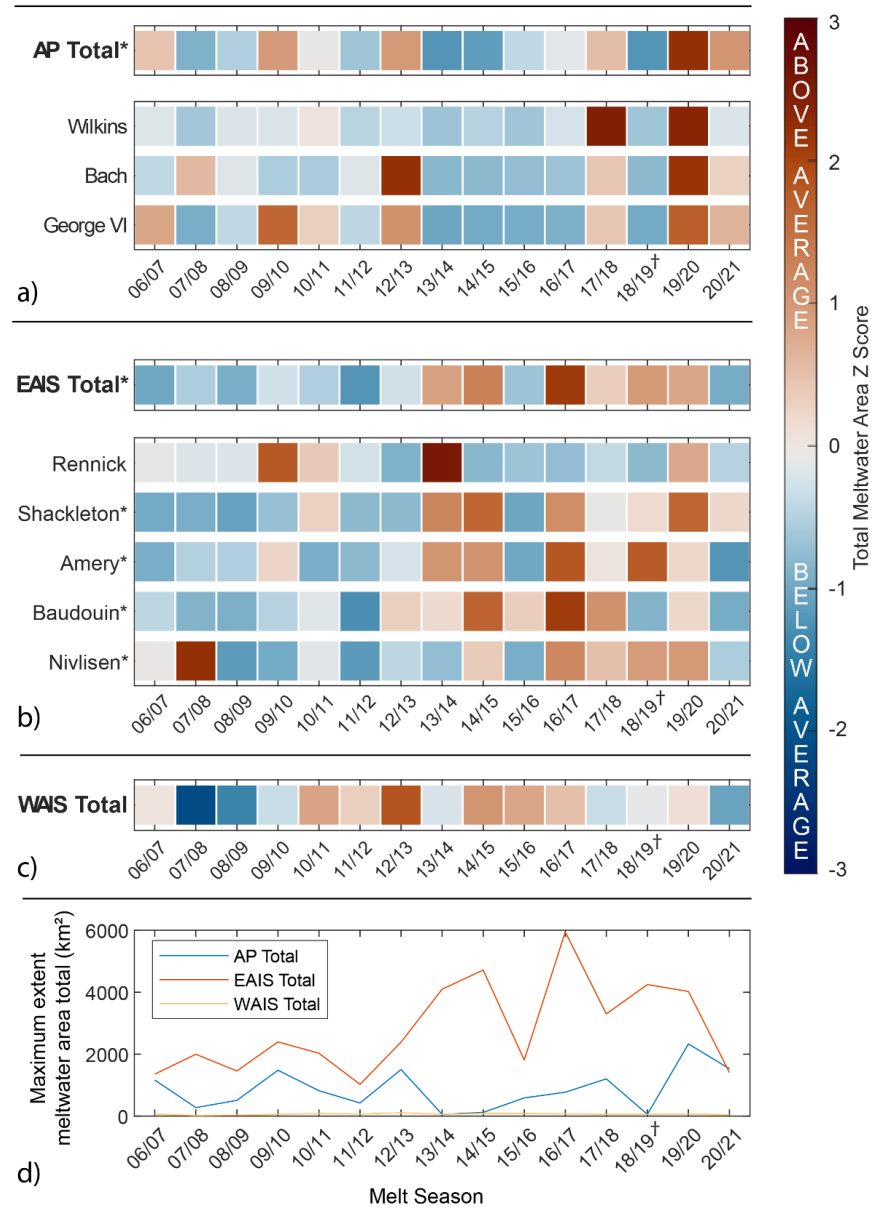
Figure 4.13. Interannual variability and trends in surface meltwater area. (a-c) Coloured boxes display standardised Z-score anomaly values for annual surface meltwater area, relative to the 15-year mean. Data are presented separately for the AP (a), EAIS (b) and WAIS (c), in addition to ice shelf regions (Section 4.2.3) that had at least 0.5% meltwater coverage during the study period. The general shift from blue to red boxes through time for the EAIS indicates increasing surface meltwater area. Asterisks denote statistically significant relationships ($p<0.05$), as shown for the AP, EAIS and several ice shelf regions in East Antarctica. (d) Absolute surface meltwater area totals for the AP, EAIS and WAIS.

The EAIS and the AP show statistically significant ($p < 0.05$) increasing trends in surface meltwater area across the 15-year study period (Fig. 4.13 & 4.13a-b). For the EAIS, this increase occurs both across the whole ice sheet (Fig. 4.14a) and individually for ice shelves with the greatest meltwater cover (Fig. 4.13b). On average, total surface meltwater area increased by 66.7 km^2 per year ($p = 0.001$) across the EAIS (Fig. 4.14a). Mean annual EAIS meltwater coverage between 2014 and 2021 (3693 ± 1493 km^2) was over double that of 2007-2013 (1807 ± 534 km^2), despite 2020/21 being a low melt year. There was also a slight positive trend in surface meltwater area across the AP (Fig. 4.14b), increasing by 12.9 km^2 per year on average throughout the study period ($p = 0.03$). This trend was largely dictated by a record high melt year in 2019/20 (Fig. 4.12 and 4.12), and no individual AP ice shelves displayed a statistically significant trend (Fig. 4.13). There was no long-term trend in surface meltwater coverage for the WAIS, and meltwater totals remained relatively low (Fig. 4.14).
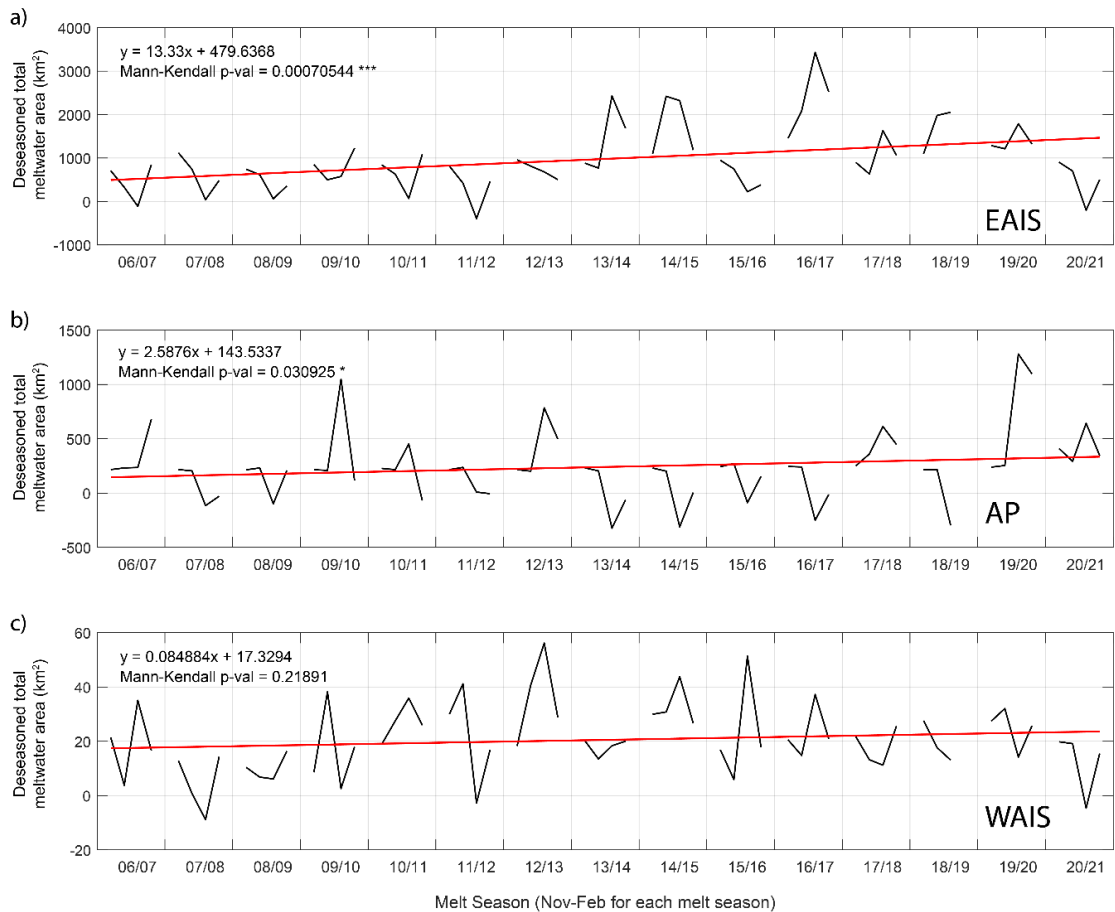
Figure 4.14. Monthly surface meltwater area time series for the East Antarctic Ice Sheet (a), the Antarctic Peninsula (b) and the West Antarctic Ice Sheet (c). The East Antarctic Ice Sheet and the Antarctic Peninsula display statistically significant increasing trends, indicated by Mann-Kendall p-values of less than 0.05. Displayed data show meltwater area totals that have had the mean seasonal component (which was centred on the long-term mean) removed.

4.3.4 Links with Antarctic climate

To determine first-order atmospheric controls on continental-scale surface meltwater coverage, I compared my meltwater area data to annual indices for the SAM, ENSO and ASL (Fig. 4.3; Section 4.2.4). The climate impacts of the three modes varies across Antarctica (Fogt et al., 2011; Raphael et al., 2016; Fogt & Marshall, 2020) so analyses were conducted separately for the EAIS, WAIS and AP. Meltwater area data were also compared against monthly PDDs for each ice sheet region.

For the EAIS, the SAM has a strong control on surface meltwater abundance. There is a statistically significant negative correlation between the detrended Summer SAM Index

and detrended maximum annual surface meltwater area (r = -0.47, p = 0.02), with greater meltwater area generally associated with negative SAM years (Fig. 4.15c). For the six years with the lowest SAM (< 0.7), median surface meltwater area was 20% greater than the 15-year average, with values up to 150% above average in some locations (Fig. 4.15d). Conversely, the six lowest EAIS melt area years coincided with a strong positive summer SAM index (> +1.5) (Table 4.3). EAIS surface meltwater area in the two most negative SAM years was 84% greater than the median (Fig. 4.15). The only year with a strong (< -1.5) negative SAM index (2016/17) corresponded with the highest annual meltwater area of the entire study period (Fig. 4.15c). No statistically significant correlations are found between EAIS surface meltwater area and ENSO or the ASL (Fig. 4.17).

Whilst EAIS surface meltwater area and PDDs are statistically significantly correlated (p < 0.001), there is not a close association between the relative magnitudes of the two variables. Unlike for EAIS meltwater area, there is not a statistically significant trend in monthly PDDs. In some years, low (< 0.5×10^5 °C) PDDs coincide with low surface meltwater area totals (e.g. during the 2007/08 and 2008/09 melt seasons; Fig. 4.18a), yet in other years which have similarly low PDDs, much higher meltwater area is observed. Conversely, not all years with high PDD peaks result in greater surface meltwater area totals. For example, January 2010 had the highest single monthly PDD sum (3.2×10^5 °C) of the study period across the EAIS, yet the maximum meltwater area total during this melt season was 2396 km^2, only the 7th highest of the 15 study years. A clearer relationship between surface meltwater area and PDDs is apparent when a ratio of the two variables is calculated. When each monthly PDD value is divided by surface meltwater area, a step change decrease (identified using the 'findchangepts' function in MATLAB) is observed from 2014/15 (Fig. 4.15e). This decrease in ratio measure implies that at any given PDD value, more meltwater ponding occurred during the second half of the study period relative to the first.
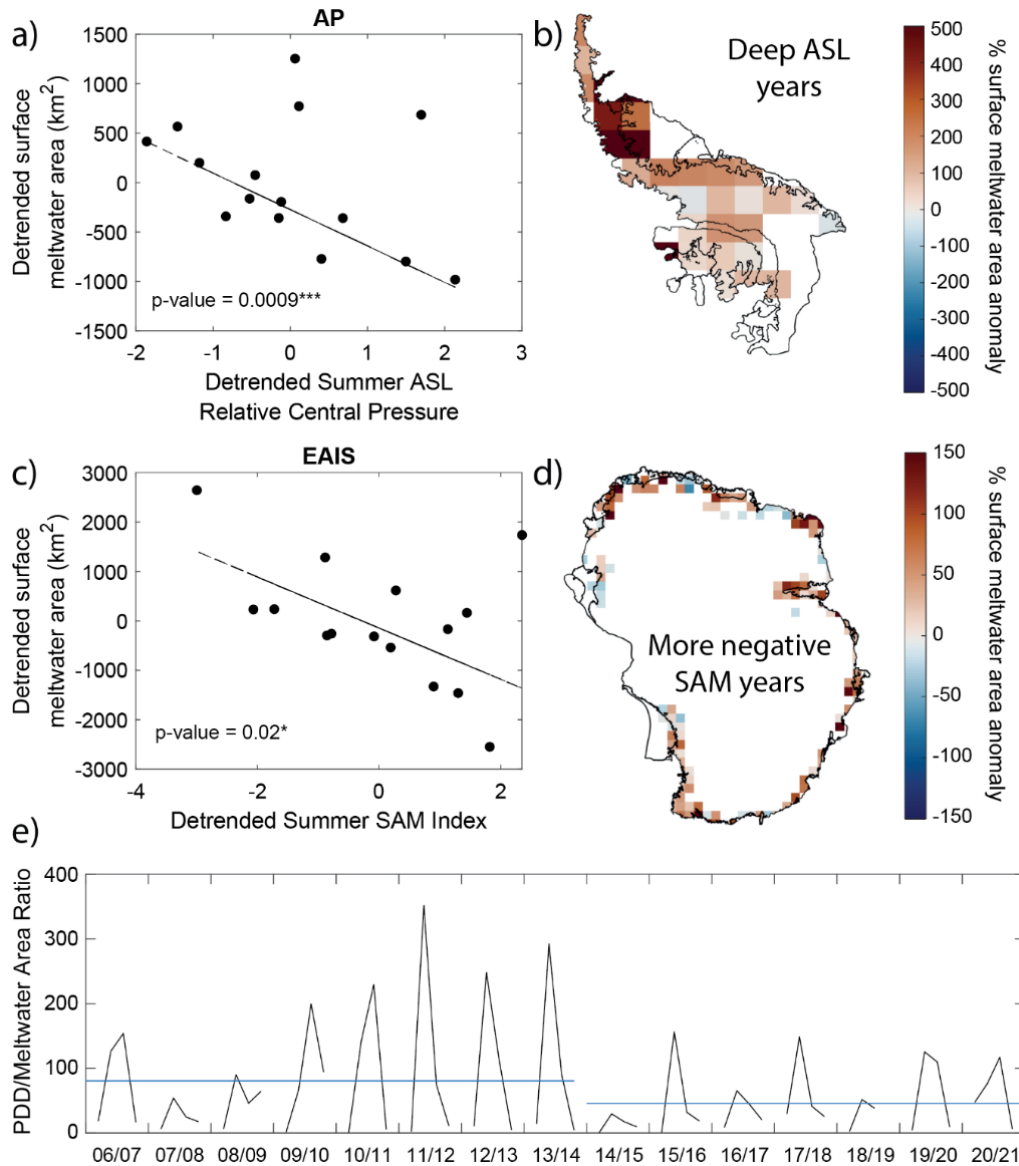
Figure 4.15. Links between Antarctic surface meltwater and climate. (a) Relationship between surface meltwater and Amundsen Sea Low (ASL) relative central pressure (RCP) on the Antarctic Peninsula. In addition to the significant ($p < 0.05$) negative linear relationship, there are three distinct outlier years with higher-than-expected surface meltwater. (b) Very high surface meltwater area anomalies (up to 500 % greater than average) in years when ASL RCP is less than -8. (c) Significant negative relationship between surface meltwater area and the summer Southern Annular Mode (SAM) index for the EAIS. (d) Surface meltwater area anomalies across the EAIS in years when the summer SAM is less than 0.7, showing widespread positive anomalies of more than 50 %. (e) Time series showing the ratio of positive degree days (PDDs) to surface meltwater area for the EAIS. The blue line shows a step change (identified using change point analysis) from 14/15 onwards, indicating greater surface ponding of meltwater relative to PDD values.

Table 4.3. Mean summer (DJF) climate indices for the Southern Annular Mode (SAM), El Nino Southern Oscillation (ENSO), Amundsen Sea Low (ASL) Relative Central Pressure (RCP), and ASL Longitude, per melt season. Corresponding annual surface meltwater totals for the EAIS, AP and WAIS are also displayed for each melt season.

| Melt Season | Climate Indices (Summer mean value) | | | | Meltwater Total Area (km^2) | | |
	SAM	ENSO	ASL RCP	ASL Longitude (°E)	EAIS	AP	WAIS
2006/07	1.63	0.7	-8.20	233.17	1355	1164	66
2007/08	3.11	-1.6	-6.11	230.75	1997	275	18
2008/09	1.81	-0.8	-7.38	266.33	1457	508	34
2009/10	-0.15	1.5	-6.79	257.33	2396	1480	57
2010/11	0.67	-1.4	-7.41	253.00	2029	821	83
2011/12	2.78	-0.9	-7.16	240.58	1026	424	71
2012/13	0.65	-0.4	-5.37	225.67	2391	1504	105
2013/14	0.5	-0.4	-5.62	203.75	4096	57	60
2014/15	3.69	0.5	-6.76	232.00	4713	120	87
2015/16	2.19	2.5	-8.06	230.83	1811	587	83
2016/17	-1.75	-0.3	-7.39	209.50	5945	771	76
2017/18	2.33	-0.9	-8.51	259.58	3298	1203	57
2018/19	1.43	0.7	-5.25	220.25	4245	58	62
2019/20	-0.96	0.5	-7.37	260.75	4023	2330	68
2020/21	2.88	-1.0	-9.35	246.67	1408	1528	41
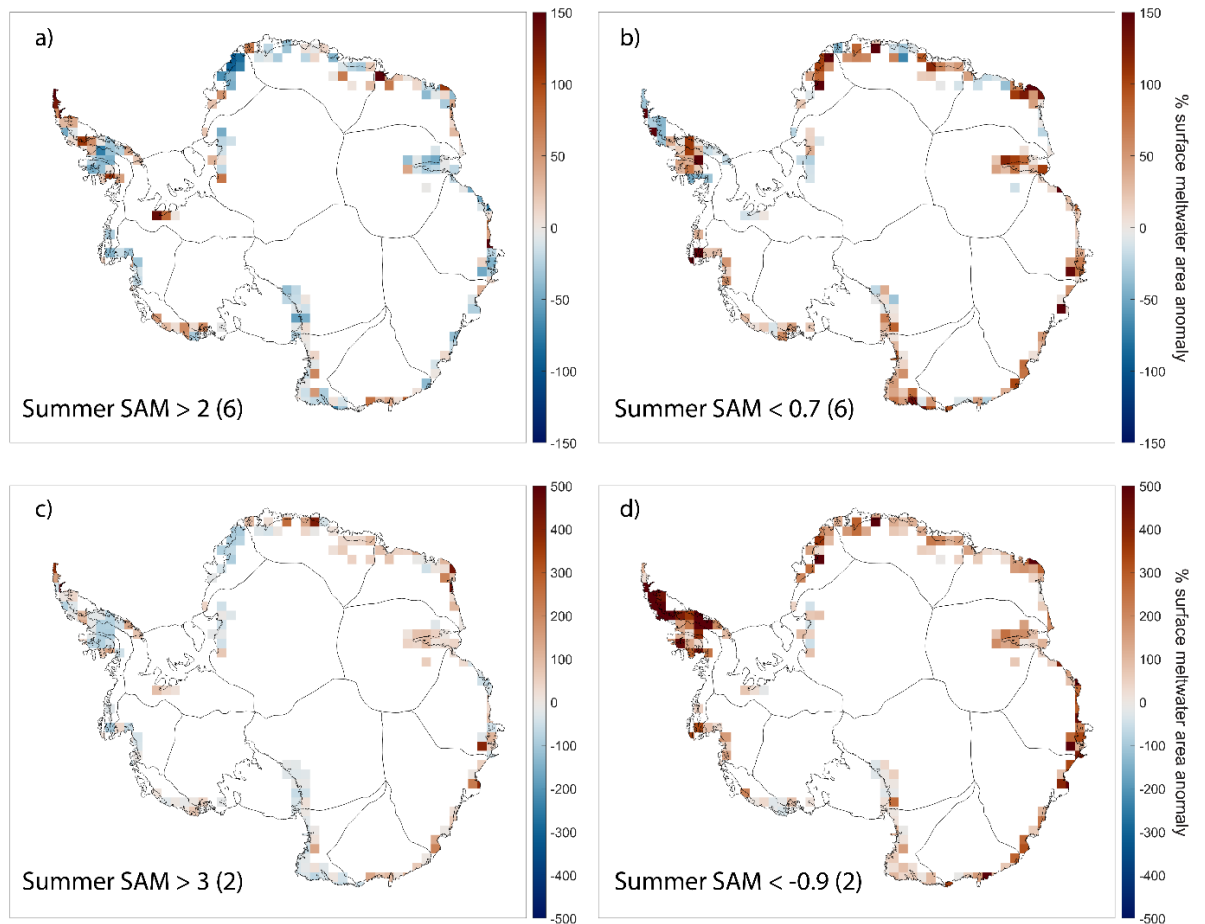
Figure 4.16. Composite maps displaying surface meltwater area percentage anomalies across Antarctica, based on selected Summer SAM index thresholds. (a) Greater than 2; (b) lower than 0.7; (c) greater than 3; (d) lower than -0.9. For each composite plot, the number of years satisfying the criteria is displayed in brackets. Note the change in scale between plots a-b and plots c-d. Anomaly values are relative to the 15-year average.
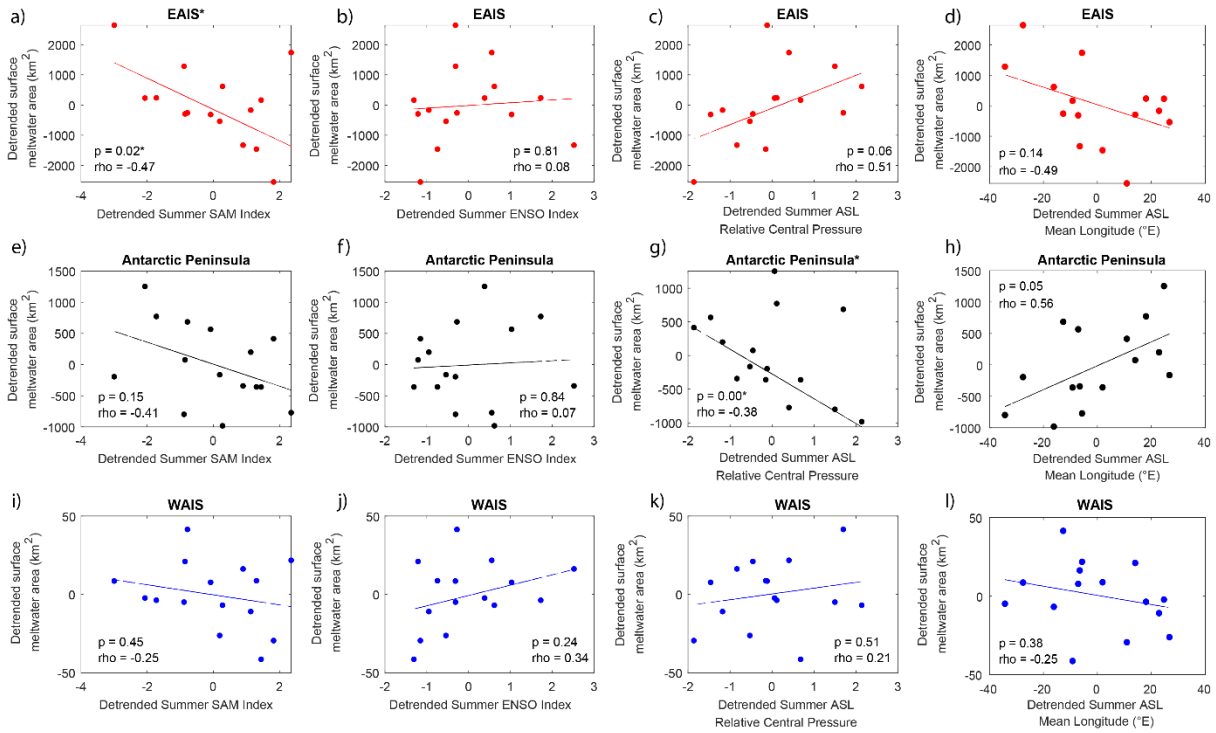
Figure 4.17. Scatter plots showing the relationship between annual maximum surface meltwater area and three climate indices. Climate indices: 1) SAM Index (a,e,i); 2) Oceanic Nino Index (b,f,j); 3) ASL relative central pressure (c,g,k) and longitude (d,h,l). The three rows display results for the EAIS (red), AP (black) and WAIS (blue) respectively. Surface meltwater area and climate index data were detrended prior to conducting linear regression. Significant relationships (p < 0.05) are indicated by an asterisk next to the plot title.
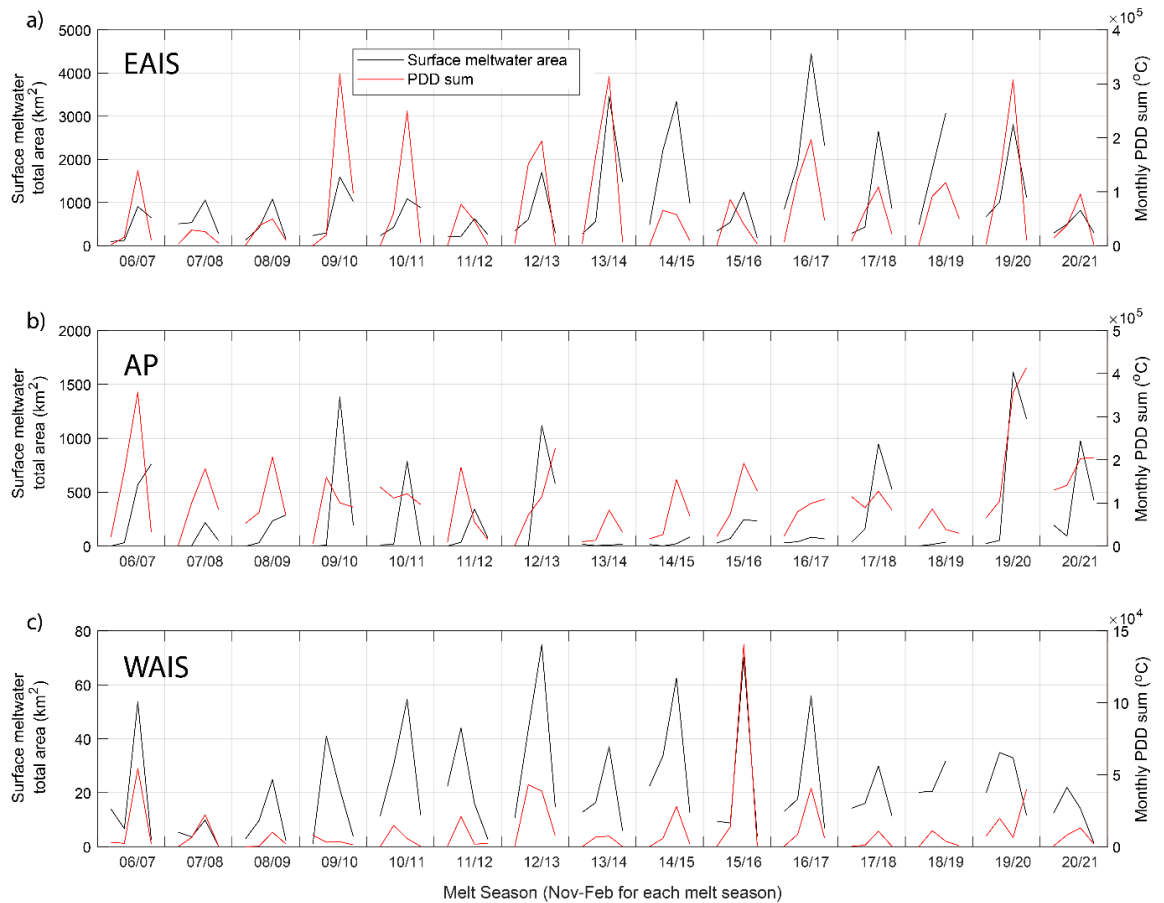
Figure 4.18. Monthly time series of austral summer surface meltwater area (black), compared with positive degree day sum (red) for the EAIS (a), AP (b) and WAIS (c). Data are displayed for November to February of each melt season.

On the Antarctic Peninsula, the strength and location of the ASL appears to influence the distribution and abundance of surface meltwater (Fig. 4.15a-b & 4.18). Summer ASL relative central pressure is negatively correlated ($r = -0.38$, $p < 0.001$) with surface meltwater area (Fig. 4.15a). Years with a deep ASL (<-8 relative central pressure) result, on average, in surface meltwater area anomalies 102% greater than the median, whilst a weaker (> -6.5) ASL results in lower-than-average meltwater ponding on the AP (Fig. 4.19a). The three highest meltwater years (09/10, 12/13 & 19/20), however, stand out as clear outliers to this relationship (Fig. 4.15a). Surface meltwater area is also typically greater when the centre of the ASL is located closer to the AP (Fig. 4.17h & 4.18c-d). For the three years where the centre of the ASL had the most easterly longitude (> 259 °E, i.e. centred closest to the Peninsula), median surface meltwater area was 119% greater than the 15-year average (Fig. 4.19c). Similarly, in years when the ASL was centred further

west, and hence further away from the AP, below average meltwater cover was recorded, particularly on the west coast of the Peninsula (Fig. 4.19d). Statistically significant relationships are not observed between surface meltwater area and either SAM or ENSO on the Antarctic Peninsula (Fig. 4.17e-f). Figure 4.16d, however, suggests that higher-than-average meltwater cover on the AP coincides with strongly negative phases of the SAM.
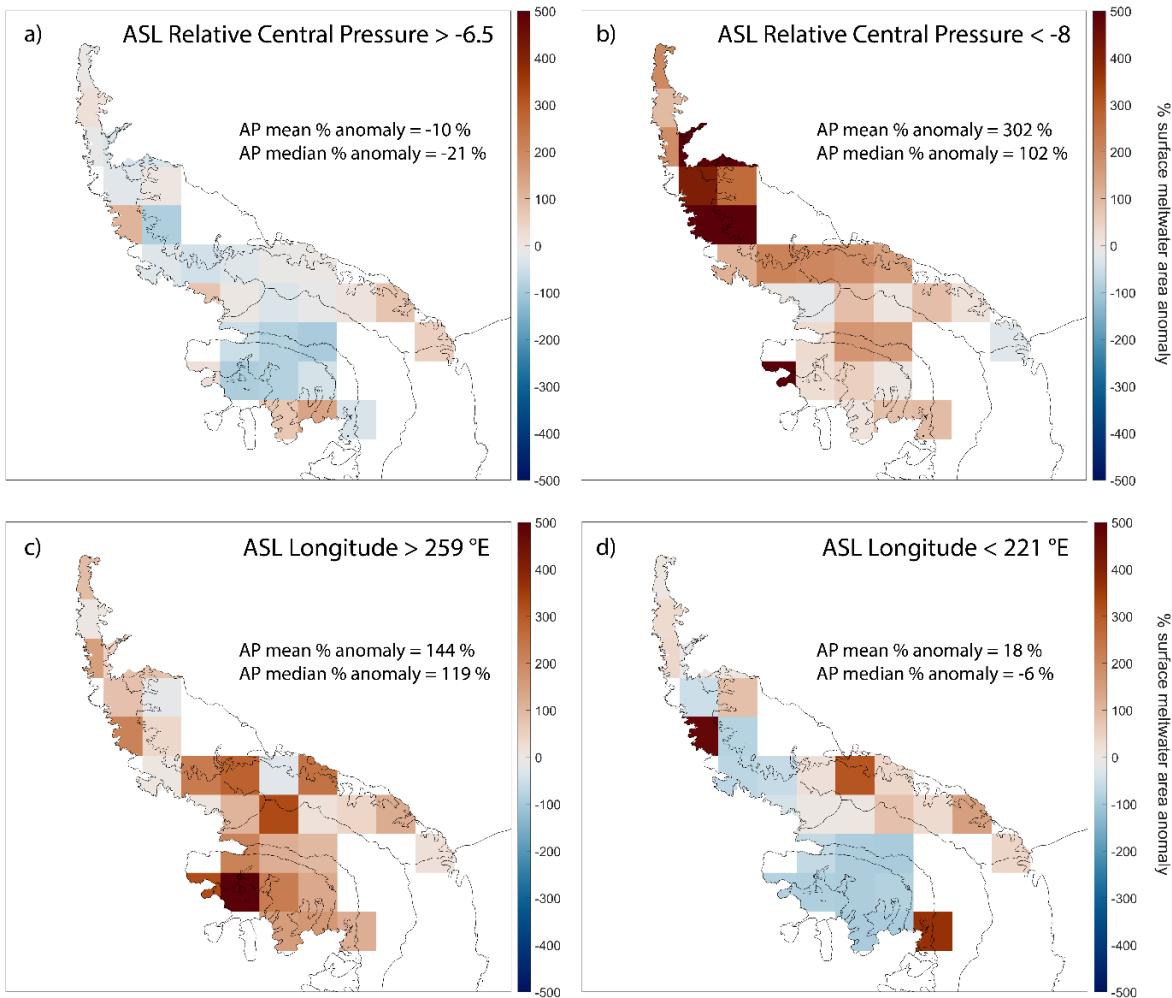
Figure 4.19. Composite maps displaying surface meltwater area percentage anomalies on the Antarctic Peninsula for selected Amundsen Sea Low (ASL) conditions. The top plots display anomaly values for the highest (a) and lowest (b) three years of ASL relative central pressure throughout the study period. The bottom plots show surface meltwater area anomalies for when the ASL central longitude is closer (c) or further away from the Antarctic Peninsula (d). Anomaly values are relative to the 15-year average.

There is a reasonably close association between PDDs and meltwater area on the Antarctic Peninsula (Fig. 4.18b). Exceptionally high meltwater cover during January and February 2020 coincided with the highest PDD values of the study period, whilst years with the low PDDs were generally accompanied by low meltwater area totals (Fig. 4.18b). The greatest discrepancy between the datasets was in January 2006 when a large spike in PDDs (3.6 x 10^5 °C) was accompanied by a relatively low meltwater area of 570 km^2. Surface meltwater area increased to a maximum of 761 km^2 in February 2006, and is one of only two years when peak meltwater occurred in February rather than January.

Across the WAIS, statistically significant associations are not observed between meltwater area and any of the studied climate indices (Fig. 4.17). Composite analysis maps also reveal no clear patterns linking the climate indices to meltwater cover, although this is largely due to a lack of ROI tiles containing meltwater data on which to base analysis (e.g. Fig. 4.16). Monthly PDD values across the WAIS were consistently lower than 0.5 x 10^5 °C, with the notable exception of January 2016 when PDD sum was 1.4 x 10^5 °C (Fig. 4.18c). Although this month experienced the second highest monthly meltwater area total (70 km^2) of the study period, similar magnitudes of surface meltwater area were also experienced in years when PDD values were much lower (Fig. 4.18c).

4.4 Discussion

4.4.1 Spatial distribution of Antarctic surface meltwater

The main controls on the overall spatial distribution of meltwater around Antarctica are already relatively well documented (Section 1.2.3), whilst regionally focused analyses are required to understand specific localised controls (e.g. Chapter 2). Here, I focus on selected novel Antarctic-wide findings from this chapter and speculate on their cause.

The generation of a continent-wide dataset has enabled me to assess the relative difference in total meltwater area between the EAIS, WAIS and AP for the first time. Results show that, on average, 75% of meltwater exists on the EAIS, 23% on the AP and just 2% on the WAIS. Most of the WAIS coastline lies at a latitude of around 75 °S, with no part of the WAIS lying at a latitude less than ~72 °S (Fig. 4.1). By contrast, the majority of the EAIS coastline lies between 65-70 °S, whilst northern sections of the Antarctic Peninsula

sit at latitudes of just 63 °S (Fig. 4.1). This geographical difference is likely the key reason why the WAIS experiences significantly less surface melting, and hence less meltwater ponding (Stokes et al., 2019). The large difference in meltwater area between the EAIS and the Antarctic Peninsula is reflective of the vast area difference between the two ice sheets; the EAIS is around twenty times larger than the Peninsula. The Antarctic Peninsula hence hosts the greatest density of meltwater relative to its size, largely due to its relative northerly latitude and maritime climate (van Wessem et al., 2016).

The majority of Antarctic meltwater studies have focussed on ice shelves (Stokes et al., 2019; Arthur et al., 2020; Table 1.1), with the traditional view being that there is negligible surface meltwater on grounded ice. Results from this chapter show that this conception is unfounded, and reveal that, on average, 30% of Antarctic-wide surface meltwater area forms on grounded ice. Almost half of surface meltwater on the WAIS forms on grounded ice, whilst annual totals of grounded meltwater in East Antarctica regularly exceed 1000 km^2 of surface water. The majority of grounded surface meltwater forms in close proximity to the grounding line, likely due to its low elevation and localised focussing of katabatic and föehn winds (Lenaerts et al., 2017; Section 4.4.2). Meltwater at higher elevations shows close spatial association with exposed nunataks, supporting the finding of Stokes et al. (2019) that low-albedo areas of bedrock and blue ice are the most important control on surface melting at high elevations. Low-albedo nunataks increase solar energy absorption and longwave radiation and can induce locally enhanced winds, thus providing energy to initiate surface melting at elevations that would otherwise be too cold for melting to occur (Kingslake et al., 2017; Stokes et al., 2019). Future ice sheet thinning, which will likely result from predicted rises in atmospheric temperature, could expose increasing numbers of nunataks, potentially increasing the abundance of surface meltwater inland from the coastline via melt-albedo feedbacks (Kingslake et al., 2017; Jakobs et al., 2021). The prevalence of grounded surface meltwater today, combined with likely future increases in grounded meltwater, hence highlights the importance of including grounded sectors of Antarctica in future surface meltwater studies (Section 4.4.3).

4.4.2 Causes of long-term trends and variability in meltwater area

Results from the EAIS show that surface meltwater area increased by 197% on average between 2006 and 2021 (Section 4.3.3), and that the SAM strongly influences annual variations in EAIS meltwater area (Section 4.3.4). Coupling between the SAM and surface meltwater in East Antarctica is consistent with work showing the influence of the SAM on surface air temperature (Fogt & Marshall, 2020; Orr et al., 2022). However, there is no significant trend in the SAM index throughout the study period (Fig. 4.3a). Additionally, I do not observe a close association between monthly PDDs and surface meltwater area (Fig. 4.18a), consistent with research that found no trend in EAIS surface melting over recent decades (Zheng et al., 2022). On a multi-annual scale, therefore, there is no clear climatic driver for the increasing trend in EAIS meltwater area.

Although I find no clear climatic driver to explain the trend in EAIS surface meltwater, I observe a step change in the ratio of PDDs to surface meltwater area from 2014/15 (Fig. 4.15e), suggesting that increased surface meltwater area is likely caused by a shift to a glaciological regime that promotes meltwater ponding. Reduced ice sheet surface permeability can occur for several reasons: enhanced wind scouring exposes ice surfaces (Lenaerts et al., 2017); multi-annual melting and freezing of water within the snowpack forms impermeable ice lenses (Hubbard et al., 2016; Buzzard et al., 2018; MacFerrin et al., 2019); and reductions in firn air content due to reduced accumulation or snowpacks becoming saturated with melt (Ligtenberg et al., 2014; Kuipers Munneke et al., 2014). Furthermore, the presence of surface meltwater can initiate a positive feedback, whereby low albedo surface water promotes melting (Kingslake et al., 2017). The specific controlling factors for any particular region will vary and cannot be explained without detailed surface process and atmosphere models, but these results suggest that smaller increases in melt on the EAIS are now able to trigger more extensive meltwater ponding than at the start of the study period.

On the Antarctic Peninsula, the strength of the ASL is shown to have a distinct broad-scale influence on annual surface meltwater area, with greater meltwater area typically experienced in years with a deeper (stronger) ASL (Fig. 4.15c). The ASL has a greater influence on the AP than, for example, in East Antarctica, due to its geographical proximity (Section 1.2.1), additionally explaining its greater influence in years with more easterly longitudes. The three highest meltwater years (09/10, 12/13 & 19/20) stand out

as clear outliers to the relationship between ASL strength and meltwater area, coinciding with a relatively weak ASL (Fig. 4.15c). These years did not have exceptionally eastward ASL longitudes (Fig. 4.3b), suggesting that local variability in surface meteorological conditions and extreme weather events are more important.

Localised melt rates on the AP are strongly influenced by variations in weather conditions including solar radiation (Elvidge et al., 2020; Gilbert et al., 2022), foehn winds (King et al., 2017; Elvidge et al., 2020), and low cloud-cover (Gilbert et al., 2020). For example, record surface meltwater cover on George VI Ice Shelf in 2019/20 was associated with sustained regionally warm (> 0°C) air temperatures from early in the melt season, likely driven by warm, low-speed northerly winds (Banwell et al., 2021). Although strongly linked to broader climatic patterns, the interaction and timing of local drivers appear key to controlling the most extreme meltwater ponding events and are likely responsible for the overall increasing trend in AP meltwater area. Increased surface meltwater area on the AP during the two most negative SAM years (Fig. 4.16d) contrasts with work suggesting that positive phases of the SAM enhance surface melting on the AP (Gilbert et al., 2022). However, this result was highly skewed by the 2019/20 melt total, and other years (e.g. 2020/21) demonstrate how high meltwater area totals occur in years with a strongly positive phase of the SAM (Table 4.3). Strong teleconnections between the SAM, ENSO and ASL (Li et al., 2021) additionally make it difficult to separate out the influence of the systems for any individual year.

Differences in the interannual and seasonal variability of total meltwater cover between the EAIS, WAIS and AP are likely partly a consequence of the number and spatial distribution of regions that contribute to the meltwater area totals. Meltwater area totals on the AP are dominated by contributions from three neighboring ice shelves (George VI, Bach and Wilkins), which mostly exhibit similar timings and relative magnitudes in meltwater cover change. In general, meltwater cover either remains low across all three ice shelves throughout the melt season, or displays a consistent rapid increase in January, presumably due to high melt events associated with regional increases in near-surface air temperature. Meltwater area totals for the EAIS, by contrast, are made up of contributions from a greater number of regions that are more widely spatially distributed (Fig. 4.9). In any given timeframe, there is therefore greater variability in meltwater area for different regions across East Antarctica (Fig. 4.13), often reducing the magnitude of change in the EAIS-wide total area. For example, during the 2018/19 melt season, the two ice shelf

regions of the EAIS that typically have the largest meltwater area (Amery and Roi Baudouin) experienced contrasting meltwater area relative to average, thus counteracting one another other in the EAIS total. The same effect can occur for individual months within a melt season, possibly explaining why seasonal variability is also greater for the AP than the EAIS. Low seasonal and interannual variability in West Antarctica is likely due to the lower magnitude and proportion of meltwater on ice shelves, which can skew meltwater area totals. Flat, low elevation ice shelves experience greater variability in meltwater cover than grounded regions, as they are more susceptible to minor changes in ice surface and near-surface climatic conditions (Arthur et al., 2020).

4.4.3 The future of Antarctic surface meltwater in a warming climate

Given the lack of coincident warming, I attribute the observed increase in EAIS meltwater between 2006 and 2021 to changes in ice sheet surface conditions. A surface which facilitates ponding, combined with predicted Antarctic-wide increases in surface melting (Trusel et al., 2015), is likely to cause accelerated expansion of surface meltwater over the coming decades. Whilst most ice shelf regions which currently host surface meltwater are thought to be resilient to hydrofracture (Lai et al., 2020), I propose that minor increases in surface melting could translate to proportionally larger rises in meltwater ponding, including expansion into more vulnerable areas. It is therefore a priority to conduct regional sensitivity analyses of ice shelves vulnerable to meltwater ponding, and to identify underlying processes responsible for the observed meltwater increases. Research should focus on ice shelves, such as Shackleton, that already show a strong positive trend in meltwater area density and extent (Arthur et al., 2022).

My data demonstrate that surface meltwater is abundant on grounded ice (close to the grounding line) around the periphery of Antarctica (Fig. 4.9; Table 4.2), where it could induce transient (Tuckett et al., 2019) and seasonal (Boxall et al., 2022) accelerations in ice motion, as is common in West Greenland (Zwally et al., 2002), the High Arctic (Bingham et al., 2003) and in mountain settings (Iken & Bindschadler, 1986). Surface-to-bed connections will likely become more common around Antarctica as surface melting increases (Bell et al., 2018), and could induce a shift to an ice dynamic regime forced by seasonal variations in surface meltwater supply (Tuckett et al., 2019)

I have shown that large-scale modes of climate variability influence annual variations in Antarctic surface meltwater, with the SAM especially influential for the EAIS and the ASL for the Antarctic Peninsula. Trends towards a more positive SAM (Fogt & Marshall, 2020) and a deeper ASL (Raphael et al., 2016) are predicted in line with continued greenhouse gas emissions. Based on the relationships I observe, this would lead to increases in surface meltwater area on the AP and decreases on the EAIS. However, these modes do not explain the multi-year increasing trends in meltwater coverage, highlighting the importance of regional climatic and glaciological conditions in controlling meltwater ponding. Intense warm periods, which are predicted to become longer and more frequent across Antarctica (Feron et al., 2021), combined with the extent to which ice surfaces are primed for meltwater ponding, will likely increase the influence of surface meltwater on future changes in ice sheet mass balance and dynamics.

4.4.4 Advances and limitations of the meltwater dataset

I have utilised the computing capability of GEE to produce the the most spatially and temporally extensive, robust dataset of Antarctic surface meltwater to date. The generation of a continent-wide, long-term monthly dataset represents a step-change in our understanding of Antarctic surface meltwater coverage and evolution. By analysing an order of magnitude more satellite images than previous studies (Table 1.1), I have been able to assess seasonal and multiannual trends in Antarctic-wide meltwater extent for the first time. Analysis of this dataset has revealed important and previously undocumented results, in particular the long-term rise in surface meltwater identified across the EAIS since 2006. The dataset has also enabled me to investigate links between meltwater ponding and large scale modes of climate variability, revealing novel associations between surface meltwater area with the SAM and the ASL. Here, I have presented the main Antarctic-wide findings relating to trends and spatial patterns in meltwater area, but the dataset could now be used for a range of further applications. For example, comprehensive studies of meltwater evolution could be conducted at regional scales (as demonstrated for the Amery Ice Shelf in Chapter 2) to investigate local controls on meltwater ponding. The dataset could additionally be compared against modelled meltwater data to explore the extent to which regional climate models can predict where meltwater ponds for different regions.

A central part of generating continuous and consistent time series of meltwater area is the incorporation of image visibility assessments within the method. However, this approach has some limitations. Large differences in image visibility are observed across Antarctica (Fig. 4.7) due to a combination of variable satellite coverage and regional differences in cloud cover. High visibility scores are recorded in coastal regions of East Antarctica due to high satellite repeat times and typically low cloud cover, whereas frequently high cloud cover associated with a maritime climate on the Antarctic Peninsula (Gilbert et al., 2020) results in lower visibility scores. Uncertainty associated with the scaling up of mapped meltwater area hence varies spatially, potentially inducing a regional bias in regional meltwater area estimates. Regression analysis of meltwater area against visibility scores suggests the influence of image visibility on meltwater area is low, however, with consistently low R^2 values observed across the Peninsula (Fig. 4.8) where the bias might be expected to be greatest. With the exception of the AP, consistently high image visibility scores are observed around coastal areas of Antarctica where surface meltwater forms, validating the use of optical techniques for conducting meltwater change analysis. Despite having some unavoidable limitations, the incorporation of visibility assessments provides a significant improvement on standard optical mapping methods, and likely provides more accurate estimates of ground-truth meltwater extent (Chapter 2).

As discussed in Section 2.5.1, the SLC striping associated with Landsat 7 data typically results in lower visibility scores compared to Landsat 8. This means that the scaling up of meltwater area totals from Landsat 7 is typically greater than for Landsat 8, introducing larger uncertainty. This potential bias needs to be taken into account when interpreting cross-sensor time series trends. The step change increase in meltwater area that I observe in East Antarctica (Fig. 4.12a) coincides with the switch from Landsat 7 to Landsat 8. I interpret this timing to be coincidental, rather than the switch in sensor being the main cause of the increase, for several reasons. First, the enhanced scaling up of Landsat 7 meltwater area values is likely to overestimate, rather than underestimate, the maximum predicted values (Section 2.5.1). This might be expected to cause a decrease in meltwater area following the switch to Landsat 8, rather than an increase. Second, the magnitude of the observed increase is much larger than would be expected if the shift was entirely due to the scaling up of data missing from SLC striping. Third, high meltwater area totals over the Amery region in 2004/05 and 2005/06 (Fig. 2.13) demonstrate that meltwater area totals from Landsat 7 are not always low, suggesting there is not a systematic reason for

the consistently low EAIS-wide meltwater totals between 2006 and 2013. Visual analysis of optical images across the study period additionally suggests that the EAIS increase is real, and not the artifact of the switch in satellites. Nonetheless, it cannot be ruled out that the shift in sensors has had no influence on meltwater area totals. Future work could look to better quantify the uncertainties associated with cross-sensor meltwater area time series to provide additional confidence to key conclusions.

One potential improvement to the mapping approach could be to incorporate a method which reduces inconsistency in the detection of slush (Section 4.3.1). The thresholds applied were not designed to identify regions of slush (Moussavi et al., 2020), and Antarctic-wide results therefore do not capture the majority of slush around Antarctica. On the Antarctic Peninsula, where extensive regions of slush often exist due to the presence of thick, saturated firn packs (Datta et al., 2019), slush was captured more frequently (Fig. 4.6). Slush is not a uniform entity, and can exist in a variety of states along a continuum of meltwater presence within the firnpack. The frequent detection of slush on the Peninsula therefore suggests that slush in this region is 'closer' to forming ponded water than in other regions of Antarctica. The existence of firn aquifers of the Antarctic Peninsula (van Wessem et al., 2021) also provide extra potential for future increases in ponded meltwater area. Areas of slush were not classed as 'misclassification error', since slush is still a form of surface meltwater, and were retained within the dataset. However, it should be noted that whilst meltwater area totals predominantly represent surface meltwater, they also include some instances of slush. A supervised classification method for differentiating between slush and ponded surface water has been applied to Antarctic ice shelves (Dell et al., 2022), and future work could include incorporating such a method within the continent-wide mapping framework used here.

4.5 Conclusions

In this chapter, I have applied a meltwater mapping method (Chapter 2) across Antarctica to produce the first continent-wide, monthly dataset of surface meltwater, spanning 2006 to 2021. Analysis of this dataset has enabled me to assess seasonal and multiannual patterns in meltwater area across different regions of Antarctica for the first time. High interannual variability in meltwater coverage across the Antarctic Peninsula and in East Antarctica correlates with large-scale modes of climate variability, but this control is

absent where meltwater coverage is comparatively low in West Antarctica. In East Antarctica, there has been a significant increasing trend in meltwater area, which, in the absence of a clear climatic trend, I attribute to ice sheet surfaces becoming more favourable to ponding. Meltwater area on the Antarctic Peninsula is influenced by changes in the strength and location of the Amundsen Sea Low, although this influence is superseded by extreme regional weather events that have triggered the largest meltwater extents. The highest densities of surface meltwater are found on ice shelves, in particular on the Antarctic Peninsula and in East Antarctica, yet an average of 30% of meltwater across Antarctica lies on grounded ice. Future increases in melt rate could cause proportionally larger increases in meltwater coverage as ice surfaces become more susceptible to ponding, with implications for the resilience of ice shelves and the likelihood of meltwater driven changes in ice flow on grounded ice.

This chapter has addressed Objectives 3 and 4, and is the third and final 'results' chapter of the thesis. In Chapter 5, I provide a broader discussion of the work presented in Chapters 2-4, and discuss the contribution of my work to the wider research field.

Chapter 4

CHAPTER 5

Discussion & Conclusions

The aim of this thesis was 'To improve our understanding of the occurrence and evolution of surface meltwater on the Antarctic Ice Sheet' (Section 1.3). In this chapter, I discuss the extent to which I have achieved this aim based on the material presented in Chapters 2-4. First, I return to the objectives set out in Section 1.3, and provide a brief overview of how each objective has been addressed (Section 5.1). Second, I provide a discussion of the methodological contributions of my work (Section 5.2). I evaluate advances made in the remote sensing of Antarctic surface meltwater, limitations of current methods, and potential future applications and directions of study. Third, I discuss what my results mean for the future of the Antarctic Ice Sheet (Section 5.3). I summarise the present-day impacts of surface meltwater in Antarctica, and discuss the existence of melt-driven ice dynamic variability on the Antarctic Peninsula. I then speculate what implications my results may have for future Antarctic mass balance (Section 5.4). Finally, I conclude the key findings and contributions from the thesis (Section 5.5).

5.1 Evaluation of objectives

Five objectives were outlined in Chapter 1 (Section 1.3) to address the aim of the thesis. Here, I state the chapters in which each objective was addressed, and summarise the key findings and contributions from each objective.

Objective 1: Develop a method for automatically mapping surface meltwater from optical satellite imagery that can be implemented in Google Earth Engine.

Objective 1 was addressed in Chapter 2, where I implemented an existing threshold based method (Moussavi et al., 2020) for mapping surface meltwater within GEE. By automating meltwater area mapping within GEE, I have produced a quick and easy open access tool for monitoring surface meltwater over large spatial and temporal scales. This represents a significant methodological advancement; reduced processing capabilities had previously limited the scale at which meltwater assessments could be conducted. My

approach additionally goes beyond previous work by incorporating a novel method for quantifying image visibility, enabling generation of robust, continuous meltwater area time series.

Objective 2: Test the mapping method at a regional scale, and evaluate regional controls on surface hydrology.

Chapter 2 addressed Objective 2, where I applied my meltwater mapping method across the Amery Ice Shelf region between 2005 and 2020. Results demonstrated the success of the method, enabling me to generate the first long-term, monthly time series of meltwater area in the region. Analysis reveals a broad scale influence of the SAM on annual meltwater area total, and shows how the spatial distribution of meltwater is strongly influenced by katabatic winds and the location of low-albedo nunataks. I also show strong and significant correlations between meltwater area and RACMO-modelled snowmelt. This provides an important regional assessment of associations between climate, glaciological conditions and meltwater ponding.

Objective 3: Apply the method across Antarctica to generate continent-wide, long-term time series of Antarctic surface meltwater for the first time.

In Chapter 4, I applied my mapping method at a continent-wide scale, achieving Objective 3. I generated lake area data on a monthly basis between 2006 and 2021 to produce the first pan-Antarctic, high-temporal resolution, meltwater dataset. This is the most comprehensive study of Antarctic surface meltwater to date, and represents a leap in our understanding of Antarctic meltwater coverage and evolution. Results show a significant increase in meltwater area over East Antarctica in recent years, suggesting EAIS ice shelves are becoming increasing vulnerable to future increases in melt, and that melt-driven dynamic effects are increasingly likely.

Objective 4: Assess the extent to which large-scale modes of climate variability influence the distribution and magnitude of surface meltwater across Antarctica.

Chapter 4 included an assessment of the influence of three large-scale modes of climate variability on meltwater area, addressing Objective 4. This analysis was made possible by the generation of a continent-wide meltwater dataset (Objective 3), and is hence the first work to explore links between large-scale atmospheric modes and meltwater area at an Antarctic-wide scale. Results show that the SAM has a strong influence on annual meltwater area total in East Antarctica, whilst the strength and location of the ASL is particularly influential for the abundance of meltwater on the Antarctic Peninsula. However, the influence of the SAM does not explain the overall increasing trend observed in East Antarctica.

Objective 5: Evaluate the behaviour of surface meltwater evolution and search for evidence of lake drainage events.

Objective 5 was addressed in Chapter 3, where I explored different styles of meltwater evolution, including lake drainage events, across a grounding zone of the Amery Ice Shelf. I achieved this by automatically generating lake volume time series for 215 study lakes (those greater than 0.5 km^2), enabling me to assess magnitudes and rates of volumetric changes. I additionally conducted manual analysis of optical satellite imagery to study lake drainage behaviours, and developed a novel method for enhancing the temporal resolution of lake volume time series using daily MODIS data, to provide better constraints on the timings of lake drainage events. Therefore, Chapter 3 takes important steps towards understanding local-scale supraglacial lake evolution processes, and provides novel methods for future research into this topic.

5.2 Methodological trajectory

A key aspect of this thesis has been the development of automated methods for studying Antarctic surface meltwater. In particular, I have taken advantage of opportunities presented by GEE (Section 1.2.4.1) for revolutionising the scale at which geospatial analysis can be conducted. In this section, I discuss the trajectory of methods used for studying surface meltwater, and how methodological contributions from this thesis could be used in future research.

5.2.1 Contributions to the scientific community

A central limitation of previous Antarctic surface meltwater assessments has been the scale at which analysis has been conducted (Section 2.5.1). User-friendly, cloud-based computational platforms for geospatial analysis have only recently been developed (Gorelick et al., 2017), meaning even fully automated processes have been restricted by data download speeds. Until recently, developing methods for Antarctic-wide analysis was deemed a low priority within the remote sensing community, since meltwater was considered spatially confined to a few specific regions (Section 1.2.2). The realisation that surface meltwater is widespread around the Antarctic margin (Kingslake et al., 2017; Stokes et al., 2019) initiated a surge in research on Antarctic surface meltwater, evidenced by the recent publication dates (the last 5-6 years) of the majority of literature cited within this thesis (Fig. 5.1). Increased scientific attention on Antarctic surface meltwater was likely partly a consequence of a wider awareness of its spatial extent, but also an increasing realisation of its potential impacts on ice shelf stability (around the continent and not just on the Antarctic Peninsula; Lai et al., 2020) and grounded ice dynamics (Tuckett et al., 2019; Boxall et al., 2022). The timing of this thesis hence coincided with an abundance of emerging work seeking to improve methodologies for studying Antarctic surface meltwater (Stokes et al., 2019; Dirscherl et al., 2020; Halberstadt et al., 2020; Moussavi et al., 2020; Dell et al., 2022).
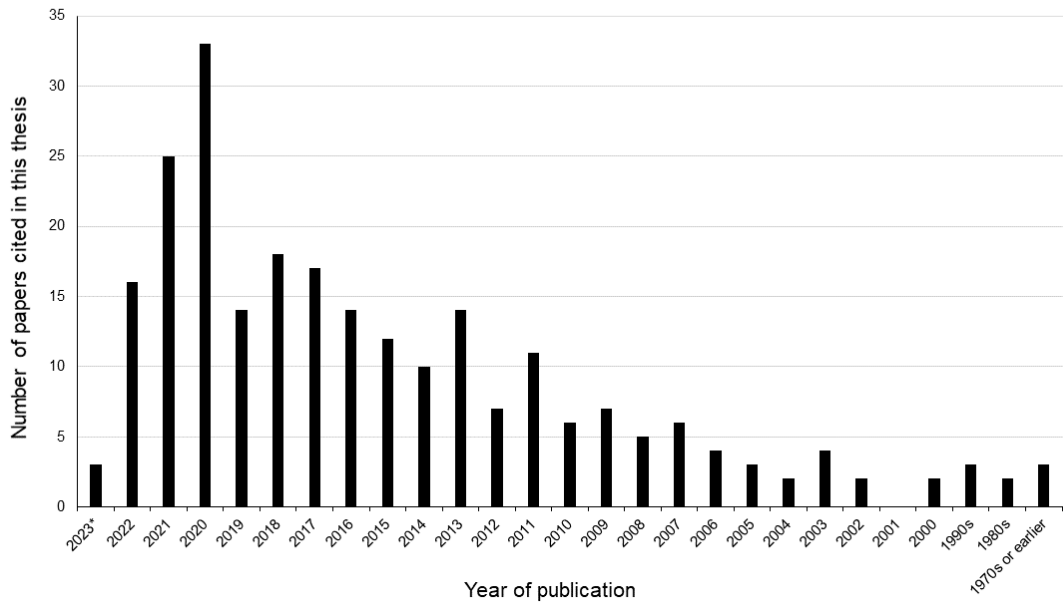
Figure 5.1. Bar chart displaying the number of papers cited in this thesis by publication date. Note how there is a gradual increase in the number of cited papers since 2000, indicative of a growing focus on Antarctic meltwater, and the particularly high number of publications from the past 5-6 years.

During approximately the same time period, there has been an exponential increase in the use of GEE for geospatial data science analysis (Pérez-Cutillas et al., 2023). A systematic review by Pérez-Cutillas et al. (2023) shows that GEE was used in more research papers between 2020 and 2022 than in the whole previous decade, following its initial release in 2010. However, the use of the platform within climate and cryospheric science has remained relatively sparse, and applications in Antarctica have been minimal (Pérez-Cutillas et al., 2023). Prior to the start of this thesis, the potential for using GEE to study meltwater on ice sheets had been demonstrated in Greenland (Lea & Brough, 2019), but the platform had rarely been used to study Antarctic meltwater. A key goal of this thesis was therefore to combine recent methodological progress in meltwater detection (Moussavi et al., 2020) with the processing capabilities of GEE, to advance the scale at which surface meltwater analysis could be conducted.

The most significant methodological contribution from my work is the development of a fully automated and open access method for mapping surface meltwater within GEE, capable of performing continent-wide analysis. The automated analysis of 133,497

Landsat satellite images (taking approximately three weeks of wall-clock time; Chapter 4) represents a step change in scale of analysis compared to previous meltwater mapping studies. This is only the second use of GEE at an Antarctic-wide scale (Liang et al., 2021; Pérez-Cutillas et al., 2023), and the first to map surface meltwater across the whole Antarctic continent. By using a time-window approach that involves looping over several ROI tiles (Section 2.3), the method is easily adaptable for application over a range of spatial and temporal scales. Chapter 2, for example, highlights how a reduced time window length can be used to generate higher temporal resolution data in regions with typically cloud-free conditions and frequent satellite coverage. Time window length could be reduced further to generate weekly or even daily data, providing sufficiently frequent satellite images are available in GEE. The continent-wide dataset presented in Chapter 4 can easily be updated on an annual basis with minimal user input required.

The framework of my mapping method has a variety of potential other applications for the study of land surface change through time. The use of optical satellite data for producing time series has common limitations regardless of scientific application; namely that it is restricted by uncertainty induced by cloud cover and image acquisition frequency. In Chapter 2, I present a novel method to account for such uncertainty, which enables the generation of consistent and continuous time series from optical data. Whilst I used a set of thresholds to detect surface meltwater in Antarctica, alternative thresholds could be used to investigate a range of earth surface changes in different locations. For example, the NDSI (Eq. 2.1; Section 2.3.2) could be used to assess monthly changes in snow cover over mountainous regions. Alternatively, the NDWI could be used to assess changes in the abundance and extent of proglacial lakes. Applications in disciplines outside of cryospheric science are also possible. By making only minor alterations to the GEE code, my method could, for example, be used to generate robust time series of vegetation cover change. By making the code open-access, it is therefore hoped that the method framework presented in Chapter 2 could be used for a wide range of remote sensing applications.

This thesis presents methodological advances in the generation of supraglacial lake volume time series (Chapter 3). Similarly to the assessment of lake area, generating lake volume time series has typically been limited in temporal and spatial scope. Supraglacial lakes studies from Greenland and Antarctica have commonly used a physically-based model for calculating lake depths and volumes (Sneed & Hamilton, 2007; Pope et al., 2016). Whilst versions of this model have previously been implemented within GEE

(Chudley, pers. comm., 2021; Zhu et al., 2022), no known studies have automated the generation of lake specific volume times series for multiple lakes across a region within GEE. In Chapter 3, I build upon previous work (Chudley, pers. comm., 2021) to automate the production of lake volume time series for multiple lakes at once. This enables detailed assessment of lake evolution processes, knowledge of which are important for constraining surface hydrology models (Datta & Wouters, 2021). Furthermore, I present a novel method that uses MODIS data in combination with data from higher spatial resolution optical satellites to increase the temporal resolution of lake volume data. Whilst this method is still in its infancy and requires further exploration, it shows strong potential for constraining the magnitudes and timings of volume changes for large (<0.5 km^2) supraglacial lakes. Though many of the processing steps have been automated throughout the thesis, this chapter highlights how there is still an important role for manual analysis when interpreting or validating data.

5.2.2 Methodological limitations and directions for future research

Methodological developments presented in this thesis advance our ability to assess the distribution and evolution of Antarctic surface meltwater. Nevertheless, there are some limitations to the work presented, and there remain several knowledge gaps in our understanding of controls on surface meltwater ponding in Antarctica. The findings of this thesis motivate further work to investigate links between surface hydrology, near-surface climate and ice surface conditions. Such further research is ultimately required to predict what impacts surface meltwater will have on future ice sheet mass balance.

Whilst the automated surface meltwater mapping method (Chapter 2) presented in this thesis offers significant methodological advances (Section 5.2.1), the method has some limitations. The use of a threshold-based method at a continent-wide scale inevitably results in some misclassification errors, although these were deemed minimal (Section 4.3.1). Variability in the threshold-based detection of slush results in spatial and temporal inconsistencies in its contribution to meltwater area totals, which future work could look to address (Section 4.4.4). A larger limitation of my mapping approach is the exclusion of mapped meltwater outputs from optical satellite imagery with a sun elevation angle of greater than 20°. This step was taken to avoid misclassification errors in low light conditions (Halberstadt et al., 2020; Section 2.3.1). This limits consistent meltwater area

data to between November and February each melt season, despite the known existence of meltwater outside of these months (Kuipers Munneke et al., 2018). In the Amery Ice Shelf region, for example, manual analysis of optical images found that surface meltwater ponds can exist in the region as late as April. Meltwater area time series therefore sometimes 'miss' the end of the melt season, and are unable to provide insights on the potential occurrence of meltwater during winter months. This highlights a key limitation to conducting meltwater analysis from optical satellite data, which can be overcome using SAR mapping techniques (Kuipers Munneke et al., 2018; Dirscherl et al., 2020).

Limitations relating to uncertainties in the scaling up of meltwater area estimates based on visibility assessments are discussed in Sections 2.5.2 and 4.4.4. Future work could look to address some of these limitations in order to reduce uncertainty associated with 'maximum estimated' meltwater area totals. For example, it could be explored whether the visibility method could be adapted to incorporate the spatial clustering of meltwater within any given ROI. This would ensure that meltwater area totals are only scaled up for locations where surface meltwater is typically known to pond, helping to reduce potential overestimates in meltwater coverage. It could also be investigated whether the number of times (within a time window) that any individual pixel is identified as water is built into the visibility metric. This would help to reduce the chances of results being skewed by a small number of particularly cloudy images.

One of the most significant discoveries of this thesis is the increase in surface meltwater area in East Antarctica over the past 15 years (Chapter 4). The lack of a coincident increase in PDDs leads me to conclude that the increase is probably driven by changes in ice surface conditions, consequently facilitating greater ponding of meltwater. Whilst Chapter 4 focusses on interpreting ice-sheet scale trends, detailed regional analyses are required to test this hypothesis for individual ice shelves using near-surface climatic and modelled data. As demonstrated in Chapter 2, RACMO modelled snowmelt data could be compared with regional meltwater area time series to assess the proportion of melt that is translated into ponded water. Comparison of meltwater area data with modelled runoff and firn air content data would additionally enable better quantification of the extent to which meltwater can be accommodated within the firn pack. However, despite recent improvements in model capabilities, regional climate models (such as RACMO) struggle to resolve localised melt-albedo feedbacks (van Wessem et al., 2014; Lenaerts et al., 2018). Similarly, firn models are currently poor at capturing meltwater interactions, in

particular the impact of liquid water on firn densification (Verjans et al., 2019). Further work to improve parameterisations in such models is hence required to provide more accurate assessments of changes in firn and ice surface conditions. One potential avenue for future research could be to use my surface meltwater dataset to test the success of surface hydrology models (e.g. Buzzard et al., 2018).

The generation of a continent-wide meltwater area dataset provides opportunities for future work to investigate local, regional or ice-sheet wide climatic controls on meltwater ponding. Whilst Chapter 4 provides analysis of the most significant, ice-sheet scale results, there is substantial scope for future work to conduct in-depth, regionally focussed analyses of the dataset. For example, ERA5 reanalysis climatic data such as air temperature, solar radiation and near-surface wind speed could be compared with lake area data, as demonstrated by Arthur et al. (2022), to determine local controls on meltwater ponding. Of particular importance could be comparison of monthly precipitation data with meltwater area. Snow accumulation rates have been shown to control the air temperature threshold required for surface melt pond formation (van Wessem et al., 2023). Modelled results indicate that relatively wet ice shelves start to pond meltwater at around -5 °C, but drier, colder, ice shelves, such as those in East Antarctica, can experience meltwater ponding at temperatures well below -15 °C (van Wessem et al., 2023). These results should therefore be compared against observed meltwater area and climate data, to test the validity of model results.

Chapter 3 provides methodological steps towards improving assessments of supraglacial lake volumes. Temporal resolution of volume data remain a key limitation to determining timings and rates of volumetric changes (Section 3.4.3). Further work should therefore be conducted to explore alternative methods for constraining lake volume changes. A key challenge, as highlighted in Section 3.4.2, is translating lake volume time series into process understanding. The specific mechanism behind any particular volume change is difficult to identify without conducting corresponding manual optical image analysis, and even then, it can be hard to identify processes such as vertical drainage from 15-30 m resolution images. Field based measurements of individual lake basins would be invaluable for constraining the timing and magnitudes of lake volume change, and for developing process understanding, as demonstrated by work conducted in Greenland (e.g. Doyle et al., 2013; Chudley et al., 2019). Fieldwork would additionally enable the collection of *in situ* lake area and volume measurements, allowing comparison with data

derived from remote sensing. However, substantial logistical challenges are associated with Antarctic fieldwork, and remote sensing approaches offer a more widely available way of conducting volume assessments. Future work should therefore focus on improving the robustness and temporal resolution of remote sensing volume measurements, and could use alternative datasets (e.g. REMA elevation data) to improve understanding of processes such as channel damming and vertical drainage.

Lake volume data, presented in Chapter 3, were generated using an optical image-based algorithm (Section 3.3.3.3), yet measurements from IceSat-2 suggest that optically derived data typically underestimate lake depths by 30-70% (Fricker et al., 2021). The generation of accurate assessments of meltwater volumes across Antarctica therefore requires multi-satellite approaches. Although depth and volume comparisons between IceSat-2 and optical satellite derived data have been conducted at a regional scale (Fricker et al., 2021), the automation of lake volume time series presented in Chapter 3 opens up the potential for larger scale comparison between the two datasets.

A key benefit of using GEE is that the platform is open-access, meaning a large proportion of the methods presented in this thesis are fully available for anyone to use. However, the majority of the post-processing stages applied in Chapters 2-4 were undertaken in MATLAB, which is not freely available. It could therefore be explored whether the MATLAB code developed here could be adapted for use within the basic, free version of the software, or if the same post-processing techniques could be implemented into open-access programming software, such as Python.

5.3 Importance of surface meltwater in Antarctica

A central motivation for this thesis has been the potential impact that surface meltwater will have on the future mass balance of the AIS. Whilst the contents of Chapters 2-4 have focussed on assessing the distribution and evolution of surface meltwater, it is useful to consider what wider implications my results may have for the future of the ice sheet. Here, I first present a summary of work I conducted on the Antarctic Peninsula to investigate whether surface meltwater is influencing grounded ice dynamics at present-day. I then provide a wider discussion of the current impacts of surface meltwater in Antarctica, and speculate what future impacts it may have based on my findings.

5.3.1 Evidence from the Antarctic Peninsula

The potential for surface meltwater to impact grounded ice dynamics provides a high level of uncertainty in modelled predictions of future Antarctic mass balance (Bell et al., 2018; Bamber et al., 2019). Results from Chapter 4 show that, on average, 1244 km^2 of grounded ice across Antarctica is covered in surface meltwater each melt season, representing 30% of the total meltwater area (Section 4.3.2); a much greater amount than previously recognised. The potential for surface-to-bed connections to exist in Antarctica is therefore high, especially given their present-day existence in most other glaciated regions of the world (Section 1.2.3.2). The Antarctic Peninsula is the warmest region of Antarctica (Section 1.2.1), and is the sector of Antarctica that most closely resembles the glaciological and climatological conditions of the GrIS, where the impact of surface meltwater reaching the bed is well-studied (Bartholomew et al., 2012; Davison et al., 2019, 2020; Stevens et al., 2022; Section 1.2.3.2). Thus, the Antarctic Peninsula is the region where melt-driven ice dynamic effects are most likely to occur, and where the most research investigating this has been conducted (Section 1.2.3.3).

The discovery of rapid, transient ice flow accelerations at five outlet glaciers on the Antarctic Peninsula (Tuckett et al., 2019) has stimulated a debate in the glaciological community regarding their forcing mechanism. An initial hypothesis, put forward in Tuckett et al. (2019), is that surface meltwater is able to drain to the ice-bed interface, subsequently causing short-lived accelerations in ice velocity via modification of the subglacial drainage system (Section 1.2.3.3; Fig. 1.8). An alternative hypothesis, summarised in Rott et al. (2020), is that transient velocity variations are the consequence of changes in sea-ice conditions, which vary the level of back-stress on glacier flow. Rott et al. (2020) additionally suggest that the speed-up events reported in Tuckett et al. (2019) are a consequence of bias in the velocity data, resulting from variations in radar penetration depth due to presence or absence of water at the ice/snow surface. Radar penetration can vary as a glacier surface evolves between ice, firn, snow and water, introducing a bias that artificially increases or decreases velocity measurements (Rott et al., 2020; Fig. 5.2). For glaciers flowing westward on the Antarctic Peninsula, a switch from frozen to melted firn would induce an apparent slow-down, with an apparent speed-up occurring during surface freezing (Fig. 5.2a-b). The bias effect would be expected to

be greatest at glaciers with ice flow perpendicular to the satellite heading (which is approximately north-south on the Antarctic Peninsula), whilst bias should be close to zero at glaciers flowing parallel to the satellite path (Fig. 5.2c-d).

Whilst exploring these two hypotheses (Tuckett et al., 2019; Rott et al., 2020) was not a primary objective of this thesis, I conducted further work to investigate whether velocity variations on the Antarctic Peninsula can be attributed to surface meltwater forcing. This work was partly conducted in preparation for a NSF-NERC grant proposal, which aims to test the existence of melt-driven dynamic responses on the Antarctic Peninsula through a combination of field-based and remote sensing methods. I processed Sentinel-1 derived ice velocity data for Flask and Edgeworth Glaciers on the Antarctic Peninsula, and explored potential bias in velocity measurements. Velocity data were generated for Flask Glacier as this is the target field site for the NSF-NERC project, whilst data were processed for Edgeworth Glacier because it flows close to parallel with the Sentinel-1 satellite heading angle. This means that the effect of potential radar-penetration bias should be minimal (Fig. 5.2). The method applied to generate velocity data is described in Tuckett et al. (2019).
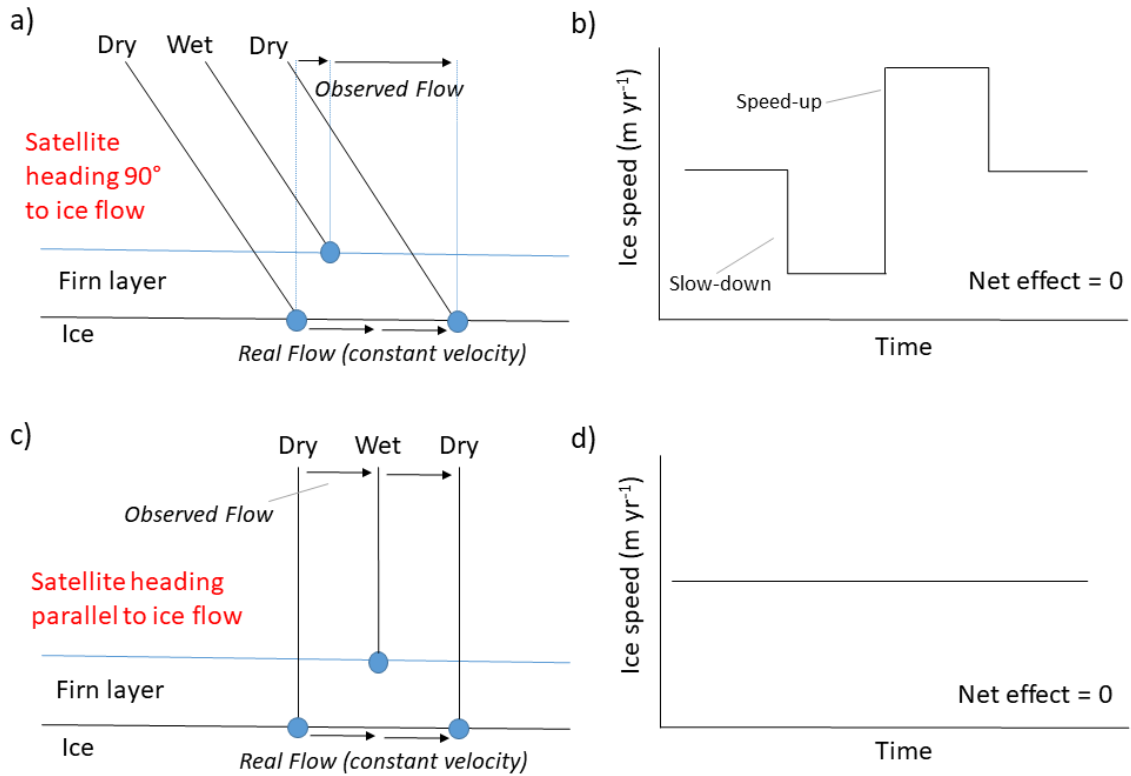
Figure 5.2. Schematic showing the potential influence (bias) of variations in radar penetration depth on ice velocity data for a glacier of constant flow. (a) and (c) show changes in radar penetration depth for glaciers flowing perpendicular (a) and parallel (c) to the satellite heading angle. Both examples show the effect induced from a change from frozen (dry) to wet firn (due to a melt event), and back to frozen. Black lines represent radar penetration depth, with blue dots indicating the position of radar reflectance measurements. Note how the radar penetrates deeper when the firn layer is dry, compared to when it is wet. Black arrows indicate the size of 'real' and 'observed' changes in displacement, with longer arrows indicating greater displacement. (b) and (d) display the corresponding effects on ice velocity of the scenarios shown in (a) and (c) respectively. Note how an apparent slow-down and subsequent speed-up occurs for the glacier flowing perpendicular to the satellite heading, whilst there is no change in measured ice velocity for the glacier flowing parallel to the satellite path.

Ice velocity data from Flask Glacier show significant accelerations which coincide with spikes in modelled snowmelt (Fig. 5.3). Transient accelerations are observed in three of the four melt seasons for which velocity data were generated (Fig. 5.3). As observed at other glaciers in the region (Tuckett et al., 2019), speed-up events are immediately followed by a subsequent slow-down. The largest speed-up events observed at Flask

Glacier, and at the five glaciers studied in Tuckett et al. (2019), all coincide with spikes in surface melt, but they do not all coincide with major changes in sea-ice (the hypothesis put forward by Rott et al. (2020)). The evacuation of sea-ice at the front of glaciers feeding the Larsen B embayment coincides with one of the major speed-up events reported in Tuckett et al. (2019), although this occurs beyond ~90 km of unchanged multi-annual fast pack ice. I interpret this sea-ice movement to be a by-product of föehn winds, which are also the trigger of large surface melt events. The observed deceleration in ice velocity following speed-up events cannot be explained by the sea-ice hypothesis, since sea-ice is not observed to reform to its pre-breakup structure. Conversely, the potential for subglacial hydrological systems to adapt to variations in surface meltwater supply provides a clear explanation for observed accelerations and subsequent slow-downs (Section 1.2.3.2). For further evidence assessing the two hypotheses, see Tuckett et al. (2020).
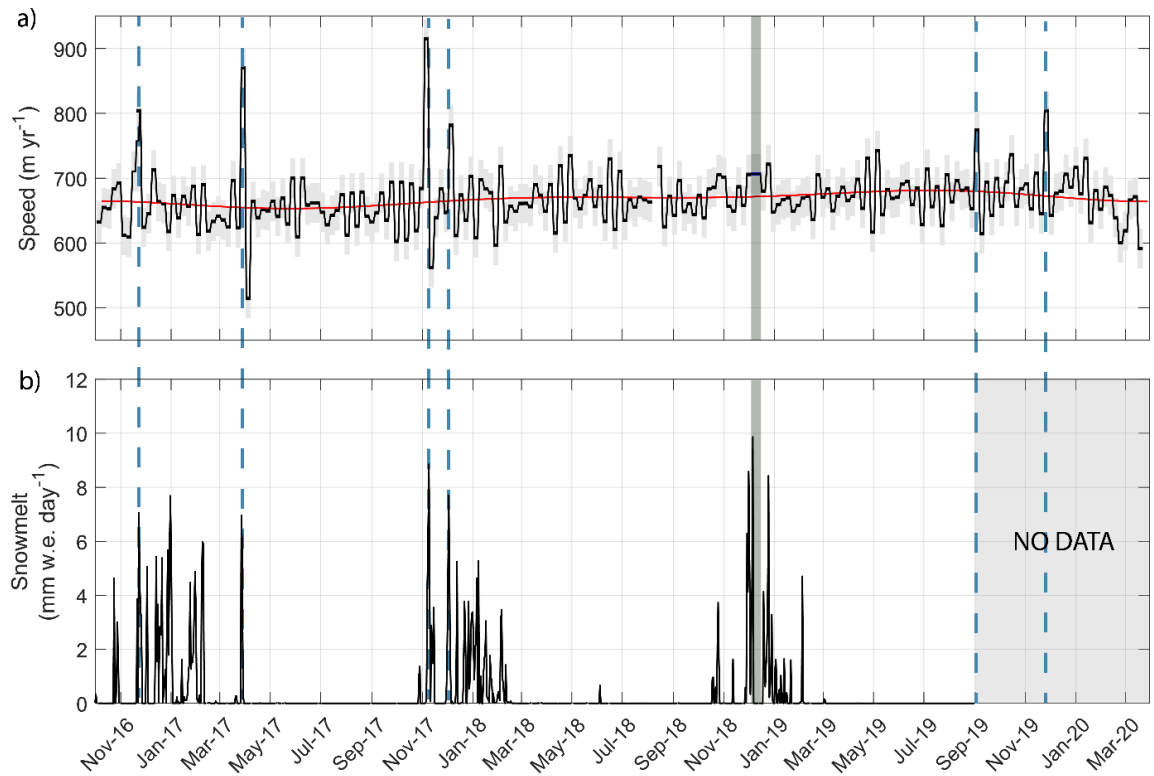
Figure 5.3. (a) Surface velocity times series for Flask Glacier between October 2016 and March 2020. Most data are from 6-day Sentinel-1 SAR image pairs, whilst the grey vertical bar indicates a 12-day pair. (b) RACMO modelled snowmelt from the same area and time period. Dashed vertical blue lines indicate speed-up events that coincide with peaks in surface melting. The lack of speed-up during the 2018/19 melt season could be because the largest melt event coincides with a 12-day velocity pair, which may have averaged out a speed-up and subsequent slow-down.

To test the possibility that speed-up events and subsequent slow-downs are the consequence of radar penetration bias, I processed velocity data for Edgeworth Glacier, which flows close to parallel with the satellite heading angle (Fig. 5.4). Hence, any bias in the velocity data resulting from changes in radar penetration depth should be close to zero. Figure 5.4 shows how similar speed-ups events are observed at Edgeworth Glacier, which also coincide with spikes in surface melt. The speed-up events, approximately 200 m yr^{-1} greater than baseline flow (Fig. 5.4), occur at the same time as those observed in Tuckett et al. (2019). The existence of speed-up events on this glacier suggests that accelerations are real, and not the consequence of radar penetration bias. Surface meltwater is observed ~15 km upglacier from the calving front (Fig. 5.4), providing further evidence in support of a melt-driven trigger.
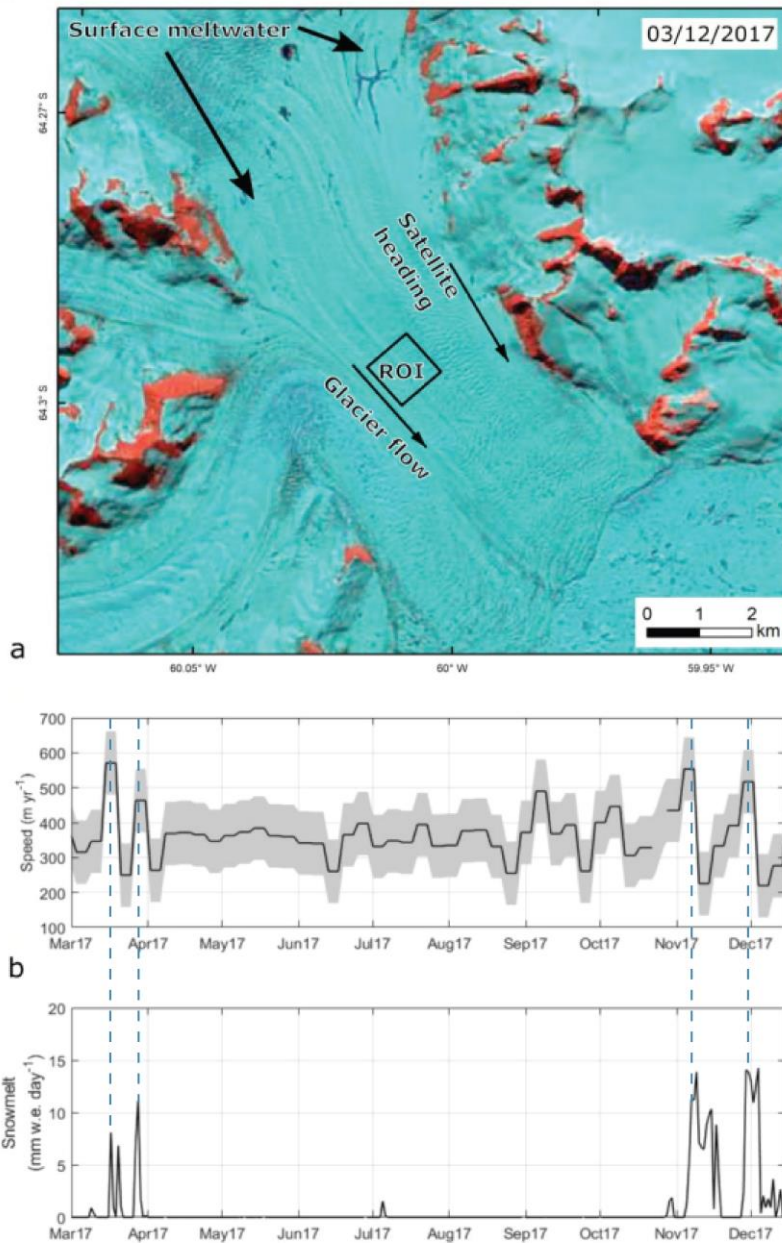
Figure 5.4. (a) Landsat image of Edgeworth glacier on the Antarctic Peninsula, highlighting the presence of surface meltwater features high-up on the glacier. The 1 x 1 km ROI, from which velocity data were extracted, contains ice flowing almost parallel to the satellite heading. (b) Surface ice velocity and RACMO modelled melt from the ROI. Note how melt events coincide with glacier speed-ups, which are highlighted by the dashed vertical blue lines.

The data from Flask Glacier (Fig. 5.3) and Edgeworth Glacier (Fig. 5.4) suggest that speed-up events are not solely the cause of methodological bias, and that surface meltwater is a more likely explanation for their trigger than changes in sea-ice. Speed-up events at Flask Glacier and the glaciers studied in Tuckett et al. (2019) have a net positive

effect (i.e., speed-ups are bigger than subsequent slow-downs; Fig. 5.3), yet accelerations are short-lived and therefore don't appear to have a major impact on overall mass loss. However, more recent work shows that glaciers in western and southern regions of the Antarctic Peninsula experience seasonal ice speed-ups, which appear to have a more significant impact on annual mass flux (Boxall et al., 2022; Wallis et al., 2022). Boxall et al. (2022) propose both surface meltwater and oceanic factors as potential forcing mechanisms for these seasonal signals.

The greater potential impact of widespread seasonal velocity signals on mass balance emphasises the importance of ascertaining their cause. The relatively low temporal resolution of satellite-derived velocity data (6-day minimum for Sentinel-1), combined with potential issues of bias from changes in radar penetration depth, highlight the need for fieldwork to conclusively determine the cause of speed-ups. *In situ* GPS velocity data would enable both horizontal and vertical displacement to be measured at sub-minute temporal resolution, providing significantly greater insight on the cause of velocity variability. Field sensors could also be used to independently test for surface meltwater presence in the subglacial environment. For example, autonomous phase-sensitive radio-echo sounders (ApRES) could be used to track changes at the ice-bed interface, providing independent assessment of whether surface meltwater reaches the bed during high melt events (Livingstone et al., 2017). Passive seismometers could additionally be used to monitor glacio-hydrualic tremors, which can provide an indication of turbulence associated with subglacial water flow (Nanni et al., 2020). Finally, a field campaign to collect ground-truth velocity measurements would enable quantification of potential bias in radar satellite-derived velocity data. By quantifying the effect of radar penetration bias on velocity data, remote sensing measurements of ice velocity could be improved in Antarctica and Greenland more broadly.

5.3.2 Present-day influence of surface meltwater

The present-day direct influence of surface meltwater on mass balance across the majority of Antarctica is minimal (Smith et al., 2020). Air temperatures are currently too low for meltwater runoff to have a significant impact on surface mass balance, and evidence for surface meltwater influencing grounded ice flow and ice shelf stability has been limited to the Antarctic Peninsula (Section 1.2.4). However, for the first time, this thesis

quantifies the area of Antarctica that is covered in surface meltwater each year, highlighting substantial amounts of water on both grounded and floating ice (Section 4.3.2). There remains a commonly held view in the wider glaciological community that surface melting in Antarctica is negligible, meaning the magnitude and extent of surface meltwater highlighted in this thesis may be of surprise to many. Furthermore, my results indicate that the area of surface meltwater is increasing in several regions of Antarctica, and further increases are likely (Trusel et al., 2015; Section 4.4.4). It is therefore hoped that this thesis, combined with other significant findings on Antarctic surface hydrology that have been published during my doctoral programme (e.g. Lai et al., 2020; Boxall et al., 2022; Arthur et al., 2022; van Wessem et al., 2023), will motivate further investigation into potential links between surface melting, ice shelf stability and grounded ice dynamics.

A growing body of evidence suggests that surface-to-bed hydraulic connections exist on grounded ice at the Antarctic Peninsula (Section 5.3.1; Tuckett et al., 2019; Boxall et al., 2022; Hodgson et al., 2022; Wallis et al., 2022), and it is possible that similar discoveries have not been made elsewhere in Antarctica simply due to a lack of investigation. Further studies investigating potential links between surface melting and grounded ice dynamics are hence required at an Antarctic-wide scale. My continent-wide meltwater area dataset (Chapter 4) could be used as a basis for identifying target regions where ponded meltwater is most likely to reach the bed. Regions for initial investigation could include grounded sections of Rennick Glacier (Fig. 4.10), Lambert Glacier (Fig. 2.1), and the outlet glaciers feeding Shackleton Ice Shelf (Fig. 4.10). Furthermore, regionally focussed studies should be conducted to search for evidence of grounded lake drainage events. Chapter 3 demonstrates novel methods for assessing lake area and volume changes from optical imagery in the Amery region. Such approaches could be applied to other regions of Antarctica to identify potential instances of surface meltwater draining to the ice sheet bed. Combining observations of surface meltwater change with ice velocity data offers the best approach for identifying melt-driven dynamic effects.

At present, Antarctic ice shelves which experience the most surface meltwater ponding (including Amery, Roi Baudouin, and George VI; Section 4.3.2) are largely resilient to meltwater-driven hydrofracture and collapse (Lai et al., 2020). For example, results from Chapters 2 and 4 show that surface meltwater covers (on average) a larger area of the Amery Ice Shelf than any other ice shelf in Antarctica. However, meltwater is strongly spatially clustered (Section 2.4.2), and substantial lateral buttressing from the valley sides

results in relatively low tensile longitudinal resistive stresses across the Amery Ice Shelf. This means that increased meltwater ponding is unlikely to cause its rapid break-up (Lai et al., 2020). Similarly, a compressive flow regime at George VI Ice Shelf means that the ice shelf is relatively stable (Lai et al., 2020; Banwell et al., 2021), despite hosting large quantities of surface meltwater during high melt years (Section. 4.3.3). The two largest ice shelves in Antarctica, the Ronne and Ross ice shelves (Fig. 1.3), experience almost no surface meltwater ponding (Fig. 4.9) and are therefore not presently vulnerable to hydrofracture. However, the potential future presence of surface meltwater near the calving front of an ice shelf could cause small-scale breakup events, even if the majority of the ice shelf remains stable.

Other ice shelves around Antarctica may be at more immediate risk to melt-driven collapse. My results show that several East Antarctic ice shelves have experienced significant increases in surface meltwater area in recent years (Fig. 4.13). One such region is Shackleton Ice Shelf, which has been previously identified as susceptible to hydrofracture (Arthur et al., 2022). Arthur et al. (2022) observe that some meltwater on Shackleton Ice Shelf intersects with regions of ice deemed as vulnerable to hydrofracture by Lai et al. (2020). For the first time, this thesis additionally reveals that Shackleton Ice Shelf has experienced consistent increases in meltwater area for the past 15 years (Fig. 4.13). As a consequence of this increasing trend, meltwater is already starting to extend away from the grounding zone to cover a more extensive area of the ice shelf. At present, less than 1% of Shackleton Ice Shelf is covered in meltwater each melt season (Fig. 4.11), but proportionally larger increases in meltwater ponding may occur alongside increasing melt rates (Section 4.4.4). A recent modelling study shows that the ice shelf will reach the temperature threshold required for widespread meltwater ponding by the end of the century, even under moderate warming scenarios (van Wessem et al., 2023). Hence, the ice shelf may be at risk of hydrofracture in coming decades.

5.3.3 Climatic influences on future melt rates

Predicting future surface meltwater extent across Antarctica relies on our ability to model ice surface processes based on projected climate scenarios. Results from Chapter 2 show a strong association between meltwater area and RACMO modelled snowmelt, providing confidence in the ability of this model to predict future melt conditions in this region.

These results show that modelled melt rates from RACMO could be used to generate first-order predictions of surface meltwater area at an annual scale in the Amery region. However, some melt conditions that lead to the formation of lakes are not currently well captured by RACMO, such as the influence of blue ice on lake formation (Fig. 2.17). Snowmelt-albedo feedbacks have a particularly strong influence on melt rates in East Antarctica (Jakobs et al., 2021), and further work is required to represent this process within mass balance models. Future work should also evaluate whether a similar relationship between modelled melt and lake area occurs for other areas in Antarctica. The surface characteristics of some regions may preclude the formation of surface lakes (e.g. if firn aquifers are present; Montgomery et al., 2020; van Wessem et al., 2021), resulting in a weaker association between modelled melt and observed lakes, even if modelled estimates are broadly accurate. It is also likely that variations in hypsometry and lateral meltwater transfer alter the lag I find between modelled melt and peak meltwater ponding (Fig. 2.13, Table 2.4).

This thesis has demonstrated links between meltwater area and large-scale modes of climate variability. The SAM is shown to influence meltwater area on an annual basis for the Amery region (Section 2.4.4), and across East Antarctica as a whole, whilst the ASL is shown to be more influential on the Antarctic Peninsula (Section 4.3.4). The influence of the SAM on future meltwater cover across Antarctica will likely be influenced by trends in both stratospheric ozone levels and greenhouse gas emissions (Fogt & Marshall, 2020). Stratospheric ozone depletion has led to positive trends in the SAM in the austral summer season over recent decades, although there are signs that recovery of the stratospheric ozone hole is starting to counter this trend (Banerjee et al., 2020). Increases in greenhouse gas emissions have been shown to have a secondary influence on the SAM by strengthening the mid-to-high latitude temperature gradient, hence resulting in a more positive SAM (Arblaster et al., 2006). Future melt rates will therefore likely be influenced by several competing climatic factors, with enhanced melt from regional warming (Trusel et al., 2015) and near-surface feedbacks potentially being offset by decreased melt associated with a positive SAM. The absolute depth of the ASL is strongly connected to the SAM, and increased meltwater production may occur in the future on the Antarctic Peninsula as a result of a deepening ASL (Raphael et al., 2016). However, the largest melt events on the Peninsula will likely be determined by the frequency and magnitude of extreme weather events (Feron et al., 2021; Chapter 4). In addition to influencing melt

rates, more frequent extreme weather events might increase atmospheric river activity (Wille et al., 2021) and enhance the size of ocean swell-waves, which could contribute to the disintegration of ice shelves in the region (Massom et al., 2018; Christie et al., 2022).

5.4 Implications on future mass balance

The impact that increasing surface melt rates will have on the future mass balance of the AIS is uncertain. On grounded ice, it seems inevitable that surface-to-bed connections will become increasingly common around the Antarctic margin as surface melt rates rise. If, as predicted (Trusel et al., 2015), large parts of Antarctica begin to experience melt rates akin to those observed in present-day Greenland over the remainder of the 21st century (Section 1.1), there appears no logical reason why melt-dynamic processes observed in Greenland (and elsewhere) would not also occur in Antarctica.

In Chapter 1, I introduced a continuum of melt-dynamic regimes, whereby the dynamic response of an ice mass to meltwater input varies based on subglacial drainage efficiency and the magnitude and timing of meltwater injection (Fig. 1.9). At present, glaciers on the Antarctic Peninsula likely lie near the start of this continuum, either displaying transient speed-up events in response to a surface melt event (Tuckett et al., 2019), or a seasonal signal in response to a short summer melt season (Boxall et al., 2022; Wallis et al., 2022). As Antarctic melt seasons become longer and increase in melt magnitude (Feron et al., 2021), it is likely that Antarctic Peninsula glaciers will shift along this continuum to a state of stronger hydrological influence. This could result in a similar situation to that currently observed in Arctic Canada, where the influence of individual melt events are superimposed on a seasonal velocity signal (Wyatt & Sharp, 2015). Furthermore, glaciers or ice streams in other regions of Antarctica (that currently have no melt-dynamic association) may enter onto the continuum. Meltwater forced hydraulic connections between the surface and bed are observed at a variety of settings around the world, ranging from small mountain valley glaciers (e.g. Iken & Bindschadler, 1986; Nienow et al., 1998), to large tidewater outlet glaciers in Greenland (e.g. Davison et al., 2020). I therefore suggest that geographical location is unimportant in determining the occurrence, or lack, of melt-driven ice flow variability. Instead, I propose that where an ice mass sits on the melt-dynamic continuum is primarily a function of the volume and

rate of meltwater reaching the bed, and see no reason why large Antarctic outlet glaciers could not enter onto the continuum at some point in the future.

The effect that widespread melt-dynamic coupling would have on Antarctic mass balance is less clear. Research from the GrIS shows that the relationship between meltwater supply and ice velocity at tidewater glaciers is complex (Davison et al., 2020). Some Greenlandic tidewater glaciers have been shown to display so-called 'ice flow self-regulation' (Sole et al., 2013; van de Wal et al., 2015), whereby accelerations in ice velocity during summer months are mediated by a subsequent slowdown of roughly proportional magnitude. This scenario results in averaged ice velocities which are relatively insensitive to interannual variability in surface meltwater supply (van de Wal et al., 2015). Furthermore, over longer timescales, there is evidence to suggest that Greenlandic land-terminating glaciers experience slight decreases in net ice flow in response to increases in surface melt (Tedstone et al., 2015). However, some glaciers experience summer speed-ups without a slow-down to below pre-acceleration level, suggesting accelerations on annual timescales with enhanced surface melt (Moon et al., 2014). Were melt-driven velocity variations to start occurring at large Antarctic outlet glaciers, detailed field and remote sensing measurements would be required to understand the net effects on annual mass balance. The presence of ice shelves, sea ice and pinning points could all influence the dynamic response of any individual ice mass. The potential impact Antarctic-wide melt-dynamic responses on mass balance could be significant, and would open a new field of Antarctic research.

The impact of increasing surface melt rates on the stability of Antarctic ice shelves is potentially of larger concern. The future vulnerability of ice shelves will be strongly influenced by the magnitude, duration, and extent of surface meltwater that covers their surfaces; factors which directly influence the risk of hydrofracture. The quantity of meltwater on ice shelves will be dictated by ice shelf surface melt rates and the amount of water that flows onto ice shelves from the grounded ice sheet (Section 3.4.1). Results from Chapter 3 demonstrate the potential for large quantities of meltwater to flow downhill onto an ice shelf throughout a melt season. Atmospheric warming will likely increase the catchment size over which surface melting occurs on grounded ice, thus possibly increasing the magnitude of meltwater available to drain onto ice shelves. Increased surface melting might also influence rates of basal ice shelf melt. The drainage of surface meltwater to the bed on grounded ice could result in the subglacial discharge

of freshwater at the grounding line, driving enhanced circulation (Section 1.2.3). Evidence for enhanced basal melting from freshwater input has already been observed at Antarctic ice shelves (Le Brocq et al., 2013; Wei et al., 2020; Flexas et al., 2022), and it is possible that this process could become amplified by surface meltwater discharge associated with the development of surface-to-bed connections on grounded ice.

Future increases in surface melt rate will cause firn densification across ice shelf surfaces, likely resulting in increased ponding of meltwater (Bell et al., 2018). The risk of hydrofracture may be increased by enhanced fracture damage to ice shelf surfaces. Repeated cycles of melting and re-freezing at the ice surface releases latent heat, weakening the ice structure and making it more prone to future climatic perturbations (Hubbard et al., 2016). Furthermore, if meltwater starts to pond at higher elevations on a regular basis, crevasses on steeper topography may start to undergo enhanced hydrofracture processes (Tuckett et al., 2019). The advection of this weakened ice structure across the grounding line could precondition ice shelf surfaces to further fracturing from greater volumes of surface meltwater ponding (Dunmire et al., 2020). However, increased surface melt rates will likely be accompanied by increased snowfall accumulation, which could mediate the impact of melt. Enhanced snowfall on ice shelves would increase the thickness of the firn layer, enabling meltwater infiltration and refreezing, thus reducing the amount of melt that ponds on the surface. Increased snowfall would also act to limit melt-albedo feedbacks, which are particularly influential on melt initiation and ponding in East Antarctica (Trusel et al., 2013; Arthur et al., 2020).

Whilst most Antarctic ice shelves are not at imminent risk of melt-driven hydrofracture (Lai et al., 2020), my results show that the area of ice shelves covered in surface meltwater is already increasing across many regions of East Antarctica. The expansion of ponded water into ice shelf regions that are vulnerable to hydrofracture could ultimately contribute to their collapse. The extent to which melt increases translates to ponded water will be key, and whether meltwater remains on the ice shelf surface or if it is evacuated off the ice shelf via lateral meltwater transport (Bell et al., 2017). The impact on mass balance of potential future ice shelf collapse events will depend on the resultant volume changes in ice discharge across the grounding line. Although unlikely to occur this century, the full or partial collapse of the largest Antarctic ice shelves would have huge ramifications for mass loss and rates of global sea level rise.

5.5 Thesis conclusions

In this thesis, I have presented work that improves our understanding of the distribution and evolution of surface meltwater across the Antarctic Ice Sheet. By implementing existing and novel methodologies within GEE, I have been able to study surface meltwater at greater spatial and temporal scales than previously accomplished.

The most significant output from this thesis is the production of a long-term, high temporal resolution, continent-wide dataset of Antarctic surface meltwater (Chapter 4). This is the first dataset of its kind, and represents a leap in scale of processing compared to previous surface meltwater studies. The meltwater mapping method I have developed (Chapter 2) represents a significant step forward in monitoring capability. By implementing a fully automated meltwater mapping method within GEE, I have produced an open-access tool which could easily be applied to study surface meltwater in other ice-covered regions of the world, or be adapted for alternative geospatial mapping applications. Furthermore, the incorporation of a thorough method for assessing image visibility enables robust, continuous, and consistent time series to be produced that account for spatial and temporal variations in optical image visibility. Whilst my approach provides major methodological advances, there remain limitations to conducting meltwater mapping from optical satellite imagery, which could be overcome in future studies using SAR data.

Analysis of my continent-wide meltwater area dataset reveals new, and potentially highly significant, findings for Antarctica. Around the margin of the EAIS, there has been a significant increase (66 km^2 per year on average) in total annual surface meltwater area since 2006. This increase is observed for the ice sheet as a whole, and individually for several ice shelf regions including Amery, Roi Baudouin and Shackleton, the last of which is considered highly vulnerable to future warming. In the absence of a clear coincident warming trend, I attribute increases in meltwater area to ice sheet and ice shelf surfaces becoming more favourable to meltwater ponding. On the Antarctic Peninsula, there is high interannual variability in meltwater area, whilst the WAIS experiences lower, though more consistent annual meltwater area. Across the entire Antarctic continent, 30% of surface meltwater exists on grounded ice on average each year. This is considerably greater than has been previously documented, and highlights the importance of including grounded regions in future surface meltwater studies.

This thesis has explored climatic drivers on surface meltwater ponding, in particular exploring associations between surface meltwater area and large scale modes of climate variability. In East Antarctica, the SAM is shown to have a strong influence on total annual meltwater area, with greater meltwater area typically experienced in years with a negative SAM. At the Antarctic Peninsula, meltwater area is generally greatest in years with a deep (stronger) ASL, and when the ASL is centred closer to the region. These findings demonstrate broad scale links between meltwater area and atmospheric circulations for the first time, although regional analyses are required to understand specific controls on meltwater ponding at smaller spatial scales. Detailed analysis from the Amery Ice shelf region highlights the importance of melt-albedo feedbacks in controlling the spatial distribution of meltwater ponding, with surface meltwater particularly abundant in wind-scoured areas of blue ice (Chapter 2). I find strong and statistically significant correlations between RACMO-modelled snowmelt and meltwater area, providing confidence in the ability of the model to project future melt in the region. However, regional climate models often struggle to resolve localised melt-albedo feedbacks, and further work is required to improve parameterisations of glaciological and near-surface climatic processes.

I have explored styles of meltwater evolution at a grounding zone of the Amery Ice Shelf (Chapter 3), developing novel methods within GEE to study changes in supraglacial lake volume. Analysis of automatically generated lake volume time series, combined with manual optical image analysis, reveal a variety of lake evolution processes. Lakes can lose large proportions of their volume via lateral or vertical drainage events, although the freezing and unfreezing of lake surfaces can make automatically detecting which of these processes occurred challenging. By using MODIS data to improve the temporal resolution of lake volume estimates, I show that large volumetric changes can occur within two days. The automated generation of supraglacial lake volume time series within GEE improves our ability to investigate individual lake-scale evolution processes, although further work is required to constrain the magnitude and timing of lake drainage events. Process understanding from remote sensing can be limited by the temporal and spatial resolution of satellite imagery, and future work could look to utilise data from new satellite missions to overcome these challenges.

The findings of this thesis are potentially of concern for the future of the Antarctic Ice Sheet. The discovery that surface meltwater is now ponding more readily around the

periphery of East Antarctica suggests that ice shelves are becoming increasingly vulnerable to future increases in melt. Surface melt rates are expected to double by 2050 (Trusel et al., 2015), meaning surface meltwater will likely continue to increase in total area and extent. Additionally, the abundance of previously unreported surface meltwater on grounded ice highlights the potential for drainage of surface water to the ice sheet bed via hydrofracture. Surface-to-bed hydraulic connections, which are likely already in existence on the Antarctic Peninsula (Tuckett et al., 2019; Boxall et al., 2022), would enable a mechanism for the ice sheet to respond rapidly to climatic changes. Melt-albedo feedbacks mean that increases in meltwater ponding could be exponential, whilst the high proportion of meltwater near the grounding line could have important implications for ice dynamics and submarine melt processes if surface-to-bed connections become widespread. Although the impact of surface meltwater in Antarctica is currently negligible, atmospheric warming and coincident melting will become increasingly important in determining future Antarctic mass balance. Further work is hence required to identify the present-day impacts of surface meltwater on grounded ice dynamics and ice shelf stability, to better predict how the ice sheet will respond to future climatic changes.

References

Alley, K. E., Scambos, T. A., Miller, J. Z., Long, D. G., & MacFerrin, M. (2018). Quantifying vulnerability of Antarctic ice shelves to hydrofracture using microwave scattering properties. *Remote Sensing of Environment*, *210*, 297–306. https://doi.org/10.1016/j.rse.2018.03.025

Arblaster, J. M., & Meehl, G. A. (2006). Contributions of External Forcings to Southern Annular Mode Trends. *Journal of Climate*, *19*(12), 2896–2905. https://doi.org/10.1175/JCLI3774.1

Arthur, J. F., Stokes, C., Jamieson, S. S., Carr, J. R., & Leeson, A. A. (2020a). Recent understanding of Antarctic supraglacial lakes using satellite remote sensing. *Progress in Physical Geography: Earth and Environment*, *44*(6), 837–869. https://doi.org/10.1177/0309133320916114

Arthur, J. F., Stokes, C. R., Jamieson, S. S. R., Carr, J. R., & Leeson, A. A. (2020b). Distribution and seasonal evolution of supraglacial lakes on Shackleton Ice Shelf, East Antarctica. *The Cryosphere*, *14*(11), 4103–4120. https://doi.org/10.5194/tc-14-4103-2020

Arthur, J. F., Stokes, C. R., Jamieson, S. S. R., Miles, B. W. J., Carr, J. R., & Leeson, A. A. (2021). The triggers of the disaggregation of Voyeykov Ice Shelf (2007), Wilkes Land, East Antarctica, and its subsequent evolution. *Journal of Glaciology*, *67*(265), 933–951. https://doi.org/10.1017/jog.2021.45

Arthur, J. F., Stokes, C. R., Jamieson, S. S. R., Rachel Carr, J., Leeson, A. A., & Verjans, V. (2022). Large interannual variability in supraglacial lakes around East Antarctica. *Nature Communications*, *13*(1), Art. 1. https://doi.org/10.1038/s41467-022-29385-3

Aubry-Wake, C., Baraer, M., McKenzie, J. M., Mark, B. G., Wigmore, O., Hellström, R. Å., Lautz, L., & Somers, L. (2015). Measuring glacier surface temperatures with ground-based thermal infrared imaging. *Geophysical Research Letters*, *42*(20), 8489–8497. https://doi.org/10.1002/2015GL065321

Bamber, J. L., Oppenheimer, M., Kopp, R. E., Aspinall, W. P., & Cooke, R. M. (2019). Ice sheet contributions to future sea-level rise from structured expert judgment. *Proceedings of the National Academy of Sciences*, *116*(23), 11195–11200. https://doi.org/10.1073/pnas.1817205116

Banerjee, A., Fyfe, J. C., Polvani, L. M., Waugh, D., & Chang, K.-L. (2020). A pause in Southern Hemisphere circulation trends due to the Montreal Protocol. *Nature*, *579*(7800), Art. 7800. https://doi.org/10.1038/s41586-020-2120-4

Banwell, A. F., Caballero, M., Arnold, N. S., Glasser, N. F., Cathles, L. M., & MacAyeal, D. R. (2014). Supraglacial lakes on the Larsen B ice shelf,

Antarctica, and at Paakitsoq, West Greenland: A comparative study. *Annals of Glaciology*, *55*(66), 1–8. https://doi.org/10.3189/2014AoG66A049

Banwell, A. F., Datta, R. T., Dell, R. L., Moussavi, M., Brucker, L., Picard, G., Shuman, C. A., & Stevens, L. A. (2021). The 32-year record-high surface melt in 2019/2020 on the northern George VI Ice Shelf, Antarctic Peninsula. *The Cryosphere*, *15*(2), 909–925. https://doi.org/10.5194/tc-15-909-2021

Banwell, A. F., MacAyeal, D. R., & Sergienko, O. V. (2013). Breakup of the Larsen B Ice Shelf triggered by chain reaction drainage of supraglacial lakes. *Geophysical Research Letters*, *40*(22), 5872–5876. https://doi.org/10.1002/2013GL057694

Banwell, A. F., Willis, I. C., Macdonald, G. J., Goodsell, B., & MacAyeal, D. R. (2019). Direct measurements of ice-shelf flexure caused by surface meltwater ponding and drainage. *Nature Communications*, *10*(1), Art. 1. https://doi.org/10.1038/s41467-019-08522-5

Barrand, N. E., Vaughan, D. G., Steiner, N., Tedesco, M., Kuipers Munneke, P., van den Broeke, M. R., & Hosking, J. S. (2013). Trends in Antarctic Peninsula surface melting conditions from observations and regional climate modeling: Antarctic Peninsula Meltwater Trends. *Journal of Geophysical Research: Earth Surface*, *118*(1), 315–330. https://doi.org/10.1029/2012JF002559

Bartholomew, I., Nienow, P., Sole, A., Mair, D., Cowton, T., & King, M. A. (2012). Short-term variability in Greenland Ice Sheet motion forced by time-varying meltwater drainage: Implications for the relationship between subglacial drainage system behavior and ice velocity. *Journal of Geophysical Research: Earth Surface*, *117*(F3). https://doi.org/10.1029/2011JF002220

Bell, R. E., Banwell, A. F., Trusel, L. D., & Kingslake, J. (2018). Antarctic surface hydrology and impacts on ice-sheet mass balance. *Nature Climate Change*, *8*(12), 1044–1052. https://doi.org/10.1038/s41558-018-0326-3

Bell, R. E., Chu, W., Kingslake, J., Das, I., Tedesco, M., Tinto, K. J., Zappa, C. J., Frezzotti, M., Boghosian, A., & Lee, W. S. (2017). Antarctic ice shelf potentially stabilized by export of meltwater in surface river. *Nature*, *544*(7650), Art. 7650. https://doi.org/10.1038/nature22048

Bevan, S. L., Luckman, A. J., Kuipers Munneke, P., Hubbard, B., Kulessa, B., & Ashmore, D. W. (2018). Decline in Surface Melt Duration on Larsen C Ice Shelf Revealed by The Advanced Scatterometer (ASCAT). *Earth and Space Science*, *5*(10), 578–591. https://doi.org/10.1029/2018EA000421

Bingham, R. G., Hubbard, A. L., Nienow, P. W., & Sharp, M. J. (2008). An investigation into the mechanisms controlling seasonal speedup events at a High Arctic glacier. *Journal of Geophysical Research: Earth Surface*, *113*(F2). https://doi.org/10.1029/2007JF000832

References

Bingham, R. G., Nienow, P. W., & Sharp, M. J. (2003). Intra-annual and intra-seasonal flow dynamics of a High Arctic polythermal valley glacier. *Annals of Glaciology*, *37*, 181–188. https://doi.org/10.3189/172756403781815762

Boxall, K., Christie, F. D. W., Willis, I. C., Wuite, J., & Nagler, T. (2022). Seasonal land-ice-flow variability in the Antarctic Peninsula. *The Cryosphere*, *16*(10), 3907–3932. https://doi.org/10.5194/tc-16-3907-2022

Bromwich, D. H., Nicolas, J. P., Monaghan, A. J., Lazzara, M. A., Keller, L. M., Weidner, G. A., & Wilson, A. B. (2013). Central West Antarctica among the most rapidly warming regions on Earth. *Nature Geoscience*, *6*(2), Art. 2. https://doi.org/10.1038/ngeo1671

Budd, W. (1966). The Dynamics of the Amery Ice Shelf. *Journal of Glaciology*, *6*(45), 335–358. https://doi.org/10.3189/S0022143000019456

Budd, W., Landon Smith, I., & Wishart, E. (1967). The Amery Ice Shelf. *Physics of Snow and Ice: Proceedings*, *1*, 447–467.

Buzzard, S. C., Feltham, D. L., & Flocco, D. (2018). A Mathematical Model of Melt Lake Development on an Ice Shelf. *Journal of Advances in Modeling Earth Systems*, *10*(2), 262–283. https://doi.org/10.1002/2017MS001155

Buzzard, S., Feltham, D., & Flocco, D. (2018). Modelling the fate of surface melt on the Larsen C Ice Shelf. *The Cryosphere*, *12*(11), 3565–3575. https://doi.org/10.5194/tc-12-3565-2018

Christie, F. D. W., Benham, T. J., Batchelor, C. L., Rack, W., Montelli, A., & Dowdeswell, J. A. (2022). Antarctic ice-shelf advance driven by anomalous atmospheric and sea-ice circulation. *Nature Geoscience*, *15*(5), Art. 5. https://doi.org/10.1038/s41561-022-00938-x

Chudley, T. R., Christoffersen, P., Doyle, S. H., Bougamont, M., Schoonman, C. M., Hubbard, B., & James, M. R. (2019). Supraglacial lake drainage at a fast-flowing Greenlandic outlet glacier. *Proceedings of the National Academy of Sciences*, *116*(51), 25468–25477. https://doi.org/10.1073/pnas.1913685116

Clason, C. C., Mair, D. W. F., Nienow, P. W., Bartholomew, I. D., Sole, A., Palmer, S., & Schwanghart, W. (2015). Modelling the transfer of supraglacial meltwater to the bed of Leverett Glacier, Southwest Greenland. *The Cryosphere*, *9*(1), 123–138. https://doi.org/10.5194/tc-9-123-2015

Clem, K. R., Orr, A., & Pope, J. O. (2018). The Springtime Influence of Natural Tropical Pacific Variability on the Surface Climate of the Ross Ice Shelf, West Antarctica: Implications for Ice Shelf Thinning. *Scientific Reports*, *8*(1), Art. 1. https://doi.org/10.1038/s41598-018-30496-5

Cook, A. J., & Vaughan, D. G. (2010). Overview of areal changes of the ice shelves on the Antarctic Peninsula over the past 50 years. *The Cryosphere*, *4*(1), 77–98. https://doi.org/10.5194/tc-4-77-2010

Cooper, M. G., & Smith, L. C. (2019). Satellite Remote Sensing of the Greenland Ice Sheet Ablation Zone: A Review. *Remote Sensing*, *11*(20), Art. 20. https://doi.org/10.3390/rs11202405

Corr, D., Leeson, A., McMillan, M., Zhang, C., & Barnes, T. (2022). An inventory of supraglacial lakes and channels across the West Antarctic Ice Sheet. *Earth System Science Data*, *14*(1), 209–228. https://doi.org/10.5194/essd-14-209-2022

Cowton, T., Nienow, P., Sole, A., Wadham, J., Lis, G., Bartholomew, I., Mair, D., & Chandler, D. (2013). Evolution of drainage system morphology at a land-terminating Greenlandic outlet glacier. *Journal of Geophysical Research: Earth Surface*, *118*(1), 29–41. https://doi.org/10.1029/2012JF002540

Das, S. B., Joughin, I., Behn, M. D., Howat, I. M., King, M. A., Lizarralde, D., & Bhatia, M. P. (2008). Fracture Propagation to the Base of the Greenland Ice Sheet During Supraglacial Lake Drainage. *Science*, *320*(5877), 778–781. https://doi.org/10.1126/science.1153360

Datta, R. T., Tedesco, M., Fettweis, X., Agosta, C., Lhermitte, S., Lenaerts, J. T. M., & Wever, N. (2019). The Effect of Foehn-Induced Surface Melt on Firn Evolution Over the Northeast Antarctic Peninsula. *Geophysical Research Letters*, *46*(7), 3822–3831. https://doi.org/10.1029/2018GL080845

Datta, R. T., & Wouters, B. (2021). Supraglacial lake bathymetry automatically derived from ICESat-2 constraining lake depth estimates from multi-source satellite imagery. *The Cryosphere*, *15*(11), 5115–5132. https://doi.org/10.5194/tc-15-5115-2021

David, S. T. W. and Priestly, R. E. (1912) Geological Notes of the British Antarctic Expedition, 1907-09, 45 pp.

Davies, B. J., Darvill, C. M., Lovell, H., Bendle, J. M., Dowdeswell, J. A., Fabel, D., García, J.-L., Geiger, A., Glasser, N. F., Gheorghiu, D. M., Harrison, S., Hein, A. S., Kaplan, M. R., Martin, J. R. V., Mendelova, M., Palmer, A., Pelto, M., Rodés, Á., Sagredo, E. A., … Thorndycraft, V. R. (2020). The evolution of the Patagonian Ice Sheet from 35 ka to the present day (PATICE). *Earth-Science Reviews*, *204*, 103152. https://doi.org/10.1016/j.earscirev.2020.103152

Davison, B. J., Sole, A. J., Cowton, T. R., Lea, J. M., Slater, D. A., Fahrner, D., & Nienow, P. W. (2020). Subglacial Drainage Evolution Modulates Seasonal Ice Flow Variability of Three Tidewater Glaciers in Southwest Greenland. *Journal of Geophysical Research: Earth Surface*, *125*(9), e2019JF005492. https://doi.org/10.1029/2019JF005492

References

Davison, B. J., Sole, A. J., Livingstone, S. J., Cowton, T. R., & Nienow, P. W. (2019). The Influence of Hydrology on the Dynamics of Land-Terminating Sectors of the Greenland Ice Sheet. *Frontiers in Earth Science*, *7*, 10. https://doi.org/10.3389/feart.2019.00010

de Roda Husman, S., Hu, Z., Wouters, B., Munneke, P. K., Veldhuijsen, S., & Lhermitte, S. (2022). Remote Sensing of Surface Melt on Antarctica: Opportunities and Challenges. *IEEE Journal of Selected Topics in Applied Earth Observations and Remote Sensing*, 1–20. https://doi.org/10.1109/JSTARS.2022.3216953

DeConto, R. M., & Pollard, D. (2016). Contribution of Antarctica to past and future sea-level rise. *Nature*, *531*(7596), 591–597. https://doi.org/10.1038/nature17145

Dell, R., Arnold, N., Willis, I., Banwell, A., Williamson, A., Pritchard, H., & Orr, A. (2020). Lateral meltwater transfer across an Antarctic ice shelf. *The Cryosphere*, *14*(7), 2313–2330. https://doi.org/10.5194/tc-14-2313-2020

Dell, R. L., Banwell, A. F., Willis, I. C., Arnold, N. S., Halberstadt, A. R. W., Chudley, T. R., & Pritchard, H. D. (2022). Supervised classification of slush and ponded water on Antarctic ice shelves using Landsat 8 imagery. *Journal of Glaciology*, *68*(268), 401–414. https://doi.org/10.1017/jog.2021.114

Depoorter, M. A., Bamber, J. L., Griggs, J. A., Lenaerts, J. T. M., Ligtenberg, S. R. M., van den Broeke, M. R., & Moholdt, G. (2013). Calving fluxes and basal melt rates of Antarctic ice shelves. *Nature*, *502*(7469), Art. 7469. https://doi.org/10.1038/nature12567

Ding, Q., Steig, E. J., Battisti, D. S., & Wallace, J. M. (2012). Influence of the Tropics on the Southern Annular Mode. *Journal of Climate*, *25*(18), 6330–6348. https://doi.org/10.1175/JCLI-D-11-00523.1

Dirscherl, M. C., Dietz, A. J., & Kuenzer, C. (2021). Seasonal evolution of Antarctic supraglacial lakes in 2015–2021 and links to environmental controls. *The Cryosphere*, *15*(11), 5205–5226. https://doi.org/10.5194/tc-15-5205-2021

Dirscherl, M., Dietz, A. J., Kneisel, C., & Kuenzer, C. (2020). Automated Mapping of Antarctic Supraglacial Lakes Using a Machine Learning Approach. *Remote Sensing*, *12*(7), 1203. https://doi.org/10.3390/rs12071203

Dirscherl, M., Dietz, A. J., Kneisel, C., & Kuenzer, C. (2021). A Novel Method for Automated Supraglacial Lake Mapping in Antarctica Using Sentinel-1 SAR Imagery and Deep Learning. *Remote Sensing*, *13*(2), 197. https://doi.org/10.3390/rs13020197

Donat-Magnin, M., Jourdain, N. C., Kittel, C., Agosta, C., Amory, C., Gallée, H., Krinner, G., & Chekki, M. (2021). Future surface mass balance and surface melt in the Amundsen sector of the West Antarctic Ice Sheet. *The Cryosphere*, *15*(2), 571–593. https://doi.org/10.5194/tc-15-571-2021

Doocey, E. (2020). The transfer of surface melt to the bed of the East Antarctic Ice Sheet and its impact on ice velocity. *Masters dissertation, The University of Sheffield.*

Doyle, S. H., Hubbard, A. L., Dow, C. F., Jones, G. A., Fitzpatrick, A., Gusmeroli, A., Kulessa, B., Lindback, K., Pettersson, R., & Box, J. E. (2013). Ice tectonic deformation during the rapid in situ drainage of a supraglacial lake on the Greenland Ice Sheet. *The Cryosphere*, *7*(1), 129–140. https://doi.org/10.5194/tc-7-129-2013

Dunmire, D., Lenaerts, J. T. M., Banwell, A. F., Wever, N., Shragge, J., Lhermitte, S., Drews, R., Pattyn, F., Hansen, J. S. S., Willis, I. C., Miller, J., & Keenan, E. (2020). Observations of Buried Lake Drainage on the Antarctic Ice Sheet. *Geophysical Research Letters*, *47*(15). https://doi.org/10.1029/2020GL087970

Echelmeyer, K., Clarke, T. S., & Harrison, W. D. (1991). Surficial glaciology of Jakobshavns Isbræ, West Greenland: Part I. Surface morphology. *Journal of Glaciology*, *37*(127), 368–382. https://doi.org/10.3189/S0022143000005803

Edwards, T. L., Nowicki, S., Marzeion, B., Hock, R., Goelzer, H., Seroussi, H., Jourdain, N. C., Slater, D. A., Turner, F. E., Smith, C. J., McKenna, C. M., Simon, E., Abe-Ouchi, A., Gregory, J. M., Larour, E., Lipscomb, W. H., Payne, A. J., Shepherd, A., Agosta, C., … Zwinger, T. (2021). Projected land ice contributions to twenty-first-century sea level rise. *Nature*, *593*(7857), Art. 7857. https://doi.org/10.1038/s41586-021-03302-y

Elvidge, A. D., Kuipers Munneke, P., King, J. C., Renfrew, I. A., & Gilbert, E. (2020). Atmospheric Drivers of Melt on Larsen C Ice Shelf: Surface Energy Budget Regimes and the Impact of Foehn. *Journal of Geophysical Research: Atmospheres*, *125*(17), e2020JD032463. https://doi.org/10.1029/2020JD032463

Elvidge, A. D., Renfrew, I. A., King, J. C., Orr, A., & Lachlan-Cope, T. A. (2016). Foehn warming distributions in nonlinear and linear flow regimes: A focus on the Antarctic Peninsula. *Quarterly Journal of the Royal Meteorological Society*, *142*(695), 618–631. https://doi.org/10.1002/qj.2489

Elvidge, A. D., Renfrew, I. A., King, J. C., Orr, A., Lachlan-Cope, T. A., Weeks, M., & Gray, S. L. (2015). Foehn jets over the Larsen C Ice Shelf, Antarctica. *Quarterly Journal of the Royal Meteorological Society*, *141*(688), 698–713. https://doi.org/10.1002/qj.2382

Ely, J. C., & Clark, C. D. (2016). Flow-stripes and foliations of the Antarctic ice sheet. *Journal of Maps*, *12*(2), 249–259. https://doi.org/10.1080/17445647.2015.1010617

Ely, J. C., Clark, C. D., Ng, F. S. L., & Spagnolo, M. (2017). Insights on the formation of longitudinal surface structures on ice sheets from analysis of their spacing, spatial distribution, and relationship to ice thickness and flow. *Journal of*

Geophysical Research: Earth Surface, *122*(4), 961–972.
https://doi.org/10.1002/2016JF004071

Fahrner, D., Lea, J. M., Brough, S., Mair, D. W. F., & Abermann, J. (2021). Linear
response of the Greenland ice sheet's tidewater glacier terminus positions to
climate. *Journal of Glaciology*, *67*(262), 193–203.
https://doi.org/10.1017/jog.2021.13

Feron, S., Cordero, R. R., Damiani, A., Malhotra, A., Seckmeyer, G., & Llanillo, P.
(2021). Warming events projected to become more frequent and last longer
across Antarctica. *Scientific Reports*, *11*(1), Art. 1.
https://doi.org/10.1038/s41598-021-98619-z

Fitzpatrick, A. a. W., Hubbard, A. L., Box, J. E., Quincey, D. J., van As, D., Mikkelsen,
A. P. B., Doyle, S. H., Dow, C. F., Hasholt, B., & Jones, G. A. (2014). A decade
(2002–2012) of supraglacial lake volume estimates across Russell
Glacier, West Greenland. *The Cryosphere*, *8*(1), 107–121.
https://doi.org/10.5194/tc-8-107-2014

Flexas, M. M., Thompson, A. F., Schodlok, M. P., Zhang, H., & Speer, K. (2022).
Antarctic Peninsula warming triggers enhanced basal melt rates throughout West
Antarctica. *Science Advances*, *8*(32), eabj9134.
https://doi.org/10.1126/sciadv.abj9134

Fogt, R. L., & Bromwich, D. H. (2006). Decadal Variability of the ENSO
Teleconnection to the High-Latitude South Pacific Governed by Coupling with
the Southern Annular Mode. *Journal of Climate*, *19*(6), 979–997.
https://doi.org/10.1175/JCLI3671.1

Fogt, R. L., Bromwich, D. H., & Hines, K. M. (2011). Understanding the SAM
influence on the South Pacific ENSO teleconnection. *Climate Dynamics*, *36*(7),
1555–1576. https://doi.org/10.1007/s00382-010-0905-0

Fogt, R. L., & Marshall, G. J. (2020). The Southern Annular Mode: Variability, trends,
and climate impacts across the Southern Hemisphere. *WIREs Climate Change*,
11(4), e652. https://doi.org/10.1002/wcc.652

Fretwell, P., Pritchard, H. D., Vaughan, D. G., Bamber, J. L., Barrand, N. E., Bell, R.,
Bianchi, C., Bingham, R. G., Blankenship, D. D., Casassa, G., Catania, G.,
Callens, D., Conway, H., Cook, A. J., Corr, H. F. J., Damaske, D., Damm, V.,
Ferraccioli, F., Forsberg, R., … Zirizzotti, A. (2013). Bedmap2: Improved ice
bed, surface and thickness datasets for Antarctica. *The Cryosphere*, *7*(1), 375–
393. https://doi.org/10.5194/tc-7-375-2013

Fricker, H. A., Young, N. W., Allison, I., & Coleman, R. (2002). Iceberg calving from
the Amery Ice Shelf, East Antarctica. *Annals of Glaciology*, *34*, 241–246.
https://doi.org/10.3189/172756402781817581

References

Fricker, H. A., Coleman, R., Padman, L., Scambos, T. A., Bohlander, J., & Brunt, K. M. (2009). Mapping the grounding zone of the Amery Ice Shelf, East Antarctica using InSAR, MODIS and ICESat. *Antarctic Science*, *21*(5), 515–532. https://doi.org/10.1017/S095410200999023X

Fricker, H. A., Arndt, P., Brunt, K. M., Datta, R. T., Fair, Z., Jasinski, M. F., Kingslake, J., Magruder, L. A., Moussavi, M., Pope, A., Spergel, J. J., Stoll, J. D., & Wouters, B. (2021). ICESat-2 Meltwater Depth Estimates: Application to Surface Melt on Amery Ice Shelf, East Antarctica. *Geophysical Research Letters*, *48*(8). https://doi.org/10.1029/2020GL090550

Fürst, J. J., Durand, G., Gillet-Chaulet, F., Tavard, L., Rankl, M., Braun, M., & Gagliardini, O. (2016). The safety band of Antarctic ice shelves. *Nature Climate Change*, *6*(5), Art. 5. https://doi.org/10.1038/nclimate2912

Gilbert, E., Orr, A., King, J. C., Renfrew, I. A., Lachlan-Cope, T., Field, P. F., & Boutle, I. A. (2020). Summertime cloud phase strongly influences surface melting on the Larsen C ice shelf, Antarctica. *Quarterly Journal of the Royal Meteorological Society*, *146*(729), 1575–1589. https://doi.org/10.1002/qj.3753

Gilbert, E., Orr, A., Renfrew, I. A., King, J. C., & Lachlan-Cope, T. (2022). A 20-Year Study of Melt Processes Over Larsen C Ice Shelf Using a High-Resolution Regional Atmospheric Model: 2. Drivers of Surface Melting. *Journal of Geophysical Research: Atmospheres*, *127*(8), e2021JD036012. https://doi.org/10.1029/2021JD036012

Glasser, N. F., Jennings, S. J. A., Hambrey, M. J., & Hubbard, B. (2015). Origin and dynamic significance of longitudinal structures ('flow stripes') in the Antarctic Ice Sheet. *Earth Surface Dynamics*, *3*(2), 239–249. https://doi.org/10.5194/esurf-3-239-2015

Glasser, N. F., & Gudmundsson, G. H. (2012). Longitudinal surface structures (flowstripes) on Antarctic glaciers. *The Cryosphere*, *6*(2), 383–391. https://doi.org/10.5194/tc-6-383-2012

Glasser, N. F., & Scambos, T. A. (2008). A structural glaciological analysis of the 2002 Larsen B ice-shelf collapse. *Journal of Glaciology*, *54*(184), 3–16. https://doi.org/10.3189/002214308784409017

Gledhill, L. A., & Williamson, A. G. (2018). Inland advance of supraglacial lakes in north-west Greenland under recent climatic warming. *Annals of Glaciology*, *59*(76pt1), 66–82. https://doi.org/10.1017/aog.2017.31

Gorelick, N., Hancher, M., Dixon, M., Ilyushchenko, S., Thau, D., & Moore, R. (2017). Google Earth Engine: Planetary-scale geospatial analysis for everyone. *Remote Sensing of Environment*, *202*, 18–27. https://doi.org/10.1016/j.rse.2017.06.031

Halberstadt, A. R. W., Gleason, C. J., Moussavi, M. S., Pope, A., Trusel, L. D., & DeConto, R. M. (2020). Antarctic Supraglacial Lake Identification Using

Landsat-8 Image Classification. *Remote Sensing*, *12*(8), 1327. https://doi.org/10.3390/rs12081327

Hochreuther, P., Neckel, N., Reimann, N., Humbert, A., & Braun, M. (2021). Fully Automated Detection of Supraglacial Lake Area for Northeast Greenland Using Sentinel-2 Time-Series. *Remote Sensing*, *13*(2), 205. https://doi.org/10.3390/rs13020205

Hodgson, D. A., Jordan, T. A., Ross, N., Riley, T. R., & Fretwell, P. T. (2022). Drainage and refill of an Antarctic Peninsula subglacial lake reveal an active subglacial hydrological network. *The Cryosphere*, *16*(12), 4797–4809. https://doi.org/10.5194/tc-16-4797-2022

Hosking, J. S., Orr, A., Bracegirdle, T. J., & Turner, J. (2016). Future circulation changes off West Antarctica: Sensitivity of the Amundsen Sea Low to projected anthropogenic forcing. *Geophysical Research Letters*, *43*(1), 367–376. https://doi.org/10.1002/2015GL067143

Howat, I. M., Porter, C., Smith, B. E., Noh, M.-J., & Morin, P. (2019). The Reference Elevation Model of Antarctica. *The Cryosphere*, *13*(2), 665–674. https://doi.org/10.5194/tc-13-665-2019

Hubbard, B., Luckman, A., Ashmore, D. W., Bevan, S., Kulessa, B., Kuipers Munneke, P., Philippe, M., Jansen, D., Booth, A., Sevestre, H., Tison, J.-L., O'Leary, M., & Rutt, I. (2016). Massive subsurface ice formed by refreezing of ice-shelf melt ponds. *Nature Communications*, *7*(1), 11897. https://doi.org/10.1038/ncomms11897

ICCI (2022). *State of the Cryosphere Report 2022 – ICCI – International Cryosphere Climate Initiative*. (n.d.). Retrieved 4 December 2022, from https://iccinet.org/statecryo2022/

Ignéczi, Á., Sole, A. J., Livingstone, S. J., Ng, F. S. L., & Yang, K. (2018). Greenland Ice Sheet Surface Topography and Drainage Structure Controlled by the Transfer of Basal Variability. *Frontiers in Earth Science*, *6*. https://www.frontiersin.org/articles/10.3389/feart.2018.00101

Iken, A. (1981). The Effect of the Subglacial Water Pressure on the Sliding Velocity of a Glacier in an Idealized Numerical Model. *Journal of Glaciology*, *27*(97), 407–421. https://doi.org/10.3189/S0022143000011448

Iken, A., & Bindschadler, R. A. (1986). Combined measurements of Subglacial Water Pressure and Surface Velocity of Findelengletscher, Switzerland: Conclusions about Drainage System and Sliding Mechanism. *Journal of Glaciology*, *32*(110), 101–119. https://doi.org/10.3189/S0022143000006936

Jackson, R. H., Nash, J. D., Kienholz, C., Sutherland, D. A., Amundson, J. M., Motyka, R. J., Winters, D., Skyllingstad, E., & Pettit, E. C. (2020). Meltwater Intrusions Reveal Mechanisms for Rapid Submarine Melt at a Tidewater Glacier.

Geophysical Research Letters, *47*(2), e2019GL085335.
https://doi.org/10.1029/2019GL085335

Jakobs, C. L., Reijmer, C. H., Kuipers Munneke, P., König-Langlo, G., & van den
Broeke, M. R. (2019). Quantifying the snowmelt–albedo feedback at Neumayer
Station, East Antarctica. *The Cryosphere*, *13*(5), 1473–1485.
https://doi.org/10.5194/tc-13-1473-2019

Jakobs, C. L., Reijmer, C. H., van den Broeke, M. R., van de Berg, W. J., & van
Wessem, J. M. (2021). Spatial Variability of the Snowmelt-Albedo Feedback in
Antarctica. *Journal of Geophysical Research: Earth Surface*, *126*(2).
https://doi.org/10.1029/2020JF005696

Jones, J. M., Gille, S. T., Goosse, H., Abram, N. J., Canziani, P. O., Charman, D. J.,
Clem, K. R., Crosta, X., de Lavergne, C., Eisenman, I., England, M. H., Fogt, R.
L., Frankcombe, L. M., Marshall, G. J., Masson-Delmotte, V., Morrison, A. K.,
Orsi, A. J., Raphael, M. N., Renwick, J. A., … Vance, T. R. (2016). Assessing
recent trends in high-latitude Southern Hemisphere surface climate. *Nature
Climate Change*, *6*(10), Art. 10. https://doi.org/10.1038/nclimate3103

Joughin, I., Das, S. B., Flowers, G. E., Behn, M. D., Alley, R. B., King, M. A., Smith,
B. E., Bamber, J. L., van den Broeke, M. R., & van Angelen, J. H. (2013).
Influence of ice-sheet geometry and supraglacial lakes on seasonal ice-flow
variability. *The Cryosphere*, *7*(4), 1185–1192. https://doi.org/10.5194/tc-7-1185-
2013

Kamb, B. (1987). Glacier surge mechanism based on linked cavity configuration of the
basal water conduit system. *Journal of Geophysical Research: Solid Earth*,
92(B9), 9083–9100. https://doi.org/10.1029/JB092iB09p09083

King, J. C., Kirchgaessner, A., Bevan, S., Elvidge, A. D., Kuipers Munneke, P.,
Luckman, A., Orr, A., Renfrew, I. A., & van den Broeke, M. R. (2017). The
Impact of Föhn Winds on Surface Energy Balance During the 2010–2011 Melt
Season Over Larsen C Ice Shelf, Antarctica. *Journal of Geophysical Research:
Atmospheres*, *122*(22), 12,062-12,076. https://doi.org/10.1002/2017JD026809

Kingslake, J., Ely, J. C., Das, I., & Bell, R. E. (2017). Widespread movement of
meltwater onto and across Antarctic ice shelves. *Nature*, *544*(7650), Art. 7650.
https://doi.org/10.1038/nature22049

Kingslake, J., Ng, F., & Sole, A. (2015). Modelling channelized surface drainage of
supraglacial lakes. *Journal of Glaciology*, *61*(225), 185–199.
https://doi.org/10.3189/2015JoG14J158

Koziol, C., Arnold, N., Pope, A., & Colgan, W. (2017). Quantifying supraglacial
meltwater pathways in the Paakitsoq region, West Greenland. *Journal of
Glaciology*, *63*(239), 464–476. https://doi.org/10.1017/jog.2017.5

References

Krawczynski, M. J., Behn, M. D., Das, S. B., & Joughin, I. (2009). Constraints on the lake volume required for hydro-fracture through ice sheets. *Geophysical Research Letters*, *36*(10). https://doi.org/10.1029/2008GL036765

Kuipers Munneke, P., Luckman, A. J., Bevan, S. L., Smeets, C. J. P. P., Gilbert, E., van den Broeke, M. R., Wang, W., Zender, C., Hubbard, B., Ashmore, D., Orr, A., King, J. C., & Kulessa, B. (2018). Intense Winter Surface Melt on an Antarctic Ice Shelf. *Geophysical Research Letters*, *45*(15), 7615–7623. https://doi.org/10.1029/2018GL077899

Lai, C. Y., Kingslake, J., Wearing, M. G., Chen, P.-H. C., Gentine, P., Li, H., Spergel, J. J., & van Wessem, J. M. (2020). Vulnerability of Antarctica's ice shelves to meltwater-driven fracture. *Nature*, *584*(7822), 574–578. https://doi.org/10.1038/s41586-020-2627-8

Langley, E. S., Leeson, A. A., Stokes, C. R., & Jamieson, S. S. R. (2016). Seasonal evolution of supraglacial lakes on an East Antarctic outlet glacier. *Geophysical Research Letters*, *43*(16), 8563–8571. https://doi.org/10.1002/2016GL069511

Le Brocq, A. M., Ross, N., Griggs, J. A., Bingham, R. G., Corr, H. F. J., Ferraccioli, F., Jenkins, A., Jordan, T. A., Payne, A. J., Rippin, D. M., & Siegert, M. J. (2013). Evidence from ice shelves for channelized meltwater flow beneath the Antarctic Ice Sheet. *Nature Geoscience*, *6*(11), Art. 11. https://doi.org/10.1038/ngeo1977

Lea, J., & Brough, S. (2019). *Supraglacial lake mapping of the entire Greenland Ice Sheet using Google Earth Engine. 2019*, C31A-1483.

Lea, J. M. (2018). The Google Earth Engine Digitisation Tool (GEEDiT) and the Margin change Quantification Tool (MaQiT) – simple tools for the rapid mapping and quantification of changing Earth surface margins. *Earth Surface Dynamics*, *6*(3), 551–561. https://doi.org/10.5194/esurf-6-551-2018

Leeson, A. A., Forster, E., Rice, A., Gourmelen, N., & van Wessem, J. M. (2020). Evolution of Supraglacial Lakes on the Larsen B Ice Shelf in the Decades Before it Collapsed. *Geophysical Research Letters*, *47*(4), e2019GL085591. https://doi.org/10.1029/2019GL085591

Lenaerts, J. T. M., Lhermitte, S., Drews, R., Ligtenberg, S. R. M., Berger, S., Helm, V., Smeets, C. J. P. P., Broeke, M. R. van den, van de Berg, W. J., van Meijgaard, E., Eijkelboom, M., Eisen, O., & Pattyn, F. (2017). Meltwater produced by wind–albedo interaction stored in an East Antarctic ice shelf. *Nature Climate Change*, *7*(1), 58–62. https://doi.org/10.1038/nclimate3180

Lenaerts, J. T. M., Ligtenberg, S. R. M., Medley, B., Berg, W. J. V. de, Konrad, H., Nicolas, J. P., Wessem, J. M. V., Trusel, L. D., Mulvaney, R., Tuckwell, R. J., Hogg, A. E., & Thomas, E. R. (2018). Climate and surface mass balance of coastal West Antarctica resolved by regional climate modelling. *Annals of Glaciology*, *59*(76pt1), 29–41. https://doi.org/10.1017/aog.2017.42

References

Li, X., Cai, W., Meehl, G. A., Chen, D., Yuan, X., Raphael, M., Holland, D. M., Ding, Q., Fogt, R. L., Markle, B. R., Wang, G., Bromwich, D. H., Turner, J., Xie, S.-P., Steig, E. J., Gille, S. T., Xiao, C., Wu, B., Lazzara, M. A., … Song, C. (2021). Tropical teleconnection impacts on Antarctic climate changes. *Nature Reviews Earth & Environment*, *2*(10), Art. 10. https://doi.org/10.1038/s43017-021-00204-5

Liang, D., Guo, H., Zhang, L., Cheng, Y., Zhu, Q., & Liu, X. (2021). Time-series snowmelt detection over the Antarctic using Sentinel-1 SAR images on Google Earth Engine. *Remote Sensing of Environment*, *256*, 112318. https://doi.org/10.1016/j.rse.2021.112318

Ligtenberg, S. R. M., Kuipers Munneke, P., & van den Broeke, M. R. (2014). Present and future variations in Antarctic firn air content. *The Cryosphere*, *8*(5), 1711–1723. https://doi.org/10.5194/tc-8-1711-2014

Livingstone, S. J., Chu, W., Ely, J. C., & Kingslake, J. (2017). Paleofluvial and subglacial channel networks beneath Humboldt Glacier, Greenland. *Geology*, *45*(6), 551–554. https://doi.org/10.1130/G38860.1

Luckman, A., Elvidge, A., Jansen, D., Kulessa, B., Kuipers Munneke, P., King, J., & Barrand, N. E. (2014). Surface melt and ponding on Larsen C Ice Shelf and the impact of föhn winds. *Antarctic Science*, *26*(6), 625–635. https://doi.org/10.1017/S0954102014000339

Lüthje, M., Feltham, D. L., Taylor, P. D., & Worster, M. G. (2006). Modeling the summertime evolution of sea-ice melt ponds. *Journal of Geophysical Research: Oceans*, *111*(C2). https://doi.org/10.1029/2004JC002818

MacAyeal, D. R., Scambos, T. A., Hulbe, C. L., & Fahnestock, M. A. (2003). Catastrophic ice-shelf break-up by an ice-shelf-fragment-capsize mechanism. *Journal of Glaciology*, *49*(164), 22–36. https://doi.org/10.3189/172756503781830863

Macdonald, G. J., Banwell, A. F., & MacAyeal, D. R. (2018). Seasonal evolution of supraglacial lakes on a floating ice tongue, Petermann Glacier, Greenland. *Annals of Glaciology*, *59*(76pt1), 56–65. https://doi.org/10.1017/aog.2018.9

MacFerrin, M., Machguth, H., As, D. van, Charalampidis, C., Stevens, C. M., Heilig, A., Vandecrux, B., Langen, P. L., Mottram, R., Fettweis, X., Broeke, M. R. van den, Pfeffer, W. T., Moussavi, M. S., & Abdalati, W. (2019). Rapid expansion of Greenland's low-permeability ice slabs. *Nature*, *573*(7774), Art. 7774. https://doi.org/10.1038/s41586-019-1550-3

Marshall, G. J. (2003). Trends in the Southern Annular Mode from Observations and Reanalyses. *Journal of Climate*, *16*(24), 4134–4143. https://doi.org/10.1175/1520-0442(2003)016<4134:TITSAM>2.0.CO;2

References

Marshall, G. J., Di Battista, S., Naik, S. S., & Thamban, M. (2011). Analysis of a regional change in the sign of the SAM–temperature relationship in Antarctica. *Climate Dynamics*, *36*(1), 277–287. https://doi.org/10.1007/s00382-009-0682-9

Marshall, G. J., & Thompson, D. W. J. (2016). The signatures of large-scale patterns of atmospheric variability in Antarctic surface temperatures. *Journal of Geophysical Research: Atmospheres*, *121*(7), 3276–3289. https://doi.org/10.1002/2015JD024665

Massom, R. A., Scambos, T. A., Bennetts, L. G., Reid, P., Squire, V. A., & Stammerjohn, S. E. (2018). Antarctic ice shelf disintegration triggered by sea ice loss and ocean swell. *Nature*, *558*(7710), Art. 7710. https://doi.org/10.1038/s41586-018-0212-1

McMillan, M., Nienow, P., Shepherd, A., Benham, T., & Sole, A. (2007). Seasonal evolution of supra-glacial lakes on the Greenland Ice Sheet. *Earth and Planetary Science Letters*, *262*(3–4), 484–492. https://doi.org/10.1016/j.epsl.2007.08.002

Miles, K. E., Willis, I. C., Benedek, C. L., Williamson, A. G., & Tedesco, M. (2017). Toward Monitoring Surface and Subsurface Lakes on the Greenland Ice Sheet Using Sentinel-1 SAR and Landsat-8 OLI Imagery. *Frontiers in Earth Science*, *5*, 58. https://doi.org/10.3389/feart.2017.00058

Montgomery, L., Miège, C., Miller, J., Scambos, T. A., Wallin, B., Miller, O., Solomon, D. K., Forster, R., & Koenig, L. (2020). Hydrologic Properties of a Highly Permeable Firn Aquifer in the Wilkins Ice Shelf, Antarctica. *Geophysical Research Letters*, *47*(22), e2020GL089552. https://doi.org/10.1029/2020GL089552

Moon, T., Joughin, I., Smith, B., van den Broeke, M. R., van de Berg, W. J., Noël, B., & Usher, M. (2014). Distinct patterns of seasonal Greenland glacier velocity. *Geophysical Research Letters*, *41*(20), 7209–7216. https://doi.org/10.1002/2014GL061836

Morlighem, M., Rignot, E., Binder, T., Blankenship, D., Drews, R., Eagles, G., Eisen, O., Ferraccioli, F., Forsberg, R., Fretwell, P., Goel, V., Greenbaum, J. S., Gudmundsson, H., Guo, J., Helm, V., Hofstede, C., Howat, I., Humbert, A., Jokat, W., … Young, D. A. (2020). Deep glacial troughs and stabilizing ridges unveiled beneath the margins of the Antarctic ice sheet. *Nature Geoscience*, *13*(2), Art. 2. https://doi.org/10.1038/s41561-019-0510-8

Morlighem, M., Williams, C. N., Rignot, E., An, L., Arndt, J. E., Bamber, J. L., Catania, G., Chauché, N., Dowdeswell, J. A., Dorschel, B., Fenty, I., Hogan, K., Howat, I., Hubbard, A., Jakobsson, M., Jordan, T. M., Kjeldsen, K. K., Millan, R., Mayer, L., … Zinglersen, K. B. (2017). BedMachine v3: Complete Bed Topography and Ocean Bathymetry Mapping of Greenland From Multibeam Echo Sounding Combined With Mass Conservation. *Geophysical Research Letters*, *44*(21), 11,051-11,061. https://doi.org/10.1002/2017GL074954

References

Mouginot, J., Rignot, E., & Scheuchl, B. (2014). Sustained increase in ice discharge from the Amundsen Sea Embayment, West Antarctica, from 1973 to 2013. *Geophysical Research Letters*, *41*(5), 1576–1584. https://doi.org/10.1002/2013GL059069

Moussavi, M. S., Abdalati, W., Pope, A., Scambos, T., Tedesco, M., MacFerrin, M., & Grigsby, S. (2016). Derivation and validation of supraglacial lake volumes on the Greenland Ice Sheet from high-resolution satellite imagery. *Remote Sensing of Environment*, *183*, 294–303. https://doi.org/10.1016/j.rse.2016.05.024

Moussavi, M., Pope, A., Halberstadt, A., Trusel, L., Cioffi, L., & Abdalati, W. (2020). Antarctic Supraglacial Lake Detection Using Landsat 8 and Sentinel-2 Imagery: Towards Continental Generation of Lake Volumes. *Remote Sensing*, *12*(1), 134. https://doi.org/10.3390/rs12010134

Munneke, P. K., Ligtenberg, S. R. M., Broeke, M. R. V. D., & Vaughan, D. G. (2014). Firn air depletion as a precursor of Antarctic ice-shelf collapse. *Journal of Glaciology*, *60*(220), 205–214. https://doi.org/10.3189/2014JoG13J183

Nanni, U., Gimbert, F., Vincent, C., Gräff, D., Walter, F., Piard, L., & Moreau, L. (2020). Quantification of seasonal and diurnal dynamics of subglacial channels using seismic observations on an Alpine glacier. *The Cryosphere*, *14*(5), 1475–1496. https://doi.org/10.5194/tc-14-1475-2020

Nienow, P., Sharp, M., & Willis, I. (1998). Seasonal changes in the morphology of the subglacial drainage system, Haut Glacier d'Arolla, Switzerland. *Earth Surface Processes and Landforms*, *23*(9), 825–843. https://doi.org/10.1002/(SICI)1096-9837(199809)23:9<825::AID-ESP893>3.0.CO;2-2

Noble, T. L., Rohling, E. J., Aitken, A. R. A., Bostock, H. C., Chase, Z., Gomez, N., Jong, L. M., King, M. A., Mackintosh, A. N., McCormack, F. S., McKay, R. M., Menviel, L., Phipps, S. J., Weber, M. E., Fogwill, C. J., Gayen, B., Golledge, N. R., Gwyther, D. E., Hogg, A. McC., … Williams, T. (2020). The Sensitivity of the Antarctic Ice Sheet to a Changing Climate: Past, Present, and Future. *Reviews of Geophysics*, *58*(4). https://doi.org/10.1029/2019RG000663

Nye, J. F. (1965). The Flow of a Glacier in a Channel of Rectangular, Elliptic or Parabolic Cross-Section. *Journal of Glaciology*, *5*(41), 661–690. https://doi.org/10.3189/S0022143000018670

Oppenheimer, M., Glavovic, B., Hinkel, J., van de Wal, R., Magnan, A. K., Abd-Elgawad, A., Cai, R., Cifuentes-Jara, M., Deconto, R. M., Ghosh, T., Hay, J., Isla, F., Marzeion, B., Meyssignac, B., & Sebesvari, Z. (2019). *Sea Level Rise and Implications for Low Lying Islands, Coasts and Communities*. https://repositorio.catie.ac.cr/handle/11554/9280

Orr, A., Deb, P., Clem, K. R., Gilbert, E., Bromwich, D. H., Boberg, F., Colwell, S., Hansen, N., Lazzara, M. A., Mooney, P. A., Mottram, R., Niwano, M., Phillips,

T., Pishniak, D., Reijmer, C. H., Berg, W. J. van de, Webster, S., & Zou, X. (2022). Characteristics of surface "melt potential" over Antarctic ice shelves based on regional atmospheric model simulations of summer air temperature extremes from 1979/80 to 2018/19. *Journal of Climate*, *1*(aop), 1–61. https://doi.org/10.1175/JCLI-D-22-0386.1

Oza, S. R., Singh, R. K. K., Vyas, N. K., & Sarkar, A. (2011). Study of inter-annual variations in surface melting over Amery Ice Shelf, East Antarctica, using space-borne scatterometer data. *Journal of Earth System Science*, *120*(2), 329–336. https://doi.org/10.1007/s12040-011-0055-8

Pérez-Cutillas, P., Pérez-Navarro, A., Conesa-García, C., Zema, D. A., & Amado-Álvarez, J. P. (2023). What is going on within google earth engine? A systematic review and meta-analysis. *Remote Sensing Applications: Society and Environment*, *29*, 100907. https://doi.org/10.1016/j.rsase.2022.100907

Phillips, H. A. (1998). Surface meltstreams on the Amery Ice Shelf, East Antarctica. *Annals of Glaciology*, *27*, 177–181. https://doi.org/10.3189/1998AoG27-1-177-181

Picard, G., Fily, M., & Gallee, H. (2007). Surface melting derived from microwave radiometers: A climatic indicator in Antarctica. *Annals of Glaciology*, *46*, 29–34. https://doi.org/10.3189/172756407782871684

Pollard, D., DeConto, R. M., & Alley, R. B. (2015). Potential Antarctic Ice Sheet retreat driven by hydrofracturing and ice cliff failure. *Earth and Planetary Science Letters*, *412*, 112–121. https://doi.org/10.1016/j.epsl.2014.12.035

Pope, A., Scambos, T. A., Moussavi, M., Tedesco, M., Willis, M., Shean, D., & Grigsby, S. (2016). Estimating supraglacial lake depth in West Greenland using Landsat 8 and comparison with other multispectral methods. *The Cryosphere*, *10*(1), 15–27. https://doi.org/10.5194/tc-10-15-2016

Raphael, M. N., Marshall, G. J., Turner, J., Fogt, R. L., Schneider, D., Dixon, D. A., Hosking, J. S., Jones, J. M., & Hobbs, W. R. (2016). The Amundsen Sea Low: Variability, Change, and Impact on Antarctic Climate. *Bulletin of the American Meteorological Society*, *97*(1), 111–121. https://doi.org/10.1175/BAMS-D-14-00018.1

Rignot, E., Casassa, G., Gogineni, P., Krabill, W., Rivera, A., & Thomas, R. (2004). Accelerated ice discharge from the Antarctic Peninsula following the collapse of Larsen B ice shelf. *Geophysical Research Letters*, *31*(18). https://doi.org/10.1029/2004GL020697

Rignot, E., Mouginot, J., Morlighem, M., Seroussi, H., & Scheuchl, B. (2014). Widespread, rapid grounding line retreat of Pine Island, Thwaites, Smith, and Kohler glaciers, West Antarctica, from 1992 to 2011. *Geophysical Research Letters*, *41*(10), 3502–3509. https://doi.org/10.1002/2014GL060140

Rignot, E., Velicogna, I., van den Broeke, M. R., Monaghan, A., & Lenaerts, J. T. M. (2011). Acceleration of the contribution of the Greenland and Antarctic ice sheets to sea level rise. *Geophysical Research Letters*, *38*(5). https://doi.org/10.1029/2011GL046583

Robel, A. A., Seroussi, H., & Roe, G. H. (2019). Marine ice sheet instability amplifies and skews uncertainty in projections of future sea-level rise. *Proceedings of the National Academy of Sciences*, *116*(30), 14887–14892. https://doi.org/10.1073/pnas.1904822116

Rosier, S. H. R., Reese, R., Donges, J. F., De Rydt, J., Gudmundsson, G. H., & Winkelmann, R. (2021). The tipping points and early warning indicators for Pine Island Glacier, West Antarctica. *The Cryosphere*, *15*(3), 1501–1516. https://doi.org/10.5194/tc-15-1501-2021

Röthlisberger, H. (1972). Water Pressure in Intra- and Subglacial Channels*. *Journal of Glaciology*, *11*(62), 177–203. https://doi.org/10.3189/S0022143000022188

Rott, H., Müller, F., Nagler, T., & Floricioiu, D. (2011). The imbalance of glaciers after disintegration of Larsen-B ice shelf, Antarctic Peninsula. *The Cryosphere*, *5*(1), 125–134. https://doi.org/10.5194/tc-5-125-2011

Rott, H., Wuite, J., De Rydt, J., Gudmundsson, G. H., Floricioiu, D., & Rack, W. (2020). Impact of marine processes on flow dynamics of northern Antarctic Peninsula outlet glaciers. *Nature Communications*, *11*(1), 2969. https://doi.org/10.1038/s41467-020-16658-y

Scambos, T. A., Bohlander, J. A., Shuman, C. A., & Skvarca, P. (2004). Glacier acceleration and thinning after ice shelf collapse in the Larsen B embayment, Antarctica. *Geophysical Research Letters*, *31*(18). https://doi.org/10.1029/2004GL020670

Scambos, T. A., Campbell, G. G., Pope, A., Haran, T., Muto, A., Lazzara, M., Reijmer, C. H., & van den Broeke, M. R. (2018). Ultralow Surface Temperatures in East Antarctica From Satellite Thermal Infrared Mapping: The Coldest Places on Earth. *Geophysical Research Letters*, *45*(12), 6124–6133. https://doi.org/10.1029/2018GL078133

Scambos, T. A., Hulbe, C., Fahnestock, M., & Bohlander, J. (2000). The link between climate warming and break-up of ice shelves in the Antarctic Peninsula. *Journal of Glaciology*, *46*(154), 516–530. https://doi.org/10.3189/172756500781833043

Scambos, T., Fricker, H. A., Liu, C.-C., Bohlander, J., Fastook, J., Sargent, A., Massom, R., & Wu, A.-M. (2009). Ice shelf disintegration by plate bending and hydro-fracture: Satellite observations and model results of the 2008 Wilkins ice shelf break-ups. *Earth and Planetary Science Letters*, *280*(1), 51–60. https://doi.org/10.1016/j.epsl.2008.12.027

References

Schoof, C. (2007). Ice sheet grounding line dynamics: Steady states, stability, and hysteresis. *Journal of Geophysical Research: Earth Surface*, *112*(F3). https://doi.org/10.1029/2006JF000664

Schoof, C. (2010). Ice-sheet acceleration driven by melt supply variability. *Nature*, *468*(7325), 803–806. https://doi.org/10.1038/nature09618

Selmes, N., Murray, T., & James, T. D. (2011). Fast draining lakes on the Greenland Ice Sheet. *Geophysical Research Letters*, *38*(15). https://doi.org/10.1029/2011GL047872

Selmes, N., Murray, T., & James, T. D. (2013). Characterizing supraglacial lake drainage and freezing on the Greenland Ice Sheet. *The Cryosphere Discussions*, *7*(1), 475–505. https://doi.org/10.5194/tcd-7-475-2013

Shiggins, C. J., Lea, J. M., & Brough, S. (2023). Automated ArcticDEM iceberg detection tool: Insights into area and volume distributions, and their potential application to satellite imagery and modelling of glacier–iceberg–ocean systems. *The Cryosphere*, *17*(1), 15–32. https://doi.org/10.5194/tc-17-15-2023

Slater, D. A., & Straneo, F. (2022). Submarine melting of glaciers in Greenland amplified by atmospheric warming. *Nature Geoscience*, *15*(10), Art. 10. https://doi.org/10.1038/s41561-022-01035-9

Smith, B., Fricker, H. A., Gardner, A. S., Medley, B., Nilsson, J., Paolo, F. S., Holschuh, N., Adusumilli, S., Brunt, K., Csatho, B., Harbeck, K., Markus, T., Neumann, T., Siegfried, M. R., & Zwally, H. J. (2020). Pervasive ice sheet mass loss reflects competing ocean and atmosphere processes. *Science*, *368*(6496), 1239–1242. https://doi.org/10.1126/science.aaz5845

Sneed, W. A., & Hamilton, G. S. (2007). Evolution of melt pond volume on the surface of the Greenland Ice Sheet. *Geophysical Research Letters*, *34*(3). https://doi.org/10.1029/2006GL028697

Sole, A., Nienow, P., Bartholomew, I., Mair, D., Cowton, T., Tedstone, A., & King, M. A. (2013). Winter motion mediates dynamic response of the Greenland Ice Sheet to warmer summers: Interannual Greenland Ice Flow Changes. *Geophysical Research Letters*, *40*(15), 3940–3944. https://doi.org/10.1002/grl.50764

Spergel, J. J., Kingslake, J., Creyts, T., van Wessem, M., & Fricker, H. A. (2021). Surface meltwater drainage and ponding on Amery Ice Shelf, East Antarctica, 1973–2019. *Journal of Glaciology*, *67*(266), 985–998. https://doi.org/10.1017/jog.2021.46

Steig, E. J., Schneider, D. P., Rutherford, S. D., Mann, M. E., Comiso, J. C., & Shindell, D. T. (2009). Warming of the Antarctic ice-sheet surface since the 1957 International Geophysical Year. *Nature*, *457*(7228), Art. 7228. https://doi.org/10.1038/nature07669

Stevens, L. A., Nettles, M., Davis, J. L., Creyts, T. T., Kingslake, J., Hewitt, I. J., & Stubblefield, A. (2022). Tidewater-glacier response to supraglacial lake drainage. *Nature Communications*, *13*(1), Art. 1. https://doi.org/10.1038/s41467-022-33763-2

Stokes, C. R., Abram, N. J., Bentley, M. J., Edwards, T. L., England, M. H., Foppert, A., Jamieson, S. S. R., Jones, R. S., King, M. A., Lenaerts, J. T. M., Medley, B., Miles, B. W. J., Paxman, G. J. G., Ritz, C., van de Flierdt, T., & Whitehouse, P. L. (2022). Response of the East Antarctic Ice Sheet to past and future climate change. *Nature*, *608*(7922), Art. 7922. https://doi.org/10.1038/s41586-022-04946-0

Stokes, C. R., Sanderson, J. E., Miles, B. W. J., Jamieson, S. S. R., & Leeson, A. A. (2019). Widespread distribution of supraglacial lakes around the margin of the East Antarctic Ice Sheet. *Scientific Reports*, *9*(1), 13823. https://doi.org/10.1038/s41598-019-50343-5

Sundal, A. V., Shepherd, A., Nienow, P., Hanna, E., Palmer, S., & Huybrechts, P. (2009). Evolution of supra-glacial lakes across the Greenland Ice Sheet. *Remote Sensing of Environment*, *113*(10), 2164–2171. https://doi.org/10.1016/j.rse.2009.05.018

Tedesco, M., Willis, I. C., Hoffman, M. J., Banwell, A. F., Alexander, P., & Arnold, N. S. (2013). Ice dynamic response to two modes of surface lake drainage on the Greenland ice sheet. *Environmental Research Letters*, *8*(3), 034007. https://doi.org/10.1088/1748-9326/8/3/034007

Tedstone, A. J., Nienow, P. W., Gourmelen, N., Dehecq, A., Goldberg, D., & Hanna, E. (2015). Decadal slowdown of a land-terminating sector of the Greenland Ice Sheet despite warming. *Nature*, *526*(7575), Art. 7575. https://doi.org/10.1038/nature15722

Tedstone, A. J., Nienow, P. W., Sole, A. J., Mair, D. W. F., Cowton, T. R., Bartholomew, I. D., & King, M. A. (2013). Greenland ice sheet motion insensitive to exceptional meltwater forcing. *Proceedings of the National Academy of Sciences*, *110*(49), 19719–19724. https://doi.org/10.1073/pnas.1315843110

The IMBIE team. (2018). Mass balance of the Antarctic Ice Sheet from 1992 to 2017. *Nature*, *558*(7709), 219–222. https://doi.org/10.1038/s41586-018-0179-y

Thompson, D. W. J., & Wallace, J. M. (2000). Annular Modes in the Extratropical Circulation. Part I: Month-to-Month Variability. *Journal of Climate*, *13*(5), 1000–1016. https://doi.org/10.1175/1520-0442(2000)013<1000:AMITEC>2.0.CO;2

References

Trusel, L. D., Frey, K. E., & Das, S. B. (2012). Antarctic surface melting dynamics: Enhanced perspectives from radar scatterometer data. *Journal of Geophysical Research: Earth Surface*, *117*(F2). https://doi.org/10.1029/2011JF002126

Trusel, L. D., Frey, K. E., Das, S. B., Karnauskas, K. B., Kuipers Munneke, P., van Meijgaard, E., & van den Broeke, M. R. (2015). Divergent trajectories of Antarctic surface melt under two twenty-first-century climate scenarios. *Nature Geoscience*, *8*(12), Art. 12. https://doi.org/10.1038/ngeo2563

Trusel, L. D., Frey, K. E., Das, S. B., Munneke, P. K., & van den Broeke, M. R. (2013). Satellite-based estimates of Antarctic surface meltwater fluxes. *Geophysical Research Letters*, *40*(23), 6148–6153. https://doi.org/10.1002/2013GL058138

Trusel, L. D., Pan, Z., & Moussavi, M. (2022). Repeated Tidally Induced Hydrofracture of a Supraglacial Lake at the Amery Ice Shelf Grounding Zone. *Geophysical Research Letters*, *49*(7), e2021GL095661. https://doi.org/10.1029/2021GL095661

Tuckett, P. A., Ely, J. C., Sole, A. J., Livingstone, S. J., Davison, B. J., Melchior van Wessem, J., & Howard, J. (2019). Rapid accelerations of Antarctic Peninsula outlet glaciers driven by surface melt. *Nature Communications*, *10*(1), 4311. https://doi.org/10.1038/s41467-019-12039-2

Tuckett, P. A., Ely, J. C., Sole, A. J., Livingstone, S. J., Davison, B. J., & van Wessem, J. M. (2020). Reply to: "Impact of marine processes on flow dynamics of northern Antarctic Peninsula outlet glaciers" by Rott et al. *Nature Communications*, *11*(1), 2970. https://doi.org/10.1038/s41467-020-16685-9

Turner, J., Bindschadler, R., Convey, P., Di Prisco, G., Fahrbach, E., Gutt, J., Hodgson, D., Mayewski, P. A., & Summerhayes, C. P. (Eds.). (2009). *Antarctic climate change and the environment: A contribution to the International Polar Year 2007 - 2008*. Scientific Committee on Antarctic Research.

Turner, J., Colwell, S. R., Marshall, G. J., Lachlan-Cope, T. A., Carleton, A. M., Jones, P. D., Lagun, V., Reid, P. A., & Iagovkina, S. (2005). Antarctic climate change during the last 50 years. *International Journal of Climatology*, *25*(3), 279–294. https://doi.org/10.1002/joc.1130

Turner, J., Marshall, G. J., Clem, K., Colwell, S., Phillips, T., & Lu, H. (2020). Antarctic temperature variability and change from station data. *International Journal of Climatology*, *40*(6), 2986–3007. https://doi.org/10.1002/joc.6378

Turner, J., Orr, A., Gudmundsson, G. H., Jenkins, A., Bingham, R. G., Hillenbrand, C.-D., & Bracegirdle, T. J. (2017). Atmosphere-ocean-ice interactions in the Amundsen Sea Embayment, West Antarctica. *Reviews of Geophysics*, *55*(1), 235–276. https://doi.org/10.1002/2016RG000532

van de Wal, R. S. W., Smeets, C. J. P. P., Boot, W., Stoffelen, M., van Kampen, R., Doyle, S. H., Wilhelms, F., van den Broeke, M. R., Reijmer, C. H., Oerlemans,

J., & Hubbard, A. (2015). Self-regulation of ice flow varies across the ablation area in south-west Greenland. *The Cryosphere*, *9*(2), 603–611. https://doi.org/10.5194/tc-9-603-2015

van Wessem, J. M., Reijmer, C. H., Morlighem, M., Mouginot, J., Rignot, E., Medley, B., Joughin, I., Wouters, B., Depoorter, M. A., Bamber, J. L., Lenaerts, J. T. M., Berg, W. J. V. D., Broeke, M. R. V. D., & Meijgaard, E. V. (2014). Improved representation of East Antarctic surface mass balance in a regional atmospheric climate model. *Journal of Glaciology*, *60*(222), 761–770. https://doi.org/10.3189/2014JoG14J051

van Wessem, J. M., Ligtenberg, S. R. M., Reijmer, C. H., van de Berg, W. J., van den Broeke, M. R., Barrand, N. E., Thomas, E. R., Turner, J., Wuite, J., Scambos, T. A., & van Meijgaard, E. (2016). The modelled surface mass balance of the Antarctic Peninsula at 5.5 km horizontal resolution. *The Cryosphere*, *10*(1), 271–285. https://doi.org/10.5194/tc-10-271-2016

van Wessem, J. M., van de Berg, W. J., Noël, B. P. Y., van Meijgaard, E., Amory, C., Birnbaum, G., Jakobs, C. L., Krüger, K., Lenaerts, J. T. M., Lhermitte, S., Ligtenberg, S. R. M., Medley, B., Reijmer, C. H., van Tricht, K., Trusel, L. D., van Ulft, L. H., Wouters, B., Wuite, J., & van den Broeke, M. R. (2018). Modelling the climate and surface mass balance of polar ice sheets using RACMO2 – Part 2: Antarctica (1979–2016). *The Cryosphere*, *12*(4), 1479–1498. https://doi.org/10.5194/tc-12-1479-2018

van Wessem, J. M., Steger, C. R., Wever, N., & van den Broeke, M. R. (2021). An exploratory modelling study of perennial firn aquifers in the Antarctic Peninsula for the period 1979–2016. *The Cryosphere*, *15*(2), 695–714. https://doi.org/10.5194/tc-15-695-2021

van Wessem, J. M., van den Broeke, M. R., Wouters, B., & Lhermitte, S. (2023). Variable temperature thresholds of melt pond formation on Antarctic ice shelves. *Nature Climate Change*, 1–6. https://doi.org/10.1038/s41558-022-01577-1

Verjans, V., Leeson, A. A., Stevens, C. M., MacFerrin, M., Noël, B., & van den Broeke, M. R. (2019). Development of physically based liquid water schemes for Greenland firn-densification models. *The Cryosphere*, *13*(7), 1819–1842. https://doi.org/10.5194/tc-13-1819-2019

Walker, C. C., Becker, M. K., & Fricker, H. A. (2021). A High Resolution, Three-Dimensional View of the D-28 Calving Event From Amery Ice Shelf With ICESat-2 and Satellite Imagery. *Geophysical Research Letters*, *48*(3). https://doi.org/10.1029/2020GL091200

Wallis, B., Hogg, A., Davison, B., & Broeke, M. van den. (2022). *Seasonal ice velocity variability of Western Antarctic Peninsula tidewater glaciers from high*

temporal resolution Sentinel-1 imagery (No. EGU22-5462). EGU22. Copernicus Meetings. https://doi.org/10.5194/egusphere-egu22-5462

Warner, R. C., Fricker, H. A., Adusumilli, S., Arndt, P., Kingslake, J., & Spergel, J. J. (2021). Rapid Formation of an Ice Doline on Amery Ice Shelf, East Antarctica. *Geophysical Research Letters*, *48*(14), e2020GL091095. https://doi.org/10.1029/2020GL091095

Weertman, J. (1973). Can a water filled crevasse reach the bottom surface of a glacier? *IAHS Publ.*, *95*, 139–145.

Wei, W., Blankenship, D. D., Greenbaum, J. S., Gourmelen, N., Dow, C. F., Richter, T. G., Greene, C. A., Young, D. A., Lee, S., Kim, T.-W., Lee, W. S., & Assmann, K. M. (2020). Getz Ice Shelf melt enhanced by freshwater discharge from beneath the West Antarctic Ice Sheet. *The Cryosphere*, *14*(4), 1399–1408. https://doi.org/10.5194/tc-14-1399-2020

Wille, J. D., Favier, V., Gorodetskaya, I. V., Agosta, C., Kittel, C., Beeman, J. C., Jourdain, N. C., Lenaerts, J. T. M., & Codron, F. (2021). Antarctic Atmospheric River Climatology and Precipitation Impacts. *Journal of Geophysical Research: Atmospheres*, *126*(8), e2020JD033788. https://doi.org/10.1029/2020JD033788

Williamson, A. G., Arnold, N. S., Banwell, A. F., & Willis, I. C. (2017). A Fully Automated Supraglacial lake area and volume Tracking ("FAST") algorithm: Development and application using MODIS imagery of West Greenland. *Remote Sensing of Environment*, *196*, 113–133. https://doi.org/10.1016/j.rse.2017.04.032

Williamson, A. G., Banwell, A. F., Willis, I. C., & Arnold, N. S. (2018). Dual-satellite (Sentinel-2 and Landsat 8) remote sensing of supraglacial lakes in Greenland. *The Cryosphere*, *12*(9), 3045–3065. https://doi.org/10.5194/tc-12-3045-2018

Wyatt, F. R., & Sharp, M. J. (2015). Linking surface hydrology to flow regimes and patterns of velocity variability on Devon Ice Cap, Nunavut. *Journal of Glaciology*, *61*(226), 387–399. https://doi.org/10.3189/2015JoG14J109

Yang, K., Smith, L. C., Sole, A., Livingstone, S. J., Cheng, X., Chen, Z., & Li, M. (2019). Supraglacial rivers on the northwest Greenland Ice Sheet, Devon Ice Cap, and Barnes Ice Cap mapped using Sentinel-2 imagery. *International Journal of Applied Earth Observation and Geoinformation*, *78*, 1–13. https://doi.org/10.1016/j.jag.2019.01.008

Zheng, Y., Golledge, N. R., Gossart, A., Picard, G., & Leduc-Leballeur, M. (2022). Estimating surface melt in Antarctica from 1979 to 2022, using a statistically parameterized positive degree-day model. *The Cryosphere Discussions*, 1–38. https://doi.org/10.5194/tc-2022-192

Zhu, D., Zhou, C., Zhu, Y., & Peng, B. (2022). Evolution of supraglacial lakes on Sermeq Avannarleq glacier, Greenland using Google Earth Engine. *Journal of*

Hydrology: Regional Studies, *44*, 101246.
https://doi.org/10.1016/j.ejrh.2022.101246

Zwally, H. J., Abdalati, W., Herring, T., Larson, K., Saba, J., & Steffen, K. (2002).
Surface Melt-Induced Acceleration of Greenland Ice-Sheet Flow. *Science*,
297(5579), 218–222. https://doi.org/10.1126/science.1072708